

UNITED STATES AIR FORCE
SUMMER RESEARCH PROGRAM -- 1995
SUMMER FACULTY RESEARCH PROGRAM FINAL REPORTS

VOLUME 3A

PHILLIPS LABORATORY

RESEARCH & DEVELOPMENT LABORATORIES
5800 Uplander Way
Culver City, CA 90230-6608

Program Director, RDL
Gary Moore

Program Manager, AFOSR
Major David Hart

Program Manager, RDL
Scott Licoscos

Program Administrator, RDL
Gwendolyn Smith

Program Administrator
Johnetta Thompson

Submitted to:

AIR FORCE OFFICE OF SCIENTIFIC RESEARCH

Bolling Air Force Base
Washington, D.C.

December 1995

Reproduced From
Best Available Copy

19981218 061

REPORT DOCUMENTATION PAGE

Form Approved
OMB No. 0704-0188

bring
in of
Suite

Public reporting burden for this collection of information is estimated to average 1 hour per response, including the and maintaining the data needed, and completing and reviewing the collection of information. Send comments information, including suggestions for reducing this burden, to Washington Headquarters Services, Directorate for 1204, Arlington, VA 22202-4302, and to the Office of Management and Budget, Paperwork Reduction Project (0704-

1. AGENCY USE ONLY (Leave Blank)	2. REPORT DATE December, 1995	3. REPORT Final
----------------------------------	----------------------------------	--------------------

AFRL-SR-BL-TR-98-

0826

4. TITLE AND SUBTITLE

USAF Summer Research Program - 1995 Summer Faculty Research Program
Final Reports, Volume 3A, Phillips Laboratory

5. FUNDING NUMBERS

6. AUTHORS

Gary Moore

7. PERFORMING ORGANIZATION NAME(S) AND ADDRESS(ES)

Research and Development Labs, Culver City, CA

8. PERFORMING ORGANIZATION
REPORT NUMBER

9. SPONSORING/MONITORING AGENCY NAME(S) AND ADDRESS(ES)

AFOSR/NI
4040 Fairfax Dr, Suite 500
Arlington, VA 22203-1613

10. SPONSORING/MONITORING
AGENCY REPORT NUMBER

11. SUPPLEMENTARY NOTES

Contract Number: F49620-93-C-0063

12a. DISTRIBUTION AVAILABILITY STATEMENT

Approved for Public Release

12b. DISTRIBUTION CODE

13. ABSTRACT (Maximum 200 words)

The United States Air Force Summer Faculty Research Program (USAF- SFRP) is designed to introduce university, college, and technical institute faculty members to Air Force research. This is accomplished by the faculty members being selected on a nationally advertised competitive basis during the summer intersession period to perform research at Air Force Research Laboratory Technical Directorates and Air Force Air Logistics Centers. Each participant provided a report of their research, and these reports are consolidated into this annual report.

14. SUBJECT TERMS

AIR FORCE RESEARCH, AIR FORCE, ENGINEERING, LABORATORIES, REPORTS, SUMMER,
UNIVERSITIES

15. NUMBER OF PAGES

16. PRICE CODE

17. SECURITY CLASSIFICATION
OF REPORT

Unclassified

18. SECURITY CLASSIFICATION
OF THIS PAGE

Unclassified

19. SECURITY CLASSIFICATION
OF ABSTRACT

Unclassified

20. LIMITATION OF ABSTRACT

UL

PREFACE

Reports in this volume are numbered consecutively beginning with number 1. Each report is paginated with the report number followed by consecutive page numbers, e.g., 1-1, 1-2, 1-3; 2-1, 2-2, 2-3.

Due to its length, Volume 3 is bound in two parts, 3A and 3B. Volume 3A contains #1-21, and Volume 3B contains reports #22-39. The Table of Contents for Volume 3 is included in both parts.

This document is one of a set of 16 volumes describing the 1995 AFOSR Summer Research Program. The following volumes comprise the set:

<u>VOLUME</u>	<u>TITLE</u>
1	Program Management Report <i>Summer Faculty Research Program (SFRP) Reports</i>
2A & 2B	Armstrong Laboratory
3A & 3B	Phillips Laboratory
4	Rome Laboratory
5A, 5B, & 5C	Wright Laboratory
6A & 6B	Arnold Engineering Development Center, Wilford Hall Medical Center and Air Logistics Centers <i>Graduate Student Research Program (GSRP) Reports</i>
7A & 7B	Armstrong Laboratory
8	Phillips Laboratory
9	Rome Laboratory
10A & 10B	Wright Laboratory
11	Arnold Engineering Development Center, Wilford Hall Medical Center and Air Logistics Centers <i>High School Apprenticeship Program (HSAP) Reports</i>
12A & 12B	Armstrong Laboratory
13	Phillips Laboratory
14	Rome Laboratory
15A&15B	Wright Laboratory
16	Arnold Engineering Development Center

SFRP FINAL REPORT TABLE OF CONTENTS

i-xiv

1. INTRODUCTION	1
2. PARTICIPATION IN THE SUMMER RESEARCH PROGRAM	2
3. RECRUITING AND SELECTION	3
4. SITE VISITS	4
5. HBCU/MI PARTICIPATION	4
6. SRP FUNDING SOURCES	5
7. COMPENSATION FOR PARTICIPATIONS	5
8. CONTENTS OF THE 1995 REPORT	6

APPENDICIES:

A. PROGRAM STATISTICAL SUMMARY	A-1
B. SRP EVALUATION RESPONSES	B-1

SFRP FINAL REPORTS

PERFORMANCE ANALYSIS OF HIGH THROUGHPUT OPTICAL COMMUNICATION NETWORKS

Behnaam Aazhang
Professor
Department of Electrical and Computer Engineering

Rice University
6100 S. Main
Houston, Texas 77251-1892

Final Report for:
Summer Faculty Research Program
Phillips Laboratory

Sponsored by:
Air Force Office of Scientific Research
Bolling Air Force Base, DC

and

Phillips Laboratory

October 20, 1995

PERFORMANCE ANALYSIS OF HIGH THROUGHPUT OPTICAL COMMUNICATION NETWORKS

Behnaam Aazhang
Professor
Department of Electrical and Computer Engineering
Rice University
Houston, Texas 77251-1892

Abstract

Practical, very high speed networks are critical to support the next generation of information technology applications, such as high-performance computing environments, access to vast electronic libraries, and multimedia communication of voice, data, graphics, and video for business, medical, and industrial needs. In this research program, we designed and demonstrated a novel multiuser optical communication network based on bipolar data encoding and decoding technology. The research work under Air Force Summer Faculty program concentrate on performance analysis of the proposed system. This novel multiuser system successfully meets the challenge of using the enormous bandwidths of optical channels by placing the burden of handling high bit rates on simple optics, rather than on ultrafast electronics or complex laser sources, making practical and economical implementation a real near-term possibility.

PERFORMANCE ANALYSIS OF HIGH THROUGHPUT OPTICAL COMMUNICATION NETWORKS

Behnaam Aazhang

Introduction

Optical networks have the potential of providing unprecedented low cost telecommunication capacity by dramatically reducing the cost per unit bandwidth. These gains will have the greatest impact as completely optical, local and metropolitan area networks, consisting of many users communicating simultaneously over a common, passive optical channel, replace traditional point-to-point links containing signal repeaters and switching electronics. Practical, very high speed networks are critical to support the next generation of information technology applications, such as high-performance computing environments, access to vast electronic libraries, and multimedia communication of voice, data, graphics, and video for business, medical, and industrial needs. This project is an interdisciplinary program to design, prototype, and evaluate a multiuser optical communication network based on novel data encoding and decoding technology that we have developed. This approach successfully meets the challenge of using the enormous bandwidths of optical channels by placing the burden of handling high bit rates on simple optics, rather than on ultrafast electronics or complex laser sources, making practical and economical implementation a real near-term possibility. Rapid development of this technology and the early implementation of optical networks will put industries in the U.S. in a unique competitive position during the next decade.

Methodology

The next generation of communication networks must be able to simultaneously serve many users and many types of applications with differing requirements for bandwidth, throughput, reliability, and security; capacities approaching a terahertz will be required. Despite the rapid progress of optical communications research, current optical communication systems utilize only a small fraction of the available bandwidth. Our approach is based on code division multiple access (CDMA), a dynamic and highly tolerant alternative to time and frequency division that has received considerable attention in the research community in the last few years [1, 2, 3, 4, 5, 6, 7]. In CDMA, each user is assigned a code as an address on a commonly shared channel. A high bandwidth channel allows the assignment of codes to a large number of users, all of whom can access the channel simultaneously, asynchronously, and at differing bit

rates. In addition, CDMA provides security against unauthorized users, and reduces interference.

In the radio frequency domain, CDMA, or spread spectrum, uses phase modulation coding. The phase of an optical signal, however, is quickly scrambled by fiber dispersion. We propose spread spectrum bipolar encoding in the optical frequency domain, which eliminates optical phase and pulse length as a source parameter, reduces dispersion as a channel constraint, and greatly increases the number of available codes and users. Consider a length- N bipolar sequence $x(n)$ that takes values from $\{-1, 1\}$; $x(n)$ can be expressed as the difference of two length- N unipolar sequences, say $u(n)$ and $\bar{u}(n)$, that take values from $\{0, 1\}$, where $u(n)$ is obtained from $x(n)$ by replacing each -1 with 0 and $\bar{u}(n)$ is its binary complement. That is: $x(n) = u(n) - \bar{u}(n)$, with $u(n) \triangleq [1 + x(n)]/2$, and $\bar{u}(n) \triangleq [1 - x(n)]/2$. Similarly, let $v(n)$ be the unipolar sequence obtained from a length- N bipolar sequence $y(n)$. Then the periodic and aperiodic crosscorrelation functions of $x(n)$ and $y(n)$ can be computed in terms of the unipolar crosscorrelation functions as follows:

$$\begin{aligned}\theta_{x,y}(l) &\triangleq \sum_{n=0}^{N-1} x(n)y(n+l) \\ &= [\theta_{u,v}(l) + \theta_{\bar{u},\bar{v}}(l)] - [\theta_{u,\bar{v}}(l) + \theta_{\bar{u},v}(l)]\end{aligned}\quad (1)$$

$$C_{x,y}(l) \triangleq \begin{cases} \sum_{n=0}^{N-1-l} x(n)y(n+l), & 0 \leq l \leq N-1 \\ \sum_{n=0}^{N-1+l} x(n-l)y(n), & 1-N \leq l \leq 0 \\ 0, & |l| \geq N \end{cases} = [C_{u,v}(l) + C_{\bar{u},\bar{v}}(l)] - [C_{u,\bar{v}}(l) + C_{\bar{u},v}(l)] \quad (2)$$

The transmitted symbols for the j^{th} user are encoded by two intensity modulation waveforms arriving at the receiver:

$$\begin{aligned}s_A^j(t) &= \lambda_j \left\{ \sum_{i=-\infty}^{\infty} [b_{j,i} \sum_{n=0}^{N-1} U_j(n) \Pi_{T_c}(t - nT_c - iT) + \right. \\ &\quad \left. \bar{b}_{j,i} \sum_{n=0}^{N-1} \bar{U}_j(n) \Pi_{T_c}(t - nT_c - iT)] \right\}\end{aligned}\quad (3)$$

$$\begin{aligned}s_B^j(t) &= \lambda_j \left\{ \sum_{i=-\infty}^{\infty} [b_{j,i} \sum_{n=0}^{N-1} \bar{U}_j(n) \Pi_{T_c}(t - nT_c - iT) + \right. \\ &\quad \left. \bar{b}_{j,i} \sum_{n=0}^{N-1} U_j(n) \Pi_{T_c}(t - nT_c - iT)] \right\},\end{aligned}\quad (4)$$

where $b_{j,i}$ is the i^{th} binary, $+1/0$, symbol; $\Pi_{T_c}(t)$ is the unit rectangular chip waveform that is zero outside $[0, T_c]$; T , T_c are the symbol and chip duration, respectively, and λ_j is the chip intensity. The signature

sequences $U_j(n)$ and $\bar{U}_j(n)$ are obtained from a length-N bipolar codeword as above. User j is decoded according to (1) and (2) with two identical matched filter pairs. Each pair has two unipolar matched filters with impulse responses $h_j(t) = \sum_{n=0}^{N-1} U_j(N-1-n)\Pi_{T_c}(t-nT_c)$, and $\bar{h}_j(t) = \sum_{n=0}^{N-1} \bar{U}_j(N-1-n)\Pi_{T_c}(t-nT_c)$. The outputs of each of the two complementary unipolar correlator pairs are optically summed and photodetected. The two photodiodes are connected in a balanced configuration so that their outputs are subtracted. The result is low-pass filtered and threshold-compared to zero to estimate the transmitted symbol.

As the matched filter pairs are identical, a configuration that requires only one pair and one photodetector is feasible. This is accomplished with an appropriate repetitive transmission, by which the symbols are Manchester-coded prior to modulation. The decoder consists of one unipolar correlator pair and one photodetector followed by a half-symbol delay and a comparator as illustrated in Fig. 2. We note that a particular case of the above general schemes, for which $U_j = (1)$, can be viewed as the binary PPM or non-coherent FSK modulation system.

We can also consider the proposed scheme in the general context of a multi-channel optical CDMA approach that assumes the shot noise nature for the photodetection process. The maximum likelihood (ML) detection for multidimensional waveforms in the Gaussian channel has been shown to be a straightforward extension of the single waveform case. Here we seek to show that the proposed scheme is the result of the maximum likelihood detection for a multi-channel optical CDMA that distributes the spreading codes over many channels to overcome the restrictions on the signal set.

The intensity of the optical source of user j is modulated by two sets of Q-dimensional, unipolar, codes \underline{u}_j and \underline{v}_j of length N according to the transmitting symbol b_j , onto Q channels. The Q-dimensional intensity waveforms $\underline{s}_r(t)$ arriving at the detector due to M simultaneously active users are given by:

$$\underline{s}_r(t) = \sum_{i=1}^M \underline{s}_j(t), \quad (5)$$

where

$$\begin{aligned} \underline{s}_j(t) &= \lambda_j \left\{ \sum_{i=-\infty}^{\infty} [b_{j,i} \sum_{n=0}^{N-1} \underline{u}_j(n) \Pi_{T_c}(t - nT_c - iT) + \right. \\ &\quad \left. \bar{b}_{j,i} \sum_{n=0}^{N-1} \underline{v}_j(n) \Pi_{T_c}(t - nT_c - iT)] \right\} \end{aligned} \quad (6)$$

The photodetectors, one for each channel, are modeled as Q independent Poisson counting processes whose outputs are i.i.d. Poisson random vectors:

$$\underline{K}^T = [\underline{K}_1^T \dots \underline{K}_Q^T], \quad (7)$$

where \underline{K}_q^T is a length- N vector whose elements are the counts measured by the q^{th} detector during each chip interval T_c in a symbol period NT_c . These elements are thus i.i.d. Poisson random variables. Without loss of generality, let user 1 be the desired user. In this study, we assume that the dark current intensities of the photodetectors are identical. Then if the users transmit their symbols synchronously, the ML statistics for user 1 can be shown to be

$$\Lambda_1 = \underline{K}^T (\underline{u}_1 - \underline{v}_1), \quad (8)$$

if and only if the Q -dimensional unipolar codes are orthogonal, i.e:

$$\underline{u}_j^T (\underline{u}_1 - \underline{v}_1) = \underline{v}_j^T (\underline{u}_1 - \underline{v}_1) = 0, j \neq 1. \quad (9)$$

For equal *a priori* symbol probabilities, the corresponding ML threshold is zero. Thus among the unipolar codes \underline{u}_1 and \underline{v}_1 , the probability of error is minimized if and only if $\underline{v}_1 = \underline{u}_1$. This also maximizes the signal distance $E[\Lambda_1|b_1 = 1] - E[\Lambda_1|b_1 = 0]$.

We now can specialize the above results for the 2-channel case. If $Q = 2$, we obtain from (9) that:

$$\underline{u}_j^T = [\underline{U}_j \quad \underline{\bar{U}}_j], \quad (10)$$

where \underline{U}_j is the unipolar code obtained from an orthogonal bipolar sequence in the manner previously discussed. The ML statistics can then be expressed as

$$\Lambda_1 = (\underline{K}_1^T \underline{U}_j + \underline{K}_2^T \underline{\bar{U}}_j) - (\underline{K}_1^T \underline{\bar{U}}_j + \underline{K}_2^T \underline{U}_j). \quad (11)$$

This is identical to the formula given by (1) and (2). We then invoke the infinitely divisible property of the Poisson random variables, allowing the correlations in (11) to be performed optically prior to photodetections.

The above formulation thus generalizes the notion of orthogonality of the spreading codes, allowing their design to be tailored to the physical communication channel. We believe that a similar multi-channel CDMA approach in the RF, or Gaussian, channel would also allow greater flexibility in the code design there. For example, there it could provide a mean to implement direct-sequence spread spectrum modulation across channels that have non-contiguous transmission bandwidths, without resorting to the hybrid frequency hopping methods. Thus, combining channel attributes into the code designs can be advantageous in both optical and radio domains.

Results

In this report, the tasks that have been completed with partial support from the Air Force Office of Scientific Research will be described.

We developed simulations blocks for the analysis of the multiuser system using the commercial block-oriented software package SPW. The SPW package is designed for RF systems, not optical systems, therefore, we had to construct new blocks to extend the applications to optical domain. The determination of error rates for high performance systems is a difficult, or at least time consuming, problem, both in monte carlo simulations and in practice. We have had some initial successes in applying the analytical technique Importance Sampling to our SPW simulations. This has reduced the time for calculations for low error rate (10^{-6}) systems from about a day to 10 minutes. We are still investigating this approach, verifying its validity and adding more efficient blocks for a complete simulations.

We can also report the first experimental demonstration of the spectral amplitude encoding and decoding technique, described earlier, with a two-user system. A portion of the spectrum of an erbium-doped superfluorescent fiber source (SFS) is encoded using a grating and an amplitude mask according to the pattern of the concatenated unipolar code $U \oplus \bar{U}$, where U is obtained from a length-N bipolar code, say X , by replacing each -1 with 0 and \bar{U} is its binary complement. The binary information symbol, $1/0$, modulates the two beams encoded with $U \oplus \bar{U}$ and $\bar{U} \oplus U$, respectively. The decoder is similar to the encoder; the amplitude mask corresponds to the desired user's codes, say V and \bar{V} , from a bipolar code Y , with the two beams coupled to a balanced photodetector pair. The balanced current output computes the true bipolar correlation of X and Y , viz. : $\theta_{X,Y} = [\theta_{U,V} + \theta_{\bar{U},\bar{V}}] - [\theta_{U,\bar{V}} + \theta_{\bar{V},U}]$. We used the mask patterns of one length-16 and two length-32 codes (from bipolar Walsh codes of lengths 8 and 16), denoted A, B and C, respectively. The chip widths vary to compensate for the non-uniform source spectrum (Fig. 2), so that the per-chip power is uniform as required by the coding.

We measured the correlations between the codes with the single-user configuration. The multiple-access interference (MAI) effect was determined with the decoder matched to the desired user in a two-user configuration. Table I summarizes the results. The entries in I(a) are the auto- and cross-correlations of the codes. The contrast is quite good except for two entries that could be due to leakage through the mask, or less than ideal compensation for the source spectrum. The relative correlation level shows that the binary information symbol can be recovered by an appropriate threshold operation. The MAI in I(b) was measured with the desired user's codes set to B or C while varying the second user's codes. The received power of the two users was comparable. As expected, the decoder cannot discriminate the interference from matched codes. For other codes, the interference level at the output is less than 10% of the desired signal, demonstrating the capability of the decoder to reject MAI.

References

- [1] R. L. Pickholtz, D. L. Schilling, and L. B. Milstein, "Theory of spread-spectrum communications —

		ENCODER					
USER		A_1	A_0	B_1	B_0	C_1	C_0
DECODER	A	1550	-1620	-30	90	15	20
	B	10	25	1360	-1300	-70	75
	C	-270	-370	78	45	1700	-1550

		INTERFERENCE					
USER		A_1	A_0	B_1	B_0	C_1	C_0
DECODER	B	240	100	2900	-2543	20	100
	C	-240	-120	-230	-90	2400	-2890

Table 1: (a) Correlations of codes and (b) multiple-access interferences

- a tutorial," *IEEE Trans. Commun.*, vol. COM-30, pp. 904-912, May 1982.
- [2] G. Foschini and G. Vannucci, "Using spread-spectrum in a high-capacity fiber-optic local network," *IEEE J. of Lightwave Tech.*, vol. 6, no. 3, pp. 370-379, March, 1988.
- [3] J. Hui, "Pattern code modulation and optical decoding - a novel code-division multiplexing technique for multifiber networks," *IEEE J. Select. Areas Commun.*, vol. SAC-3, no. 6, pp. 916-927, Nov 1985.
- [4] P. R. Prucnal, M. A. Santoro, and S. K. Sehgal, "Ultrafast all-optical synchronous multiple access fiber network," *IEEE J. Select. Areas Commun.*, pp. 1484-1493, December, 1986.
- [5] J. A. Salehi, "Code division multiple access techniques in optical fiber networks: Part-I: Fundamental principles," *IEEE Trans. Commun.*, vol. COM-37, no. 8, pp. 824-833, Aug. 1989.
- [6] J. A. Salehi and C. A. Brackett, "Code division multiple access techniques in optical fiber networks: Part-II: Systems performance analysis," *IEEE Trans. Commun.*, vol. COM-37, no. 8, pp. 834-842, Aug. 1989.
- [7] A. Weiner, J. Heritage, and J. Salehi, "Encoding and decoding of femtosecond pulses," *Optics Letters*, vol. 13, no. 4, pp. 300-302, April 1988.

DEVELOPMENT OF A TIME-DOMAIN ELECTROMAGNETICS SIMULATION
ENVIRONMENT

John H. Beggs
Assistant Professor
Department of Electrical and Computer Engineering

Mississippi State University
Box 9571
Mississippi State, MS 39762

Final Report for:
Summer Faculty Research Program
Phillips Laboratory

Sponsored by:
Air Force Office of Scientific Research
Bolling Air Force Base, DC

and

Phillips Laboratory

September 1995

DEVELOPMENT OF A TIME-DOMAIN ELECTROMAGNETICS SIMULATION ENVIRONMENT

John H. Beggs

Assistant Professor

Department of Electrical and Computer Engineering
Mississippi State University

Abstract

A time-domain computational electromagnetics simulation environment was developed. This environment includes a time-domain electromagnetics solver which is based upon the Finite-Difference Time-Domain (FDTD) method and an X-window graphical user interface (GUI) to simplify the problem setup and definition. The electromagnetics solver was written in FORTRAN and the user interface was written in the scripting language TCL/TK. The codes can be used together to analyze a variety of electromagnetic problems including scattering, radiation, coupling and biological SAR computations. These codes are at a production level and will be made available to users at their request subject to export control restrictions set forth by the United States Air Force.

DEVELOPMENT OF A TIME-DOMAIN ELECTROMAGNETICS SIMULATION ENVIRONMENT

John H. Beggs

1 Introduction

During 1993-1994, a time-domain computational electromagnetics simulation capability was developed at Phillips Laboratory for use in modeling High Power Microwave (HPM) antennas, ultra-wideband antennas and for electromagnetic coupling calculations. This electromagnetics code is called "TEMAC3D" for Temporal ElectroMagnetics Analysis Code for 3-Dimensional problems. It is a FORTRAN code and is based on a three-dimensional implementation of the Finite-Difference Time-Domain (FDTD) method for electromagnetics [1]. The TEMAC3D code models perfectly conducting and lossy dielectric objects and includes a second order Liao [2] outer-radiation boundary condition. It also includes a near to far field transformation and has point and slice sensors of most electromagnetic quantities. It has a choice of plane wave or point source excitation and has a choice of several time-domain pulses that can be used for the excitation. The TEMAC3D code interfaces with the Anastasia mesh generator that is part of the Temporal Scattering And Response (TSAR) electromagnetics code package (from Lawrence Livermore National Laboratory) and it interfaces with the IMAGE code (also comes with the TSAR code) that is used for mesh display/verification.

For the TEMAC3D code to be more effective in the design and analysis process of HPM systems, some modifications and new capabilities were required. The modifications and added capabilities encompass three major areas. First, an easier interface with current mesh generation and visualization tools (Anastasia and IMAGE) was desired. Second, a means for obtaining more types of electromagnetic quantities and interpolated sampling values was desired. Third, simplified user input for problem setup and definition was desired. To achieve the objectives, the TEMAC3D source code was modified and a graphical user interface (GUI) was developed using the scripting language TCL/TK.

The final objective with this effort was the development of a computational electromagnetic simulation environment that eliminated the requirement to edit TEMAC3D source code or header files every time a different problem was defined. Hand editing FORTRAN source code files consumes valuable time that could be spent on analysis or design and it sometimes introduces errors. Therefore the code modifications and user interface development proceeded along a path that eventually brought the TEMAC3D code and the user interface to this point.

Section 2 provides a Statement of Work and lists each of the TEMAC3D code modifications and Section 3 describes these modifications in more technical detail. Section 4 briefly describes additional capabilities that were added to the TEMAC3D code which were not outlined in the original Statement of Work. Section 5 provides a description of the GUI development and capabilities and Section 6 provides some results of this effort. Section 7 gives the system requirements for this electromagnetics package, Section 8 outlines the procedure for code distribution and Section 9 gives some concluding remarks.

2 Statement of Work

After consultation with Phillips Laboratory personnel, the following list was developed as a set of new capabilities and modifications for the TEMAC3D code that would greatly improve its functionality and range of applications. This list is a direct result of experience using the TEMAC3D code for electromagnetics applications at Phillips Laboratory. As TEMAC3D was being used, certain areas of the code were noted that could use some improvement to increase the its effectiveness and bring it to a comparable level to other electromagnetics codes. The TEMAC3D modification list was:

1. Adjust the code to begin calculations with grid indices $i, j, k = 0$.
2. Write all diagnostic files immediately following initialization of the code.
3. Develop a standardized input deck which is read into the code upon execution.
4. Create a routine which allows interpolation in field sampling.

5. Update the excitation routines to allow a delta-gap source to be specified with any unit vector direction.
6. Create a routine which allows the field sample types to be specified by string quantities instead of integers.
7. Implement a multiple look-angle capability for the near to far field transformation.
8. Develop a suite of benchmark problems which can be included with the code distribution.
9. If time permits, then development of a graphical user interface (GUI) will take place.

The initial goal of adding the new capabilities listed above is to avoid the problem of editing several FORTRAN source code or header files to set up each problem and possibly introducing errors. After this work is completed, only two files should need to be modified: the input file containing the problem run-time parameters and a header file containing the compile-time parameters.

The final goal with development of a GUI is to remove *all* hand-editing of the header and input file from the user, and instead transfer this problem definition and setup to a more pleasing and functional X-Window point, click and type interface. Therefore, any possible errors in problem setup can be checked by the user interface and immediately corrected by the code user. Once the problem definition is completed, the user then saves the header and input files and will be able to compile and run the TEMAC3D code without any errors.

Both the initial and final objectives outlined above were attained during this summer research program. In fact, several new capabilities above and beyond those outlined in the statement of work were also added to the TEMAC3D code to further improve its functionality. All of the TEMAC3D modifications were completed after about eight weeks of effort including parallel development of the graphical user interface. The remaining time was spent on code verification and further user interface development. The following sections outline the TEMAC3D modifications and the GUI capabilities. However, current versions of the GUI and the TEMAC3D code are preliminary versions and if additional

funding is obtained, these tools can be developed further into a full-fledged and dynamic electromagnetics simulation environment.

3 TEMAC3D Modifications

This section describes each new capability added to the TEMAC3D code in detail. After each new capability was implemented, the code was verified against a previous version of the code that did not have that capability.

The purpose of adjusting the code to begin calculations with grid indices of $i, j, k = 0$ is to make the code consistent with the grid generation (Anastasia) and mesh visualization (IMAGE) codes currently in place at Phillips Laboratory by mapping real space directly to computational space. All of the header include files were edited to change the dimensions for all arrays that depended on grid indices (i, j, k) to begin at 0 instead of 1. These arrays are dimensioned using three parameters that define the size of the computational domain in a header file named `setup.h`. All do loops in the source code files that used the grid indices were modified appropriately. A section of code used to translate the grid indices by 1 when a mesh was read into the code was deleted.

The purpose of having the TEMAC3D code write all diagnostic files immediately following initialization of the code is so that the user can check the specified parameters at initialization for possible errors rather than wait until the simulation is complete. The overall length of time required for a computational design or analysis is reduced as errors with the code run can be corrected immediately instead of after several hours of useless CPU time. To accomplish this task, the locations of the open and close statements for the diagnostics and error files were changed so that they would be written to disk and closed immediately following initialization of the code.

The purpose of developing a standardized input deck is to eliminate the previous requirement to edit multiple subroutines per run to define run-time parameters. This input deck was developed as a set of FORTRAN NAMELISTs which include the number of time steps, plane wave or point source information; pulse type, shape and parameters; point and

slice sensor locations and types, material parameters and near to far field transformation parameters. Various subroutines were modified to read in these NAMELISTS at different times during code initialization. Once the input deck was developed, the code was tested on a benchmark problem and produced identical results with a code that did not have the input deck capability.

The purpose of creating a routine which allows interpolation of sampled field values is so that a field or current value can be sampled anywhere within the defined computational volume and the sampling is not restricted to pre-defined grid points. This subroutine also samples a nonorthonormal component of a field quantity by specifying the scalar components of a unit vector direction. Thus, electric or magnetic field can be sampled along any direction and is not restricted to sampling of field components parallel to a coordinate axis. A set of real sampling coordinates is passed to the subroutine which converts each coordinate into a cell number (integer) and into a real remainder. Based upon this cell number, the subroutine obtains field values at the eight corners of the cell through linear interpolation. The remainder (between 0 and 1) specifies where the actual sampling point is located within the computed cell number. This remainder is then used to linearly interpolate the field values at the corners of the cell to the specified sampling point within the cell. The interpolation is first done 4 times in the x direction using the eight corner values to obtain 4 new values at the x sampling coordinate along the cell edges parallel to the x axis. The interpolation is next done 2 times in the y direction using these 4 new values to obtain 2 field values located on the top and bottom faces of the cell at the x and y sampling coordinates. The interpolation is completed once in the z direction using the 2 new field values to obtain a field value at the exact sampling point location. If the field is desired along a particular unit vector direction, the subroutine performs the dot product

$$\begin{aligned} E_{\text{samp}} &= \vec{E}^{\text{intrp}} \cdot \hat{n} = (E_x^{\text{intrp}} \hat{x} + E_y^{\text{intrp}} \hat{y} + E_z^{\text{intrp}} \hat{z}) \cdot (n_x \hat{x} + n_y \hat{y} + n_z \hat{z}) \\ &= E_x^{\text{intrp}} n_x + E_y^{\text{intrp}} n_y + E_z^{\text{intrp}} n_z \end{aligned}$$

where \vec{E}^{intrp} is the interpolated electric field vector and \hat{n} is the unit vector direction. Thus for nonorthonormal field sampling, the subroutine *must* interpolate E_x , E_y and E_z . This final value, E_{samp} , is returned from the subroutine as the interpolated value. This subroutine was tested against a previous version of the code by specifying the real coordinates to

coincide with an actual field grid point and performing sampling only parallel to a coordinate axis and the results were identical.

The purpose of modifying the excitation routines is to allow a delta-gap source to be specified by any unit vector direction instead of only \hat{x} , \hat{y} , or \hat{z} . Thus, a delta-gap source can now be specified to be oriented in a particular direction and is not restricted to having the source be parallel to a coordinate axis. The form of the delta-gap source driving routine was changed to compute the following quantity

$$\vec{E}^{source} = E_0 f(t) \hat{p}$$

where E_0 is the amplitude of the driving source, $f(t)$ is the time-domain pulse function and \hat{p} is the unit vector. The user specifies the cell number and the components of \hat{p} (p_x , p_y and p_z) and the applied field in the x direction is therefore given by

$$E_x^{source} = E_0 f(t) p_x$$

Similar relations apply for the y and z components. This routine was tested against a previous code version by using a point source and specifying either p_x , p_y or p_z to be 1.0 with the other two being 0.0 and the results were identical.

The purpose of creating a routine which allows the field sample types to be specified by string quantities instead of integers is because it makes defining the point and slice sensors easier and more intuitive by using string quantities instead of cross-referencing a table to obtain the appropriate integer value for the sensor quantity. The point and slice sensor field sampling types were modified to accept strings of the form “SctExFld” to denote the scattered electric field in the x direction. The user specifies these string variables in the NAMELIST input deck and the code uses an integer variable internally. Thus, the user now has a much more intuitive way to specify the field sampling types than to constantly reference a table in the source code comments. The point and slice sensor output data file names were also changed to easily identify the sampled field and the sensor number. For example, a point sensor file name may be of the form “SctHzFld001.Pnt” for point sensor 1 sampling scattered magnetic field in the z direction. A slice sensor file name may be of the form “TotEyFld001.Slc” for slice sensor 1 sampling total electric field in the y direction.

The purpose of implementing a multiple look-angle capability for TEMAC3D is so that data can be obtained for several scattering (or radiation) angles in one run instead of several runs. The header files were modified to add an additional dimension to the far field arrays. This dimension is controlled by a parameter in the `setup.h` header file. The far field subroutines were also modified to loop over each far field observation angle when calculating far field quantities. All data generated with the revised far field subroutines is compatible with the formats required by the post-processing Radar Cross Section (RCS) and antenna radiation codes. This multiple look angle capability was compared to a previous version with no multiple angle capability and the same scattering angles and the results were identical.

The purpose of developing a suite of benchmark problems is so that these problems could be used to verify code output. Users who are either obtaining the code from distribution or who have modified the original source code will have a set of problems they can execute and verify results with the master version. To date, two benchmark problems have been developed that will be distributed with the TEMAC3D code. One is scattering from a dielectric sphere and the other is a 1/2-wave dipole antenna radiation problem. The mesh, header, include and output data files are included with the TEMAC3D distribution. Other benchmark problems are currently under development and come from the ElectroMagnetics Code Consortium (EMCC) suite of benchmark problems. The meshes for these problems have been developed and the header and include files are will soon be developed. Once these benchmark problems have been fully analyzed, they will be included with the TEMAC3D distribution as well.

4 Additional TEMAC3D Capabilities

Additional capabilities not in the statement of work were added to the TEMAC3D code to improve its functionality, execution speed and memory requirements. The first is that all FORTRAN source code files are run through the C-preprocessor (`cpp`) when compiling. The setup header file (`setup.h`) includes several logical flags that are set by the user depending upon what capabilities of the code are being used. These flags include or eliminate blocks of code or arrays from the final TEMAC3D executable using the C-preprocessor.

For example, if the user decides not to use the near to far field transformation, the “farfld” flag is set to false, and all FORTRAN source code and arrays associated with the near to far field transformation are eliminated. Another example is that if magnetic materials are not being used, the flag “magnet” is set to false and three of the six material type arrays are eliminated, resulting in a large savings in memory. By setting these flags, the user can configure the code at will and save memory and execution time.

The ability to perform steady-state antenna radiation calculations was added to the TEMAC3D code. Previously, the user had to use a separate FDTD code designed specifically for time-harmonic antenna calculations along with a post-processing code to provide antenna gain patterns. This capability was incorporated into TEMAC3D by the use of an “antena” flag which eliminates the transient near to far field transformation and includes a special time-harmonic near to far field transformation. This flag also automatically turns on the time-harmonic excitation. The output data is still consistent with the antenna post-processing code.

The ability to specify a “custom” excitation pulse was also added. The user must write a FORTRAN program statement for this custom pulse which is included during compilation inside a header file called `custom.h`. The user can also specify the excitation to be a file of time-domain data that is read by the code during initialization. This data is read into an array and then a separate subroutine interpolates this time-domain data in time to correspond to the TEMAC3D code time steps.

5 XTEAR GUI Development

Development of the graphical user interface to accompany the TEMAC3D code proceeded in parallel with the TEMAC3D modifications during the entire summer research period. This allowed the user interface and TEMAC3D to become tightly coupled and improves the functionality and ease of use for TEMAC3D.

The resulting GUI was named “XTEAR” for **X** Temporal Electromagnetic Analysis and Response and is written in the scripting language TCL/TK. TCL/TK was chosen

over X-window programming because the development time with TCL/TK was shorter and TCL/TK is in the public domain. Figure 1 shows the XTEAR main window with a menubar, various entry boxes, radio and pushbuttons. With XTEAR, the user can define *all* relevant parameters for a given problem and then save the `setup.h` header file and the input NAMELIST file (`input.nml`). Once these two files have been saved, the TEMAC3D code can be compiled and executed. More specifically, the main XTEAR window is subdivided into groups of related parameters that must be defined for each problem. For example, the section labeled “Grid” contains entry boxes for setting the size of the grid (in cells) in the *x*, *y* and *z* directions and also the cell size in each direction. The total number of time steps required for the problem is also defined in this section.

The menubar at the top of the XTEAR main window has several functions available to choose from. The “File” function is used to load files (setup, mesh or input), save files (setup or input) and quit. The “File-Load-Setup” command is for loading the `setup.h` file or another setup file of the same format but with a different name. The file is scanned for the grid size, cell size, mesh file name, raw data file name, and logical flag parameters. As the file is being scanned, a fillbar showing the percentage of the file loaded appears on the screen while XTEAR sets the various options and checks for errors. The “File-Load-Mesh” command is used to load a mesh file specified by the file name that was either loaded within the `setup.h` file or that was typed in the entry box in the main window. The mesh file is scanned for the grid and cell sizes and XTEAR sets these parameters. The fillbar also appears and the file is scanned for the number of different materials that are being used. The material parameters for these materials must then be defined by the user. The “File-Load-Input” command is for loading the input file (usually named `input.nml`) containing various run-time parameters such as pulse shape and type, number of time steps and sensor type and locations. Again, the fillbar appears on the screen and XTEAR sets the various parameters while checking for errors. The format of this file (and the setup file) will be different based upon what options are selected through XTEAR, so it is highly recommended that the user **does not** edit the `setup.h` or `input.nml` files by hand. XTEAR should be used instead as this will prevent unnecessary errors when running the TEMAC3D code. The “File-Load-All” command is used to load all three of these files at once. The “File-Save-Setup” option is used to save the `setup.h` file and the “File-Save-Input” option

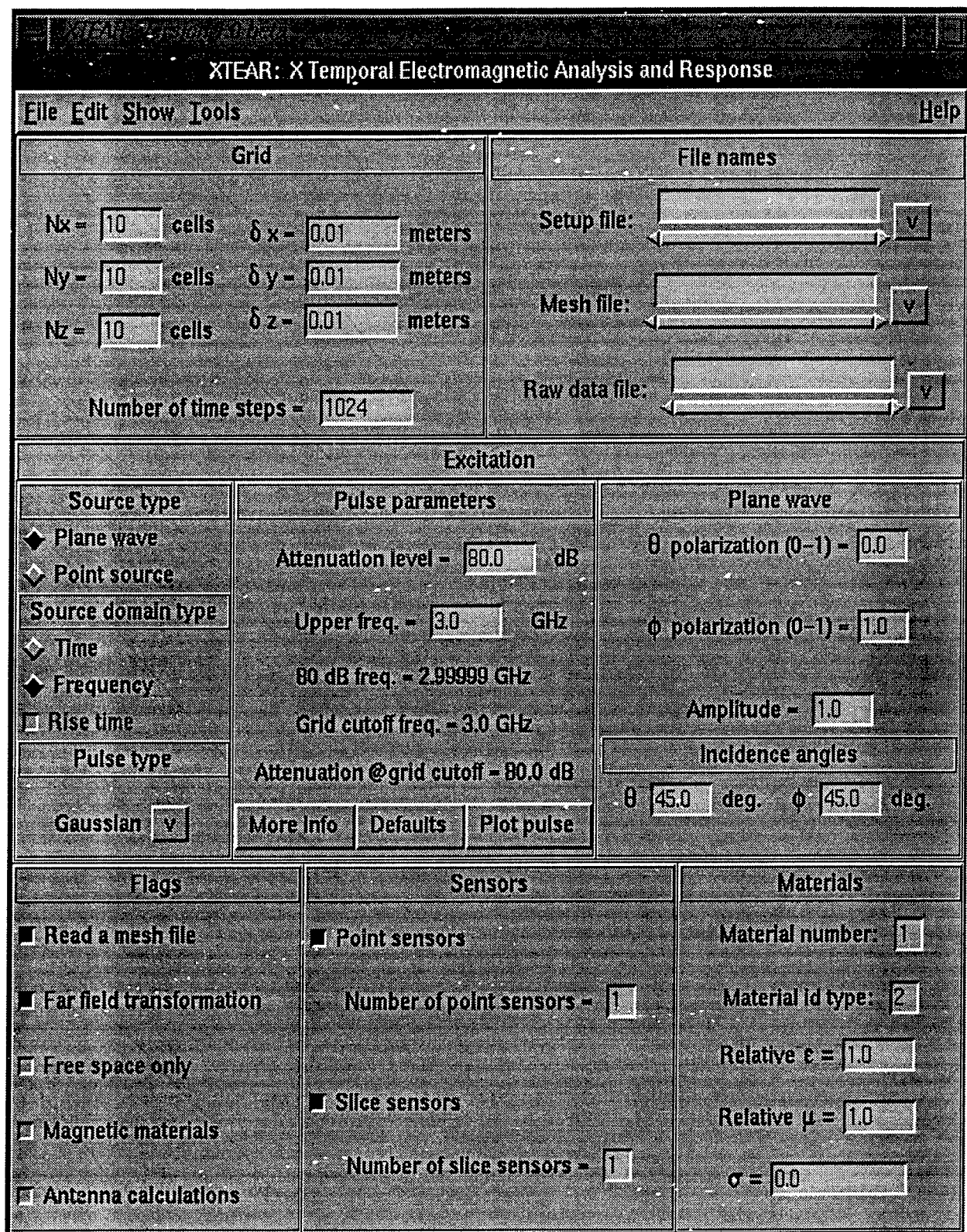


Figure 1: XTEAR main window.

is used to save the `input.nml` file. These are the two primary files that are generated by XTEAR for use in running TEMAC3D. The “File-Save-All” menubar command saves both of these files at once. Of course, the “File-Quit” command exits the XTEAR program.

The “Edit” menubar function is used for editing the sensors, point source, material parameters, scattering angles and the custom pulse. The “Edit-Sensors-Point” is used to edit the point sensor parameters such as the x , y and z locations, the sensor type and what time step it turns on or off. The sensor can also sample along a particular unit vector direction by entering the unit vector components in entry boxes. While editing point sensors, several options are also provided. The “Copy previous” option copies entries from the previous point sensor to the current point sensor and is useful when defining sensors with many of the same parameters. The “Apply defaults” option resets the current sensor to a set of predefined default values and the “Show sensors” option displays a separate window listing all defined point sensors and their respective parameters. The “Dismiss” option is used to dismiss the window when finished. The “Edit-Sensors-Slice” command is used to edit the slice sensor parameters such as the slice plane type, minimum and maximum cell numbers, etc. The same options are provided as for the point sensors to copy the previous values, apply defaults, etc. The “Edit-Point Source” command is used to edit the point source parameters and the “Apply defaults” and “Dismiss” options are provided. The “Edit-Materials” command is used to edit the material parameters and the “Defaults”, “Show” and “Dismiss” options are provided. These parameters can also be changed in the main window and any changes in either window are reflected in the other window. The “Edit-Scattering angles” command is used to edit the far field scattering angles. A button is provided to set the scattering angles equal to the incidence angles which disables all other editing capabilities in this window and sets the number of far field scattering angles to one. Otherwise, both θ and ϕ can be entered by hand or set automatically by using the “Auto set” command and providing a starting value and an increment value. The “Show” and “Dismiss” options are also provided. The “Edit-Custom pulse” command is used to edit the header file `custom.h`. The user must enter a function of time using a FORTRAN statement and then save the file. When the TEMAC3D code is compiled and executed, it uses the `custom.h` header file to define the excitation pulse type.

The “Show” menubar function is used to show the scattering angles, materials, initialization information or point and slice sensor information. Most of these “Show” windows can also be activated through the “Edit” submenu commands, but cannot be activated twice. Thus, if “Show-Point sensors” has been selected, the “Show” option under the “Edit-Sensors-Point” command will be disabled and vice-versa.

The “Tools” menubar function provides a shell option, a basic file editor and a command to print a hard copy of the current pulse. The “Help” function contains an “About” option to show some brief information about XTEAR and also has a “Checklist” option to provide a checklist of things that must be done to complete the problem setup for the current settings in XTEAR. As these settings are changed, the checklist changes also.

The “Excitation” section of the XTEAR main window is where the parameters and flags that define the time-domain excitation are set. The left portion has two radiobuttons for selecting a source type of plane wave or point source and two other radiobuttons for selecting time or frequency specification. For time specification, the user must specify a pulse width or rise time and for frequency specification the user must specify a frequency bandwidth and pulse attenuation. Other types of parameters can be defined for frequency specification depending on the pulse that is selected through the “Pulse Type” pulldown menubutton.

The center portion of the “Excitation” section is where the actual parameters that define the shape of the pulse are entered. This portion of the main window is dynamic and will change based upon what type of pulse is selected and what type of pulse specification is selected (time or frequency). The “More Info” button provides more information about the pulse that is not displayed in the main window, such as rise time and pulse widths. The “Defaults” button sets the pulse parameters to a set of default parameters based upon the cell size and time step. The “Plot pulse” button plots the current pulse into a Gnuplot window and the button changes its label to “Dismiss plot” when the Gnuplot window is active. The right portion of the “Excitation” section is where parameters for the plane wave or point source are entered. If “plane wave” is selected as the source type, then this portion of the main window will let the user enter the θ and ϕ polarizations, the amplitude

and the θ and ϕ incidence angles. If “point source” is selected, then this main window section changes and the user can enter the cell coordinates of the point source in addition to the unit vector along which the point source is defined.

The “Flags” section within the XTEAR main window is where various code options can be selected. The user can select to read a mesh file (otherwise generate the mesh by hand), turn on/off the near to far field transformation, do free space only calculations (no object), set the flag for using magnetic materials and set the flag for doing antenna calculations. Based upon these flag settings, the main window is dynamically changed to turn buttons and menu items on or off. The “Sensors” section is where the user can turn on or off the point or slice sensors. An entry box is also provided for defining the number of sensors that will be used during the calculations. Finally, the section labeled “Materials” is used for entering the values for various material parameters.

The XTEAR program is designed to interface with the TEMAC3D code through the use of up to five different files: `setup.h`, `input.nml`, `custom.h`, a mesh file and a data file of time-domain excitation data. The `setup.h` and `input.nml` files are always used and the `custom.h`, mesh and time-domain data files are optional, depending if one or more of those options has been selected. These files will be saved in the working problem directory where the user wants the output data to be stored. The user can then “make” the TEMAC3D executable in the current problem directory and the TEMAC3D executable code will use the required files from the current directory.

6 Results

To date, the XTEAR code has been used in conjunction with the TEMAC3D code to analyze scattering from a dielectric sphere and radiation from a 1/2-wave dipole antenna. XTEAR was used to set up each problem and then to save the header and input files to TEMAC3D. The TEMAC3D code was then compiled and executed without any errors and the results from these two problems were verified against the previous and unmodified version of TEMAC3D. Therefore, it was illustrated that these two codes removed the requirement to hand-edit any source code to define and execute an electromagnetics problem.

The XTEAR graphical user interface provides a much easier and error-free method of problem setup and definition. Other benchmark problems are currently under development and will be added to the XTEAR/TEMAC3D distribution after they have been fully analyzed.

7 System Requirements

The XTEAR/TEMAC3D software package is designed specifically for UNIX based workstations and not for personal computers. The system requirements for XTEAR are that the host system has TCL version 7.3 and TK version 3.6, Gnuplot, a C compiler and make capabilities. The minimal system requirements for TEMAC3D include an optimizing FORTRAN compiler that runs the C-preprocessor (cpp). For grid generation, the host system should have BRL-CAD, Anastasia and Image. Since the TEMAC3D code is based upon the FDTD method, it is memory and CPU intensive. Thus, the more memory the host system has, the larger the problem that can be analyzed with TEMAC3D; and the faster the CPU, the less amount of CPU time the calculations will take. As a rule of thumb, a system with 96 MB of memory can run a problem with around 3 million grid points. To date, both XTEAR and TEMAC3D have been installed and executed on Sun and Silicon Graphics workstations.

8 Code Distribution

Since the XTEAR and TEMAC3D codes were developed under the sponsorship of the Air Force Office of Scientific Research (AFOSR) and the Phillips Laboratory, they are in the public domain. These codes will be distributed to interested users who request the code by writing to Phillips Laboratory and they must complete a "Statement of Terms and Conditions" form that is used for release of Air Force owned or developed computer software packages. This will insure export control over these codes. The point of contact at Phillips Laboratory is Major Daniel T. McGrath, PL/WSR, 3550 Aberdeen Ave. SE, Kirtland AFB, NM 87117-5776.

9 Conclusions

A basic time-domain computational electromagnetics simulation environment has been developed. This environment consists of an electromagnetics solver based upon the Finite-Difference Time-Domain method that is written in FORTRAN. This solver is named TEMAC3D and it interfaces with an X-Window graphical user interface that is used to define all relevant parameters for each simulation. The X-Window user interface is named XTEAR and it writes header and input files that the electromagnetics solver reads for compile-time and run-time parameters. This simulation environment has been successfully applied to two classical benchmark problems and an ongoing effort will apply these codes to other benchmark problems where measurements are available for comparison. This simulation environment avoids the need to edit any FORTRAN source code, header or input files for problem setup and definition and provides an almost error-free method for defining and analyzing electromagnetics problems. Further development of this environment is anticipated as additional funding is obtained.

References

- [1] K. Kunz and R. Luebbers, *The Finite Difference Time Domain Method for Electromagnetics*, Boca Raton: CRC Press, 1993.
- [2] Z. Liao, H. L. Wong, B. Yang and Y. Yuan, "A Transmitting Boundary for Transient Wave Analyses," *Scientia Sinica (Series A)*, vol. XXVII, no. 10, pp. 1062–1076, Oct. 1984.

A STUDY OF THE TILT ANGULAR ANISOPLANATIC CORRELATION AND ITS
EFFECT ON THE FULL APERTURE TILT MEASUREMENT TECHNIQUE WITH A
LASER GUIDE STAR

Mikhail S. Belen'kii
Principle Research Scientist
Electro-optics, Environment, and Materials Laboratory
Georgia Tech Research Institute

Georgia Institute of Technology
925 Dalney Street
Atlanta, Georgia 30332-0834

Final Report for:
Summer Faculty Research Program
Phillips Laboratory

Sponsored by:
Air Force Office of Scientific Research
Bolling Air Force Base, DC

and
Phillips Laboratory

September 1995

A STUDY OF THE TILT ANGULAR ANISOPLANATIC CORRELATION AND ITS
EFFECT ON THE FULL APERTURE TILT MEASUREMENT TECHNIQUE WITH A
LASER GUIDE STAR

Mikhail S. Belen'kii
Principle Research Scientist
Electro-optics, Environment, and Materials Laboratory
Georgia Tech Research Institute

Abstract

A tilt angular anisoplanatic correlation is studied both theoretically and experimentally. It is shown that a tilt angular correlation scale is determined by the ratio of the telescope diameter to the effective altitude of the turbulent atmosphere, and it diminishes with decreasing telescope diameter. Variations of the outer scale of turbulence essentially affect a tilt angular correlation. Therefore, a finite size of the outer scale of turbulence should be taken into account to obtain reliable estimates for the tilt angular anisoplanatic correlation. A tilt angular anisoplanatic correlation is weakly sensitive to the functional form of the vertical profile of the refractive index fluctuations. To verify the results obtained a Moon-edge jitter experiment, which permits us to study a tilt angular correlation for a variable angular separation between the observation points and a variable telescope diameter is designed. A preliminary analysis of the measured data show that they are consistent with the theoretical predictions. Requirements of the parameters of additional telescopes in the full aperture tilt measurement scheme with a laser guide star are determined. It is shown that these telescopes should be small in diameter and should have a wide FOV. A Polar star image jitter experiment that permits us to exclude the effect of uncontrolled telescope motion on the measured data and to study a contribution of the stratospheric turbulence to star image motion is designed.

A STUDY OF THE TILT ANGULAR ANISOPLANATIC CORRELATION AND ITS
EFFECT ON THE FULL APERTURE TILT MEASUREMENT TECHNIQUE WITH A
LASER GUIDE STAR

Mikhail S. Belenkii

Introduction

Both astronomical and laser power beaming applications require wavefront sensing and correction in real time {1-3}. Adaptive optics systems with a laser guide star can potentially solve this problem. However, there is a fundamental limitation to the laser guide star method, that is its inability to sense a full aperture tilt.

The technique that permits us to sense a full aperture tilt with a laser guide star has recently been developed {4}. A proposed method exploits a bistatic laser guide star scheme and requires two additional receiving telescopes separated from the transmitter. A full aperture tilt is determined in the proposed technique by measuring a laser guide star image motion in the imaging plane of an additional telescope and by averaging this motion over the laser beacon angular extent. If successful, such a technique {4} provides great advantages for adaptive optics. This is due to the fact that it permits us to considerably improve these system's performance.

A tilt angular anisoplanatic correlation is a key effect of the proposed technique. Quantitative estimates for this effect are required to design a tilt measurement scheme and perform a tilt measurement experiment. The goal of this development is to study a tilt angular correlation both theoretically and experimentally and to obtain the data that are required to design a tilt sensing experiment with a laser guide star.

Tilt angular correlation theory

To study a tilt angular anisoplanatic correlation we use Zernike polynomials, $Z_q(\rho)$, where q is the mode number {5,6}. In polar coordinates (ρ, θ) the modes with the number $q = 1, 2$ [$(n,m,l) = (1,1,1), (1,1,-1)$] represent the longitudinal (parallel to the displacement), X, and lateral or perpendicular to the displacement, Y, tilts, respectively. An arbitrary wave front $\phi(r, \theta)$ might be expended in terms of Zernike polynomials over a telescope aperture of radius R in the form

$$\phi(R_p, \theta) = \sum_q a_q Z_q(\rho), \quad (1)$$

were $\rho = r/R$, and the coefficient a_q is given by

$$a_q = \int d^2\rho W(\rho) \phi(R\rho, \theta) Z_q(\rho). \quad (2)$$

Here $W(\rho)$ is the window function, defined as $W(\rho) = 1/\pi$, $\rho \leq 1$, and $W(\rho) = 0$, $\rho > 1$. Expressions for the covariance matrix elements $\langle a_q a_{q'} \rangle$, where $\langle \rangle$ represents a statistical average, for Kolmogorov spectrum with infinite outer scale of turbulence, L_0 , were derived in {5,6}.

We take into account a finite size of the outer scale of turbulence and introduce the 3-D spectrum of the refractive index fluctuations in the form

$$\phi_n(K) = 0.033 C_n^2 (K^2 + K_0^2)^{-11/6}, \quad (3)$$

where $K_0 = 3.08/L_0$. We consider a correlation of the Zernike tilts as a function of observation angles for plane waves. If the displacement between the two sources of plane waves is an angle θ , than for the spectrum (3) a tilt angular correlation coefficient has the form

$$b_{x,y}(\theta) = \frac{\int_0^H dh C_n^2(h) \int_0^\infty dK (K^2 + K_0^2)^{-11/6} J_2^2(K) \left[J_0\left(\frac{2\theta h}{D} K\right) - J_2\left(\frac{2\theta h}{D} K\right) \right] / K}{\int_0^H dh C_n^2(h) \cdot \int_0^\infty dK (K^2 + K_0^2)^{-11/6} J_2^2(K) / K} \quad (4)$$

where $C_n^2(h)$ is the vertical profile of the refractive index fluctuations, L is the propagation path, J_0 and J_2 are the Bessel functions, and $D = 2R$.

In the case of a horizontal path ($C_n^2 = \text{constant}$) the h integration in Eq. (4) might be performed, and it can be written as

$$b_{x,y}(\theta) = \frac{\int_0^H dK K^{-14/3} J_2^2(K) (F_2[1/2; 1, 3/2; -(\alpha K)^2] - \frac{1}{6} (\alpha K)^2 F_2[3/2; 5/2, 3; -(\alpha K)^2])}{\int_0^\infty dK K^{-14/3} J_2^2(K)} \quad (5)$$

where $\alpha = \theta/(D/L)$ is the angular displacement between the sources normalized to the angular size of the telescope, and ${}_p F_q$ is the generalized hypergeometric function. The results of computer calculations are shown in Fig.1. The tilt angular correlation coefficients for both lateral and longitudinal tilts are plotted versus the displacement for different ratios of the outer scale of turbulence to the telescope diameter. From the results obtained the following conclusions might be made:

1. the characteristic scale for the tilt angular correlation is determined by the angular size of the telescope and does not depend on any turbulent characteristics of the atmosphere;
2. this scale for the lateral tilt considerably exceeds that for the longitudinal one;
3. the ratio of the outer scale of turbulence to the telescope diameter essentially affects a behavior of the tilt angular correlation. Therefore, a finite size of the outer scale should be taken into account to obtain the reliable estimates for the tilt angular correlation.

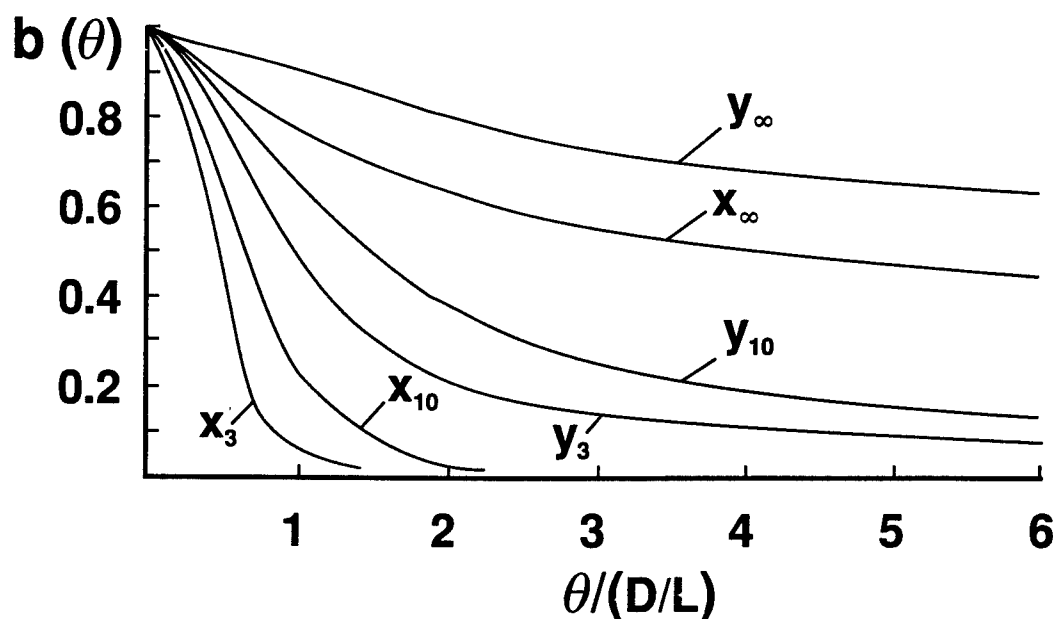


Fig.1. Angular correlation coefficients for the lateral (Y) and longitudinal (X) tilts for different outer scale/diameter ratios (shown by the subscripts) for horizontal propagation path.

Now let us consider a vertical propagation path. In this case integration in Eq.(4) should be performed by taking into account a vertical profile $C_n^2(h)$. To simplify the integration we use an exponential approximation for the conventional Hufnagel-Valley 5/7 model $C_n^2(h)$. It is easy to show that the first two moments: $\mu_0 =$

$\int_0^\infty C_n^2(h) dh$ and $\mu_1 = \int_0^\infty C_n^2(h) h dh$, for this model and the model described by the formula $C_n^2(h) = C_{n0}^{-2} \exp(-h/\bar{h})$, where $C_{n0}^{-2} = 2.39 \times 10^{-15} \text{ m}^{-2/3}$ and $\bar{h} = 934 \text{ m}$, coincide with each other. The parameter \bar{h} that is equal to the ratio $\bar{h} = \mu_1/\mu_0$ has a sense of an effective altitude of the turbulent atmosphere.

By using the above approximation for the vertical profile $C_n^2(h)$, h integration in Eq.(4) might be performed, and the results of calculations are presented in Fig.2.

From this figure it is easy to see that

1. the characteristic scale of the tilt angular correlation for the vertical path is determined by the ratio of the telescope diameter to the effective altitude of the turbulent atmosphere;
2. the tilt angular correlation scale diminishes with decreasing telescope aperture. Therefore, the additional telescopes in a full aperture tilt measurement scheme should be small in diameter;
3. the variations of the outer scale of turbulence on a vertical propagation path, similar to the horizontal path, essentially affect the tilt angular correlation;
4. the values of the correlation coefficients for the vertical and horizontal propagation paths (for the same correlation scale and outer scale/diameter ratio) are close to each other. This means that the tilt angular correlation is insensitive to the functional form of the vertical profile of $C_n^2(h)$.

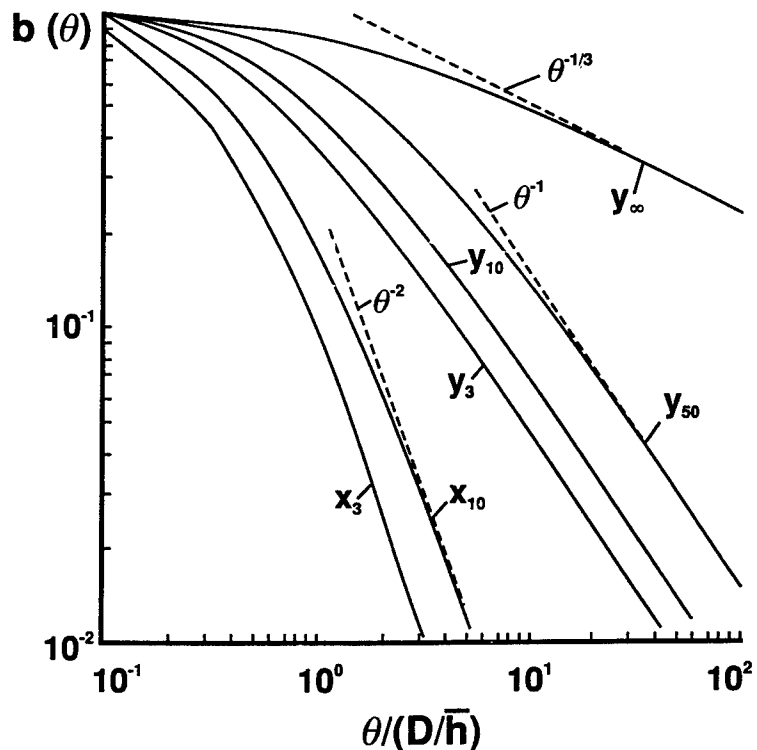


Fig.2. Angular correlation coefficient for the lateral and longitudinal tilts and different outer scale/diameter ratios (shown as the subscripts) for a vertical propagation path.

The results of the above theoretical development will be used to design a full aperture tilt measurement experiment with a laser guide star and will be prepared for publication. Unfortunately, a lack of information about an effective outer scale of turbulence on the vertical propagation paths does not permit us to obtain reliable estimates for the tilt angular correlation. To overcome this difficulty an experiment to study a tilt angular correlation was designed.

Experimental study of a tilt angular correlation

To study a tilt angular correlation on a vertical or inclined propagation path, a Moon-edge jitter experiment has been designed. The main idea of this experiment is the following. The edge of the Moon is an extended incoherent source or a collection of point sources. If a small portion of an image with an angular size smaller than a tilt isoplanatic angle is selected, a lateral (transverse to the edge) one-axis tilt component might be measured.

By selecting the two smallest portions of the image of the edge at different angular separations between them, one can study the tilt angular correlation. As opposed to the binary stars, this method permits us to study a tilt angular correlation with a variable separation between the observation points and a variable telescope diameter. Thus, Moon-edge image jitter measurements should be performed with variable telescope diameter ($D = 0.1, 0.2, 0.5, 0.75, \text{ and } 1.5 \text{ m}$) and a wide FOV of the receiver (on the order of 60 arcsec).

The following dependencies might be determined in such an experiment:

- a dependence of the tilt variance on the telescope diameter;
- a dependence of the tilt angular correlation coefficient on the telescope diameter and an angular separation between observation points;
- a dependence of the tilt angular structure function on the angular separation between observation points;
- a dependence of the jitter variance of an integrated image on the edge image angular extent;
- a dependence of the tilt power spectrum on the telescope diameter and exposure time.

The receiver is a Lincoln Laboratory Camera configured as 64x64 pixels operating at 200 Hz. Exposer time is in the range from 0.6 to 4 ms. Total observation time is 100 s. Neutral density filters are used to have the same brightness of the image for different telescope diameters.

The first measurements of a Moon-edge image jitter were performed at SOR Phillips Laboratory on August 1995. A preliminary analysis of the data obtained shows that the measured data are consistent with the theoretical predictions. The data processing will be continued, and the results will be presented for publication. These results will be also used to design a full aperture tilt measurement experiment with a laser guide star.

Stratospheric turbulence effect on star image motion

As a typical laser guide star altitude exceeds the altitude of the tropopause ($H = 10$ km), a non-Kolmogorov stratospheric turbulence might contribute to an image motion of a natural star and a laser guide star. This effect was studied theoretically in {7}, and the techniques that permitted us to single out the contribution of the stratospheric turbulence to star image motion were suggested. To exclude the effect of uncontrolled telescope motion on the measured data, simultaneous measurements of two stars images situated at the zenith distance larger than an isoplanatic angle were proposed. However, there are not many bright binary stars in the sky with a required angular separation. To overcome this difficulty we designed an experiment with a Polar star.

The idea of this experiment is to measure image motion of a Polar star with a motionless telescope having a wide FOV. The estimates show that, if a FOV of the telescope is on the order of 60 arcsec, it takes 300 s for a polar star to move across the FOV.

Therefore, an angular position of a star image might be continuously recorded, and a jitter variance might be determined. If such measurements are performed for different seeing conditions and with a variable telescope diameter, the stratospheric effect might be estimated from the dependence of the jitter variance on the seeing conditions or telescope diameter.

Additional developments

In addition to the above developments a dependence of the radar returns power on the sounding angle or aspect sensitivity of radar returns was quantitatively estimated based on an axial symmetric non-Kolmogorov model for the turbulent inhomogeneities and by taking into account an intermittency of atmospheric turbulence. It is shown that an agreement between the theoretical predictions and the measured data is greatly improved if a turbulence intermittency is taken into account. From the estimates it follows that an anisotropy coefficient of turbulent inhomogeneities is in the range 10-20 at altitudes 62-76 km,

Conclusion

A tilt angular anisoplanatic correlation is studied both theoretically and experimentally. It is shown that a tilt angular correlation scale is determined by the ratio of the telescope diameter to the effective altitude of the turbulent atmosphere, and it diminishes with decreasing telescope diameter. Variations of the outer scale of turbulence, or the ratio of outer scale to telescope diameter, essentially affect the tilt angular correlation. A tilt angular anisoplanatic correlation is weakly sensitive to the functional form of the vertical profile of the refractive index fluctuations. A Moon-edge jitter experiment that permits us to study a tilt angular anisoplanatic correlation for a variable angular separation between the observation points and a variable telescope diameter is designed, and measurements are performed.

Requirements of the parameters of the additional telescopes in the full aperture tilt measurement scheme with a laser guide star are determined. It is shown that the additional telescopes should be small in diameter and should have a wide FOV. A Polar star image jitter experiment that permits us to exclude the effect of uncontrolled telescope motion on the measured data and to study a contribution of the stratospheric turbulence to star image motion is also designed.

References

1. R.Q.Fugate et.al., "Experimental demonstration of real time atmospheric compensation with adaptive optics employing laser guide star," *Bull.Am.Astron.Soc.* **23**, 898(1991).
2. R.Q.Fugate et.al., "Measurements of atmospheric wavefront distortion using scattering light from a laser guide star," *Nature (London)* **353**, 144-146(1991).
3. C.A.Primmerman et.al., "Compensation of atmospheric optical distortion using a synthetic beacon," *Nature(London)* **353**, 141-143(1991).
4. M.S.Belen'kii, "Full aperture tilt measurement technique with a laser guide star" *Proceedings of SPIE Meeting, April, 1995*, **2471**, 289-300(1995).
5. R.J.Noll, "Zernike polynomials and atmospheric turbulence," *J.Opt.Soc.Am.*, **63**, 207-211(1976).
6. P.H.Hu, J.Stone, and T.Stanley, "Application of Zernike polynomials to atmospheric propagation problem," *J.Opt.Soc. Am.*, **A 6**, 1595-1608(1989).
7. M.S.Belen'kii, "Effect of the stratosphere on star image motion," *Optics Letters*, **20**, 1359-1361(1995).

INVESTIGATION OF THE SPINNABILITY OF SPECIALTY POLYMERS

Gajanan S. Bhat
Assistant Professor
Department of Textiles

University of Tennessee
230 Jessie Harris Building
Knoxville, TN 37996

Final Report for:
Summer Faculty Research Program
Phillips Laboratory

Sponsored by:
Air Force Office of Scientific Research
Bolling Air Force Base, DC

and

Phillips Laboratory

August 1995

INVESTIGATION OF THE SPINNABILITY OF SPECIALTY POLYMERS

Gajanan S. Bhat, Assistant Professor
University of Tennessee, Knoxville

Abstract

There was a special need to produce fibers with a unique combination of properties. As the selected polymers were not designed for spinning, it was important to study their processability in a melt spinning set-up. The polymers were investigated for their properties and attempts were made to spin them using a home-built spinning set-up. Findings from the processing studies of these polymers are documented. The two polymers investigated were, Ultem, a high temperature polyetherimide resin, and a popular commodity resin polymethyl methacrylate (PMMA). Although both of these are commercially available resins, they are mainly engineering plastics, and pose problems during the fiber formation process. From the rheological studies, it was evident that Ultem can be spun at high temperatures. However, use of high temperature also causes the problem of degradation, leading to gelation and slow hole formation. PMMA also has a narrow window of processing temperature due to its low degradation temperature. For both the polymers it was shown that one can produce decent quality fibers when spun under well controlled conditions.

INVESTIGATION OF THE SPINNABILITY OF SPECIALTY POLYMERS

Introduction

While there are several polymers and many polymeric fibers, for some special applications existed a need for fibers with unique combination of properties. For this reason two polymers were selected for studying the feasibility of converting them into small diameter fibers by melt spinning. The two polymers investigated were, Ultem and Polymethylmethacrylate (PMMA).

Ultem is a high performance Polyetherimide (PEI) resin introduced in 1982 by General Electric Company. It is a copolymer with ether molecules between imide groups. The fully reacted polyimide with the imide group being part of the linear polymer chain makes this polymer thermoplastic and easily dissolvable. Being an amorphous thermoplastic polyimide, the Ultem resin combines the high performance associated with exotic specialty polymers and the good processability of typical engineering plastics [1]. In addition to high strength and modulus, and heat resistance, the polymer has high dielectric strength, broad chemical resistance, transparency and good processability. Another advantage is that this polymer dissolves readily in methylene chloride.

GE has been marketing this polymer mainly for aerospace, marine, automotive, dielectric and electrical applications, where their long-term high temperature capabilities meet the stringent requirements [2]. Polyimide films are used as electrical insulation for electric motors, magnet wires, and aircraft and missile wiring. Because of their inherent flame resistance polyimide films are also used as fire barriers in aircraft and marine applications. Polyetherimide exhibits this exceptional balance of properties without sacrificing processability, providing a material capable of meeting the difficult design requirements of many applications [3]. Many grades of this resin are available, each suitable for certain applications. The lowest viscosity material of the available grades was used for fiber spinning.

Although possibility of spinning fibers from Ultem [4] has been reported, it is not commercially produced. It was demonstrated that Ultem can be extruded into fibers and

filaments, and then can be drawn and subsequently processed to textiles in conventional ways. The textile like properties of these fibers enable it to be used in several applications including hot gas filtration and thermoplastic composites. The major advantage of PEI fibers is their ability to retain tensile properties at temperatures up to 200 °C.

Another resin investigated was poly(methyl methacrylate) or PMMA. This is a very common plastic, also called *b*Plexiglass,*b* but not used as a fiber forming polymer due to its brittleness. PMMA is a transparent resin with reasonable mechanical properties, but relatively poor impact strength. It has a service temperature of upto 125 °C, is chemically resistant to weak acids and alkalies, and dissolves in chlorinated hydrocarbons and ketones [5]. PMMA is generally a clear plastic although a range of translucent grades are also produced.

PMMA is an amorphous polymer with glass transition temperature (T_g) of around 100 °C. It is one of the polymers that decomposes into monomers once heated above 300 °C. As can be seen from the TGA (**Figure 1**), PMMA loses all its weight by 400 °C, whether in nitrogen or in air. The rapid loss in weight after the onset of decomposition follows the kinetics of depolymerization. In fact it has been noted that the yield of monomer is 100 % of the weight of the polymer lost over a large fraction of the reaction [6]. In fact, this property was one of the main reasons for exploring the possibility of making fibers from PMMA. Some of the relevant property information on both the resins is listed in **Table 1** .

Rheological Measurements

For a polymer fluid to be good fiber forming material, in addition to being thermally and chemically stable under the conditions of spinning, it should be capable of yielding long, continuous fluid threads when extended, easily transformable into solid polymer and possessing the required physical properties when solidified and subjected to appropriate finishing treatment. Considering all these, knowing the rheology of any fiber forming material is essential. Rheology is the study of the flow behavior of polymeric liquids, either melts or solutions. The main task of rheology is to derive relations between stress in a material subjected to deformation and the deformation conditions [7, 8]. This relation

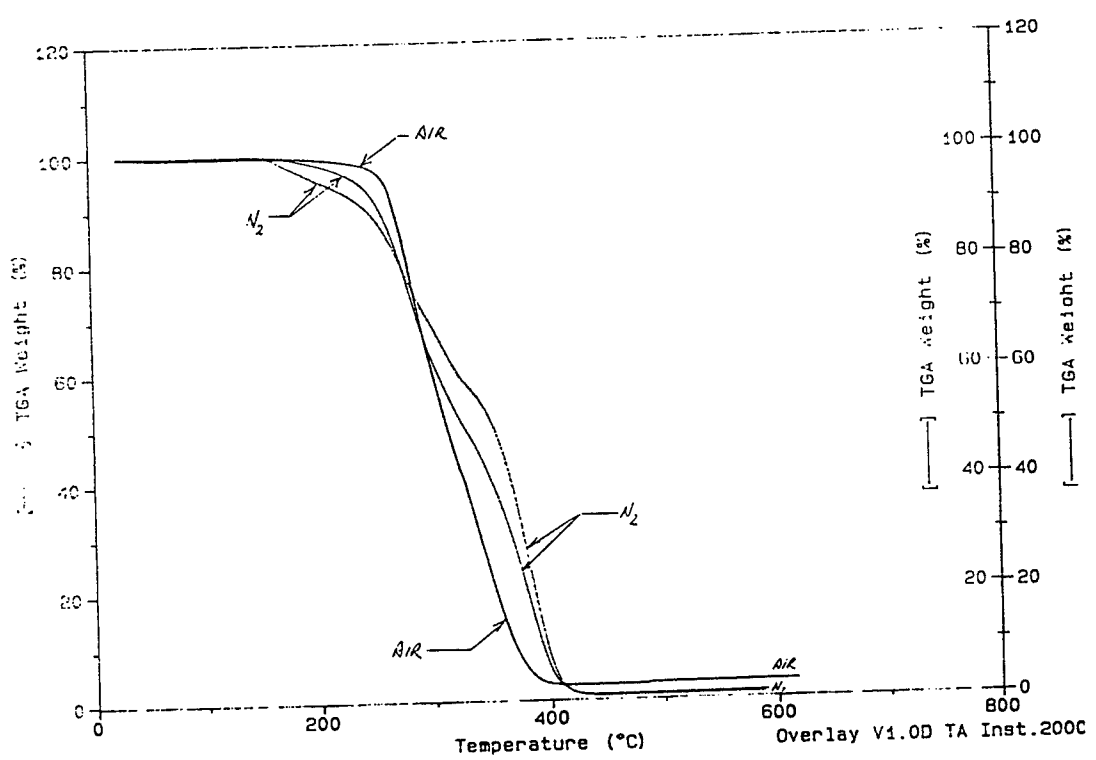


Figure 1. TGA of PMMA in Air and in Nitrogen.

involves certain material characteristics, such as viscosity, modulus, and relaxation time. Other factors connected with the flow, such as temperature are also important.

In this case, the rheological measurements were done using a dynamic viscometer. For this the polymer pellets were first dried in an oven at 140 °C for four hours, and then the dried polymer was pressed into small 15 mm diameter discs of about 5mm thickness. These discs were used to get the viscosity and loss modulus measurements. The experiment was conducted at a temperature range of 300 to 400 °C. The results obtained for Ultem 1000 and Ultem 1010 are shown in **Figures 2 and 3**.

It is clear from the rheology data that the melt viscosities are very high for both the polymers. While the preferable processing temperature is of lower range of about 350 °C, the viscosity values were greater than 10000 poise for both grades of Ultem at that temperature. Even at 400 °C, the viscosities were above 1000 poise, whereas for good processing a viscosity of about 500 poise or less will be ideal. Although the shear rate used in the measurement was only 10 sec⁻¹, whereas in actual spinning shear rates of 100-1000 sec⁻¹ are observed, the apparent viscosity is not likely to be significantly lower. The effect of shear rate on viscosity is being measured to get that data as well. Of the two grades, Ultem 1010 has significantly lower melt viscosity, in fact less than half of that of Ultem 1000. This indicates that for ease of processability Ultem 1010 is preferable as a fiber forming polymer. Also evident from the Tan δ data is that the polymer melts have high elasticity. This causes problems such as die swell and spinning conditions will have to be carefully controlled.

Melt Spinning

Of the three methods of producing fibers-melt spinning, wet spinning and dry spinning- melt spinning is the simplest to design. All that is required is a means of melting or softening the polymer, a means of forcing the melt through the capillary and, after the threadline has cooled and solidified, a device for collecting the filament.

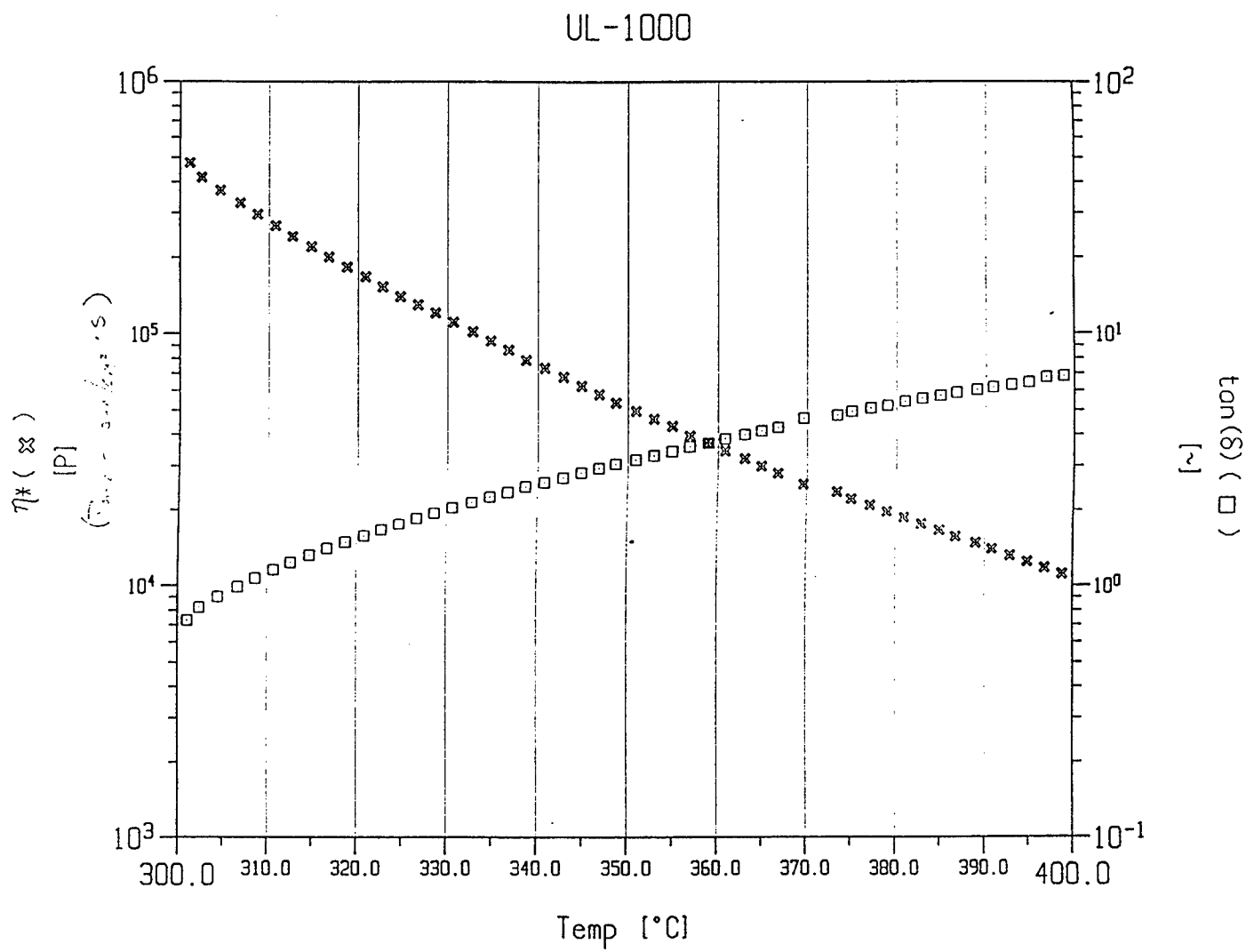


Figure 2. Viscosity and $\tan \delta$ vs Temperature for Ultem 1000.

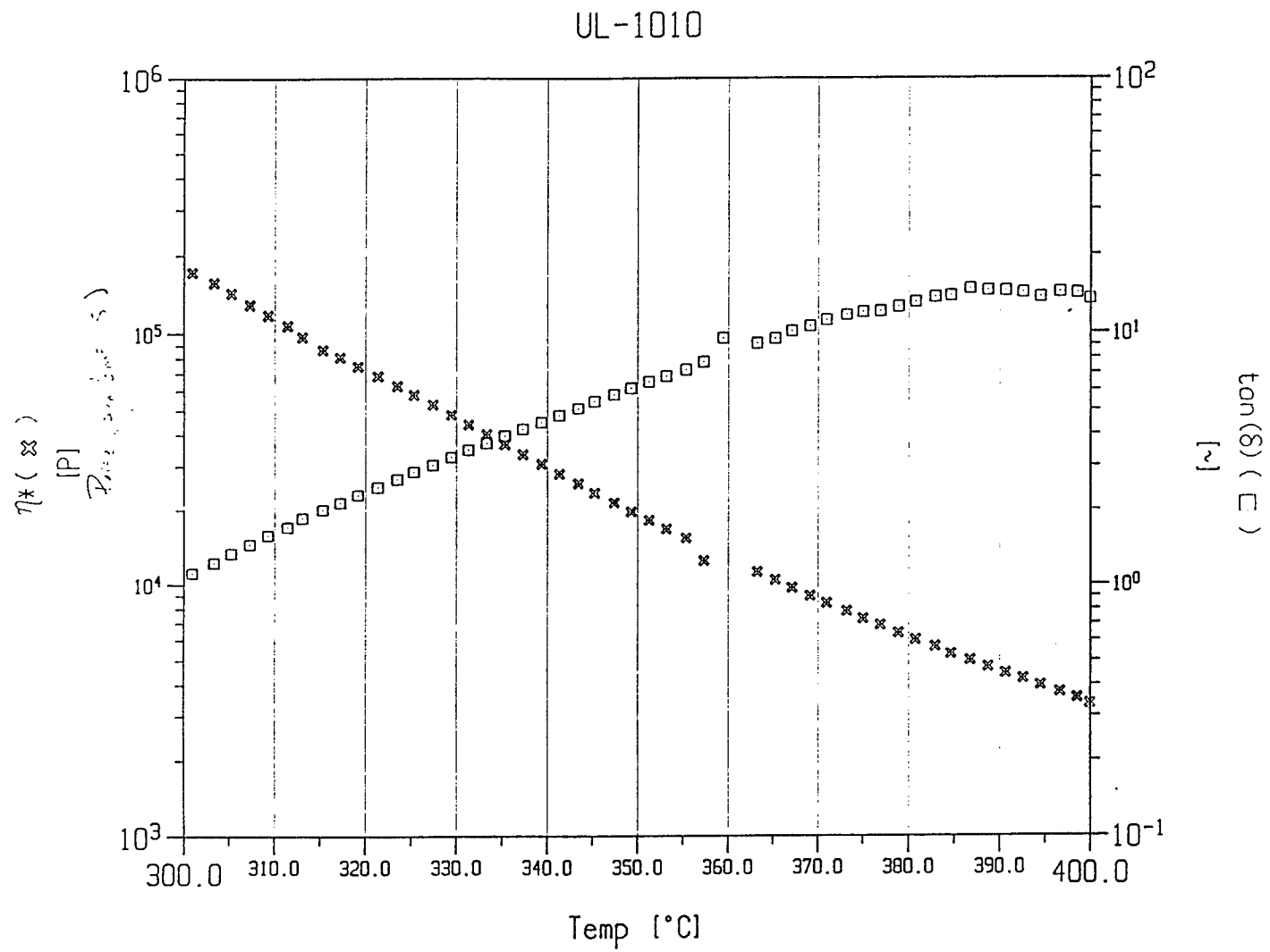


Figure 3. Viscosity and $\tan\delta$ vs Temperature for Ultem 1010.

Melt Spinning Set-Up

A special laboratory scale melt spinning unit was built for conversion of Ultem and other melt spinnable resins into fibers of required properties. The main advantages of the small scale fiber extrusion system are that (i) it helps in assessing the fiber forming potential of a genuinely novel polymeric substance, (ii) it is possible to investigate the feasibility of improving the fiber properties of an already established polymeric system by altering the polymer system or by altering the extrusion conditions, and (iii) the effect of process variables such as extrusion velocity, spinneret geometry, quenching condition and take up speed on the structure and properties of the formed fibers. The system built by Dr. Wapner at the laboratory is a ram-and-cylinder type of spinning head. For non-continuous fiber formation from the melt, the piston-and cylinder, or ram-and-cylinder, or rod-spinner is a simple and straightforward way of producing small quantities of fiber which, if the extrusion conditions are properly controlled, may yield fibers of extremely high quality [9].

Figure 4 and 5 show the schematic of the melt spinning apparatus. The polymer in the form of pellets or powder as fed into the RAM injector and forced into the melting zone. High pressure air from the cylinder is used to force the ram and the air pressure can be adjusted to the required level. There is also a provision to draw vacuum from the cylinder that will help in reducing the probability of air bubbles in the polymer melt. The melting zone as well as the melt transfer zone, which feeds the melt to the metering pump are enclosed by heaters, and their temperatures can be separately controlled (h1 and h2).

The polymer melt feed rate is controlled by the Zenith metering pump. The pump is enclosed by heaters and the temperature can be independently controlled. Polymer fluid enters the pump through a port drilled into the rear side plate (the side opposite the drive shaft). The fluid fills the exposed gear tooth volumes and is transported around the outer diameter of the gear pocket. As the gears mesh together, the fluid is displaced in a very precise amount out through the discharge port that is drilled alongside the inlet port in the rear plate. The fluid throughput is controlled by the pump speed which can be varied from 3-180 rpm, and the rate is 0.16 cc per revolution.

From the pump the molten polymer is fed to the spinpack, which is also enclosed by a heater with a separate temperature controller. Just before the melt enters the

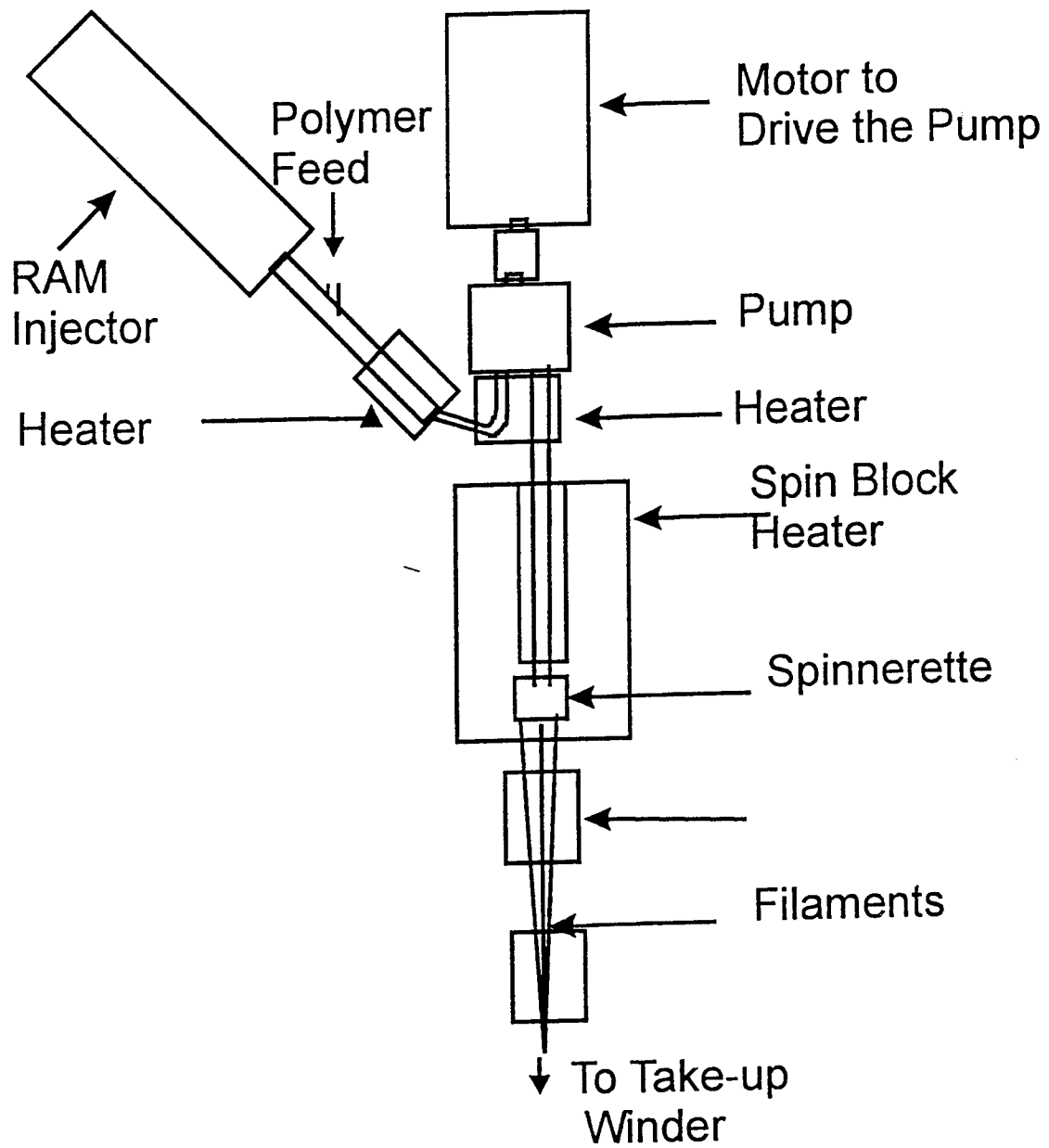


Figure 4. Melt Spinning Set-Up.

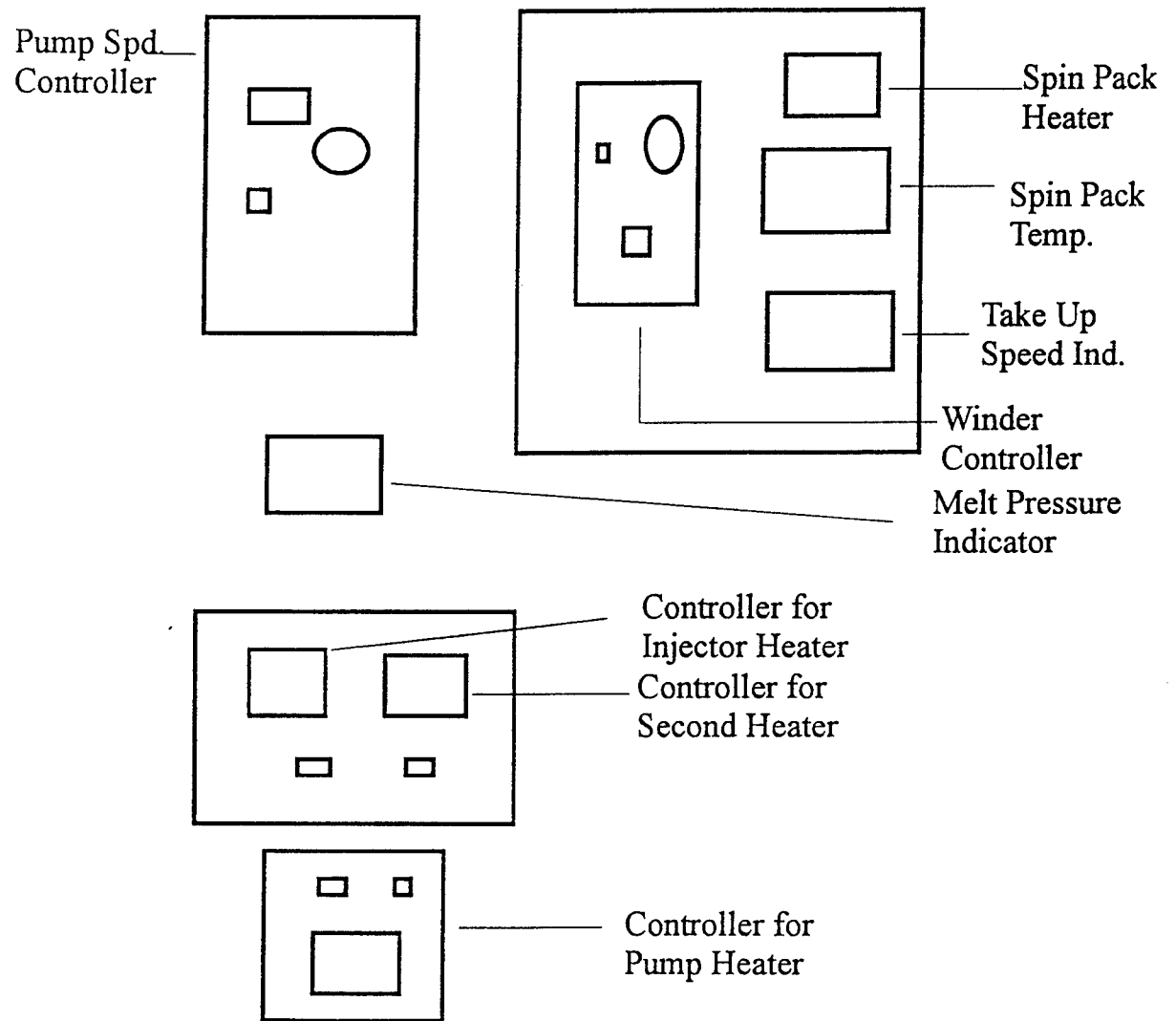


Figure 5. Controllers for the Melt Spinning Unit.

spinpack there is pressure transducer to monitor the melt pressure. The spinpack has a filier which prevents the flow of unmolten polymer, or any other contaminant into the spinneret which might otherwise block the spinneret holes. The spinnerets used had different size holes and varying L/D ratios. Almost all of them had 12 holes per spinneret. For majority of the spinning trials, spinnerets with 200um dia holes were used.

The winding system consists of a roller, the speed of which can be continuously varied. The filament is fed into the winder through a traversing guide to help in building the package. The traverse drive is coupled with the speed of the winder so as to maintain a good package build at all speeds. There is a provision to hook up a tensiometer to the threadline so that the fiber tension can be determined.

A simplified spinning system was built to some of the high temperature sensitive polymers. In this, the polymer is fed from the Ram Injector directly into the spinpack avoiding transfer pipes and the metering pump. The advantages of a having a simpler system is that the melt flows through a simple path avoiding the tortuous route of going into and out of metering pump. For polymers that are sensitive to high temperatures, a shorter path means reduced level of degradation. Of course, this does not give a controlled flow, but in reality one has to give up something for something better. While PMMA, which has narrow range of processing temperatures was processed only using this set-up, even Ultem was tried using this system. The idea behind processing Ultem with the simplified system was that shorter dwell time in the molten stage means reduced level of gelation, and slow holes can be eliminated or controlled significantly.

The important variables in spinning are, melt temperature, melt pressure, spinneret (no of holes, and hole shapes and dimensions), quenching conditions and winding speed. These conditions were varied within the reasonable range for both the polymers investigated. The range of spinning conditions tried is listed in Table 2 .

Processing Observations

A range of processing conditions were tried to obtain fibers from the Ultem resin. However, there were several problems in continuously winding the fibers. The problem was mainly due to 'slow-hole' formation. Slow holes are observed whenever the spinneret holes are partially clogged. With the partly blocked hole/s, melt can not flow in a steady manner. Instead there will be fluctuations causing no filament formation for a while and then a thick filament coming out for some time. This phenomenon continues like this unless that hole is completely blocked or the gel comes out. The probability of that gel/contaminant coming out is very low, unless the temperatures and pressures are raised to very high levels, which can lead to other problems. Even one slow hole is enough to make the winding of filaments very difficult.

As mentioned above, slow holes are formed by the deposition of contaminants along the wall of the spinneret hole. Although most of the contaminants, external or internal, are filtered by the filter in the spinpack, for sensitive polymers, gelation can occur by the time the polymer leaves the filter and reaches the spinneret hole. This is more likely the case because of high temperatures used in spinning. The use of higher processing temperatures is mandated by the polymer which has extremely high viscosity. Although further increase in temperatures can lead to additional decrease in viscosity and smoother flow, the threadline will not be stable due to poor melt strength. Another factor that leads to gelation of the polymer melts is the presence of catalyst traces and end groups which react with filter material and contaminants at these high temperatures. Therefore using extremely clean parts in the system is essential.

Recommendations for Future Work

Although it was possible to extrude fibers from both Ultem and PMMA resins, some problems were observed in collecting the fiber. As the majority of the problems with ultem were due to slow holes, it is recommended that the system be modified to minimize the length of stay for the molten polymer. In the system with metering pumps, a means to connect the spinpack just before the beginning of spinning will help. This way all the polymer which might have degraded to some extent can be forced out and only when a

fresh batch of polymer starts coming out of the pump, the spinneret can be connected. This will considerably reduce the possibility of degradation and gelation. It is also important to clean all the parts of the spinpack that come in contact with the polymer since even trace amounts of the contaminant can initiate degradation and lead to gelation of the polymer, further leading to the problem of slow holes.

It is also recommended that other techniques of fiber formation be explored. Wet spinning can solve many problems associated with high temperatures. Although use of solvents poses new set of problems related to environment, health and safety, these are routinely handled. Preliminary studies have to be conducted to optimize several conditions related to wet spinning such as solvent, dope concentration and coagulation bath concentration. Melt blowing is another option, especially for producing small diameter fibers. Even in melt blowing high temperatures are problem with high temperature resins. Alternatively, use of plasticizers to reduce the processing temperatures need to be investigated.

Bibliography

1. H. R. Penton, *Modern Plastics Encyclopedia* , mid October issue, 87 (1993).
2. Ultem Polyetherimide Resin, Company literature, GE Plastics.
3. I. W. Serfaty, in *Polyimides* , ed. by K. L. Mittal, Plenum Press, New York (1988).
4. *Textile Applications of Performance Polymers*, *Textile Month* , July, 20 (1991).
5. R. V. Malby, in *Plastics Technology*, McGraw Hill, New York, pp. 299-308 (1973).
6. Billmeyer, *Textbook of Polymer Science*,
7. A Ziabicki, in *Man Made Fibers: Science and Technology* , Vol. 1, ed. H. F. Mark, S. M. Atlas and E. Cernia, John Wiley & Sons, New York (1971).
8. T. G. Fox, S. Gratch and S. Loshack, in *Rheology* Vol.1, F. Eirich, Ed., Academic Press, New York (1956).
9. D. B. Green in *Applied Fiber Science*, Vol. 3, ed. by F. Happy, Academic Press, New York, pp. 197-234 (1973).

Table 1. Properties of the Polymers Used.

<u>Property</u>	<u>Ultem</u>	<u>PMMA</u>
Glass Transition Temp. (°C)	215	100
Density (g/cc)	1.27	1.19

Table 2. Processing Conditions Used for Spinning Trials.

	Ultem	PMMA
Heater 1 (°C)	385	----
Heater 2 (°C)	380-390	-----
Pump Temp. (°C)	370	-----
Melt Temp. (°C)	350-385	250-300
Melt Pressure	400-2500	200-400
Pump Spd. (rpm)	5-20	-----
Winding Speed	120-200	-----

Computer Simulations of synchronous and Asynchronous
Multi-User Optical Code Division Multiple Access Digital
Communication Systems

Daniel C. Bukofzer
Professor
Electrical and Computer Engineering Department

California State University
Fresno, CA

Final Report for:
Summer Research Program
Phillips Laboratory

Sponsored by:
Air Force Office of Scientific Research
Bolling Air Force Base, Washington DC

and

Phillips Laboratory

August 1995

**COMPUTER SIMULATIONS OF SYNCHRONOUS AND ASYNCHRONOUS
MULTI-USER OPTICAL CODE DIVISION MULTIPLE ACCESS DIGITAL
COMMUNICATION SYSTEMS**

Dr. Daniel C. Bukofzer, Professor and Chairman
Department of Electrical and Computer Engineering
California State University
Fresno California 93740-0094

Abstract

This report presents performance results of digital communication systems that support multiple users using a specific optical code division multiple access (O-CDMA) technique. These performance results are obtained strictly via computer methods utilizing block oriented simulation software. More specifically, both synchronous (same bit rate per user) and asynchronous (different user bit rates with unrelated clocks) systems have been studied via simulation in which multiple users using bipolar codes obtained from a cyclically shifted maximal length sequence transmit signals simultaneously by on-off modulating carriers at set frequencies. (For most simulations these frequencies were set from 2 MHz upward in steps of 2 MHz). Tests were performed assuming both an ideal channel and a non-ideal channel which was modeled as a soft nonlinearity. Although many parameters could be varied in each simulation run, such as the number of users and their bit rates, carrier frequencies and their associated guard bands, receiver filter characteristics and bandwidth, photodiode efficiency factor, and channel nonlinear characteristics, because of report limitations, only a few of the performance results obtained are shown here. Varying the above parameters iteratively would produce many more performance plots than could be presented in this report. Therefore the results focus on describing the simulation system and demonstrating the development of a series of lower hierarchical level software implementations that yield appropriate results for the systems being considered. In most cases, the key results involve demonstrating the appropriate recovery of the bit stream of each of the users, and the effect on performance when specific system parameters as described above are varied. The work completed can be and is intended to be used as the starting point for more sophisticated performance testing efforts in which systems involving a greater number of users operating under various operational scenarios can be simulated to include the effect of noise as well as varying the parameters described above.

TABLE OF CONTENTS

LIST OF FIGURES	5-3
ACKNOWLEDGMENTS	5-4
INTRODUCTION	5-5
Section 1 The Unipolar O-CDMA System	5-6
Section 2 The Bipolar O-CDMA System	5-7
Section 3 The Simulation System	5-8
Section 4 Simulation Results	5-9
CONCLUSIONS AND RECOMMENDATIONS	5-10
REFERENCES	5-20

LIST OF FIGURES

FIGURE 1: Block Diagram Design (BDD): 7 User Synchronous O-CDMA System ..	5-11
FIGURE 2: Block Diagram Design (BDD): Encoder ("encodefl")	5-11
FIGURE 3: Block Diagram Design (BDD): Channel Nonlinearity	5-12
FIGURE 4: Block Diagram Design (BDD): Preliminary Decoder ("decodem4")	5-12
FIGURE 5: Block Diagram Design (BDD): Decoder ("decusrfl")	5-13
FIGURE 6: Signal Calculator Page (SCP): User #1 Output With Nonlinearity	5-13
FIGURE 7: Signal Calculator Page (SCP): User #4 Output With Nonlinearity	5-14
FIGURE 8: Signal Calculator Page (SCP): User #7 Output With Nonlinearity	5-14
FIGURE 9: Signal Calculator Page (SCP): User #1 Output Without Nonlinearity	5-15
FIGURE 10: Signal Calculator Page (SCP): User #4 Output Without Nonlinearity	5-15

- FIGURE 11: Signal Calculator Page (SCP): User #7 Output Without Nonlinearity 5-16
- FIGURE 12: Block Diagram Design (BDD): 7 User Asynchronous O-CDMA System 5-16
- FIGURE 13: Signal Calculator Page (SCP): User #1 Output, PD Eff. = 100000 5-17
- FIGURE 14: Signal Calculator Page (SCP): User #4 Output, PD Eff. = 100000 5-17
- FIGURE 15: Signal Calculator Page (SCP): User #7 Output, PD Eff. = 100000 5-18
- FIGURE 16: Signal Calculator Page (SCP): User #1 Output, PD Eff. = 10000 5-18
- FIGURE 17: Signal Calculator Page (SCP): User #4 Output, PD Eff. = 10000 5-19
- FIGURE 18: Signal Calculator Page (SCP): User #1 Output, PD Eff. = 10000 5-19

ACKNOWLEDGMENTS

This work was supported by the U.S. Air Force Phillips Laboratory, Kirtland AFB, New Mexico, under the auspices of the Air Force Office of Scientific Research, Bolling AFB.

The author gratefully acknowledges the input provided and time spent during the many technical discussions by Dr. James Chan of RDL, Inc. Additionally, Dr. Benhaam Aazhang, Professor of Electrical Engineering at Rice University is to be thanked for his technical assistance to this project.

At the U.S. Air Force Phillips Laboratory, the author recognizes Mr. Frank Fisk for proposing that this analysis and simulation effort be carried out, and providing the necessary support.

Mr. Scott Licoscos and Ms. Johnetta Thompson of RDL Inc. assisted with the administrative requirements of this contract and as such are thanked for their timely support.

The author recognizes and thanks the head of the U.S. Air Force Office of Scientific Research for supporting the Summer Faculty Research Program which allows university faculty members the opportunity to become involved in projects of importance to the U.S. Air Force while at the same time providing a mechanism for faculty members to be involved in and contribute toward solving significant technical problems of interest to the U.S. Air Force.

INTRODUCTION

The last 20 years have witnessed an explosive growth in information transmission supported by fiber optic channels. An excellent account of the development of the technology and the principles of fiber optic communications may be found in [1]. With a goal of constantly increasing the speed of digital transmission, accommodating larger numbers of simultaneous users while increasing the overall system reliability, significant efforts have been devoted to the study and development of very high speed, multi-user lightwave communication networks. (See [2] and the references therein.) While many of the performance improvements realized have resulted from the development of more sophisticated devices, others are due to a better understanding of the physical limitations imposed by optical (and non-optical) components, (see [3] for example), and very elaborate methods for mitigating system impairments, [4].

Although many techniques exist for developing reliable high speed multi-user communication systems, one in particular, the optical code division multiple access (O-CDMA) approach is the method on which this research effort and report focuses. The development of optical (multi-user) CDMA techniques in digital communication applications has been on-going since before 1985. These techniques are based on the use of orthogonal (or near orthogonal) digital codes for the purpose of attaching the equivalent of a digital signature to each user. Although non-optical CDMA techniques are also based on the assignment of different (spreading) codes to each of the users (in typical spread spectrum modulation applications, [5]), the method by which the data to be transmitted interacts with the spreading code is different in O-CDMA systems. Detailed explanations of the many approaches used in O-CDMA systems are not possible here. The reader can find an excellent treatment on the subject in the original work presented in [6]. Additionally the work reported on in [7] and [8] is a detailed presentation on the characterization and performance of optical codes in a CDMA environment, while [9] deals with an analytical approach to describing the performance of such systems. While O-CDMA systems can operate in a serial mode (to become somewhat like TDMA systems), as well as a parallel mode, the focus of this work is on the latter. The work reported on in [10] presents an excellent account of how O-CDMA systems operate in a serial mode while in [11], pioneering work is reported on dealing with a parallel system in which bipolar codes are used. The advantage of this novel approach lies in the fact that recovery of the binary information is based on decisions made against a zero threshold. This, as explained in the next two sections is fundamental to the practical operation of O-CDMA systems. A system whose threshold is dependent on operational parameters such as the number of users active, presents severe design challenges that may be difficult to overcome.

Although the scope of this report is narrow, and the effect of noise on system performance has not been incorporated, its usefulness is not diminished as the presence of noise of various statistical characteristics and power levels can be easily incorporated into the existing software simulations.

Section 1: The Unipolar O-CDMA System

The optical (unipolar) CDMA system under consideration can be described as follows. Let d_{ni} represent a {0, 1} binary sequence of bits generated at a rate R bits/sec associated with the ith user of an N user system. Such user is assigned a spreading code or mask u_i , where u_i consists of K logic states 0 and 1. A logic 1 in u_i implies light transmission while a logic 0 implies no (or very low) light transmission. A very broadband light source is employed from which K distinct frequencies are extracted and each assigned to one of the logic states associated with the mask. When d_{ni} equals 1, those frequencies associated with a logic 1 state in u_i are transmitted (light is "on") while frequencies associated with a logic 0 state in u_i are not transmitted at all (or transmitted at a very low level perhaps as much as 30 dB below the "on" signal level). When d_{ni} equals 0, those frequencies associated with a logic state 1 in u_i are transmitted at a level low enough to represent leakage light (thus modeling the inability to completely turn off the light source), while those frequencies associated with a logic state 0 in u_i are not transmitted at all or at a very low level, as previously explained. This effectively produces on-off keyed modulation signals at each of the transmitted frequencies of the broadband source, which are summed to produce a composite signal that is equivalent to a wavelength multiplexed digital signal. At the receiver, the different frequency components present in the composite signal are separated, identified, and extracted. Photodetectors are used to produce a photon count that is proportional to the light intensity present at each frequency. When the overall photon count associated with all frequencies that can be transmitted for a given mask exceeds a specified threshold, a logic 1 is associated with d_{ni} whereas if the threshold is not exceeded, a logic 0 is declared.

Simulation results for the unipolar system described above are not presented here although such a system was implemented (in software) and its performance tested. The simulation system was constructed by having a random data generator for each user whose bit stream controlled a bank of switches. The input to each switch was either a high or low constant whose output multiplied a sinusoid of a specific frequency. One switch per component (i.e., logical state) in the mask was utilized, and the high or low amplitude sinusoidal bursts produced at the different frequencies were added together. The receiver separated each of the frequency components of the signal by simple bandpass filtering and light intensity was measured by squaring the filter output and integrating it over the duration of one data bit (i.e., $1/R$ sec). The result of this integration was modeled as a Poisson distributed random variable and summed with all other such outputs for which frequency components were present. The decision on d_{ni} being 0 or 1 over any one bit interval was made by a simple binary comparison against a pre-set threshold. While the simulation results pointed toward a system that worked properly, it was found that key to its operation was the ability to correctly set the threshold for the binary decisions. More importantly, the correct threshold setting as simulation results showed, proved to be very much dependent on the number of users present. It was felt that unless adequate prior knowledge existed about how many users were simultaneously active, it would be difficult

if not impossible to have such a system operate properly, unless very sparse user codes (or masks) were used that produced little or no interference amongst users. This, although possible, would require very long user codes u_i (because each mask would be mostly made up of logical 0 states) and therefore a very broadband source, or shorter user codes accommodating a small number of users. Because of these limitations and the fact that more flexible bipolar codes can be used, the focus of this work centered on simulating such codes under various operational scenarios.

Section 2: The Bipolar O-CDMA System

The optical (bipolar) CDMA system under consideration can be described as follows. As in Section 1, let d_{ni} represent a {0, 1} binary sequence of bits generated at a rate R bits/sec associated with the ith user of an N user system. Such user is assigned a spreading code or mask u_i , where u_i consists of K logic states 0 and 1. Associated with code u_i is the complementary code \bar{u}_i , where each element of the latter is the logical complement of the former. A concatenation of u_i and \bar{u}_i is formed to produce a code (or mask) of 2K logical states, denoted U_i . As before, a logic 1 (in U_i) implies light transmission while a logic 0 implies no (or very low) light transmission. A very broadband light source is employed from which 2K distinct frequencies are extracted and each assigned to one of the logic states associated with the mask. When d_{ni} equals 1, those frequencies associated with a logic 1 state in U_i are transmitted (light is "on") while frequencies associated with a logic 0 state in U_i are not transmitted at all (or transmitted at a very low level perhaps as much as 30 dB below the "on" signal level). When d_{ni} equals 0, those frequencies associated with a logic state 1 in U_i are transmitted at a level low enough to represent leakage light (thus modeling the inability to completely turn off the light source), while those frequencies associated with a logic state 0 in U_i are not transmitted at all or at a very low level, as previously explained. In addition to forming a concatenated code or mask, the bipolar system differs from the unipolar one by forming the complement \bar{U}_i of the concatenated code U_i . This complement code \bar{U}_i is operated upon by \bar{d}_{ni} , the complement of the binary sequence associated with the ith user. The same 2K frequencies extracted from the broadband source are assigned to each one of the logic states associated with the mask. When \bar{d}_{ni} equals 1, those frequencies associated with a logic 1 state in \bar{U}_i are transmitted (light is "on") while frequencies associated with a logic 0 state in \bar{U}_i are not transmitted at all (or transmitted at a very low level perhaps as much as 30 dB below the "on" signal level). When \bar{d}_{ni} equals 0, those frequencies associated with a logic state 1 in \bar{U}_i are transmitted at a level low enough to represent leakage light (thus modeling the inability to completely turn off the light source), while those frequencies associated with a logic state 0 in \bar{U}_i are not transmitted at all or at a very low level, as previously explained. This effectively produces on-off keyed modulation at each of the transmitted frequencies of the broadband source which are summed to produce a composite signal that is equivalent to a wavelength multiplexed digital signal. At the receiver the different frequency components present in the composite signal are

separated, identified, and extracted. Photodetectors are used to produce a photon count that is proportional to the light intensity present. The overall photon count associated with all frequencies that can be transmitted for the U_i mask is compared to the overall photon count associated with all frequencies that can be transmitted for the \bar{U}_i mask. If the former exceeds the latter, a logic 1 is associated with d_{ni} whereas if the latter exceeds the former, a logic 0 is declared. This is equivalent to subtracting the two values of the photon count and comparing that number with zero. The clear advantage of this method versus the (unipolar) previous one is that the threshold used to decide on the logical state associated with d_{ni} is independent of the number of users present. This important feature of the bipolar method leads to a system that is both implementable and attractive from a performance standpoint.

Section 3: The Simulation System

The simulation system was built by creating individual elements that were redefined as new blocks (but called symbols in SPW) and interconnecting blocks in accordance with the model under study. Fig. 1 shows the system at its highest hierarchical level from a simulation standpoint. It can be observed that the overall simulation system is made up first of encoder blocks, each connected to a random data generator. The sum of the each encoder block output forms the channel signal which is allowed to be applied directly to that part of the system that constitutes the receiver, or as shown in Figure 1, first propagated through a channel nonlinearity before reaching the receiver. There is a difference between the simulation of the synchronous system versus the asynchronous system. From Figure 1 it can be observed that the received signal is applied directly into a preliminary decoder block that feeds its output to a separate decoder block, one for every user. This is how the synchronous system operates. The asynchronous system has a preliminary decoder for each user whose output is connected to an individual decoder block. The reason for this difference can be appreciated once the elements of the simulation system have been explained and understood.

Focusing first on a typical encoder block (by looking at the inside of the block "encodef1" as shown in Fig. 2), its input is the output of the random data generator, which produces a random bit stream of prescribed bit rate. The encoder block accepts this input and converts the logical states to integer voltage levels. Complex tone generators create sinusoids of prescribed frequencies, which in this case take on values in MHz, $2m$, where $m = 1, 2, \dots, 30$. From these complex tones the real component is extracted and used to produce on-off keyed modulated signals where the random data controls the operation of switches that allow these tones to be multiplied either by a unity factor (corresponding to a logical 1 in the mask), or a very small factor (corresponding to a logical 0 in the mask). The mask, being user unique, results in a different encoder block for each user. The sum of all these on-off keyed modulated signals at the $2m$ (in MHz) distinct frequencies forms the channel signal. (Recall that in the bipolar system the mask for each user is dictated by U_i and \bar{U}_i as explained in Section 2.) This channel signal can be allowed to propagate through a soft nonlinearity which for simulation purposes has been allowed to take the

form $y = \text{Atanh}(Bx)$, where x and y are the input and output, respectively, and A as well as B are variable parameters that control the amplitude and the degree of curvature of the nonlinearity, respectively. Fig. 3 shows the implementation for simulating this nonlinearity. Whether or not the signal propagates through the nonlinearity, the intermediate decoder (labeled "decodem4") processes the channel output by separating the frequency components via a bank of bandpass filters as shown in Fig. 4. These filters are centered at the $2m$ (in MHz), $m = 1, 2, \dots, 30$, frequencies with bandwidth sufficiently large to capture much of the energy associated with each on-off keyed modulation signal. For simulation purposes, since the data rate of the users was typically in the 100 KBPS range, a bandpass filter bandwidth of 500 KHz proved adequate. The output of these filters was squared and integrated over the bit duration interval. Each one of these outputs was a measure of signal energy in each of the $2m$ (in MHz) frequencies. In order to model the random photon count that occurs when light impinges on a photodetector, and the efficiency with which light energy is converted to an electric current, two more blocks were added following the integrate and dump operation. One block added is called a Poisson Block in SPW which is a device that generates a random number (i.e., random variable) that is Poisson distributed, having mean value that is proportional to the size of the input to the block. The random number that is generated, one for each of the $2m$ (in MHz) frequencies, is representative of the energy of the signal at these frequencies, and is further processed by the next block that encompasses the decoder operation. The efficiency of the energy conversion process was accounted for by simply adding a scalar gain operation in front of the Poisson block. The decoder block, which involves a specific signal processing operation, as can be seen from Fig. 1, requires a separate such device that is unique to each user. As explained in Section 2, the decoder adds the random (Poisson distributed) numbers generated at each frequency for which the $2K$ elements of U_i and \bar{U}_i have logical 1's. The sum involving the elements of \bar{U}_i is subtracted from sum involving the elements of U_i . The difference that is produced is a random number that is compared to a zero threshold. If the threshold is exceeded a logical 1 in the data associated with the particular user is declared, otherwise a logical zero is declared. This operation has been implemented in each decoder block appropriate to each user. One such example (labeled "decusrfl") is shown in detail in Fig. 5. Specific results obtained from the use of these interconnected blocks in simulations are presented in the next section.

Section 4: Simulation Results

Results of all simulation runs are too numerous to present here in their entirety. The focus here is demonstrating the proper functioning of the software evidenced by the results produced and at the same time demonstrate the effect on performance due to variations in key system parameters. Simulation runs were carried out with seven user operating simultaneously in a synchronous mode at a 100 KBPS data rate. Tests were carried out with and without a channel nonlinearity present as well as different settings of the photodiode efficiency factor. Figs. 6-8 and 9-11 show the SPW Signal Calculator Page output for three of the seven active users without and with the nonlinearity present, respectively.

On the top trace a portion of the original bit stream can be seen, while the trace below shows the corresponding portion of the recovered bit stream. The other three traces show the sum of the Poisson variables that are subtracted prior to comparison with the zero threshold, thereby giving a sense of system level of noise immunity. (See explanation in Sec. 2.) In these particular figures, it can be seen that recovery of the bit stream is nearly exact, mostly due to the photodiode efficiency set to 100000. The nonlinearity is defined above with $A = 75$ and $B = 0.0075$. Decreasing this efficiency factor resulted in the observation of errors at significant rates. Simulation runs were also carried out with users operating simultaneously in an asynchronous mode. The high level simulation system shown in Fig. 12, demonstrates that preliminary decoders for each user are required. The bit rates selected for user #1 through #7 (in KBPS) were 100, 77, 43, 113, 66, 93, and 81.75, respectively. As before, tests were carried out with and without the channel nonlinearity present as well as different values of photodiode efficiency. Figs. 13-18 show the SPW Signal Calculator Page output for three of the seven active users with the nonlinearity present (having values of A and B as given above). In Figs. 13-15 the photodiode efficiency is set to 100000 while in Figs. 16-18 it is set to 10000. Observe the presence of errors in the recovered bit stream of each user. Clearly the effect of varying other system parameters can be observed by similar methods using the developed software.

CONCLUSIONS AND RECOMMENDATIONS

The research effort reported on, focuses on the software development used to obtain performance results of a specific multi-user optical code division multiple access (O-CDMA) digital communication system via computer simulation using block oriented tools. The simulations results clearly identified the difficulty associated with an optical CDMA system that utilizes unipolar as opposed to bipolar codes. The simulation results presented using bipolar codes involve a system accommodating multiple users (seven in this case, which can be increased to any desired number, but results in greater computational requirements) operating in either synchronous or asynchronous mode. The simulation results obtained are consistent with the theory and at the same time allow the investigation of system performance under different operational scenarios that could not be easily evaluated via strictly analytical means. Because of the constraints associated with this research project, the following recommendations are made regarding further investigations in this area.

1. To continue the computer modeling/simulation effort in order to evaluate the performance of systems with large number of users.
2. To evaluate the potential usefulness of codes (or masks) other than maximal length, such as Gold codes (extensions of maximal length codes), Walsh codes, or Kasami codes.
3. The exhaustively evaluate performance of the systems of interest via simulation as a function of the many parameters that can vary in practice.
4. To incorporate the effect of noise on system performance, and account for noise in the channel and the photodetectors.
5. To do a detailed study of bit error rate system performances under different operational scenarios using importance sampling techniques in order to reduce computational time required to quantify low error rates at high signal to noise ratios.

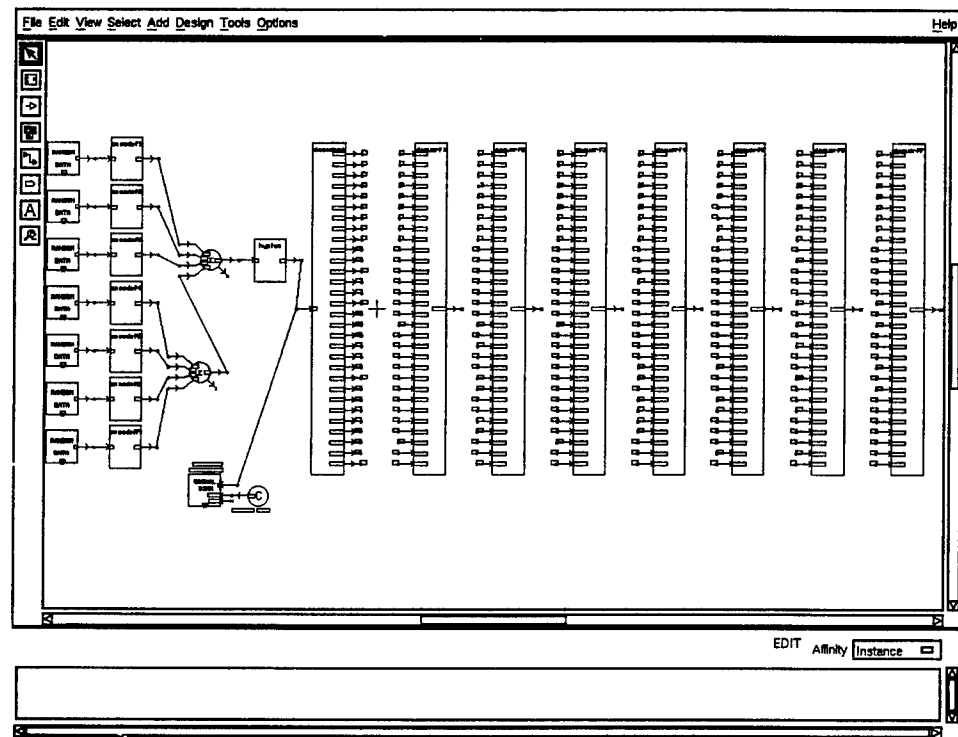


FIGURE 1: Block Diagram Design (BDD): 7 User Synchronous O-CDMA System

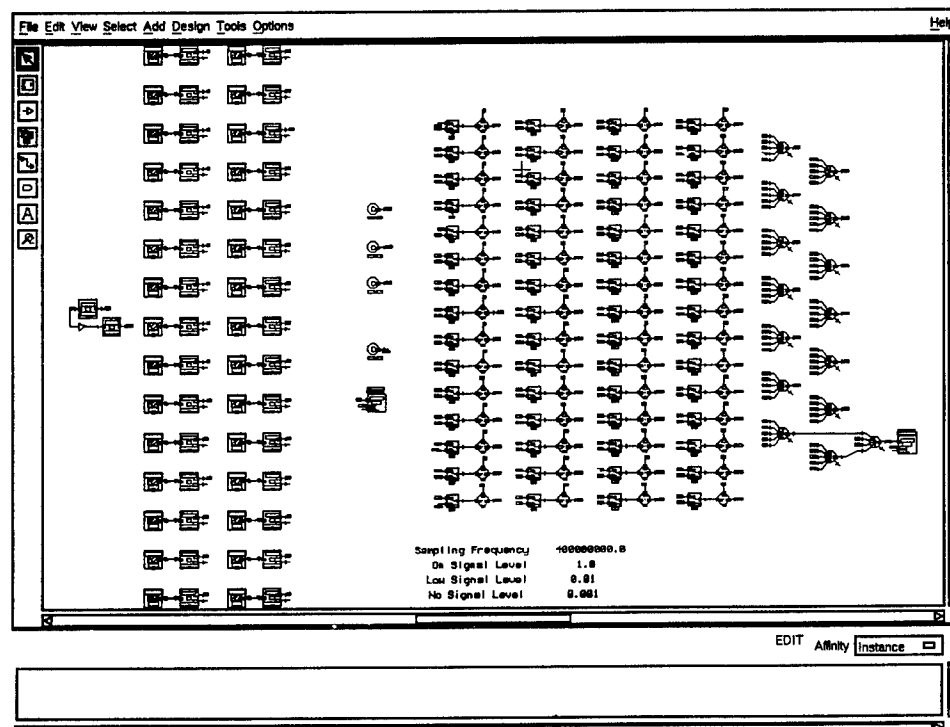


FIGURE 2: Block Diagram Design (BDD): Encoder ("encodelf")

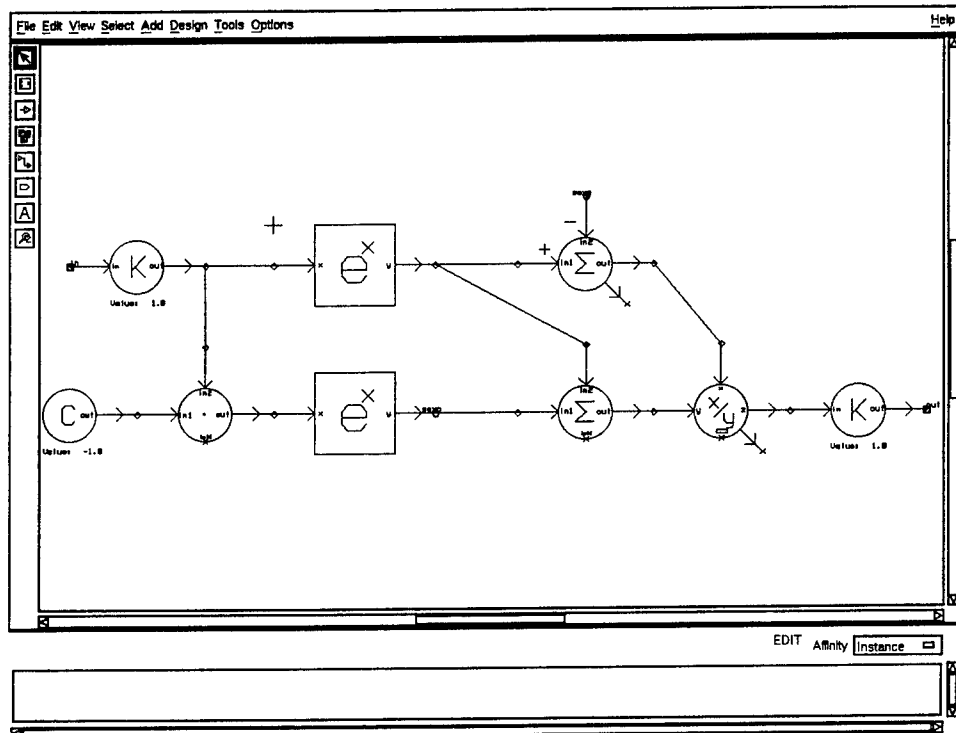


FIGURE 3: Block Diagram Design (BDD): Channel Nonlinearity

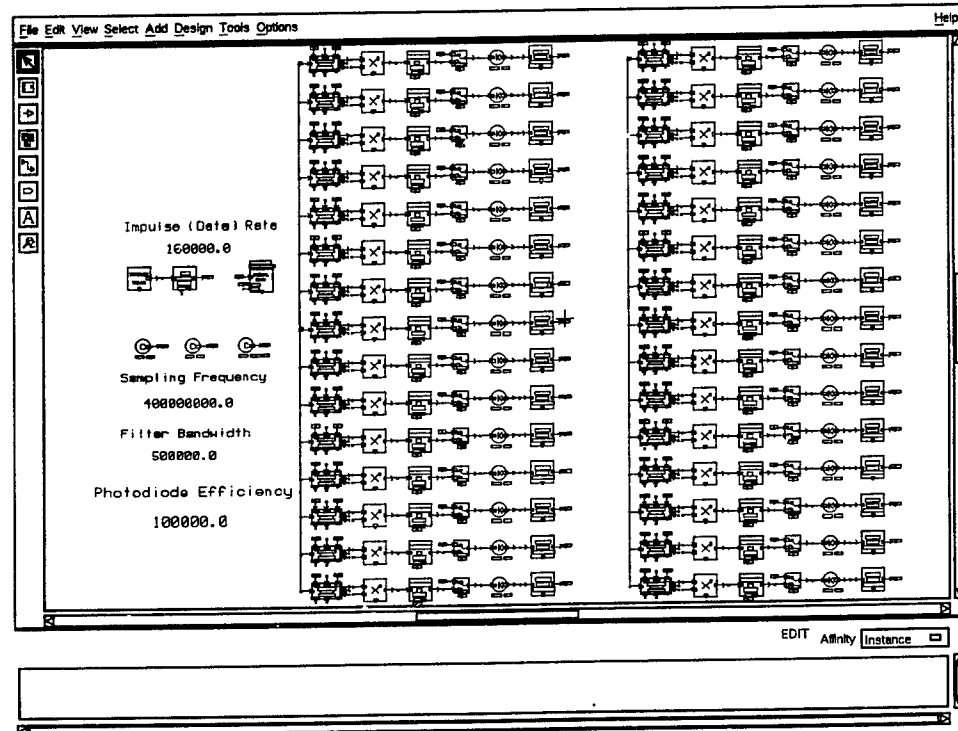


FIGURE 4: Block Diagram Design (BDD): Preliminary Decoder ("decodem4")

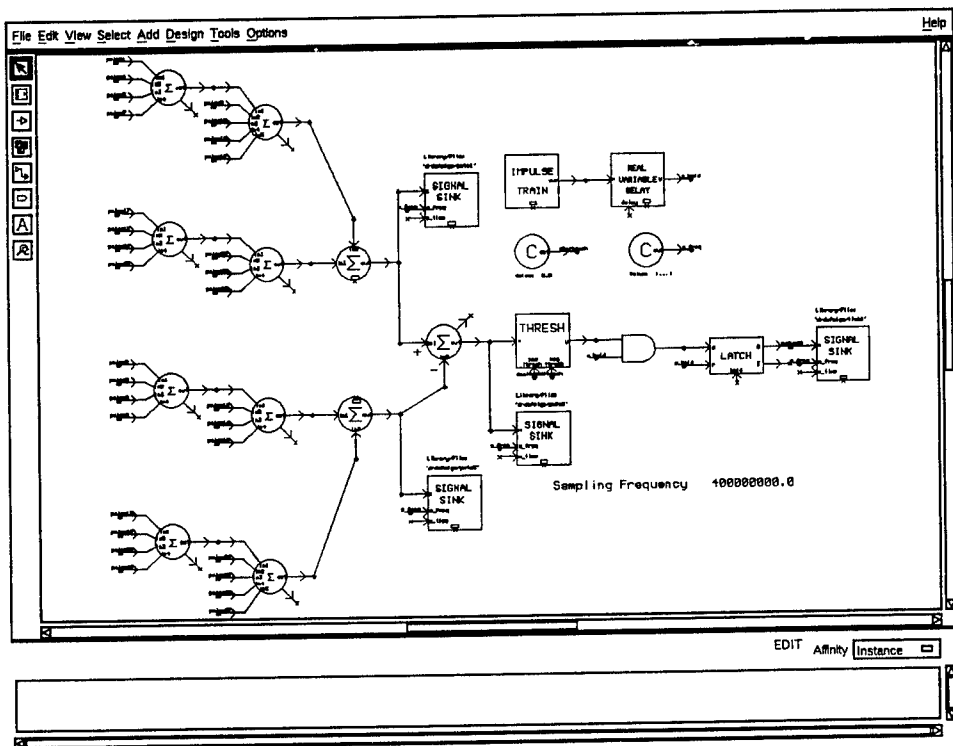


FIGURE 5: Block Diagram Design (BDD): Decoder ("decusrf1")

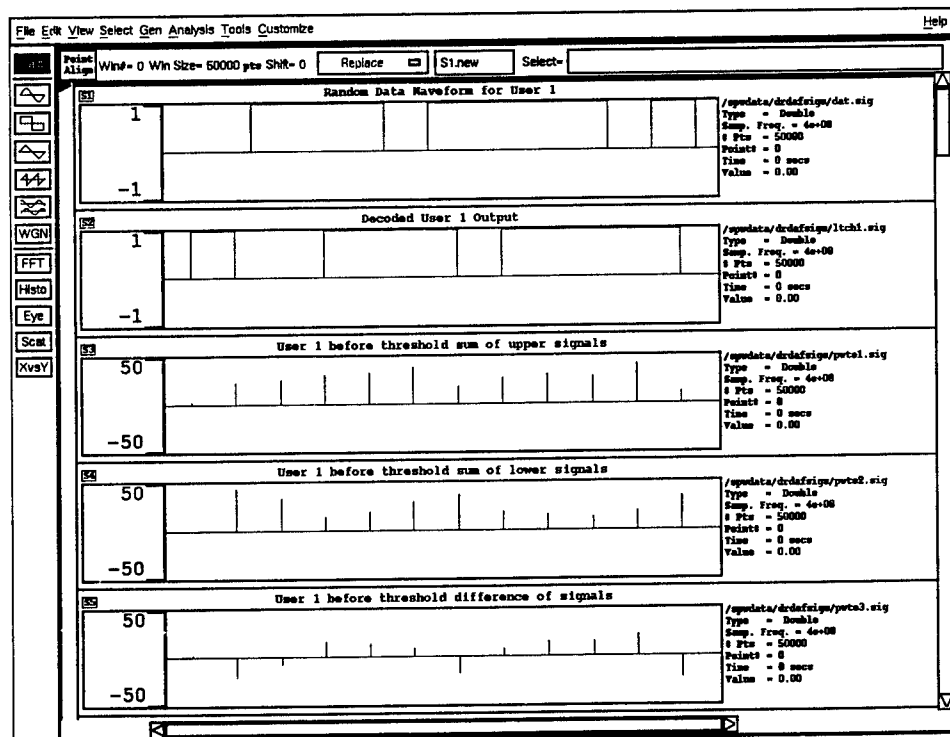


FIGURE 6: Signal Calculator Page (SCP): User #1 Output With Nonlinearity

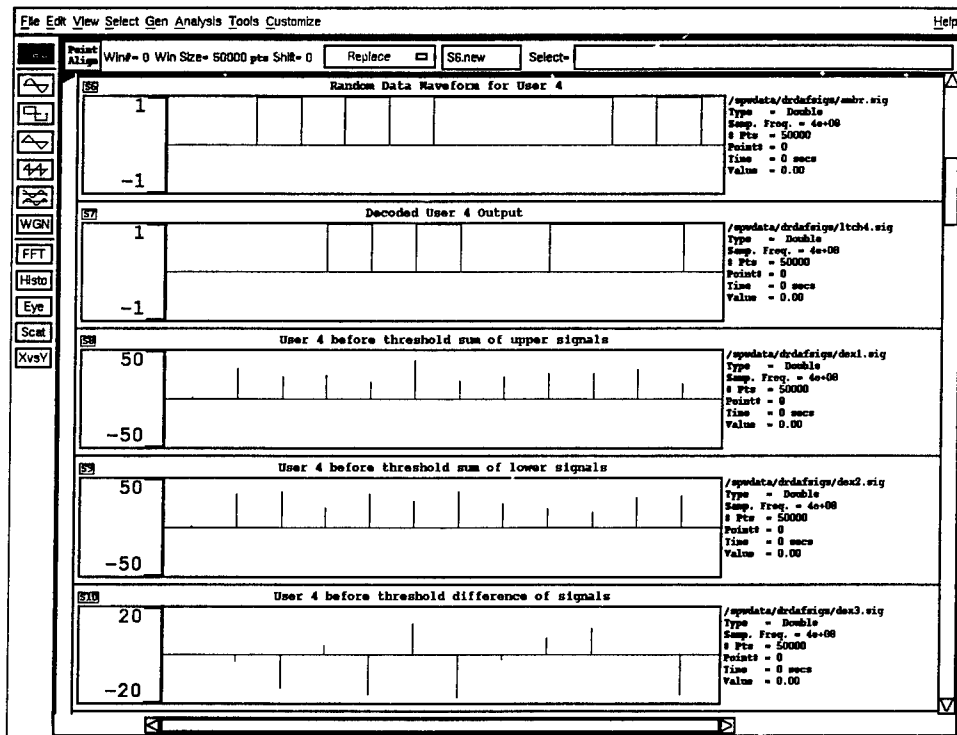


FIGURE 7: Signal Calculator Page (SCP): User #4 Output With Nonlinearity

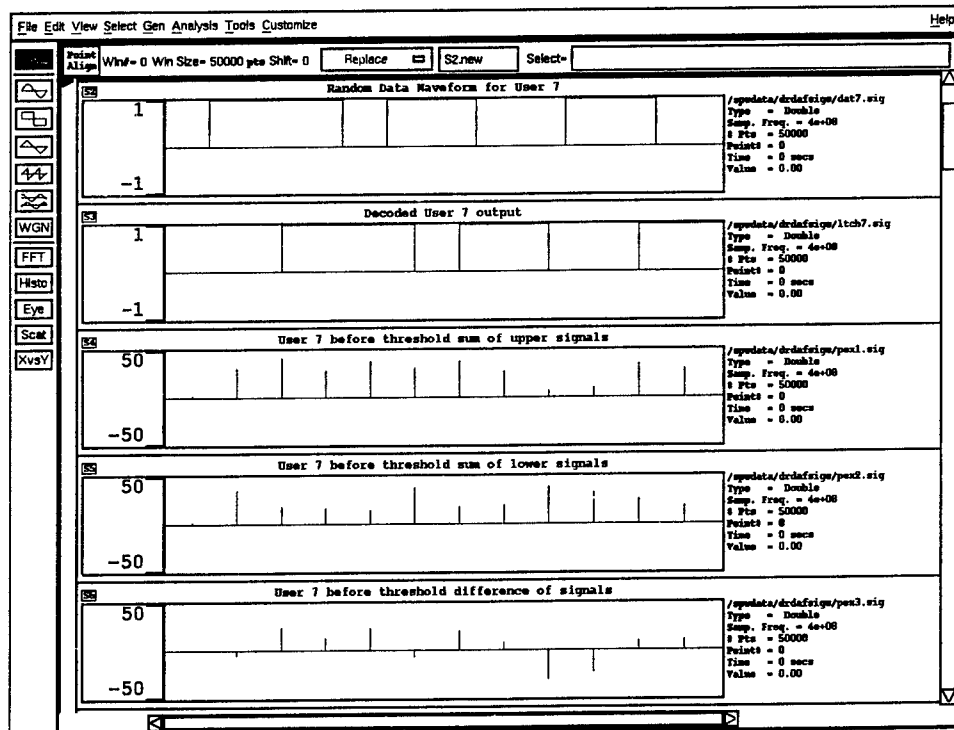


FIGURE 8: Signal Calculator Page (SCP): User #7 Output With Nonlinearity

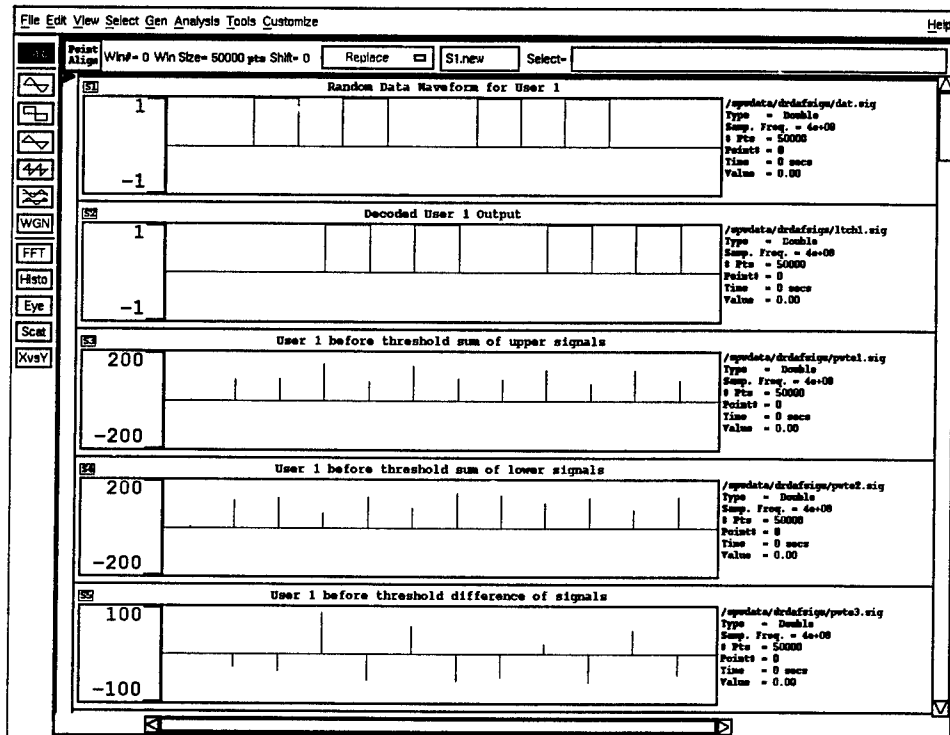


FIGURE 9: Signal Calculator Page (SCP): User #1 Output Without Nonlinearity

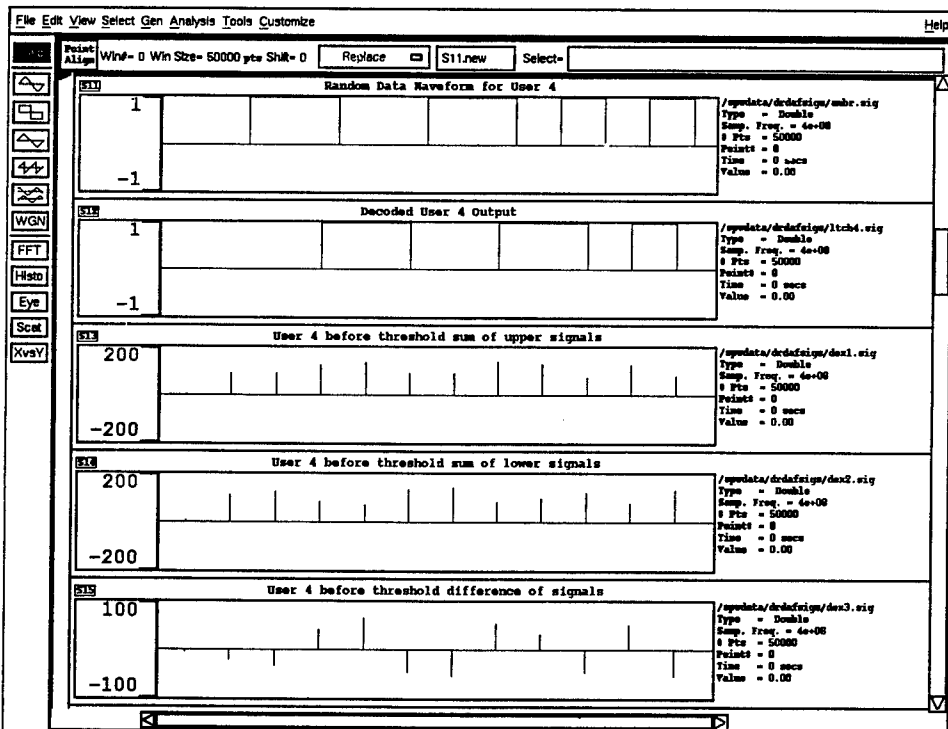


FIGURE 10: Signal Calculator Page (SCP): User #4 Output Without Nonlinearity

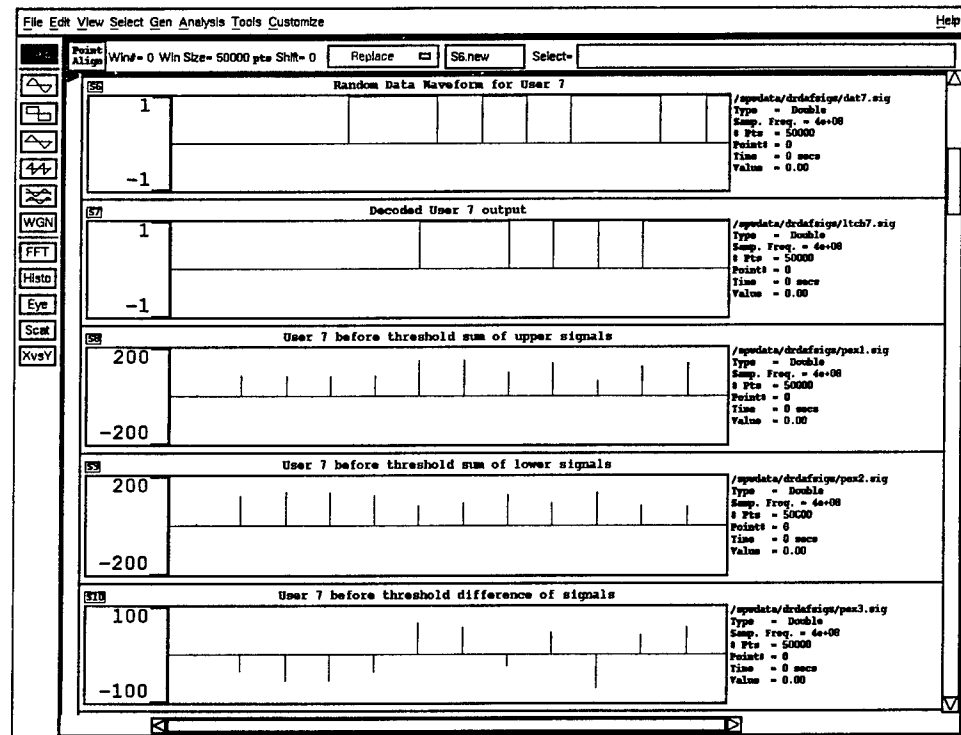


FIGURE 11: Signal Calculator Page (SCP): User #7 Output Without Nonlinearity

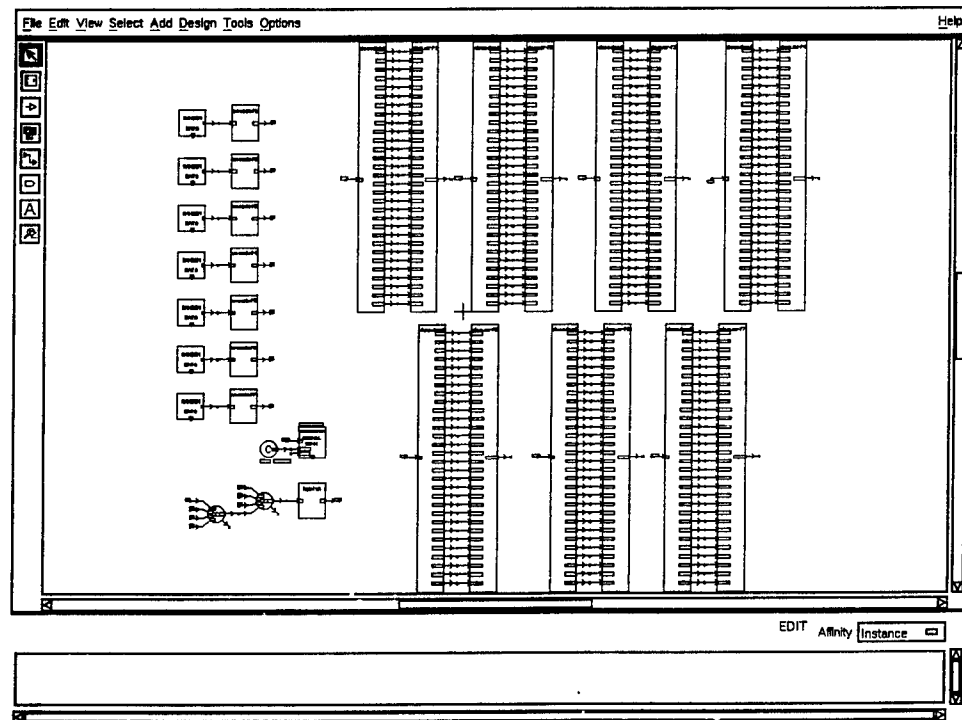


FIGURE 12: Block Diagram Design (BDD): 7 User Asynchronous O-CDMA System

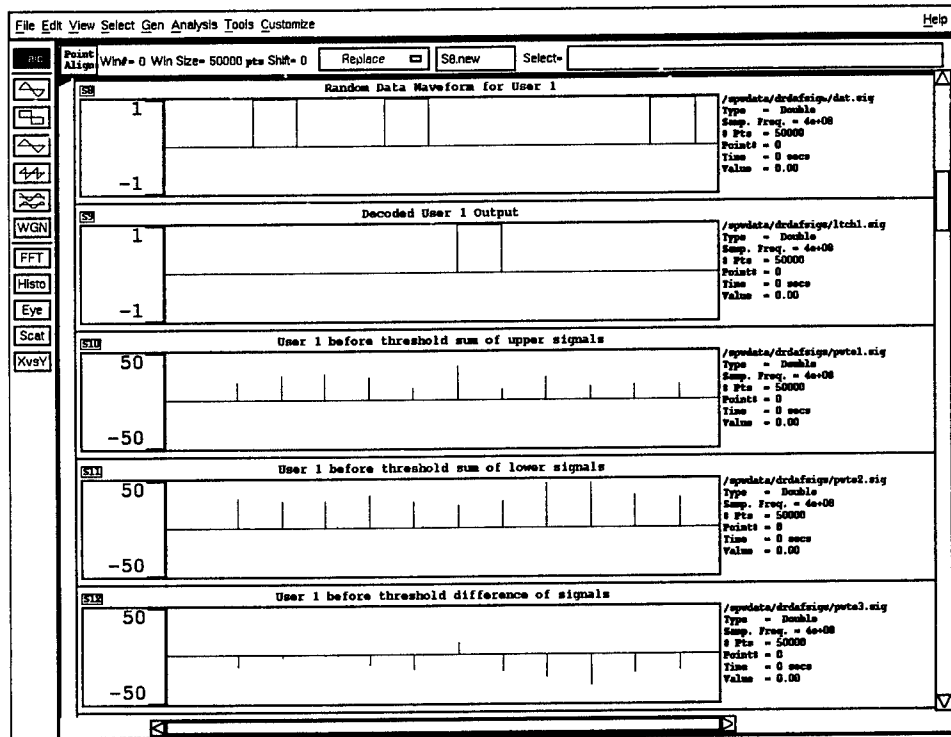


FIGURE 13: Signal Calculator Page (SCP): User #1 Output, PD Eff. = 100000

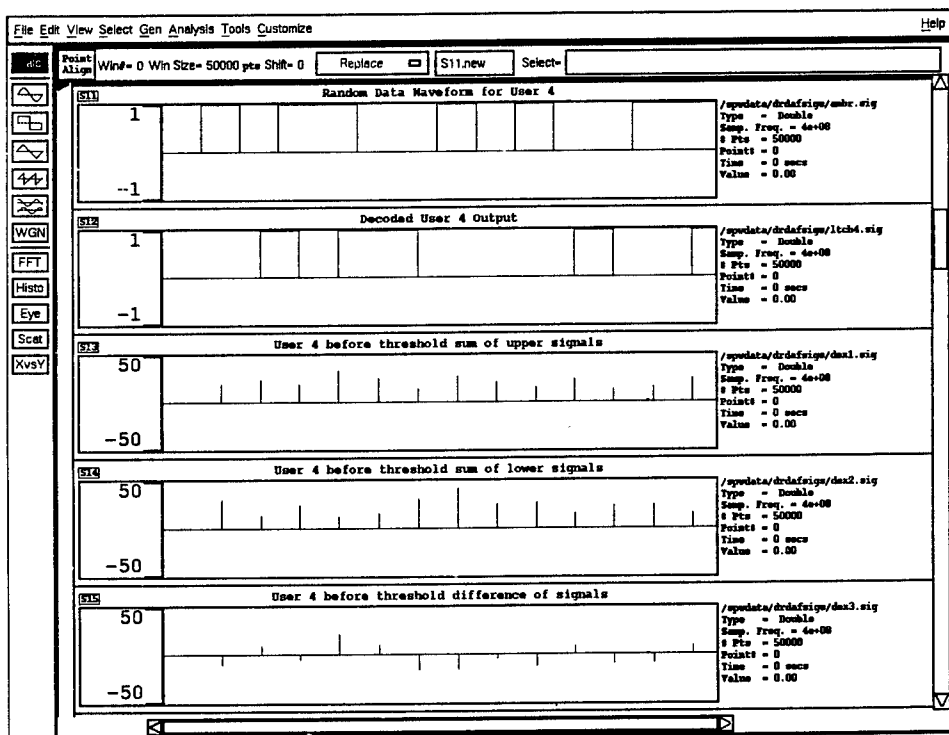


FIGURE 14: Signal Calculator Page (SCP): User #4 Output, PD Eff. = 100000

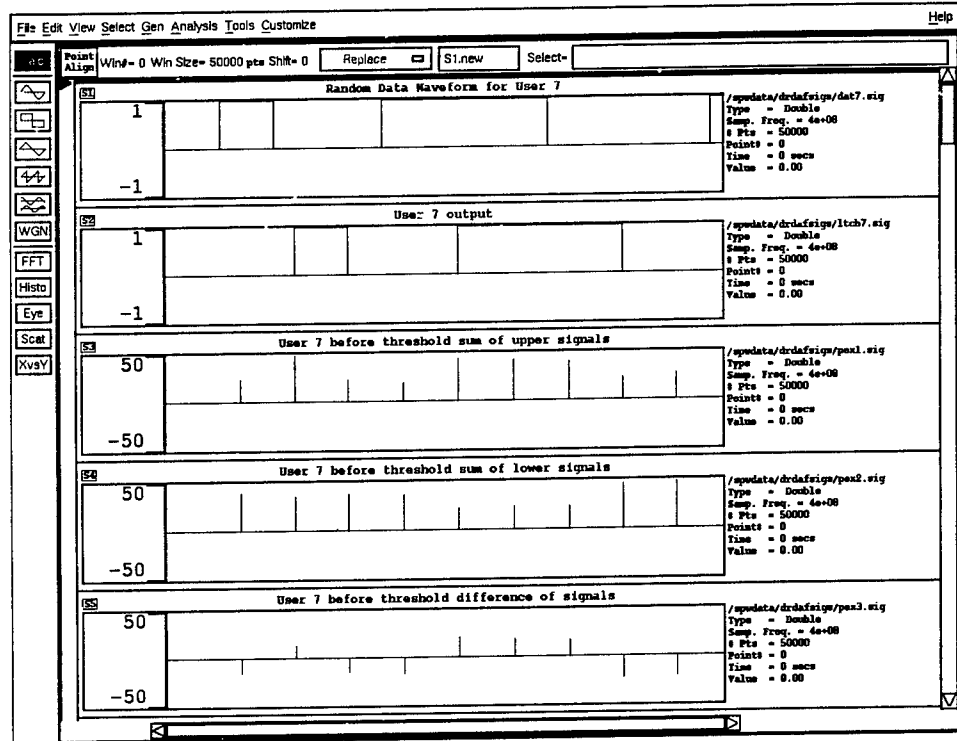


FIGURE 15: Signal Calculator Page (SCP): User #7 Output, PD Eff. = 100000

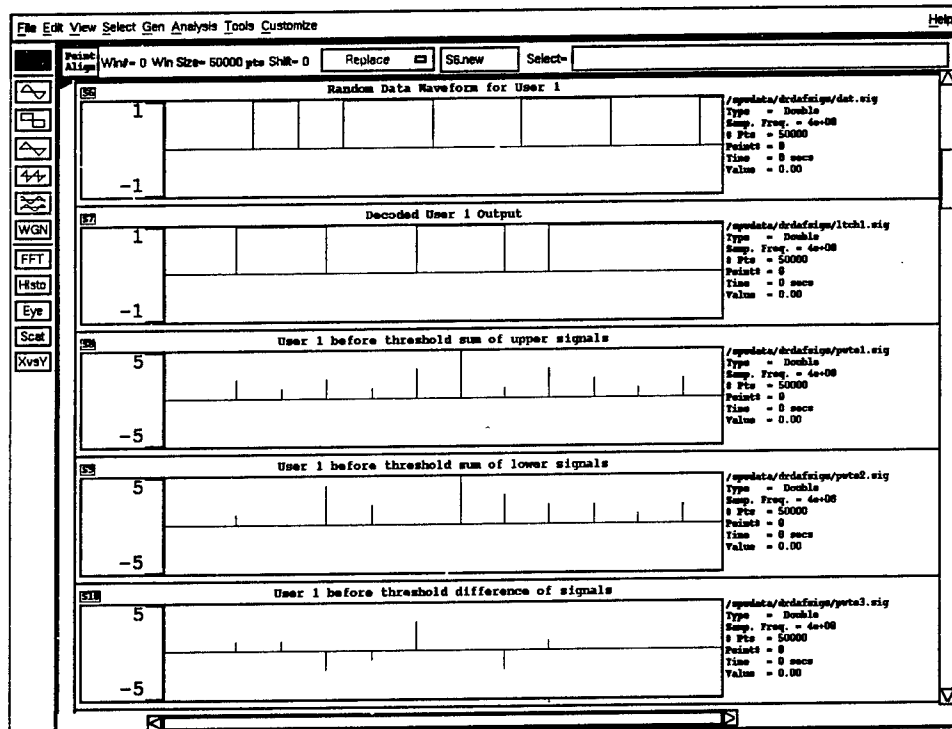


FIGURE 16: Signal Calculator Page (SCP): User #1 Output, PD Eff. = 10000

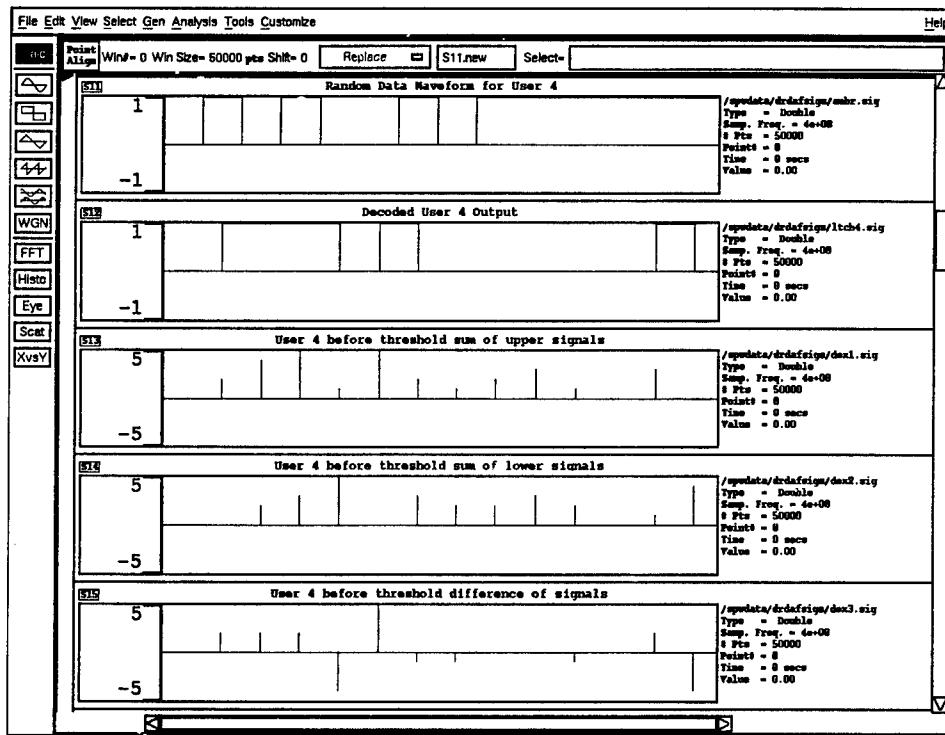


FIGURE 17: Signal Calculator Page (SCP): User #4 Output, PD Eff. = 10000

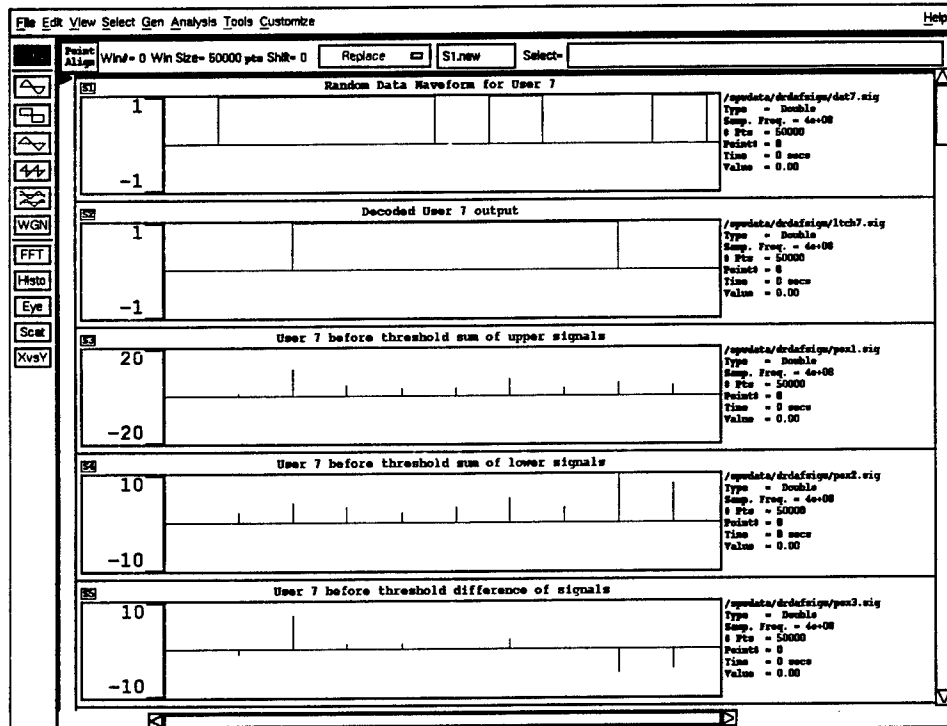


FIGURE 18: Signal Calculator Page (SCP): User #7 Output, PD Eff. = 10000

REFERENCES

- [1] Green, Paul A. Jr., *Fiber Optic Networks*, Prentice Hall, Englewood Cliffs, NJ, 1993.
- [2] Ramaswami, Rajiv, *Multiwavelength Lightwave Networks for Computer Communication*, IEEE Communications Magazine, Feb. 1993, pp. 78-88.
- [3] Winters, Jack H., Gitlin, Richard D., and Kasturia, Sanjay, *Reducing the Effects of Transmission Impairments in Digital Fiber Optic Systems*, IEEE Communications Magazine, June 1993, pp. 68-76
- [4] Tomlinson, W. J., and Stolen, Roger H., *Nonlinear Phenomena in Optical Fibers*, IEEE Communications Magazine, April 1988, pp. 36-44.
- [5] Ziemer, Rodger E., and Peterson, Roger L., *Digital Communications and Spread Spectrum Systems*, Macmillan Publishing Company, New York, 1985, Chp. 7, 8.
- [6] Hui, J. Y., *Pattern Code Modulation and Optical Decoding - A novel Code Division Multiplexing Technique for Multifiber Networks*, IEEE Journal on Selected Areas in Communications, vol. SAC-3, no. 6, Nov. 1985, pp. 916-927.
- [7] Salehi, Jawad A., *Code Division Multiple-Access Techniques in Optical Fiber Networks - Part I: Fundamental Principles*, IEEE Transactions on Communications, vol. 37, no. 8, August 1989, pp. 824-833.
- [8] Salehi, Jawad A., *Code Division Multiple-Access Techniques in Optical Fiber Networks - Part II: Systems Performance Analysis*, IEEE Transactions on Communications, vol. 37, no. 8, August 1989, pp. 834-842.
- [9] Brady, David and Verdu, Sergio, *A Semiclassical Analysis of Optical Code Division Multiple Access*, IEEE Transactions on Communications, vol. 39, no. 1, Jan. 1991, pp. 85-93.
- [10] Brandt-Pearce, M., and Aazhang, B., *Multiuser Detection for Optical Code Division Multiple Access Systems*, IEEE Transactions on Communications, vol. 42, no. 4, April 1994, pp. 1801-1810.
- [11] Nguyen, L., Aazhang, B., and Young, J. F., *All-optical CDMA with Bipolar Codes*, Electronic Letters, Vol. 31, no. 6, March 16, 1995, pp. 469-470.

Joseph Calo Report not available at time of publication.

Paul Cefalo Report not available at time of publication.

MESOSCALE MODEL EXPERIMENTS ON CLOUD SHADING EFFECTS

Chia-Bo Chang
Associate Professor
Department of Geosciences

Texas Tech University
Lubbock, TX 79409

Final Report for:
Summer Faculty Research Program
Phillips Laboratory

Sponsored by:
Air Force Office of Scientific Research
Bolling Air Force Base, DC

and

Phillips Laboratory

August 1995

MESOSCALE MODEL EXPERIMENTS ON CLOUD SHADING EFFECTS

Chia-Bo Chang
Associate Professor
Department of Geosciences
Texas Tech University

Abstract

This study examined the distribution of cloud fraction associated with the PSU/NCAR MM4 model and the effects of cloud shading on short-range mesoscale numerical weather prediction. These effects were evaluated using real-data model simulation experiments. The experiments conducted were as follows:

- 1) Experiment 1 was a 12-h MM4 forecast with the complete model physics. Low, middle, and high cloud fraction were parameterized based on relative humidity.
- 2) Experiment 2 was similar to Experiment 1 except without the effects of cloud shading.
- 3) Experiment 3 was similar to Experiment 1 except that the model cloud fractions were determined based on relative humidity in conjunction with the model cloud water.

Results indicated that without the effects of cloud shading the model surface temperatures were too high and consequently the model atmosphere became less stable causing erroneous convection. Also, cloud shading tended to enhance the low-level baroclinicity between the cloudy and clear areas. The involvement of cloud water in Experiment 3 reduced the total cloud cover and resulted in a better simulation of surface flow field in this case.

Introduction

In the atmosphere, the dynamic systems of all scales, ranging from small mesoscale convective clouds to very large planetary-scale disturbances, originate from thermal convection (warm air rising and cold air sinking). It is well known that radiation is the primary mechanism and energy source for the generation of thermal convection. The dynamic systems develop within the baroclinic zones as a result of horizontal differences in radiation budgets (differential heating). On the other hand, the cloud and moisture distribution associated with the dynamic systems will modify the radiation field. Such radiation-dynamics interaction may prove to have a significant role in mesoscale circulation.

Clouds are the principal modulator of radiation in the atmosphere. The presence of clouds increases the counter radiation. Clouds considerably reduce the effective outgoing infrared radiation and radiative cooling in the atmosphere below the clouds. Also, a substantial depletion of insolation takes place at the cloud top because of its large albedo which, except for cirrus, is on the order of 0.5 (Stephens and Webster, 1981). This depletion process may not be significant so far as the absorption of solar radiation in the atmosphere is concerned. However, it will have a controlling effect on surface energy budget over land.

Because land surface receives more radiative energy from the sun than it loses in the form of infrared radiation during the daytime, some of the excess in radiative energy will be transferred from ground to the atmosphere in the form of heat flux. The intensity of sensible heat flux (surface heating) is largely dependent upon the characteristics of surface and the atmospheric conditions, for example, cloud cover. The disruption of radiative transfer due to cloud shading can strongly influence surface temperature as well as the thermal structure (e.g., static stability and regional baroclinicity) of the lower troposphere. Lipton (1993) showed that the assimilation of cloud shading derived from satellite cloud information could improve the model prediction of surface temperature. Surface temperature is the essential element in defining surface energy sources for the development of mesoscale systems.

This study examined the role of cloud shading in short-range mesoscale numerical weather prediction

(NWP) using real-data model simulation experiments. For this purpose the mesoscale modeling system known as MM4 developed at the Pennsylvania State University (PSU) and National Center for Atmospheric Research (NCAR) was employed. In addition to the current parameterization method based on relative humidity, a modified approach of defining the model cloud fraction was evaluated. The distribution of MM4 model cloud fraction and its impact on forecast have not been examined before. The results of this study will be most useful for those MM4 users interested in air-land thermal interaction and related moist processes.

Modeling system

A brief overview of MM4 system summarized from Gill (1992) and Grell et al. (1994) is given in this section. MM4 is a comprehensive mesoscale modeling system consisting of objective analysis and initialization codes, dynamic prediction model, and the post-forecast diagnosis codes. The MM4 dynamic prediction model is a three-dimensional primitive equation model using a σ grid in the vertical and a Cartesian grid casting on a Lambert conformal projection in the horizontal.

The model basic equations are the equations of motion, hydrostatic equation, first law of thermodynamics, moisture conservation equations for water vapor, cloud water, and rainwater. The model physics are as follows:

- 1) Parameterization of subgrid-scale moist convection,
- 2) Dry convective adjustment,
- 3) Microphysics in the grid-scale cloud and precipitation processes,
- 4) Planetary boundary layer (PBL) processes,
- 5) Atmospheric radiation and surface energy budget.

In this study the model initial state was obtained from the objective analysis of the National Weather Service (NWS) upper-air and surface observations. The National Meteorological Center (NMC) gridded data was used as a first guess in the analysis. The dynamic model had 29 levels with the σ values ranging

from 1 at the surface to 0 at the model top (~ 50 mb) and a considerably higher resolution in the PBL (about 10 σ levels below 900 mb). Two-way interactive nested grid was used. The coarse-mesh domain had 50×55 grid points, while the nested fine-mesh domain had 67×85 grid points. The grid mesh sizes were 45 km and 15 km, respectively. For the coarse-mesh model, time-dependent conditions generated from the observations were imposed on the lateral boundaries. Other numerical aspects of the model including the horizontal grid structure, finite difference approximation for space and time derivatives, and lower and upper boundary conditions were summarized in the paper by Modica et al. (1994). A modified Arakawa-Schubert scheme and the associated microphysics in the model cloud water equation were employed.

The central issue for this study is how cloud shading impacts the surface energy budget over land. The surface energy budget involved incident solar and infrared irradiance, sensible heat flux and latent heat (moisture) flux into the atmosphere, and heat conduction into the sub-surface layer. The surface heat fluxes were determined using a bulk-aerodynamical formulation. In the radiation computation, only water vapor was considered as an optically active gas in the model atmosphere, and radiative heating/cooling in the model atmosphere was neglected. The ground temperatures were computed from the surface energy budget equation.

The cloud attenuation of solar radiation and enhancements of infrared radiation were parameterized. The reduction of insolation at the surface should result in lower ground temperatures and consequently smaller sensible heat flux and moisture flux. Three cloud layers (low, middle, and high clouds) were considered. The empirical formula for cloud fraction (n) based on relative humidity in the lower atmosphere (between $\sigma = 0.96$ and 0.75) and middle atmosphere (between $\sigma = 0.75$ and 0.35) was

$$n = 4 \text{ RH} - 3,$$

and in the upper atmosphere ($\sigma \leq 0.35$)

$$n = 2.5 \text{ RH} - 1.5,$$

where RH was the maximum relative humidity found in the respective layers. Note that although cloud water was predicted in the model, cloud fraction was not directly correlated with the model cloud water distribution. The evaporation of cloud water was invoked in the cloud water equation when the air was unsaturated. The existence of cloud water denoted a 100% RH. Hence indirectly n was influenced by the cloud water distribution. As described in the next section, an experiment involving the model cloud water in the cloud fraction calculation was conducted.

Methodology

The real-data model simulation experiments were conducted on the 23-24 August 1993 case. The experiments were aimed at a quantitative assessment of the role of cloud shading in regional circulation. The case study represented a weak synoptic situation. No significant meteorological event occurred in the United States during the 24-h period. This case was selected for an ongoing satellite-model coupled analysis research at Atmospheric Science Division, Phillips Laboratory. The objective analysis and model initialization carried out earlier enabled us to engage in the model experiments in a relative short time. Also, the availability of satellite cloud imageries could provide information for a qualitative verification of the model cloud cover later.

The simulation experiments and related scientific questions to be stressed are summarized below.

- 1) Experiment 1 (E1) was a 12-h forecast with the complete model physics as listed earlier. Cloud fraction (n) was computed based on RH only.
- 2) Experiment 2 (E2) was similar to E1 except without the effects of cloud shading ($n = 0$).
- 3) Experiment 3 (E3) was similar to E1 except that n was computed based on RH in conjunction with the model cloud water.

E1 is regarded as a benchmark run. The coarse-mesh model output of E1 will be compared with observations (gridded fields) for a qualitative evaluation of the model performance. The only discrepancy between E1 and E2 was in the computation of incident radiant energy at the surface. E2 was designed to

test the hypothesis that the effects of cloud shading could significantly impact the model forecast. Careful comparison between E1 and E2 should help us to achieve a physical understanding of such impact. In E3 a positive n based on RH was set equal to zero if the corresponding layer mean cloud water was lower than the threshold value of 0.001 gm/kg. Within a layer of very small cloud water content, it was possible that $n = 0$ even if RH = 100%. E3 was designed to reveal whether the model cloud cover could be improved by invoking the predicted cloud water. The threshold value somewhat arbitrary is more than two orders of magnitude below the typical liquid water content in stratus clouds (Rogers, 1979). The sensitivity of the model to the change is very interesting to examine. Because of the two-way interactive nested-grid approach, there will be minor differences between the coarse-mesh and fine-mesh results. Thus, except for cloud fraction, the model simulations over the fine-mesh domain will be used for inter-comparison between the experiments.

Results of the model simulations

The model was initialized at 1200 UTC 23 August 1993 for all experiments. Figure 1 shows the analyzed initial surface ($\sigma = 0.995$, approximately 50 m above the ground) temperatures and vector winds. The coarse-mesh model domain covered the eastern half of the United States. The relatively large temperature gradient zones, one over Kansas and Missouri and the other extending from Illinois southeastward to Georgia, were associated with the surface cold and warm fronts, respectively. The wind field displayed some direction shifts across the fronts in eastern Kansas and in the southeastern states. Also, the advection of warm air from the south toward the north-central states was quite evident. The southern portions of the fronts started to dissipate in the next 12 hours. At 500 mb (not shown) a nearly north-south oriented trough (between North Dakota and Kansas) was located slightly to the west of the model domain and a ridge dominated the eastern states. The upper-air jet streams were confined to the northwest corner of the domain. The synoptic setting suggested little upper-air triggering mechanism for the formation of convective storms over the eastern United States.

Figure 2 shows the observed and 12-h simulated (E1) surface temperatures at 0000 UTC 24 August 1993. Because of the high terrain, a strip of lower temperature was manifest over the Appalachian. The observed temperature patterns indicated the eastward movement of cool air behind the cold front toward Illinois and Missouri. The cool air pushed the northward intrusion of warm air behind the warm front toward Indiana and Ohio. A major forecast error occurred in Illinois and Missouri where the model was 5-10°C warmer than the observations. The model performed better inside the fine-mesh grid as well as in the upper air (not shown); the forecast errors were on the order of 1°C.

Figure 3 shows the observed and 12-h simulated (E1) surface vector winds at 0000 UTC 24 August. As in the case of temperature, the model also overpredicted the wind speeds in Missouri, Illinois, and Indiana. Other notable errors included the erroneous southerlies in southern Alabama and the north winds instead of the observed west winds near the west coast of Florida. Better agreement with the observations was found over the open water.

Figure 4 shows the 6-h and 12-h model cloud fractions for E1. The distribution of cloud fraction (n), which is not a model variable, was constructed using the MM4 post-forecast analysis codes. Over the eastern states there was extensive low-cloud cover. Between 6 h and 12 h minor changes occurred in the lower cloud cover, and a decrease in cloudiness in the middle layer and slight increase in cloudiness in the higher layer were observed. The areas of maximum n in the middle layer at 6 h were correlated with the areas of minimum n in the lower layer. The two circular areas of high clouds in the southeast at 12 h were caused by convection. Superposing the three layers of clouds, we notice rather cloudy conditions in the east at both times.

Figure 5 shows the 6-h and 12-h model cloud fraction for E3. The total area of low cloud cover was considerably smaller than that of E1. The use of the threshold value of 0.001 gm/kg produced very sharp gradient in cloud fraction between the cloudy and clear skies. The low clouds became less organized 6 h later. In the middle layer, several isolated small areas of large cloud fraction were found over their

counterparts in the lower layer. In the upper layer, cloud fraction at 12 h over the southeast did not show tight gradients as in the lower and middle layers. The causes of such structure change are not clear. It could be a result of using slightly different formulas in computing RH between the model and post-forecast process codes.

The large error in the temperature forecast in E1 over Illinois and Missouri (Fig. 2) appeared to be caused by too much surface heating. The model ground temperatures (not shown) at the 6 h simulation (around the local noon) had a maximum isotherm of 34°C in the general area. It was noted that the model failed to reproduce the light rainfall (about half inch in 24 h as revealed in the daily weather maps) in Illinois and Missouri. The dry surface in conjunction with the limited cloud cover (Fig. 4) could contribute to the high ground temperatures and too strong surface heating in the model.

In both coarse-mesh and fine-mesh simulations, more organized convective rainfall was produced in E2 than in other two experiments during the 12-h simulations. Very little non-convective precipitation was predicted in all experiments. Figure 6 shows the 12-h fine-mesh simulated convective precipitation. A band of convective cells with maximums over 3 cm located primarily in western North Carolina and many scattered convective cells were predicted in E2. E1 produced the least convection, while E3 resembled somewhat E2 in the general patterns but with fewer convective cells. Unfortunately, at this time we do not have adequate precipitation data for a quantitative assessment of the model performance in precipitation forecasting. Based on the daily weather maps, which showed very little precipitation in western North Carolina during the period of 23-24 August, E1 appeared to have the highest skill and E2 the lowest in precipitation forecasting.

Figures 7, 8, and 9 show the 12 h simulated surface temperatures and vector winds over the fine-mesh domain for E1, E2, and E3, respectively. In general the temperatures of E2 (without cloud shading) were about 1-2°C higher than those of E1 which had extensive cloud cover over the fine-mesh domain (Fig. 4). Because of the terrain distortion of σ level the tight gradients in the areas surrounding the Appalachian

mountains were misleading. In western Florida, and southern Alabama and Georgia, both E1 and E3 had lower temperatures but higher gradients than E2 suggesting the enhancement of surface thermal contrast due to the effects of cloud shading. In the upper layers (e.g., 200 mb), except in the vicinities of convection the temperature fields (not shown) of all three experiments were quite similar. Substantial impact of the shading effects on the flow patterns was noted. For example, there were off-shore flows in E1 and generally on-shore flows in E2 along the coast of Florida Panhandle, and clear changes in the wind directions over Alabama and Georgia from E1 to E2. Some departures of E3 from E1 were also manifest in Florida and Alabama. Because the effects of cloud shading reduced the model convection, the wind fields in E1 had less small-scale features than the other experiments at all levels.

Summary and recommendations

The effects of cloud shading on short-range mesoscale NWP were examined based on the real-data model simulation experiments. The model results indicated that the cloud shading effects should not be overlooked in mesoscale NWP. Without the shading effects the model surface temperatures were too high and consequently the model atmosphere became less stable causing erroneous convection. Also, cloud shading tended to increase the low-level baroclinicity between cloudy and clear areas. In the coastal areas, where land-water contrast played a dominant role in the regional circulation, the model dynamic responses to the enhanced baroclinicity were most recognizable. For example, in western Florida the presence of clouds cooled the land and resulted in the off-shore surface flows (land breezes), while without the shading effects intense surface heating was responsible for the enhanced on-shore flows. The major differences in the upper air flows between the model experiments could be attributed to the changes in convection.

In comparison with the parameterization approach based on RH, the use of cloud water represented a more dynamically consistent way in locating the model clouds. The involvement of cloud water reduced the total cloud cover and improved the model simulation of surface winds in this case study. It suggested that the model was sensitive to the changes in cloud fraction estimation. However, the responses of motion

field to the effects of cloud shading may vary from case to case depending on surface conditions (e.g., soil type, canopy). More case studies with longer model integrations and extensive model verification and diagnosis are necessary in search of a reliable empirical formula for defining cloud fraction. Such formula, in addition to RH as used in most NWP models, should involve other relevant model parameters such as cloud water and vertical motion.

Acknowledgements

I am grateful to RDL/AFOSR and Phillips Laboratory for the research opportunity at Hanscom AFB. I wish to express my appreciation to Mr. George Modica for his technical assistance and patient guidance in preparing the complex modeling system used in this research. I wish to thank Mr. Donald A. Chisholm, for his help in many administrative aspects of this program. It has been an enjoyable experience to work with many colleagues in the laboratory. They were always available to answer questions concerning the computers and operating systems, and sciences.

The model simulation experiments were performed on the Navy c90 computer as well as the Army c90 and CRAY-YMP computers.

References

- Gill, D. O., 1992 A user's guide to the Penn State/NCAR mesoscale modeling system. NCAR/TN-381+IA, National Center for Atmospheric Research, Boulder, CO.
- Grell, G. A., J. Dudhia, and D. R. Stauffer, 1994 A description of the fifth-generation Penn State/NCAR mesoscale model (MM5). NCAR/TN-398+IA, National Center for Atmospheric Research, Boulder CO, 107 pp.
- Lipton, A. E., 1993 Cloud shading retrieval and assimilation in a satellite-model coupled mesoscale system. *Mon. Wea. Rev.*, **121**, 3062-3081.
- Modica, G. D., S. T. Heckmab, and R. M. Rasmussen, 1994 An application of an explicit microphysics mesoscale model to a regional icing event. *J. Appl. Meteor.*, **33**, 53-64.
- Rogers, R.R., 1979 A Short Course in Cloud Physics. Pergamon Press, 235 pp.
- Stephens, G. L., and P. J. Webster, 1981: Clouds and climate: Sensitivity of simple systems. *J. Atmos. Sci.*, **38**, 235-247.

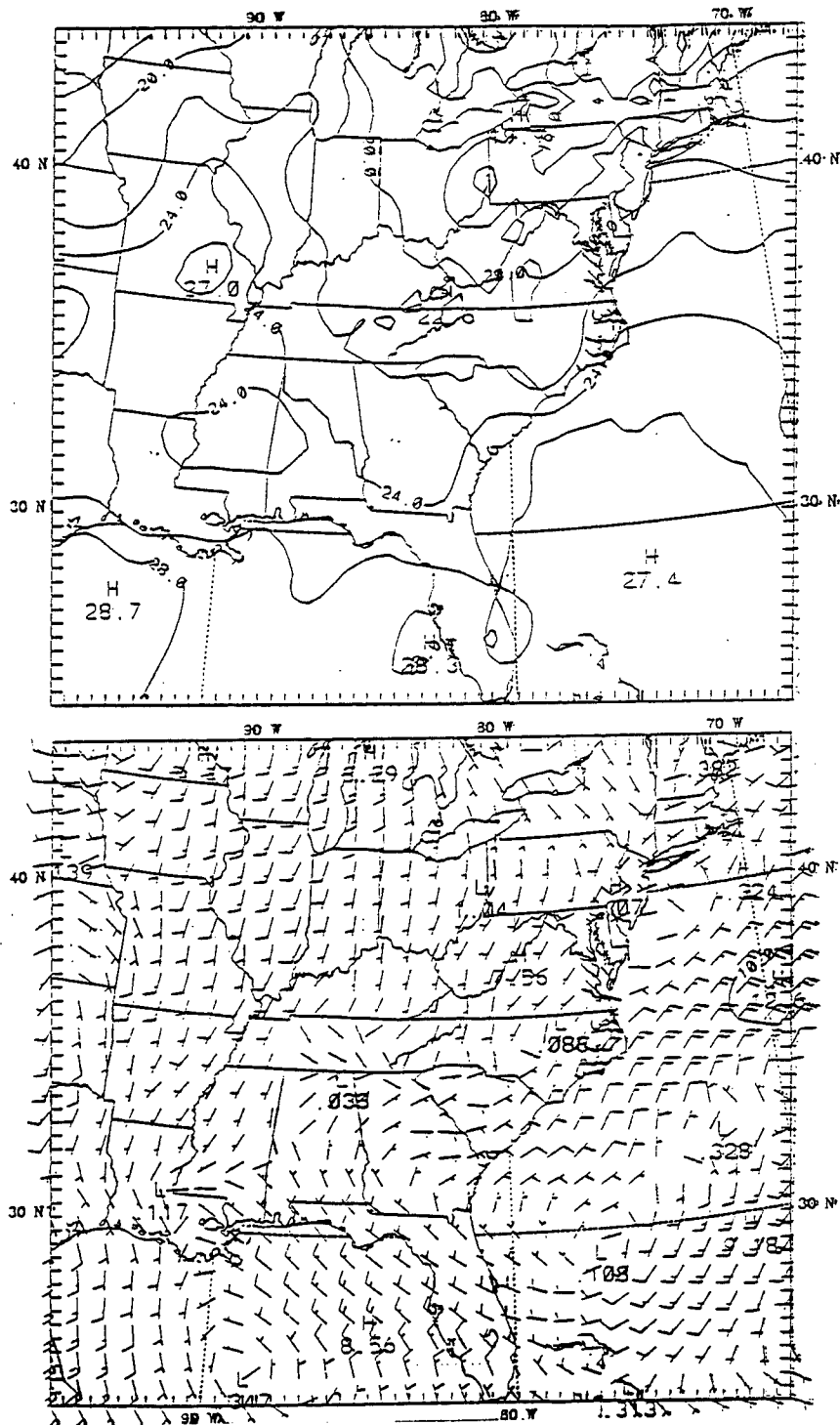


Fig. 1. The model initial surface temperatures ($^{\circ}\text{C}$) and vector winds (knots) at 1200 UTC 23 August 1993. The temperature interval is 2°C .

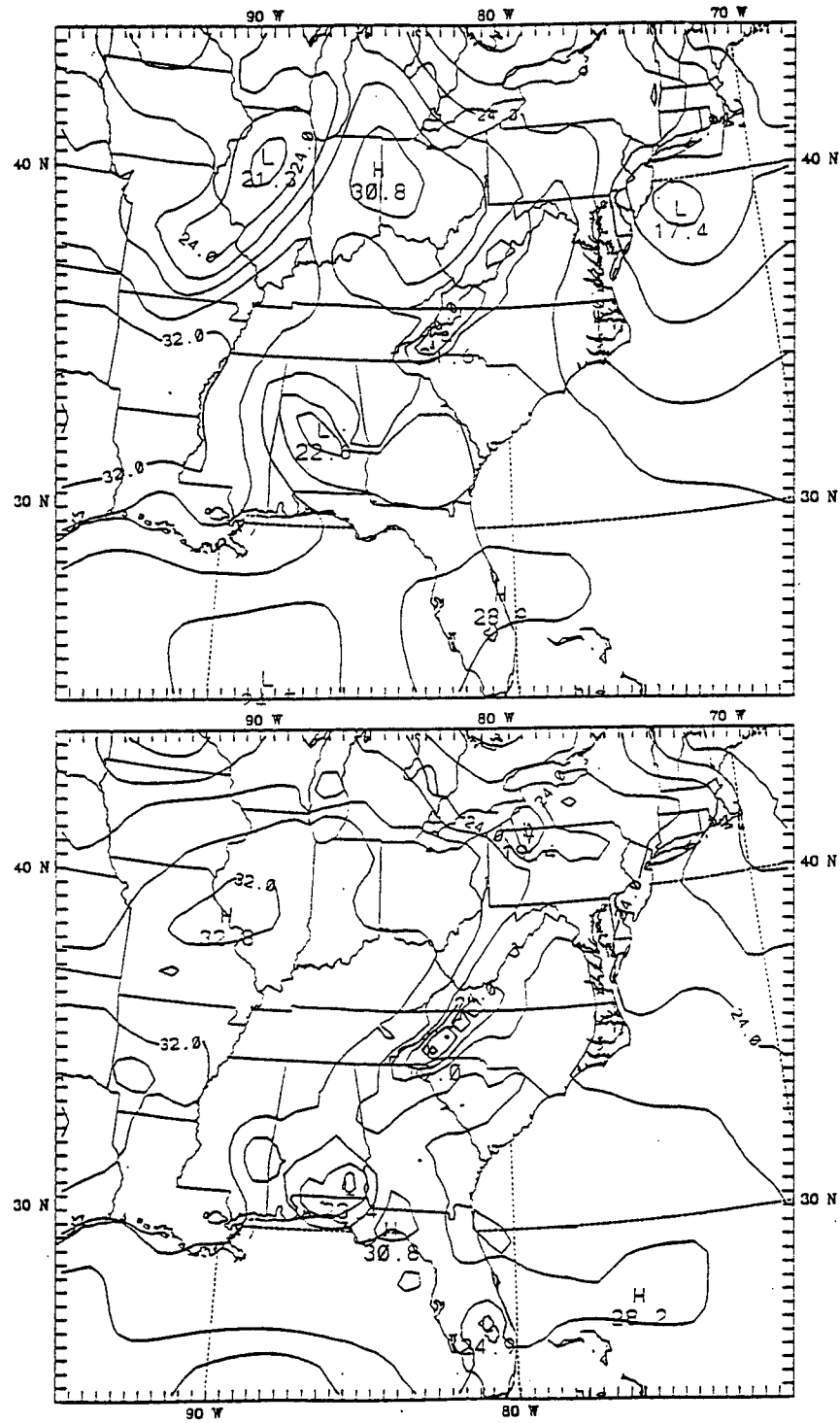


Fig. 2. The observed (upper panel) and 12-h simulated (E1) surface temperatures at 0000 UTC 24 August 1993. The interval is 2°C .

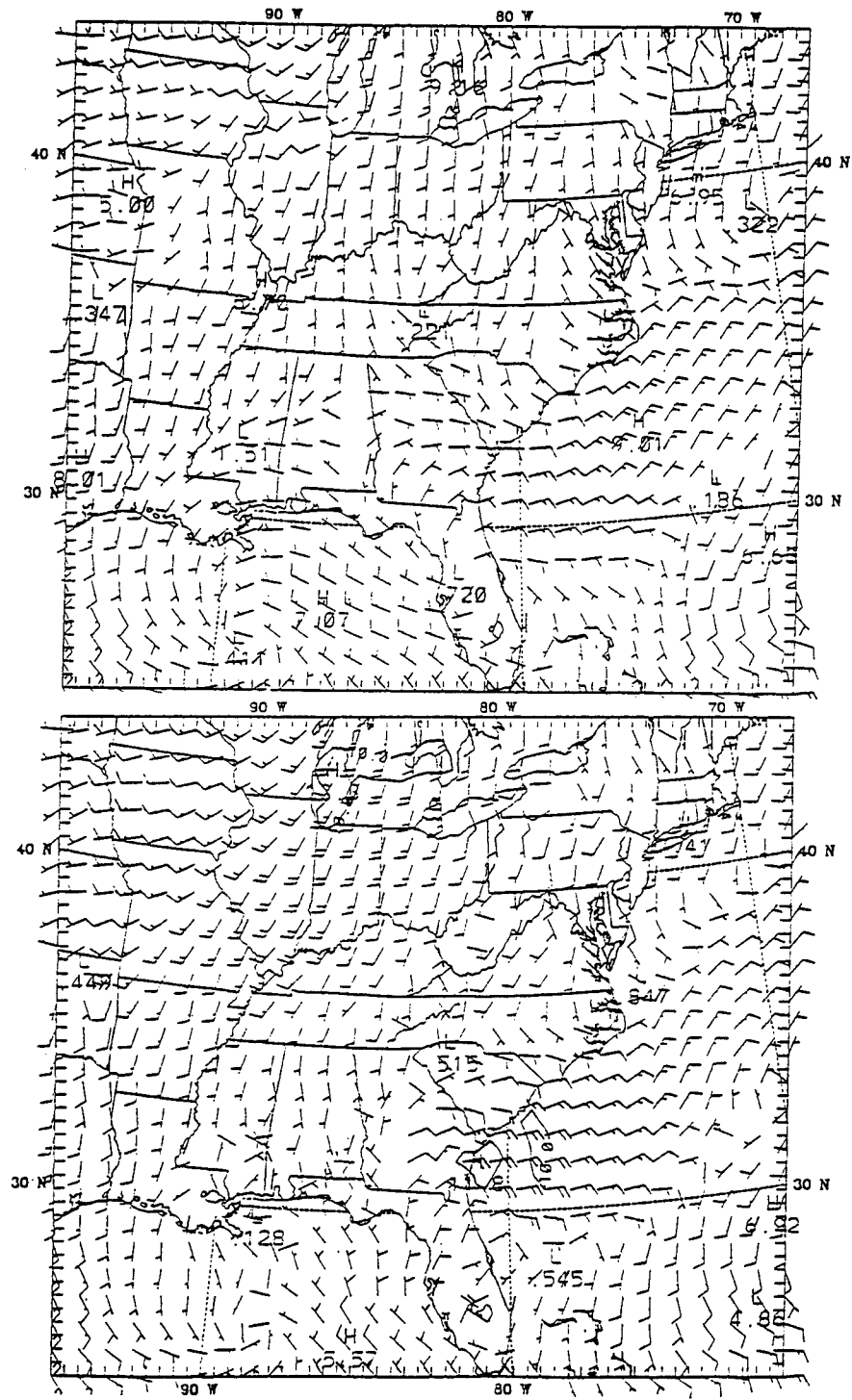
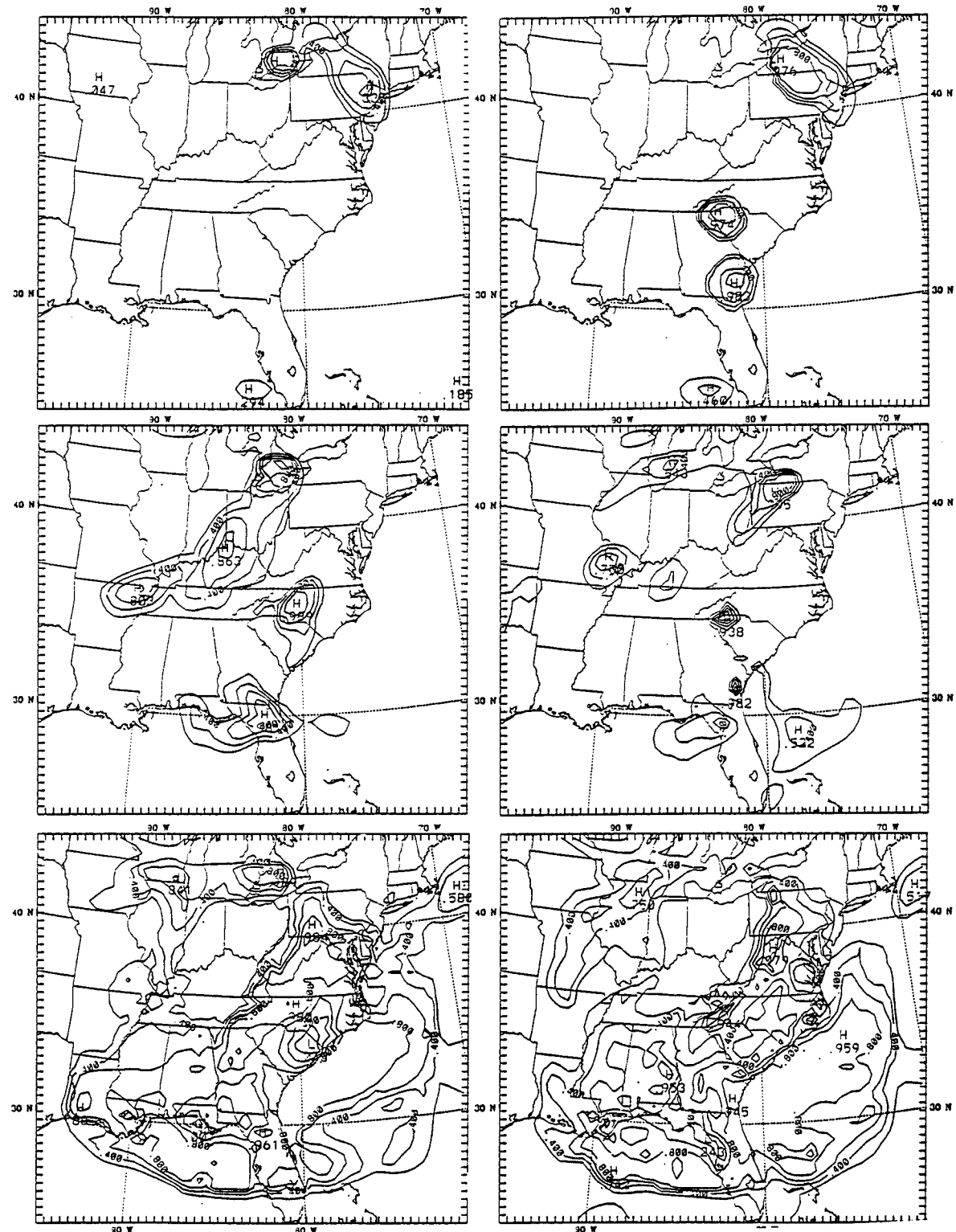


Fig. 3. The observed (upper panel) and 12-h simulated (E1) surface vector winds (knots) at 0000 UTC 24 August 1993.



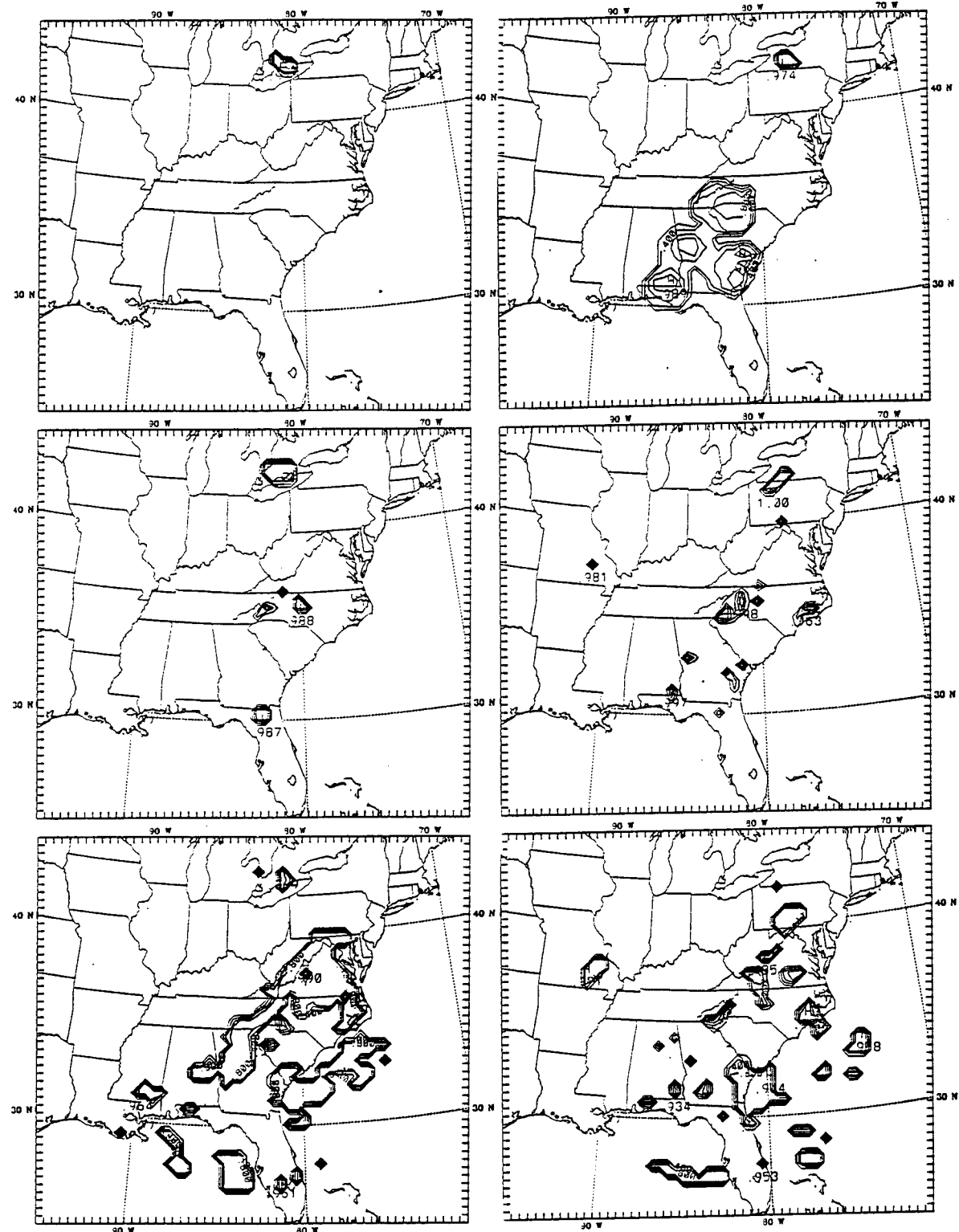


Fig. 5. As in Fig. 4 except for E3.

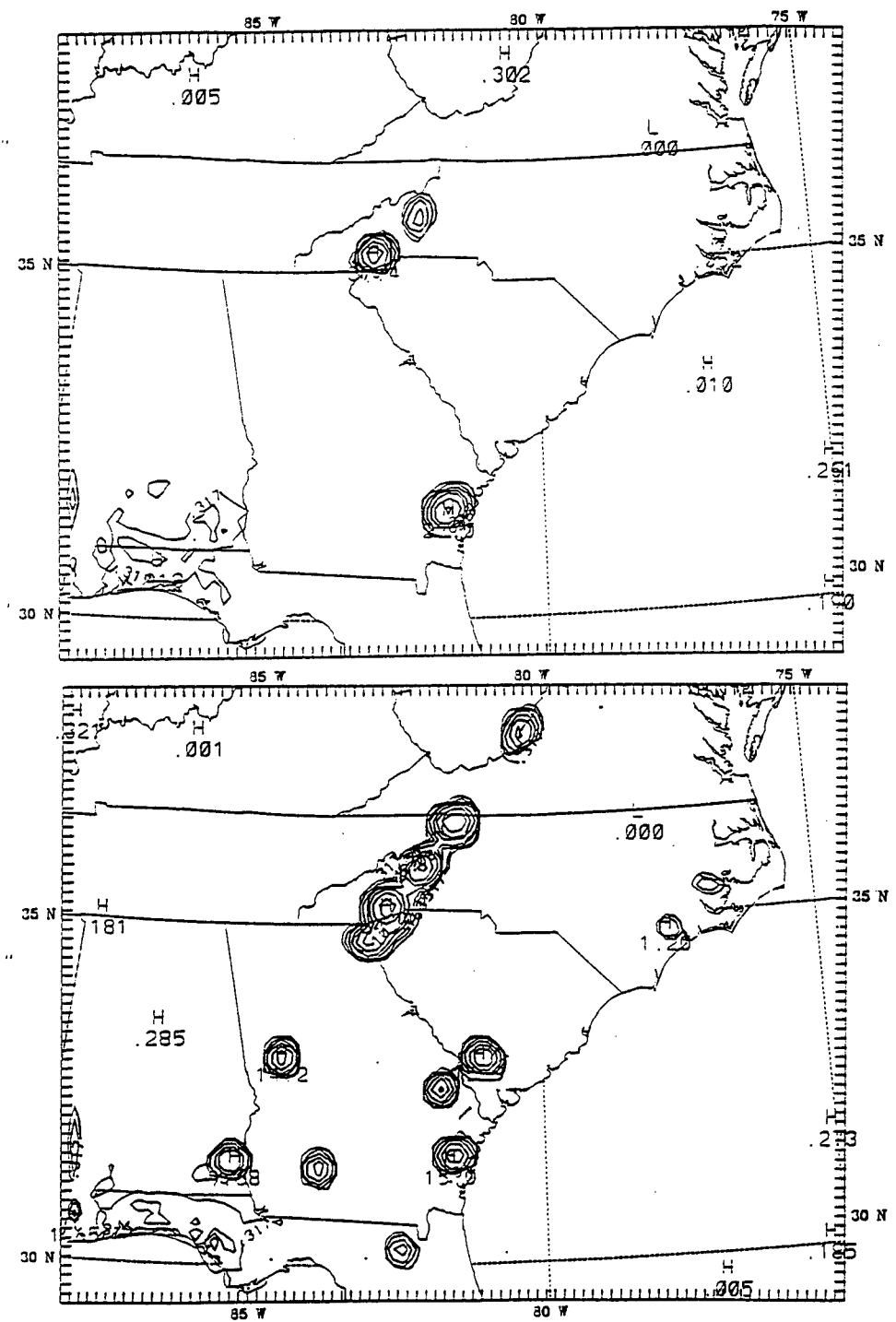


Fig. 6. The 12-h fine-mesh simulated accumulated convective precipitation for E1 (upper panel) and E2. The interval is 5 mm.

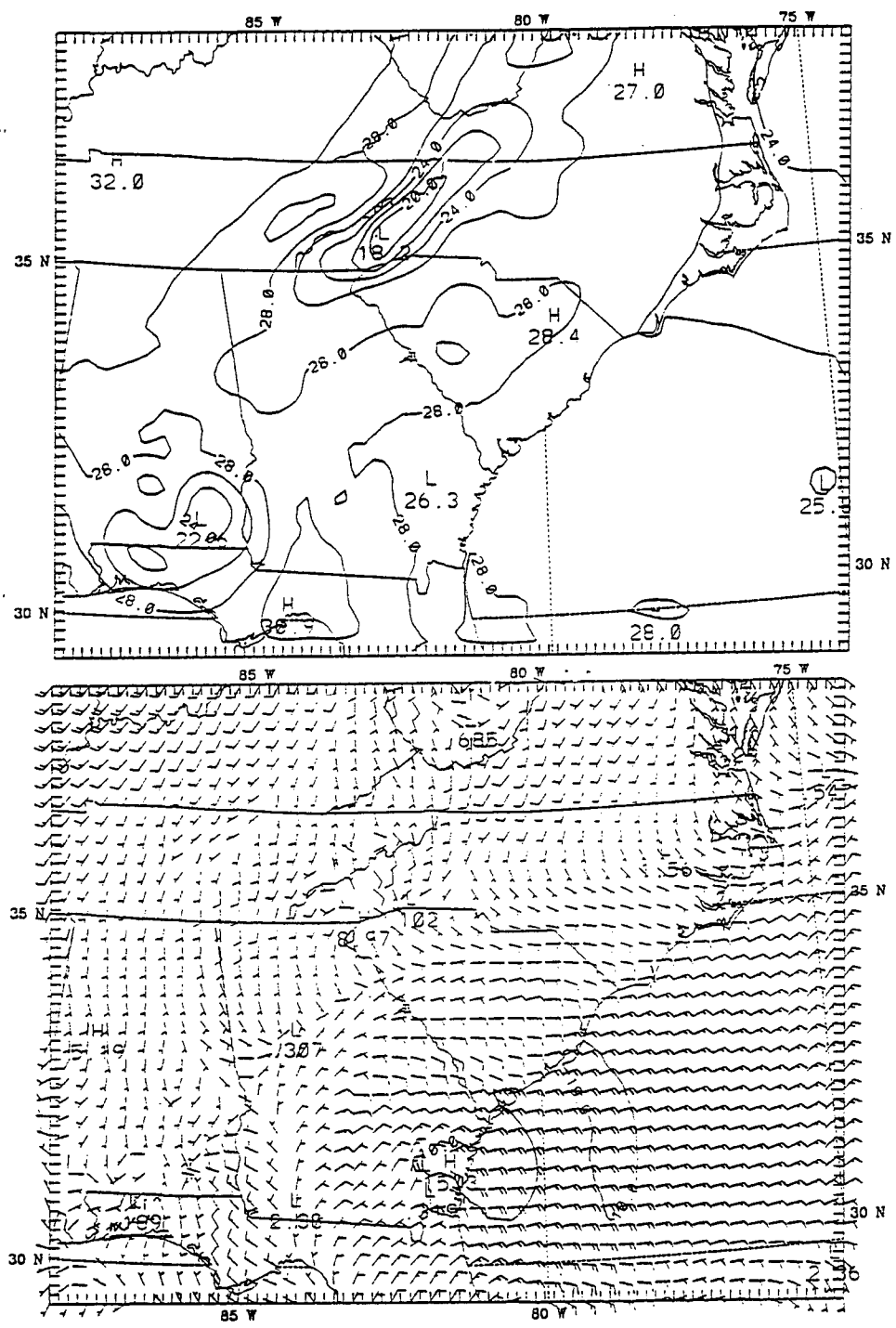


Fig. 7. The 12 h fine-mesh simulated surface temperatures and vector winds (knots) for E1. The temperature interval is 2 °C

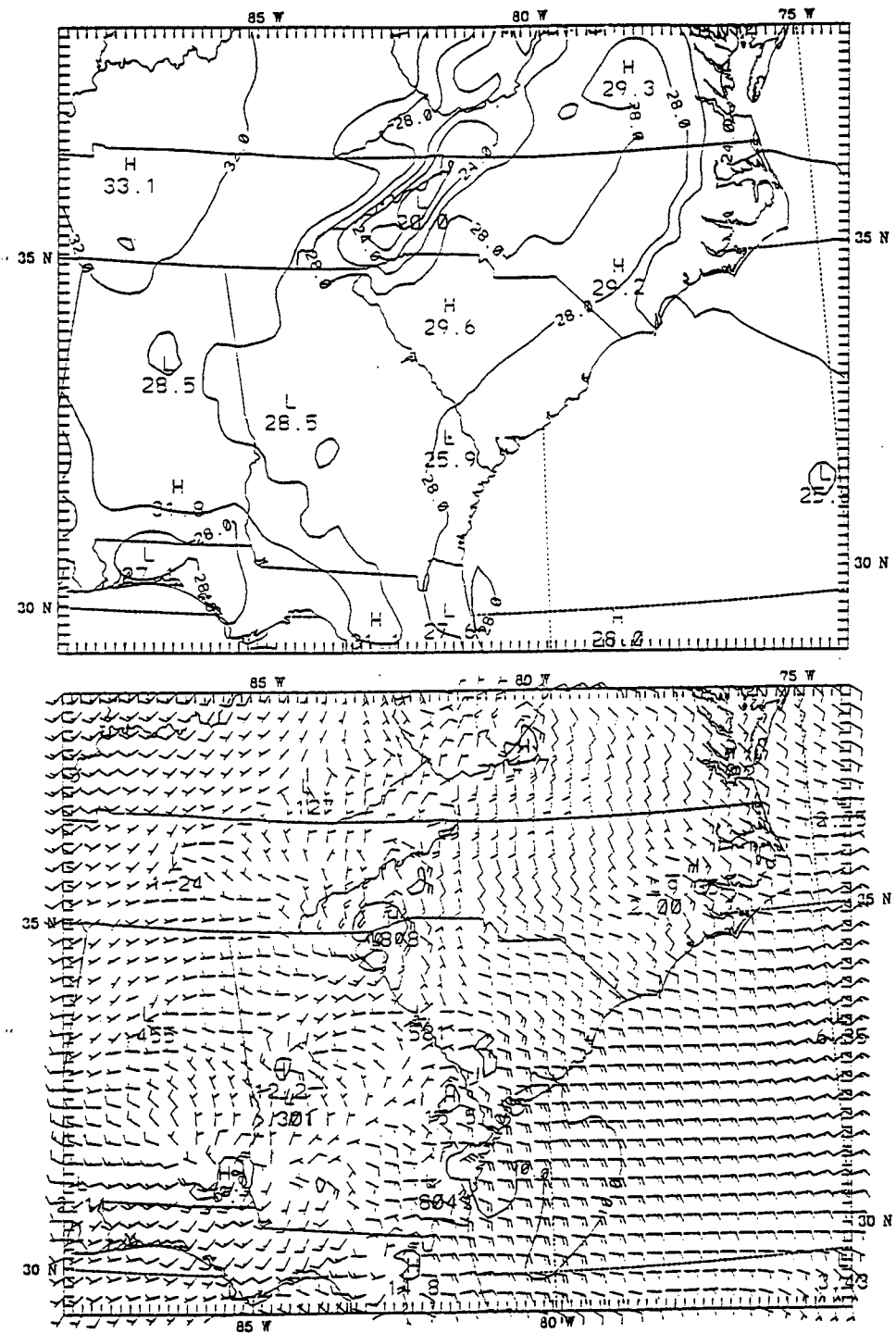


Fig. 8. The 12 h fine-mesh simulated surface temperatures and vector winds (knots) for E2. The temperature interval is 2°C

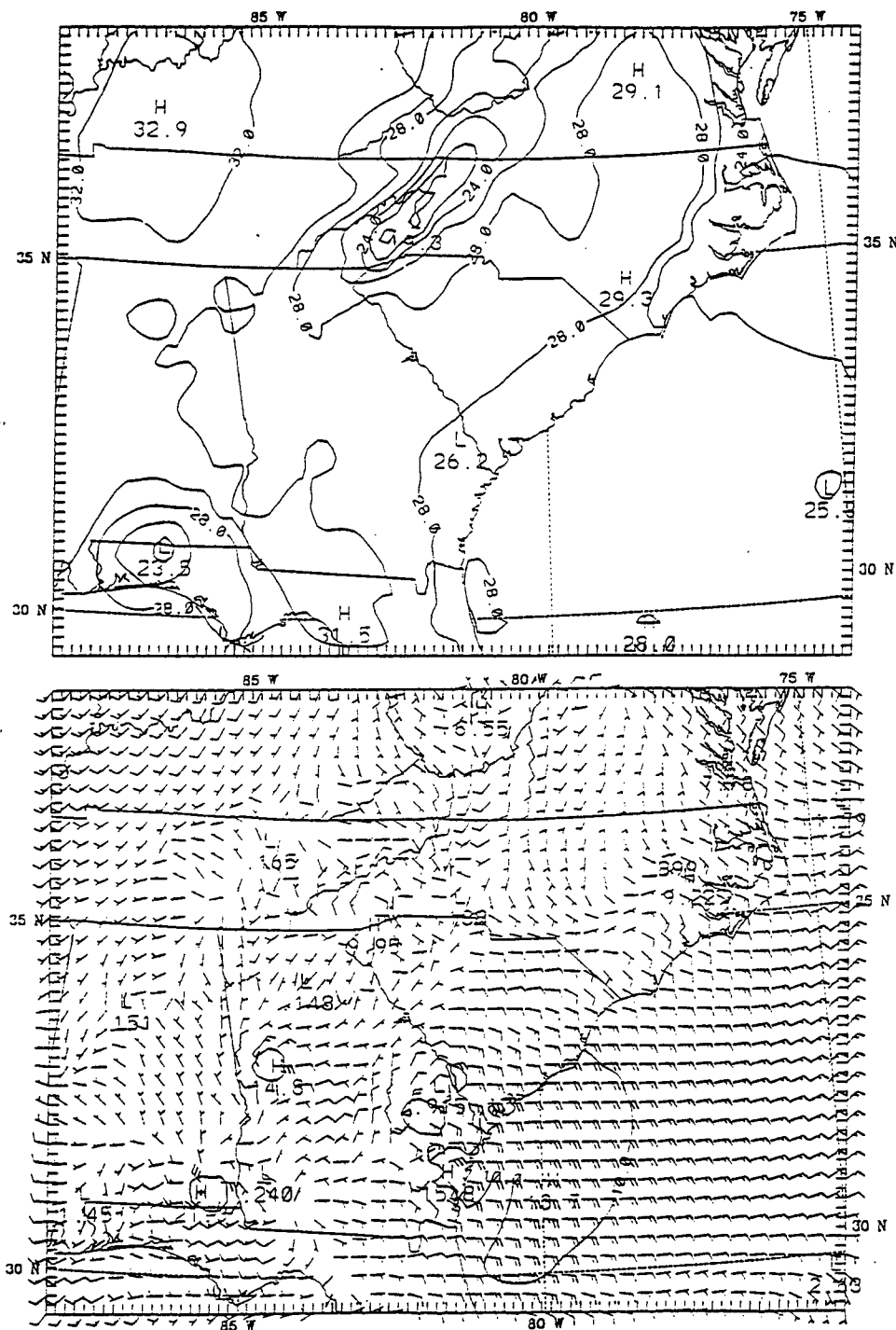


Fig. 9. The 12 h fine-mesh simulated surface temperatures and vector winds (knots) for E3. The temperature interval is 2°C

Analysis to Determine the Quality Factor of a Celestron-8 Telescope

Ronald R. DeLyser
Assistant Professor
Engineering Department

Peyman Ensaf
Graduate Student
Engineering Department

University of Denver
Denver, CO

Final Report for:
Summer Research Program
Phillips Laboratory

Sponsored by:
Air Force Office of Scientific Research
Bolling Air Force Base, Washington DC

and

Phillips Laboratory

October 1995

September, 1995

Analysis To Determine The Quality Factor
Of A Celestron-8 Telescope

Ronald R. DeLyser
Assistant Professor of Electrical Engineering
Peyman Ensaaf
Graduate Student
Department of Engineering
University of Denver

Abstract

Due to geometrical similarities between the Celestron-8 telescope and some of the space telescopes, calculating near fields within the Celestron-8 telescope was important for survivability/vulnerability assessments of space telescopes. In this analysis our goal is to use the software package CARLOS-3D [2], to calculate the near fields within the cavity of the Celestron-8 telescope and compare the results obtained using two different discretizations. This report provides some of the formulations and approaches used for this type of assessment along with the errors in results and some suggested improvements.

Overview

Our initial contact with this project was on February 1, 1995, resulting from AFOSR contract F49620-C-0063. The objective of this contract was to perform numerical analysis on a Celestron-8 telescope (Figure 1). We were asked to continue these analysis for the duration of our summer 1995 tour at the Satellite Assessment Center (SAC), Phillips Laboratory.

Our initial approach was to model the telescope's outer most shell as an open ended cylinder with an end cap at the top. At the top portion of the cylinder, there is an aperture for the eyepiece. Considering the aperture to be very small compared to the larger wavelengths, we decided to model the top end of the telescope as an end cap. We modeled the resulting open ended cylinder using Mathematica [1], and analyzed that model using CARLOS-3D [2]. As a starting point, we analyzed the open cylinder model over a frequency range of 0.7 GHz - 3.0 GHz in order to avoid a computationally extensive problem. Once the data for the open cylinder model was analyzed, we proceeded with creating the model which included the interior geometry of the telescope. The interior geometry, consisted of two interior cylinders. These interior cylinders (Figure 1) are at the center of the aperture, where a convex reflecting mirror resides (the short plastic cylinder) and at the eyepiece (the long metal cylinder). The two reflecting mirrors are not shown in Figure 1. The CARLOS model (Figure 2) was analyzed for a frequency range of 0.5 GHz up to 3.0 GHz. Each of the models, the open cylinder and that shown in Figure 2, are discretized with triangular cells, each having sides $\lambda/10$ in length corresponding to a frequency of 1.0 GHz. The models are illuminated at incidence angles θ and ϕ (see figure 2) both equaling 45° .



Figure 1. Celestron-8 telescope.

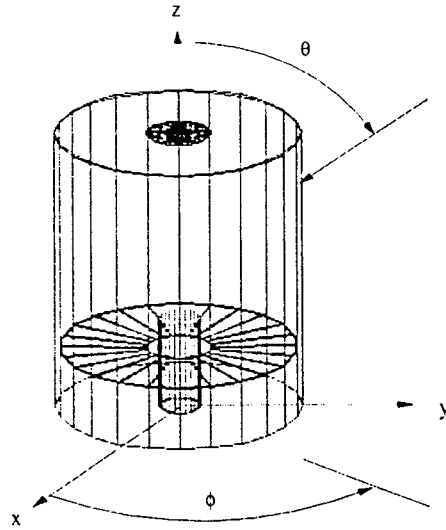


Figure 2. CARLOS model for the telescope.

Parallel to this analysis using CARLOS, we used another software package called GEMACS [3]. GEMACS offers three techniques which can be used to analyze a geometry. Geometrical Theory of Diffraction (GTD) and Method of Moments (MOM) to analyze the exterior of a geometry and the Finite Difference method (FD) to analyze the interior regions. We are interested in comparing the near field results obtained using GEMACS's MOM to the near field results obtained using MOM implemented in CARLOS. Furthermore, using the FD technique in GEMACS, we are trying to obtain cavity field results which should prove to be numerically more accurate. Due to the problems encountered with CARLOS we were unable to compare results with GEMACS. This is still a topic for further study.

Also of interest is the verification and validation of the results using different discretization techniques. We, therefore, discretized the model in Figure 2, to $\lambda/5$ at 1.0 GHz. We analyzed this model for a frequency range of 0.5 GHz-3.0 GHz. Comparing the results of the Quality Factor (Q), total energy, and exiting power for the $\lambda/5$ discretized model to those of $\lambda/10$ model, we noticed pronounced differences in the spectrums. These results along with other problems encountered with CARLOS, and methods for rectification are discussed in the following.

Preliminary Observations

The model of Figure 2 was discretized into triangles having sides no longer than $\lambda/10$ in length at 1.0 GHz frequency. The interior of this geometry was divided into cubes of side length 1.5 cm ($\lambda/10$ at 2.0 GHz). A total of 3717 grid points were created. These grid points are the location of the near field points calculated by

CARLOS. The model in Figure 2 was analyzed for a frequency range of 0.5 GHz up to 3.0 GHz. Using the fundamental equations describing the electric and magnetic energies along with power exiting the cavity, we calculated Q [4, 5] given by

$$Q = \omega \frac{U}{P} \quad (1)$$

where ω is the operating angular frequency, U is the total energy in the cavity and P is the power exiting the cavity. Figure 3 shows Quality Factor vs. Frequency for the model of Figure 2. Resonances for various frequencies are evident in Figure 3, along with the fact that the ϕ polarization dominates the θ polarization. From Figure 3, it is evident that the θ and ϕ polarizations follow a similar trend throughout the spectra.

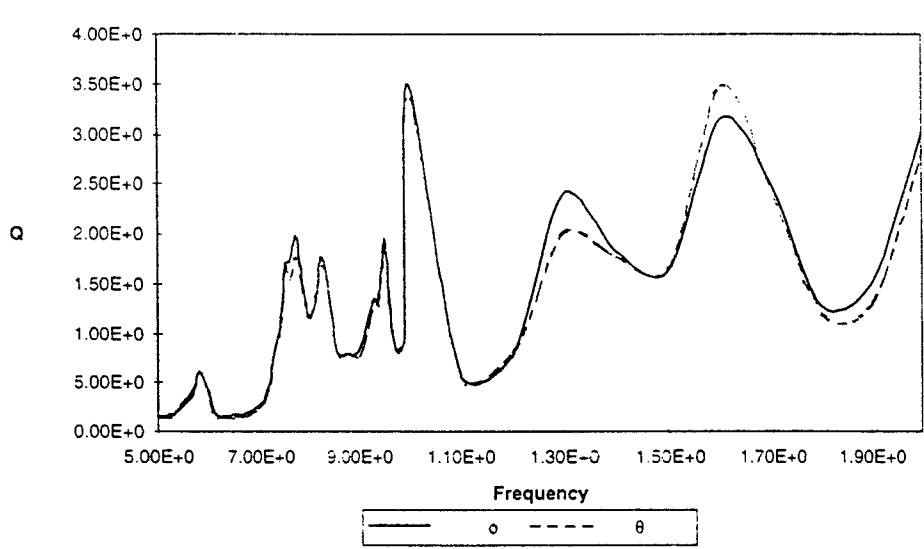


Figure 3. Quality factor vs. frequency, θ and ϕ polarization with $\lambda/10$ discretization.

The next step was to investigate mesh sizes. We, therefore, discretized the model of Figure 2 to $\lambda/5$ at 1.0 GHz, and analyzed that model over frequency range of 0.5 GHz up to 3.0 GHz. Figure 4 shows the spectrum for the $\lambda/5$ and $\lambda/10$ discretization. It is evident from Figure 4 that the two spectra are profoundly different. These discrepancies led us to further investigate meshes using only the open cylinder model, using two different discretization schemes, $\lambda/10$ and $\lambda/20$. We analyzed these models for a frequency range of 0.1 GHz up to 2.0 GHz. Figure 5 shows these results. Obviously the two discretization techniques provide different results.

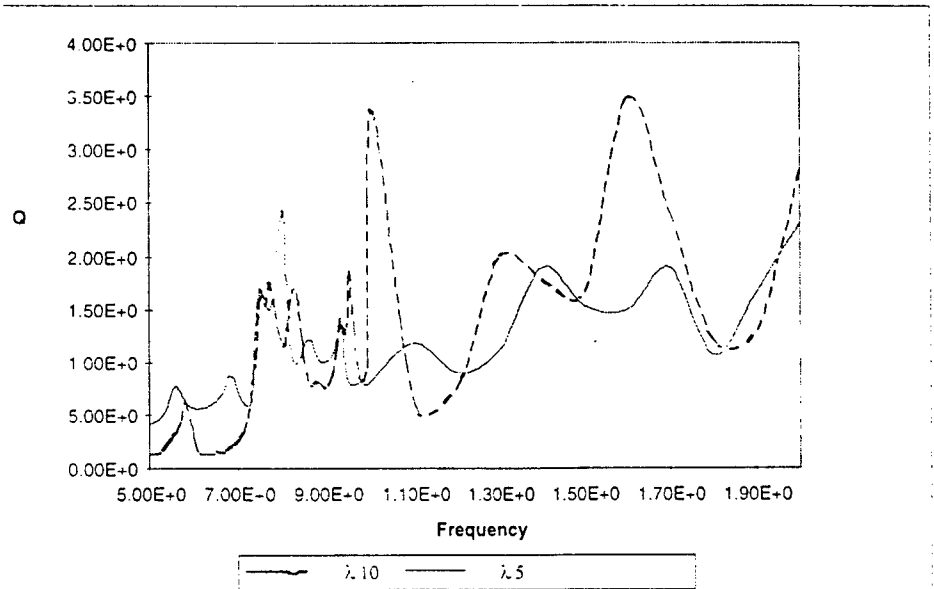


Figure 4. Comparison of quality factors, θ Polarization, $\lambda/5$ and $\lambda/10$ discretizations.

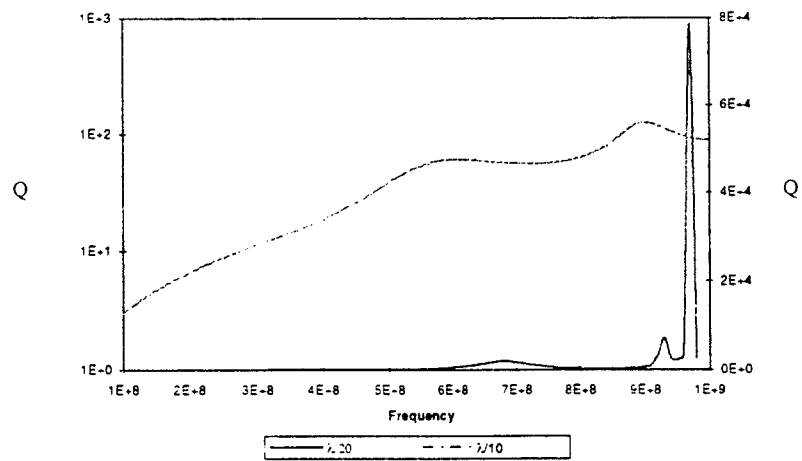


Figure 5. Comparison of the quality factors, ϕ polarization, $\lambda/10$ and $\lambda/20$ discretizations.

Field Calculation method and results

We first approached the meshing problem by comparing the field quantities for the models ($\lambda/10$ and $\lambda/20$).

Doing this, we realized that there is a large difference in the field values near the cylinder walls than those field values more towards the center of the cylinder. CARLOS calculates the near field quantities using the current at the centroid of each triangular cell. In this scenario, each current source will now act as an infinitesimal dipole. Therefore, the field quantities are calculated using [6]

$$E_z(x, y, z) \propto \sum_{n=1}^N \frac{e^{-jk_r n}}{kr_n^3} \cos(\theta) J_n \quad (2)$$

where k is the propagation constant, J_n is the n^{th} surface current, and r_n is the distance from the n^{th} surface current to the field point. However, the current is distributed across the surface. Therefore the distance r from the field point varies according to where the current is calculated on the surface. The distance r is a very critical quantity since for small r , its variations will have a large effect on the field calculations. Figures 6, 7 and 8 show the percent difference, between the $\lambda/10$ and $\lambda/18$ discretizations, in the electric field quantities at the end cap, the center, and at the aperture. Iterative refinement (see succeeding sections) was implemented for creating the Figures 6, 7 and 8.

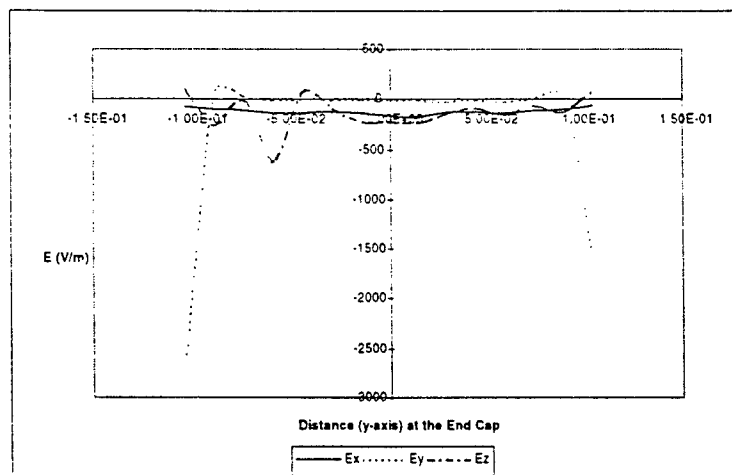


Figure 6. Percent difference in the electric field quantities, ϕ Polarization, $\theta=90$, $\phi=0$, 500 MHz, end cap.

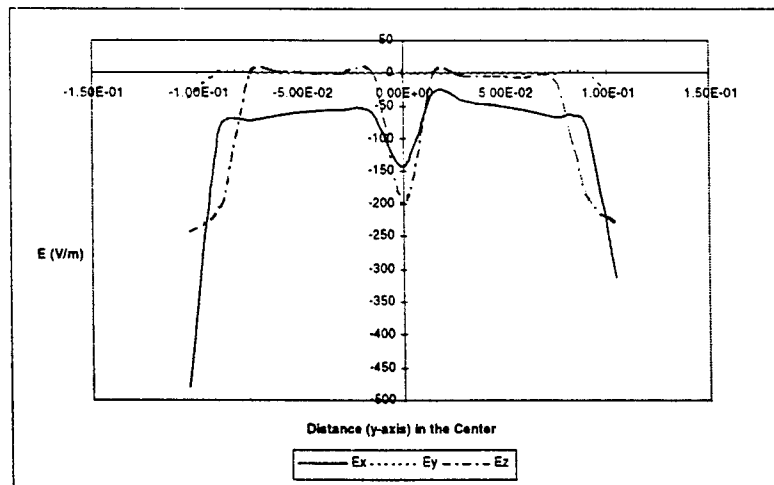


Figure 7. Percent difference in the electric field quantities, ϕ Polarization, $\theta=90$, $\phi=0$, 500 MHz, center.

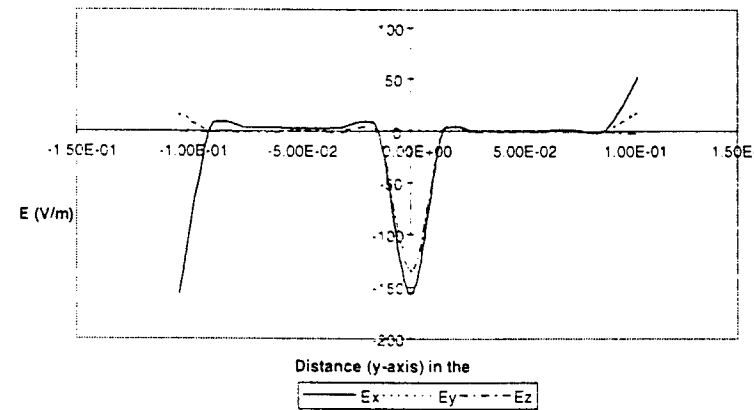


Figure 8. Percent difference in the electric field quantities, ϕ Polarization, $\theta=90$, $\phi=0$, 500 MHz, aperture.

It is evident in Figures 6, 7 and 8. that the biggest differences are close to the cavity boundary. This error is caused by the crude approximation used to calculate the near fields. A more suitable approach would be to use a solution technique which considers the changes in r along with changes in J . This solution is given by [7]

$$E^s(r) = -j\omega\mu \int_{\partial V_s} J_s(r') g(r, r') ds + \nabla \int_{\partial V_s} \frac{1}{j\omega\epsilon} \nabla \cdot J_s(r') g(r, r') ds' \quad (3)$$

where

$$g(r, r') = \frac{e^{-jk|r-r'|}}{4\pi|r-r'|} \quad (4)$$

ω is the angular operating frequency, ϵ and μ are the permittivity and permeability of free space, respectively.

Meshing Methods And Results

In the neighborhood of a conducting edge, electric and magnetic field components behave in a particular manner dependent on the wedge angle ϕ_o (see Figure 9). From [8] the behavior of the surface current density in the vicinity of the edge is

$$\mathbf{E} \propto \rho^v \sin(v\phi) \quad \mathbf{J} \propto \rho^{v-1} \quad (5)$$

where

$$v = \frac{\pi}{\phi_o} \quad (6)$$

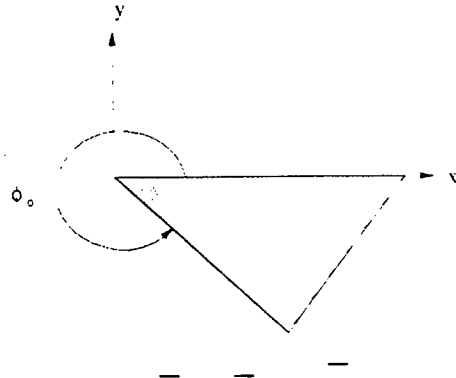


Figure 9. Wedge angle ϕ_0 .

where for the top edge of the Figure 2, $\phi_0=2\pi$, and for the bottom edge $\phi_0=3\pi/2$. For our geometry then, at the top edge, $J_\phi \propto \rho^{-1/2}$ and at the bottom edge, $J_\phi \propto \rho^{-2/3}$.

The edge condition is an additional constraint that is needed for a unique solution whenever a geometric singularity, such as a sharp edge, exists. The edge condition states that the energy density in the vicinity of an edge, or any geometrical singularity, must be integrable, that is

$$\operatorname{Re} \int_S \mathbf{E} \times \mathbf{H}^* \cdot d\mathbf{S} \rightarrow 0 \quad (7)$$

as the surface S enclosing the edge shrinks to the edge. The edge condition dictates that the edge shall not radiate any energy because it is not a source. In order to accurately model the edge surface currents we used a meshing scheme as shown in Figure 10. Figure 11 shows the z , ρ and ϕ directed surface currents for the meshing scheme of Figure 10.

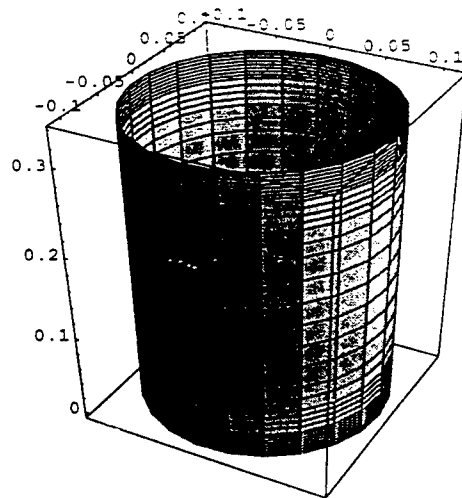


Figure 10. Non-uniform discretization.

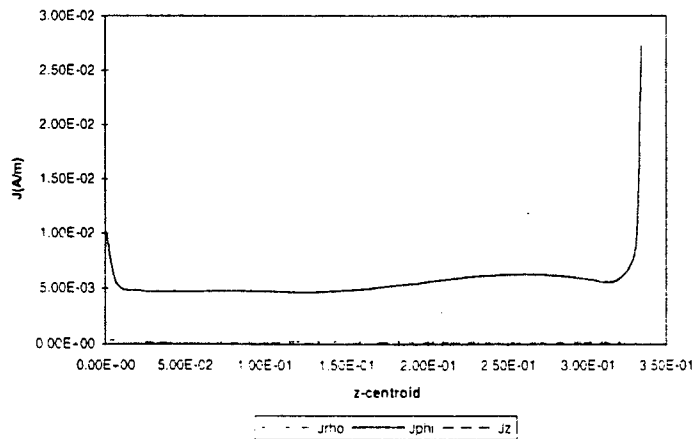


Figure 11. Surface currents for figure 9 at $\phi=10^\circ$, 500 MHz, $\theta=90^\circ$, $\phi=0^\circ$.

In addition to the accurate modeling of edge currents, we also looked at the problem of generating a mesh for a circular disk. For problems of circular symmetry, the cells near the center of circles become exceedingly narrow. A simple transition to a non-symmetric gridding, as shown in Figure 12 would be desirable to maintain reasonable cell sizes. Dr. Pat McDaniel, wrote a program to accomplish this task, and also give a finer meshing for cells closer to the edges. Figure 13 shows some results for this meshing scheme.

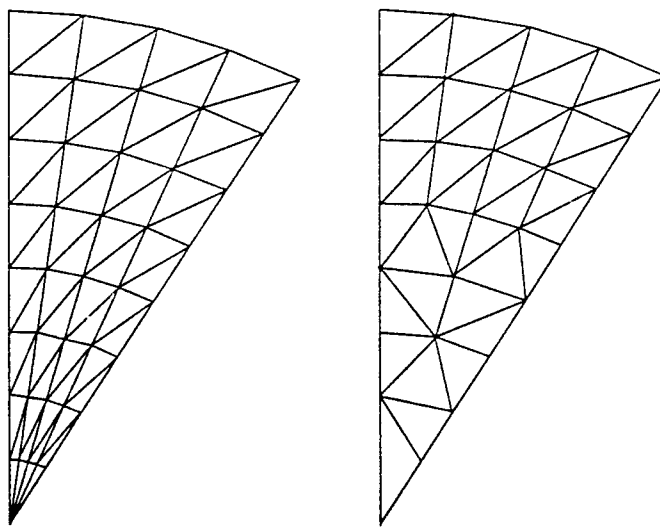


Figure 12. Alternate gridding scheme for circular geometry.

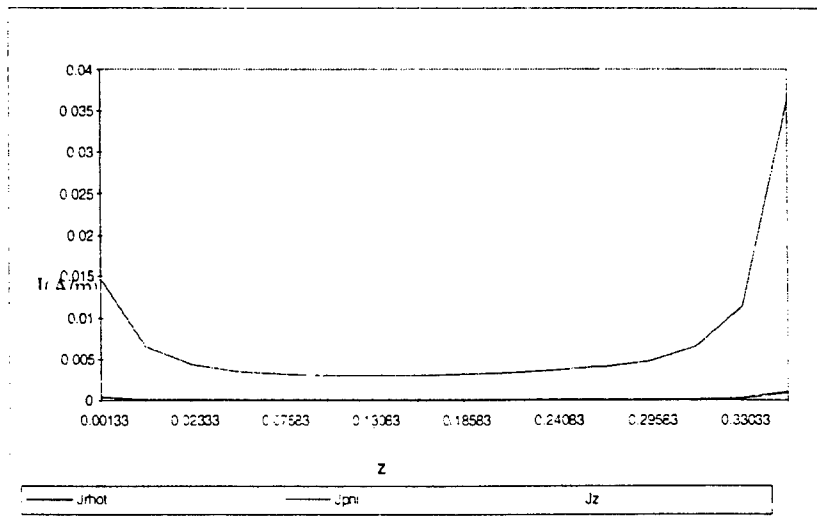


Figure 13. Surface currents using Dr. McDaniel's meshing scheme at $\phi=13^\circ$, ϕ Polarization, $\phi=45^\circ$, $\theta=135^\circ$

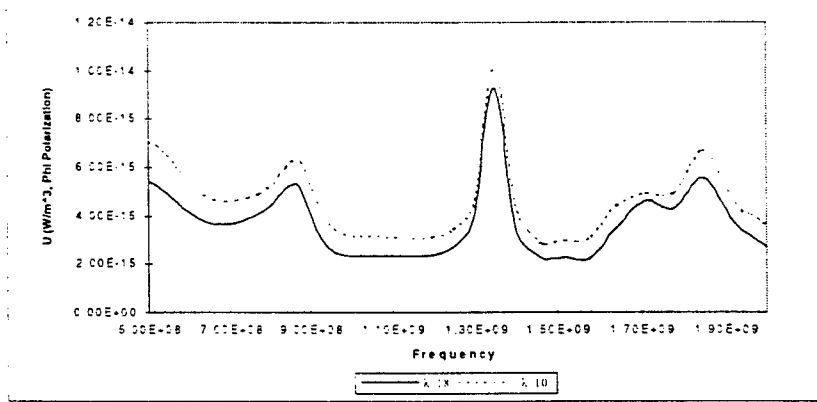


Figure 14. Energy for the two discretizations using Dr. McDaniels meshing scheme, 500 MHz, $\theta=90^\circ$, $\phi=0^\circ$.

It is evident from Figure 14 that using the new meshing scheme has made the energy distribution much more compatible for the two discretization. However, there is no improvement in the results for power. This could be due to the fact that we are summing over a much smaller number of grid points in the aperture and thereby not obtaining comparable accuracy in the results. Also, since the fields vary rapidly as the conducting side wall is approached, perhaps a finer field mesh is needed in the aperture.

Accuracy and results for high condition number

Other numerical difficulties resulting from using CARLOS, may be due to the large condition number of the matrix for large models. The condition number of the matrix may be defined as its largest element value divided by its smallest [9]. A matrix is typically considered ill-conditioned if its corresponding inverse matrix is unstable numerically. Taking another point of view, a zero, or near zero determinant indicates that the matrix has, in effect, two rows that are identical or approximately identical. In a system of linear algebraic equations,

a zero determinant (two identical rows) means that two of these equations are either redundant or inconsistent. In an approximate-solution method such as MOM, the redundancy and inconsistency in a system of linear equations manifest themselves as numerical instabilities. A large condition number indicates that the matrix may be ill-conditioned. The condition numbers are not always reliable in predicting the stability of a matrix. We have to know how large the condition number must be before we declare the matrix ill-conditioned. A practical rule of thumb is that the matrix is ill-conditioned if the inverse of the condition number approaches the computer's floating-point precision. For an ill-conditioned matrix equation, the iterative methods are generally more suitable. An iterative refinement technique is implemented by Dr. Pat McDaniel and is discussed here.

It is not always easy to obtain greater precision for the solution of a linear set than the precision of your computer's floating-point. In direct methods of solution, round-off errors accumulate, and they are magnified to the extent that the matrix is close to singular. Under these conditions, matrices, which were far from singular, can lose two or three significant figures. Iterative refinement (improvement) is an approach to restore full machine precision [10]. Suppose that a vector \mathbf{x} is the exact solution of a linear set

$$\mathbf{A} \cdot \mathbf{x} = \mathbf{b} \quad (8)$$

However, the exact solution \mathbf{x} is not known. What is known, in this case, is a slightly wrong solution $\mathbf{x} + \delta\mathbf{x}$, where $\delta\mathbf{x}$ is the unknown error. Therefore, from equation (8), it is evident that when multiplied by the matrix \mathbf{A} , the slightly wrong solution gives a product slightly discrepant from the desired right-hand side \mathbf{b} , such that

$$\mathbf{A} \cdot (\mathbf{x} + \delta\mathbf{x}) = \mathbf{b} + \delta\mathbf{b} \quad (9)$$

Now, subtracting equation (8) from (9) gives

$$\mathbf{A} \cdot \delta\mathbf{x} = \delta\mathbf{b} \quad (10)$$

Using equation (10) to solve for $\delta\mathbf{b}$ and then substituting that into equation (9) gives

$$\mathbf{A} \cdot \delta\mathbf{x} = \mathbf{A} \cdot (\mathbf{x} + \delta\mathbf{x}) - \mathbf{b} \quad (11)$$

The right side of equation (11) is known, since $\mathbf{x} + \delta\mathbf{x}$ is the wrong solution that requires refinement. Therefore solving equation (11) for $\delta\mathbf{x}$, subtracting it from the wrong solution will provide an improved solution.

Numerical Integration Of The Matrix elements

The integral of a function is approximated by the sum of its functional values at a set of equally spaced points, multiplied by certain aptly chosen weighting coefficients. The idea of Gaussian Quadrature is to give the user the freedom to choose not only the weighting coefficients, but also the location of the abscissas at which the function is to be evaluated, hence they will no longer be equally spaced. Using Gaussian Quadrature formulas, one can arrange the choice of weights and abscissas to make the integral exact for a class of integrands.

Therefore, the weighting function $W(x)$ can be chosen to remove integrable singularities from the desired integral. Hence, one can find a set of weights w_i and abscissas x_i such that the approximation

$$\int_a^b W(x)f(x)dx \approx \sum_{i=1}^N w_i f(x_i) \quad (12)$$

is exact if $f(x)$ is a polynomial. CARLOS is a MOM code and hence its primary calculation is surface currents. Figures 15 and 16 present the differences in ϕ directed currents and z directed currents along the wall of the cavity. The primary purpose of these figures is to show the difference in the results using iterative refinement and iterative refinement with improved Gaussian Quadrature.

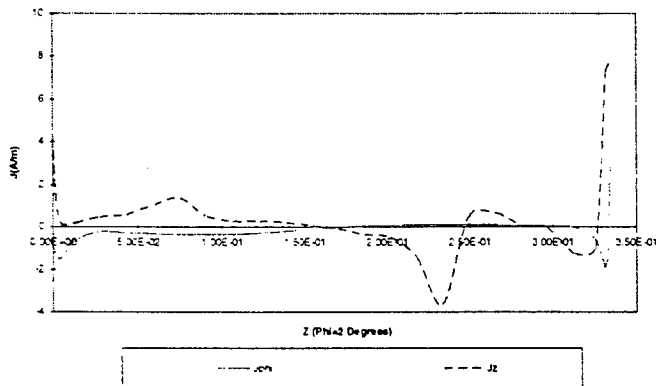


Figure 15. % difference of currents using iterative refinement vs. iterative refinement improved Gaussian. 500 MHz, $\theta=90^\circ, \phi=0^\circ$.

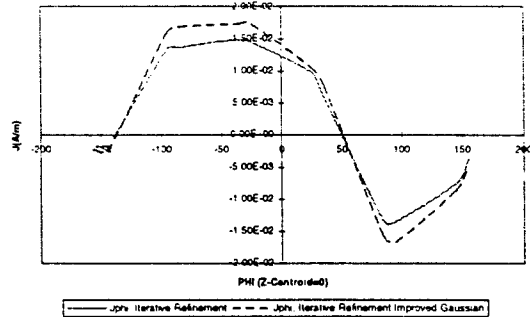


Figure 16. % difference of currents using iterative refinement vs. iterative refinement improved Gaussian, 500 MHz, $\theta=90^\circ, \phi=0^\circ$.

From Figures 15 and 16, it is evident that using improved Gaussian Quadrature formulas does make an improvement in the results obtained. Figure 15 shows a very small difference in the surface currents for the two discretizations, however, this small difference may reflect a large difference in the near field calculations.

HFSS description and results

The Hewlett Packard (HP) High Frequency Structure Simulator (HFSS) is a full three dimensional finite element simulator. In the simulator, the geometric model is automatically divided into a large number of tetrahedrons and is called the finite element mesh. Within each tetrahedron, the vector field components perpendicular to the edges and tangential to the edges are mathematically modeled using polynomials. The finer the mesh, the more accurate the solution. Of course, the finer the mesh, the greater the demands on computational facilities in terms of memory, disk space and solution time. In order to find a good solution to the problem and minimize computer resources, HFSS uses "an iterative process in which the mesh is automatically refined in critical regions." The simulator first solves the problem using a coarse initial mesh, refines the mesh in areas of high error density, generates a new solution, etc. until selected S-parameters converge to within a desired limit, or until all computer resources have been exhausted.

The computer that we use to run HFSS is an IBM RS6000 model 570 Powerstation with 128 MBytes of RAM and a 2 GByte hard drive. We have access to all of the RAM, about 200 MBytes of swap space, and (at the time of this study) 340 MBytes of disk space for user files. During the solution process, a convergence menu can be monitored containing memory and file size values. Two matrices are written to disk (user files), the A matrix is the "full matrix" and the U is the "upper triangular matrix". All other memory size values indicated on the convergence menu are RAM usage. As stated above, the iterative process of mesh refinement is continued until convergence, or until the computer resources are exhausted. If the disk space is exhausted (which was the limiting resource for our models), the solution did not converge.

A total of eight projects were created HFSS. The most important ones described here are:

- 1. telescop.pjt - A full model of the telescope with the exception that the large mirror is flat. We could not get the 2-D cross-section to close using the true radius of curvature. Since the 2D cross-section would not close, the 3D mirror could not be revolved about the z-axis to be created. Thus, a flat mirror with approximate tilt was created. The center of the mirror is at $z = 72$ mm and the outside is at $z = 73.8$ mm. This model is excited by a circular waveguide port located at the eye piece.
- 2. telehf.pjt - A model of the telescope excluding the volume behind the large mirror and with the radiation boundary located 17 mm from the large cylinder boundary. This model was specifically created at a frequency of 4.5 GHz in an attempt to have a model at a frequency higher than the cutoff frequency of the inner cylinder (4.4 GHz.)
- 3. cyltest2.pjt - An open cylinder excited by a square coaxial probe at the center of the cylindrical shell with the probe oriented along the x axis. The square cross-section probe was used to alleviate the problem of a high mesh density at the small cylindrical probe. The inner conductor (probe) of the coaxial feed is 4 mm wide, the outer conductor has a 9.2 mm inside width. The radiation boundary was chosen to accommodate a 0.75 GHz - 1.5 GHz frequency range.

4. cyltest3.pjt - This project is the same as cyltest2.pjt with the exception that the radiation boundary is closer to accommodate a 1.5 GHz - 2 GHz frequency range.

Once again, we ran up against memory (RAM) and disk storage limitations. Table 1 shows the details of the various projects and models at the given frequencies along with the memory requirements (disk space and RAM) of each. We were unable to converge to a 2 GHz model for the telescop.pjt. Also, the telehf.pjt model did not converge. Even though a good model was not generated at 4.5 GHz telehf.pjt, we looked at the radiation results for the best model generated. When compared to the radiation plot of telescop.pjt at 1.18 GHz, it is clear that once we get above the cutoff frequency of the inner cylinder, the radiation increases substantially. It is interesting to note that even though the frequency of excitation

Table 1. Summary of HFSS projects and resource requirements.

Name of Project	Frequency	A matrix Disk Space (K)	U matrix Disk Space (K)	csolve RAM (K)	Total Time
telescop.pjt	1 GHz	14.130	77.376	66.332	17:13
	1.5 GHz	23.122	164.935	103.132	41:48
	2 GHz	---	>340,000	---	---
telehf.pjt	4.5 GHz	---	>340,000	---	---
cyltest2.pjt	1.5 GHz	34.083	211.128	107.996	2:40:00
cyltest3.pjt	2 GHz	39.834	243.013	114.396	3:03:00

for telescop.pjt (1.18 GHz) is below the cutoff frequency of the inner cylinder waveguide, field plots of the electric fields show that there are calculable fields at the end of the inner cylinder and at the aperture of the large cylinder. The magnetic field plots also show significant fields between the large mirror and the outer cylinder.

The most successful models were cyltest2.pjt and cyltest3.pjt. HFSS results for S_{11} are shown in Figure 17.

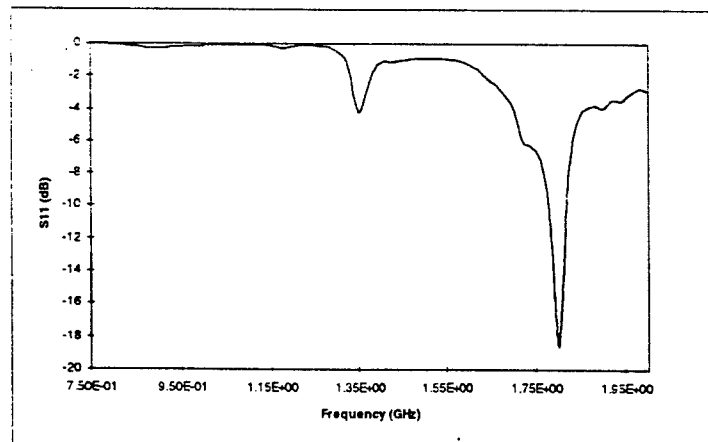


Figure 17. HFSS results for the probe excited open cylinder (20 MHz resolution.)

Figure 18 shows results for a test of the Celestron 8 Telescope with a coaxial probe positioned as for cyltest2.pjt. As a reference, the TE_{211} and TE_{311} modes for a closed cylindrical cavity of the dimensions of our open cavity resonate at 1.36 GHz and 1.822 GHz. The electric field plots at 1.35 GHz and 1.8 GHz for these HFSS models clearly indicate that the transverse modes are TE_{21} and TE_{31} respectively. So our simple model of an open cylinder accurately models the telescope for these low frequency resonances.

Figures 18 and 19 represent the physical test results using a probe excitation. In one scheme, a 3 cm probe was placed at the center of the most outer shell and a set of S_{11} measurements were taken. This measurement was done once having a conducting plate at the aperture of the telescope and then same measurements were done having no cover plate at the aperture. In both cases a receiver horn (probe) antenna was placed at the eyepiece of the telescope. The probe antenna was 0.88 inches in full length with aperture dimensions of 0.49 inches in length and 0.40 inches in height. Figure 18 shows the results having no cover plate, and Figure 19 shows the same measurements with a conducting cover plate at the aperture. It is evident from Figure 18 that this test result follow the same trend as the result obtained using HFSS shown in Figure 17.

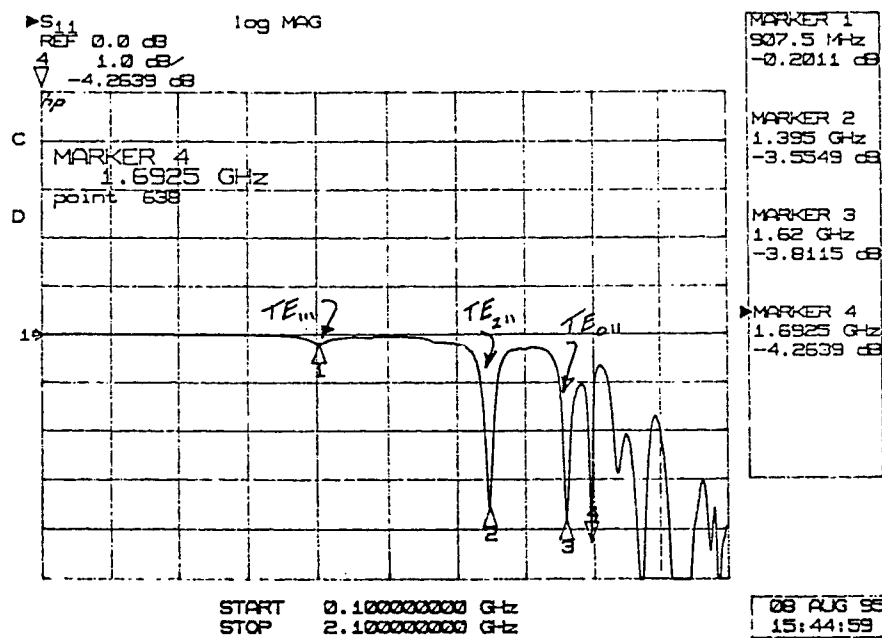


Figure 18. S_{11} measurements of the Celestron-8 telescope using a center mounted 3 cm probe - no cover plate.

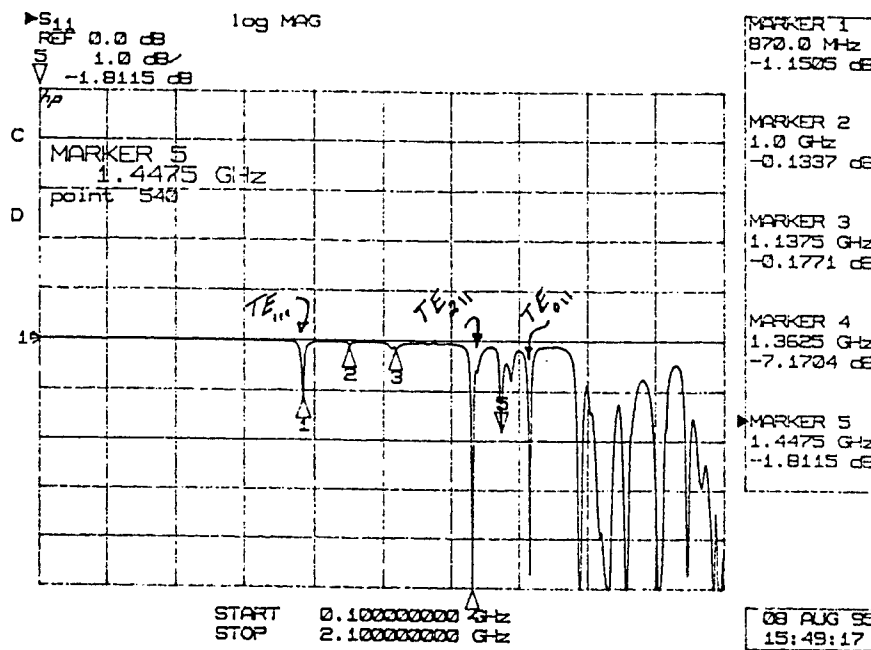


Figure 19. S_{11} measurements of the Celestron-8 telescope using a center mounted 3 cm probe - with cover plate.

Test description and results

Testing was done by Hugh Pohle over a frequency range of 1 GHz - 40 GHz. For these measurements, the telescope was excited by a transmitting antenna 40.0 inches in front of the aperture. A probe antenna was mounted at the eyepiece. The transmitting horn antenna was 3.02 inches in full length with aperture dimensions of 1.60 inches by 1.21 inches. The probe horn antenna was 0.88 inches in full length with aperture dimensions of 0.49 inches by 0.40 inches. Figure 20 shows one series of these measurements.

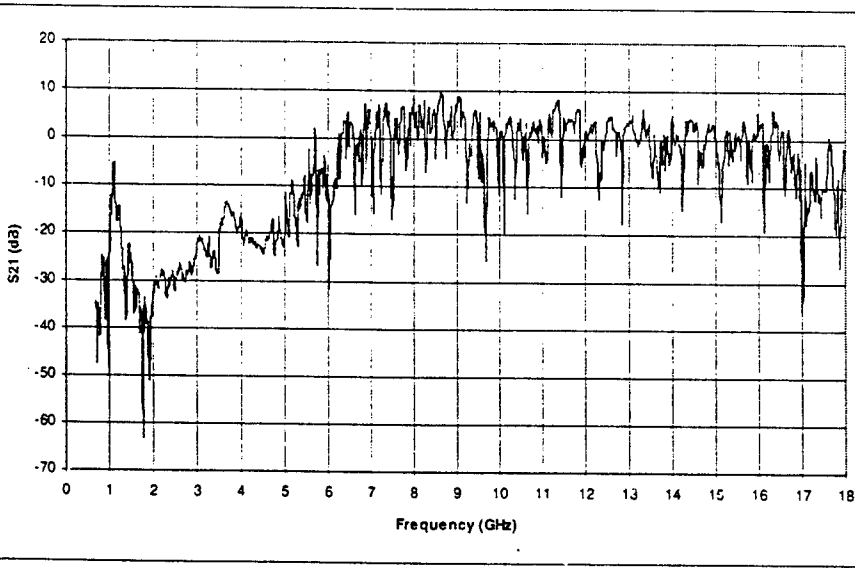


Figure 20. S_{21} Measurements of the telescope.

New approach suggested by Dr. Coffey [11]

It is known from experiment that the resonances of the cavities under consideration do not vary much from the closed empty cavity case. This knowledge is used to extend the traditional eigenvalue approach to a more general approach that is suitable for open-ended cavities. The method includes the following:

- 1) *Solve the eigenvalue problem for Dirichlet and Neumann boundary conditions on the openings and Dirichlet boundary conditions elsewhere.* This is the classic eigenvalue/eigenvector problem. From this step we can obtain estimates of eigenvalues and eigenvectors for the open-cylinder case. In a transmission line analogy, the Dirichlet conditions correspond to short-circuit loads, while the Neumann conditions correspond to open-circuits loads.
- 2) *Use the eigenvectors obtained in step 1 as basis functions to generate an equivalent impedance matrix $Z_{int}(r,r')$ that fully describes the interior problem at any frequency.*
- 3) *Use GEMACS (General Electromagnetic Model for the Analysis of Complex Systems) to obtain an equivalent impedance matrix $Z_{out}(r,r')$ that fully describes the exterior problem at any frequency.* We know that if the FD/FE (Finite Element) lattice extends to the far-field sphere, the impedance matrix is diagonal with terms equal to 376.7 ohms per square. The impedance matrix at the cavity opening(s) is not diagonal but dense, and the matrix terms vary extensively. However, by not having to work a FD/FE problem in the exterior, great computational savings can be made. GEMACS can be used to "bring the infinite boundary to the opening." This is a MOM/UTD (Unified Theory of Diffraction) hybrid problem (not an FD/FE problem). In the transmission line approach, this might be seen as referring a load impedance to another point along the transmission line via equations or smith chart.
At the same time, GEMACS may bring a source or sources from their exterior locations to equivalent sources at the opening. The combination of impedance matrix and equivalent excitation completely describes the exterior physics to the interior problem.
- 4) *Utilize Householder's method of modified matrices to combine the matrices together, enforcing E and H continuity at the open boundary.* This is the technique used in GEMACS, by Harrington and Mautz, and by K. K. Mei. In the transmission line (TL) analogy it is like connecting two (or more) lines together at a single point. The act of "connection" ensures the transmission line voltage is the same on either side of the junction (analogous to E-field continuity) and the transmission line currents are equal and opposite on either side of the junction (analogous to H-field continuity).
- 5) *Find the stationary points of the combined problem. At these points will be the complex resonant frequencies. From the complex resonant frequencies, obtain the resonances and Q's for each mode.*
Depending on how rapidly the exterior equivalent impedance varies with frequency, this may require more than a matrix eigenvalue computation.
- 6) *Utilize the eigenvectors of step 1 as basis functions for the coupling problem.* Since these are not orthonormal for the open-cavity case, the Rayleigh-Ritz-Galerkin procedure will not yield a diagonal matrix.

However, only the eigenvectors corresponding to eigenvalues near the operating frequency are required. Thus, the matrix problem to be solved for field coupling in the open-cavity case is quite small, perhaps no more than 20x20.

Conclusion

We have observed that using the method of iterative refinement did not make noticeable improvements in the near field calculations. However, all the methods in this report were applied to an empty open-ended cylindrical cavity. Therefore, we may or may not see different responses to the method of iterative refinement related to changes in the internal geometry. Using suitable Gaussian Quadrature did make substantial difference in the results. However, an adaptive method of integration is necessary in order to avoid comprehensive analysis trying to find the appropriate Gaussian Quadrature.

Using non-uniform meshing schemes which provide a model for the edge currents, did make a substantial improvement in the energy calculations. A denser field mesh in the aperture will undoubtedly improve the power calculations. However, until the appropriate formulation for calculating the near fields, to include the variations of current and of distance to the field point over individual cells, is implemented in CARLOS adequate accuracy of near fields can not be obtained.

CARLOS calculations in this report were only done for an empty open-ended cylindrical cavity. We ran up against memory (RAM) and disk storage limitations beyond a $\lambda/9$ discretization at 2 GHz. Once the interior geometry of the telescope is implemented, it would be necessary to increase these computational capabilities in order to continue with these calculations.

If Dr. Coffey's approach is successful, it will enable us to use other more computationally intensive codes over a more limited frequency range. It seems that once a high enough frequency is reached, computational resources will be strained. If we can limit use of those resources to frequency ranges of interest, our analytical problem will be substantially reduced. Of course, much research and validation needs to be done in order to obtain confidence in such a method.

Finally, the concept of determining energy at a particular point or area in a system by doing the inverse (antenna) problem is an attractive one. The vast amount of information contained in the HFSS solution can be used to determine optimum incidence angles to couple the energy into the system, field quantities anywhere in the system, system resonances, quality factor for the system, etc. HFSS was used in this study to demonstrate the concept; perhaps other types of codes (finite difference - time domain, MOM, etc.) could also be used to solve the "antenna" problem. CARLOS would be a good candidate to do the antenna problem because of its

ability to handle dielectrics as well as conductors. We encourage its modification to include port and wire excitations and post processing to give radiation patterns and radiation efficiency.

References

- [1] Wolfram. S., Mathematica, Addison-Wesley, 1991.
- [2] J.M. Putnam, L.N. Madgyesi-Mitschang and M.B Gedera, CARLOS-3DTM Three Dimensional Method Of Moments Code, McDonnell Douglas Aerospace-East, December 1992.
- [3] General Electromagnetic Model for the Analysis of Complex Systems (GEMACS) - Version 5, Rome Air Development Center, Griffiss Air Force Base, NY, December 1990.
- [4] R. R. DeLyser and P. Ensaf, "Analysis to Determine the Quality Factor of a Complex Cavity," Final Report for the Summer Faculty Research Program at the Phillips Laboratory, Sponsored by the Air Force Office of Scientific Research, September, 1994.
- [5] R. R. DeLyser, "An Analysis Approach to Determine Quality Factors of Large , Complex Cavities," Final Report for the Summer Faculty Research Program at the Phillips Laboratory, Sponsored by the Air Force Office of Scientific Research, September, 1993.
- [6] Balanis. C.A., Antenna Theory, John Wiley & Sons, New York, pp. 100-109, 1989.
- [7] Johnson J.H. Wang, Generalized Moment Method In Electromagnetics, John Wiley & Sons, New York, pp. 74-75, 1991.
- [8] Ishimaru, Akira, Electromagnetic Wave Propagation, Radiation, and Scattering, Prentice Hall, New Jersey, pp. 578-580, 1991.
- [9] Canning, Francis X. "Singular Value Decomposition of Integral Equations of EM and Applications to the Cavity Resonance Problem". IEEE Trans. Antennas Propagat., vol. AP-37, no. 9, pp. 1156-1163, 1988.
- [10] William H. Press, Brian P. Flannery, Saul A. Teukolsky, William T. Vetterling, Numerical Recipes, Cambridge University Press, New York, pp. 47-48, 1986
- [11] Edgar L. Coffey, III, "Electromagnetic Coupling to Open-Ended Cavities", Proposal Report to Phillips Laboratory, August, 1995.

UNIDIRECTIONAL RING LASERS AND LASER GYROS
WITH MULTIPLE QUANTUM WELL GAIN MEDIA

Jean-Claude Diels

Professor

Department of Physics and Astronomy

University of New Mexico

800 Yale Blvd. NE

Albuquerque, New Mexico 87131

Final Report for:

Summer Faculty Research Program

Phillips Laboratory

Sponsored by:

Air Force Office of Scientific Research

Bolling Air Force Base, DC

and

Phillips Laboratory

September 1995

UNIDIRECTIONAL RING LASERS
WITH MULTIPLE QUANTUM WELL GAIN MEDIA

Jean-Claude Diels

Professor

Department of Physics and Astronomy

University of New Mexico

800 Yale Blvd. NE

Albuquerque, New Mexico 87131

ABSTRACT

Multiple Quantum Well gain structures have been designed and grown with a finite gain (equal in both directions) a zero reflection from one side, and a finite reflection from the other side.

UNIDIRECTIONAL RING LASERS AND LASER GYROS WITH MULTIPLE QUANTUM WELL GAIN MEDIA

Jean-Claude Diels

Objective

The short term objective is to demonstrate a unidirectional ring laser with asymmetric reflection properties.

The long term objective is to demonstrate gyro response of a dual ring laser operating on a small cube of semiconductor material.

A simple unidirectional ring laser

The prototype unidirectional laser will consist in a free suspended Multiple Quantum Well (MQW) structure, optically pumped by a Ti:sapphire laser, and accurately aligned in the laser cavity with the faces normal to the beam. As will be explained in the next section, the MQW structure has zero reflectivity from the left, and a finite reflectivity from the left. A clockwise propagating beam has therefore a lower threshold, since it experiences reduced losses. With proper alignment of the gain layers, the counterclockwise circulating mode is reflected into the clockwise circulating one. Computer simulation indicate a near total extinction of the counterclockwise mode in favor of the clockwise one.

Principle of “non-reciprocity”

Introduction

The principle of the asymmetry in reflection of the structure can best be understood by considering just a pair of two ultrathin (thickness \ll wavelength) reflecting layers, one being a dielectric “delta function”, and the other a pure

gain discontinuity. This ultra-simplified pair provides a base of understanding for the more complex multilayer structure of the MQW. We will consider successively single dielectric layers, single gain layers (imbedded in a dielectric with the same real part for the dielectric constant), pairs of layers, and finally more complex structures.

Because one is used to deal with continuous structures of dimension larger than the wavelength, optical properties of such structures are counter-intuitive. For instance, the usual concept of a “self-saturation” and a “mutual saturation” does not apply to the ultrathin gain medium. The saturation is uniquely determined by the value of the *local* field at the layer, which could be the node or antinode of a standing wave. Unlike the situation in a continuous gain medium, the field reflection of the single gain layer is comparable to the field gain in transmission.

Single layer

A dielectric layer

Let us consider first a single dielectric layer imbedded in a uniform dielectric medium.

For the electric field, we choose a linearly polarized plane wave with electric field amplitude:

$$E(t) = \tilde{E}(t) + c.c. = \frac{1}{2} \tilde{\mathcal{E}}(t) e^{i(\omega_e t - kz)} + c.c. \quad (0.1)$$

The field is incident on a dielectric slab of thickness d . The reflected and transmitted fields can be calculated by considering the slab as a Fabry-Perot etalon, or using propagation matrix formalism, and going to the limit $d \rightarrow 0$. Another approach is to consider the slab to be made of a layer of dipoles with polarizability $\chi\epsilon_0$. The total polarization is thus $\tilde{P} = \chi\delta(z)\epsilon_0\tilde{E}$. Inserting this polarization as a source term in Maxwell's equations:

$$\frac{\partial^2 \tilde{E}}{\partial z^2} + k^2 \tilde{E} = -\mu_0 \epsilon_0 \omega_e^2 \chi \delta(z) \tilde{E} = -\frac{\omega_e l l^2}{c^2} \chi \delta(z) \tilde{E}. \quad (0.2)$$

We will use $_0$, $_r$ and $_t$ as indices for the incident, reflected and transmitted waves, respectively. Continuity of the tangential component of the field across

the dielectric layer imposes that:

$$\tilde{\mathcal{E}}_0 + \tilde{\mathcal{E}}_r = (1 + \tilde{r})\tilde{\mathcal{E}}_0 = \tilde{\mathcal{E}}_t = \tilde{t}\tilde{\mathcal{E}}_0. \quad (0.3)$$

Integrating Maxwell's equation (0.2) across the dielectric layer:

$$[-ik\tilde{\mathcal{E}}_t] - [-ik\tilde{\mathcal{E}}_0 + ik\tilde{\mathcal{E}}_r] = -\frac{\omega_t^2}{c^2}\chi\tilde{\mathcal{E}}_0(1 + \tilde{r}). \quad (0.4)$$

Taking into account the relation (0.3), we find:

$$\frac{\tilde{r}}{1 + \tilde{r}} = -i\frac{\omega_t\chi}{2nc} = -i\beta, \quad (0.5)$$

where n is the index of refraction of the host medium. Solving for the reflection and transmission coefficient:

$$\tilde{r} = \frac{-i\beta}{1 + i\beta} \quad (0.6)$$

$$\tilde{t} = \frac{1}{1 + i\beta}. \quad (0.7)$$

A gain layer

Let us consider next a gain layer imbedded in a uniform dielectric. For the gain medium, χ is purely imaginary. Since β is proportional to the susceptibility, for a gain medium, we will have a reflection and transmission of the form:

$$\tilde{r} = \frac{\alpha}{1 - \alpha} \quad (0.8)$$

$$\tilde{t} = \frac{1}{1 - \alpha}. \quad (0.9)$$

These two expressions apply as well for an absorbing medium, and have been checked numerically using matrix multiplication methods. While the agreement is excellent for small values of α , there is some discrepancies for $\alpha > 0.1$, which is of no concern in practical cases, but points to some hidden approximation in substituting a δ function for the polarizability. It is interesting to note the symmetry between forward and backward directions in the case of an absorbing or amplifying layer. For any value of α , the field reflection is equal to the field gain (attenuation) in the forward direction. This result is consistent with a simple argument that the emitting layer being much thinner than the wavelength has no information on the direction of the field, hence has equal probability of emission in forward and backward directions. Again consistent with the

semiclassical approximation, in a gain (absorbing) layer or volume of dimensions much smaller than the wavelength, the local dipole induced by the light has no space dependence, hence cannot have any “traveling wave” dependence. In the case of a macroscopic volume as a laser gain medium, atoms at different positions along z are excited in phase, hence the radiation in the forward direction has the same k vector as the exciting wave, while the radiation in the backward direction averages out. Note that it is the *field* gain, rather than the gain in energy, that is symmetric. In terms of the reflected and transmitted energy, the reflection is second order with respect to the transmission gain.

As in the case of the dielectric layer, it is the basic property that the *tangential component of a field is continuous across an interface* that has as consequence that the reflected field is equal to the gain in transmitted field. One is used to associate the gain (absorbing) medium with a discontinuity in field (i.e., a larger field at the output of the medium than at the input). This view is incorrect for layers thinner than the wavelength. For the amplifying thin layer, the dipolar radiation emits on both sides of the plane. For the absorbing layer, the induced dipoles make a “sink” for the field, bringing it down equally on both sides of the layer.

It is a peculiar coincidence that the quantum field description of stimulating emission of a single atom, being emitted exclusively in the direction of the exciting mode, is consistent with the *macroscopic* limit of the semiclassical theory, and not the microscopic one. Quantum electrodynamics cannot easily be extended from a single atom consideration to an atomic layer.

Energy conservation

The energy conservation for the gain (or absorbing, if α is negative) layer is:

$$|\tilde{r}|^2 + |\tilde{t}|^2 = 1 + G \quad (0.10)$$

which, after substitution, reads:

$$\frac{\alpha^2}{(1-\alpha)^2} + \frac{1}{(1-\alpha)^2} = 1 + \frac{2\alpha}{(1-\alpha)^2} \quad (0.11)$$

The intensity gain is thus the product of 2α by the local intensity [which is, in this case $|t|^2 = 1/(1-\alpha)^2$].

The non-reciprocal element

The ultimate in simplicity

The pairing of a thin gain layer with a dielectric reflecting layer leads to a structure that has non symmetric reflection properties. Let us consider, from left to right, a thin gain layer (transmission $E_t = (1 + \alpha)E_i$; reflection $E_r = \alpha I_i$) followed at a distance $\ell = 3\lambda/8$ by a dielectric layer (reflection $E_r = irE_i$; transmission $E_t = \sqrt{1 - r^2}E_i$). The round trip between the two layers corresponds to a phase factor $\exp\{-2ik\ell\} = i$. Let us neglect for simplicity multiple reflections. The combined reflection from both interfaces, for a beam incident from the left, is: $E_r = (\alpha - r)E_i$, which is zero if $\alpha = r$. For a beam incident from the right: $E_r = i(\alpha + r)E_i$, which is finite if $\alpha = r$. It is important for gyro related applications that this finite reflectivity has a phase factor of $\pi/2$ with respect to the transmission from left to right. Other cases are possible. For instance, if the spacing between the layers is $\ell = \lambda/8$, then it is the reflection from the right that can be made equal to zero. But the non-zero reflection from the left is then in phase (or π out of phase) with the transmission from the right, which is an undesirable situation for laser gyro applications.

Energy conservation

One might wonder how energy can be conserved for this simple two layer structure. For light incident from the left, the incident energy is equal to the transmitted energy augmented with the gain. The same amount of light incident from the right should be equal to the (same) transmitted energy augmented with the gain and the reflected energy. The explanation is that the gain is different in both cases, because the local field at the gain layer is different.

Relation to unidirectional laser

If such a pair of elements is used as a gain medium for a ring laser, the finite reflection will re-inject energy from one sense of rotation into the other, which will dominate, make the ring laser nearly unidirectional.

The properties of non-reciprocity in reflection can be generalized to more complex multiple quantum well structures. In the calculations that are pre-

sented below, a standard matrix calculation is used to calculate the transmissivity and reflectivity of a multiple quantum well structure.

A practical multilayer structure

There are several practical and fundamental limitations to the two-layer nonsymmetrical structure discussed above:

- the overall gain is quite limited
- there is no control over the phase shift on transmission/reflection

A single gain/dielectric layer can be replaced by a succession of multiple quantum well optically pumped/pассивные layers separated by a half wavelength. As in the case of the simple two layer structure discussed above, a MQW structure can be designed to have a zero-reflectivity from the left, a finite reflectivity from the right, and an overall gain. The material parameters of $\text{Ga}_x\text{Al}_{(1-x)}\text{As}$ are sufficiently well known to make a reasonable prediction of the optimum structure possible. The number of parameters to be adjusted is fairly large. For instance:

- the thickness of the individual gain MQW (GaAs) should be adjusted to have the lasing resonance corresponding to the design wavelength (860 nm)
- an antireflection structure (of MQW) should be included ion the growth process, on either side of the asymmetric structure, with a residual reflectivity negligible compared to that of the structure (in the reflecting direction)

There are more parameters to optimize than just the reflection properties. Parameters that can be adjusted are the phase shift upon transmission, reflection, and the local field at the gain layers.

Phases

If the phase ϕ_ϵ of the backscattering coefficient $\tilde{\epsilon}$ is such that the reflection has a component in phase with the counterclockwise field $\tilde{\mathcal{E}}_2 \exp\{i[\omega t + kz]\}$, the

latter will be “injection locked” by the backscattering. There is no injection locking if the backscattering is 90^0 out of phase with the field $\tilde{\mathcal{E}}_2$.

For use in a ring laser, it is essential that the phase of the reflected wave be at 90^0 from that of the transmitted wave. This phase relationship will prevent locking of the laser gyro.

Let us consider a structure inserted in a ring cavity, with the clockwise beam incident first upon the face of zero reflection. Let φ_t be the phase shift upon transmission, and φ_r the phase shift upon reflection of the second surface. The resonance condition for the ring cavity is that the phase shift for the light path outside the MQW structure be $-\varphi_t$. The condition that counterclockwise wave reflected at the right interface be 90^0 out of phase with the transmitted phase is:

$$\begin{aligned} (-\varphi_t) + \varphi_r &= \varphi_t + \frac{\pi}{2} \\ \varphi_r - 2\varphi_t &= \frac{\pi}{2}. \end{aligned} \tag{0.12}$$

For the high gain structure of Table 0.1, $\varphi_t = -1.13915$; $\varphi_r = -0.70910$; and the difference $\varphi_r - 2\varphi_t = 1.5692$, or an excess of -0.0016.

Gain and saturation

The gain of the structure is not simply given by the product of the gain/layer times the number of layers. To calculate the gain, it is necessary to compute the (rather complex) field distribution in the structure. A high overall gain requires that (a) the gain MQW layers be located at the *antinodes* of the electric field, and (b) that the local field at the layers be large compared to the external field incident on the structure (resonance condition).

A "robust" structure

This last condition is the essential test of practicality. Given an error on any of the growth parameter (error bar on index of refraction, layer thickness and composition), the change in structure properties should be negligible. This "robustness" of the structure was found to vary over wide ranges depending on the particular choice of parameters.

There is, at this point, no systematic method to search simultaneously for zero reflection from one direction, maximum reflection from the other, an optimum phase shift upon reflection and transmission, a maximum gain, and a robust structure. The calculation proceed along a tedious "trial and error" approach.

Sample growth and characterization

The first two sets of samples were grown by MOCVD at the Center for High Technology Material (CHTM) of the University of New Mexico. The multiple layer structure was grown on a GaAs wafer. The substrate was subsequently etched away (since the GaAs is opaque to the generated radiation of 860 nm). Characterization of the first sample was made through absorption and reflection spectroscopy, and luminescence spectroscopy. The complexity of the absorption and reflection spectra, compounded by the inaccuracy of the MOCVD process, were such that it was impossible to match calculated and measured the peaks of the spectra. Other problems that obscured the evaluation of the first sample were related to the stop-etch layer of AlAs. The overall thickness of the structure

material	thickness (nm)	index (r)	index (i)	comment
air		1.	0.000	boundary
$Al_{0.25}Ga_{0.75}As$	126.30	3.3967	0.000	stop etch layer
$AlAs$	71.90	2.9835	0.000	
$Al_{0.25}Ga_{0.75}As$	63.15	3.3967	0.000	
$AlAs$	71.90	2.9835	0.000	AR
$Al_{0.25}Ga_{0.75}As$	63.15	3.3967	0.000	
$AlAs$	71.90	2.9835	0.000	AR
$Al_{0.25}Ga_{0.75}As$	63.15	3.3967	0.000	
$AlAs$	71.90	2.9835	0.000	AR
$Al_{0.25}Ga_{0.75}As$	41.00	3.3967	0.000	reflector
$AlAs$	85.00	2.9835	0.000	reflector
$Al_{0.25}Ga_{0.75}As$	59.00	3.3967	0.000	spacer $r = \alpha$
$AlAs$	76.62	2.9835	0.000	(2 layers)
$Al_{0.25}Ga_{0.75}As$	59.00	3.3967	0.000	spacer $r = \alpha$
$AlAs$	76.62	2.9835	0.000	(2 layers)
$Al_{0.25}Ga_{0.75}As$	1108.78	3.3967	0.000	spacer $r = \alpha$
$GaAs$	10.00	3.6470	-0.014	Quantum well
$Ga_{0.80}Al_{0.20}As$	115.00	3.4130	0.000	pump layer
$GaAs$	10.00	3.6470	-0.014	Quantum well
$Ga_{0.80}Al_{0.20}As$	115.00	3.4130	0.000	pump layer
...	19 pairs total between —
$GaAs$	10.00	3.6470	-0.014	Quantum well
$Ga_{0.80}Al_{0.20}As$	115.00	3.4130	0.000	pump layer
$GaAs$	10.00	3.6470	-0.014	Quantum well
$Ga_{0.80}Al_{0.20}As$	115.00	3.4130	0.000	pump layer
$GaAs$	10.00	3.6470	-0.014	last Quantum well
$Al_{0.25}Ga_{0.75}As$	1108.78	3.3967	0.000	spacer
$AlAs$	76.62	2.9835	0.000	(1 layer)
$Al_{0.25}Ga_{0.75}As$	59.00	3.3967	0.000	spacer
$AlAs$	76.62	2.9835	0.000	(1 layer)
$Al_{0.25}Ga_{0.75}As$	35.50	3.3967	0.000	reflector
$AlAs$	71.90	2.9835	0.000	reflector
$Al_{0.25}Ga_{0.75}As$	63.15	3.3967	0.000	AR
$AlAs$	71.90	2.9835	0.000	AR
$Al_{0.25}Ga_{0.75}As$	63.15	3.3967	0.000	AR
$AlAs$	71.90	2.9835	0.000	AR
$Al_{0.25}Ga_{0.75}As$	63.15	3.3967	0.000	AR
$AlAs$	71.90	2.9835	0.000	AR
$Al_{0.25}Ga_{0.75}As$	126.30	3.3967	0.000	etch layer
$AlAs$	10.00	2.9835	0.000	1st etch
$GaAs$		3.6470	0.000	substrate

Table 0.1: Detailed constitution of the $GaAlAs$ MQW structure optimized for zero reflection at 860 nm, and maximum robustness. The overall gain is 7%.

was too thin to prevent stresses to deform the membrane that constituted the sample. Further degradation of the transmission/reflection was due to fast oxydation of the stop layer of AlAs. It appeared also that the sample was damaged by the pump laser used for the luminescence spectrum. The solution chosen for all these problems is to use a $\text{Ga}_{0.1}\text{Al}_{0.9}\text{As}$ stop etch layer (much less sensitive to oxydation) of $1 \mu\text{m}$ thickness. The diameter of the etched zone will be kept as small as possible, compatible with the size of the pump and laser beams. Such a structure (table 0.1) is presently being grown by MOCVD at the CHTM, and by MBE at Sandia National Labs.

The last MOCVD growth is being made by monitoring after each "calibration run" the reflectivity in amplitude *and phase*, using a technique that we recently developed. The diagnostic instrument is basically an accurately compensated Michelson interferometer, of which the delay in one arm is monitored with an absolute accuracy of 15 nm with a He-Ne laser. The complex Fourier transform of the interferogram gives a complete description of the reflective properties of the sample.

Ion-Molecule Reactions at Very High Temperatures

**Itzhak Dotan
Professor
Chemistry Department**

**The Open University of Israel
Ramat-Aviv, Tel-Aviv Israel**

**Final Report for:
Summer Research Program
Phillips Laboratory**

**Sponsored by:
Air Force Office of Scientific Research
Bolling Air Force Base, Washington DC**

and

Phillips Laboratory

September 1995

ION-MOLECULE REACTIONS AT VERY HIGH TEMPERATURES

Itzhak Dotan
Associate Professor
The Open University of Israel
16 Klausner St.
Ramat-Aviv, Tel-Aviv
Israel

Abstract

Rate coefficients for a few ion-molecule reactions have been measured in the range 300-1500K. The measurements were carried out in a flowing afterglow apparatus designed for the measurement of ion-molecule reaction rate coefficients at temperatures higher than any previous measurement. Reactions measured were $\text{Ar}^+ + \text{CO}_2$, $\text{Ar}^+ + \text{SO}_2$, $\text{N}^+ + \text{O}_2$, $\text{CO}_2^+ + \text{O}_2$. These results are compared with previous studies of temperature and translational energy dependence of ion-molecule reaction rate coefficients. Preliminary results were obtained for the reactions $\text{O}^+ + \text{N}_2$, $\text{Ar}^+ + \text{O}_2$, $\text{N}_2^+ + \text{O}_2$. Experimental problems relating to operation of a flowing after-glow apparatus at high temperatures were solved and discussed.

ION-MOLECULE REACTIONS AT VERY HIGH TEMPERATURES

Itzhak Dotan
Associate Professor

Introduction

It has long been recognized that information on energy and temperature dependences of rate coefficients of ion-molecule reactions is desirable both for scientific and practical reasons {1}.

The immediate motivation for measuring rate coefficients at very high temperatures is to provide data and guidance for modeling high-temperature plasmas which occur naturally (e.g. auroras and the ionosphere) or man-made (e.g. around vehicles in hypersonic flight, re-entry vehicles, or engine exhausts). However, it is clear that many interesting questions arise at high temperatures: new reaction channels may become activated and esoterica such as “entropy-driven” reactions {2} become more accessible for study.

A typical variable-temperature flowing afterglow or selected ion-flow tube (SIFT) apparatus can operate at temperatures as high as 500-600K. In the early 1970s', Lindinger et al. {3} modified a flowing afterglow apparatus at the National Oceanic and Atmospheric Administration (NOAA) laboratories, to permit operation as high as 900K. At about the same time the same group built the flow-drift tube {4} which could measure rate coefficients between room temperature and 3eV center of mass translational energy.

The NOAA group reported temperature dependence of nine positive-ion reactions {3}. Reactions which were fast (collisional) at 300K were found to be temperature independent within experimental uncertainty. Reactions which were slow at 300K were seen to decrease with increasing temperature, but in two cases a shallow minimum was observed - for $O^+ + N_2$ at 850K and for $CO_2^+ + O_2$ at about 700K. For

most of the reactions studied by the NOAA group data also existed from flow-drift tube experiments. Generally speaking, the temperature variation of the reaction rate coefficients mimicked results from flow-drift tube data on the kinetic energy dependence of reaction rates.

The data reported herein show a very good agreement with previous data for temperature and low-energy dependence of rate coefficients. At higher temperatures there are distinct differences between temperature and kinetic energy dependence. The role of internal (vibrational and rotational) energy in ion-molecule reactions may be deduced from this comparison. It is known that many reactions are strongly dependent upon internal excitation {5}.

Experimental Details

The measurements were made using a recently constructed High Temperature Flowing Afterglow (HTFA) apparatus. The details of the HTFA will be presented elsewhere, but a brief description of its special features is given here.

In most aspects the HTFA is a standard flowing afterglow instrument {6}, consisting of an electron-impact ion-source, flow-tube, gas inlets and a detection system. Special properties to operate at high temperature include:

- ceramic (alumina) flow-tube.
- silicon carbide heaters in a 3-zone commercial furnace.
- upstream end of flow tube is out of the furnace; all electrical and gas connections are made through a cap that clamps to this end. The cap is water-cooled.

The downstream end of the furnace simply abuts the cooled metal mating piece.

This necessitates enclosing the whole apparatus in a vacuum box to prevent leaks into the flow-tube.

- The downstream end of the flow simply terminates ~ 1R from sampling tube.
- All inlet tubes are ceramic.
- Sampling plate is molybdenum and sealed by a ceramic "O-ring".
- 100 amp 220 volts to run the furnace at full power.

A detailed description of the apparatus is given in Fig. 1.

Working at high temperatures causes experimental problems that we had to overcome.

The main problems are:

- Decrease in the signal due to diffusion. Diffusion rate is proportional to $T^{3/2}$.
Thermionic emission of (mainly) Na^+ ($M=23$) and K^+ ($M=39$) from the molybdenum sampling aperture plate. This causes a major problem in measuring Ar^+ ($M=40$) reactions.
- Positive and negative surface ionization on flow-tube walls.
- Possible decomposition of reactant gas on surfaces.

Results

Four positive ion-molecule reactions were studied as a function of temperature between 300 to 1500K. Preliminary results exist for three more reactions.



Results for reaction (1) are shown in Fig. 2 and Fig. 3. The results are compared with rate constants measured as a function of kinetic energy in a flow-drift tube {7}. At the low temperatures (up to about 700K) there is no difference between the two sets of data. At the higher temperatures the HTFA data is lower (up to a factor of 2 at 1500K) than the flow-drift tube data.



Results for reaction (2) shown in Fig. 4. Here again there is a good agreement between the HTFA data and the flow-drift tube data at the low temperature range. The HTFA data show a distinct minimum at about 1000K whereas the flow-drift tube data {8} show this minimum at a higher effective temperature (about 3000K). This reaction has two channels, charge-transfer and dissociative charge transfer. The latter is endothermic by 0.4 eV. This channel causes the rate coefficient to increase at high energies. It is not clear if we get this channel at the high temperatures.



Reaction (3) was a subject of a few studies {3, 9,10}. The NOAA group measured it as a function of temperature up to 900K. They saw a shallow minimum at about 700K. Our data (Fig. 5) agrees with the NOAA data. The minimum in the temperature dependence of the rate coefficient is well established. In Fig. 6 we compare rate coefficients measured in a few systems. There is a very good agreement at the energy range. The high temperature data is close to the data measured in Ar buffer, showing the effect of the internal excitation of CO_2^+ by Ar. The agreement between the present data and previous data measured in the Philips laboratory using variable temperature SIFT-drift apparatus is remarkable.



The results for this important atmospheric reaction are shown in Fig. 7. There is a very good agreement with the NOAA data {3} at the low temperature range. The rate coefficient increased faster with temperature than with kinetic energy {11}, showing the effect of internal excitation.

Discussion and Future Work

The data shown in Figs. 2-7 show a distinct difference between the kinetic energy and temperature dependence of the four reactions studied. We also saw the same effect for the three reactions where we have only preliminary results. ($\text{O}^+ + \text{N}_2$, $\text{Ar}^+ + \text{CO}$, $\text{N}_2^+ + \text{O}_2$).

We plan to analyze the data and try to deduce the role of internal energy in these reactions. For reaction (2), we shall try to fit the high temperature data to an Arrhenius

plot and get the endothermicity of the dissociative charge transfer channel. For reaction (4) we plan to measure the branching ratio as a function of temperature.

Our data shows the importance of measuring rate coefficients of ion-molecule reactions at very high temperatures. Using kinetic energy dependence or extrapolating, low temperature data may lead to very serious mistakes in modeling plasmas at high temperatures of interest to the Air Force.

References

1. See, for example, "Gas Phase Ion Chemistry", Vol. 2, Ed. M.T. Bowers (Academic Press, New York, 1979).
2. M. Meot-Ner (Mautner), J. Phys. Chem., **95** 6580 (1991).
3. W. Lindinger, F.C. Fehsenfeld, A.L. Schmeltekopf and E.E. Ferguson, J.G.R., **79** 4753 (1974).
4. M. McFarland, D.L. Albritton, F.C. Fehsenfeld, E.E. Ferguson and A.L. Schmeltekopf, J. Chem. Phys., **59** 6610 (1973).
5. A.A. Viggiano et al., J. Chem. Phys., **93** 1149 (1992).
6. E.E. Ferguson, F.C. Fehsenfeld and A.L. Schmeltekopf, in "Advances in Atomic and Molecular Physics", Ed. D.R. Bates, Academic Press, New-York, 1969.
7. I. Dotan and W. Lindinger, J. Chem. Phys. **76** 4972 (1982).
8. I. Dotan, D.L. Albritton and F.C. Fehsenfeld, J. Chem. Phys., **64** 4334 (1976).
9. W. Lindinger, M. McFarland, F.C. Fehsenfeld, D.L. Albritton, A.L. Schmeltekopf and E.E. Ferguson, J. Chem. Phys. **63** 2175 (1975).
10. E.E. Ferguson, J.M. Van Doren, A.A. Viggiano, R.A. Morris, J.F. Paulson, J.D. Stewart, L.S. Sunderlin and P.B. Armentrout, Int. J. Mass Spectrom. Ion . Proc. **117** 261 (1992).
11. M. Mc. Farland, D.L. Albritton, F.C. Fehsenfeld, E.E. Ferguson and A.L. Schmeltekopf, J. Chem. Phys. **59** 6620 (1973).

Figure Captions

Fig. 1 - High Temperature Flowing Afterglow Apparatus.

Fig. 2 - Rate constants for the reaction of Ar^+ ions with CO_2 as a function of effective kinetic temperature. $(\text{KE}_{\text{cm}}) = \frac{2}{3} \text{kTeff}$ including both HTFA and Flow-Drift Tube data.

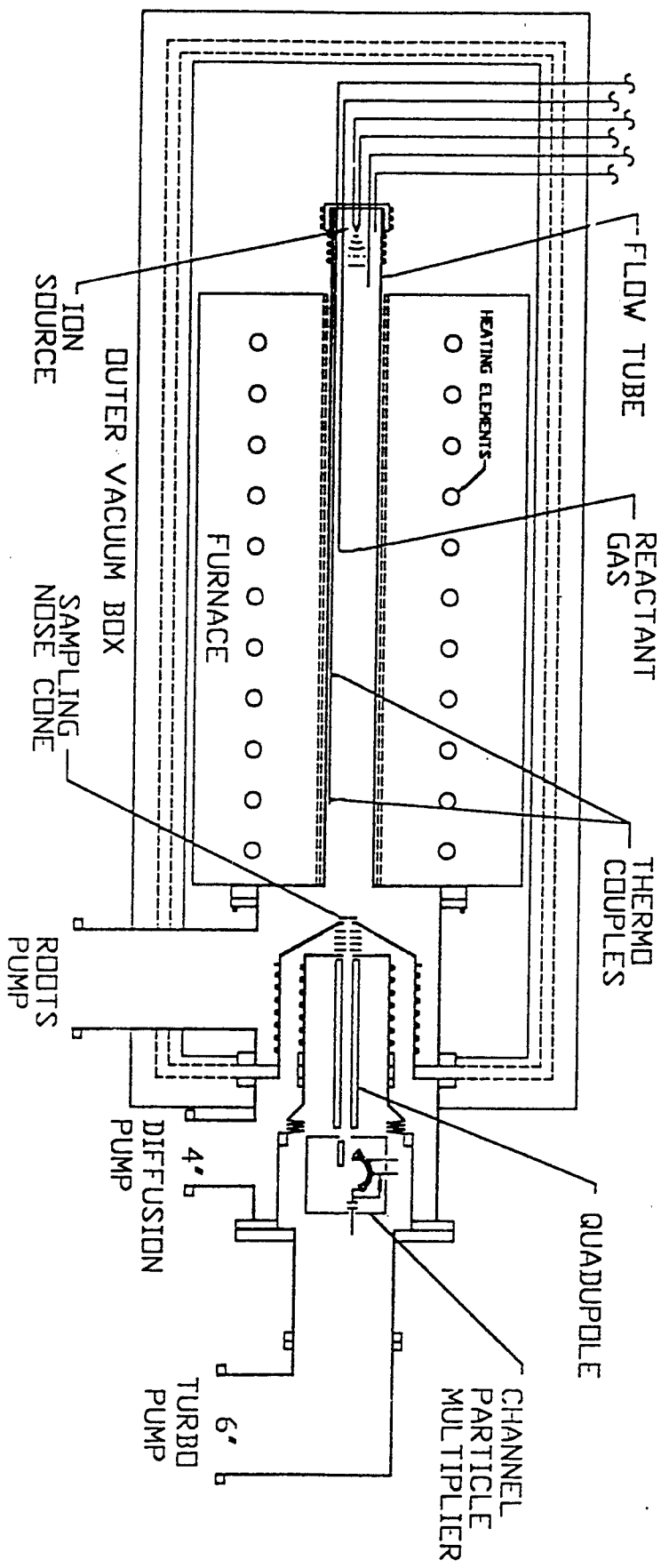
Fig. 3 - Rate constants for the reaction of Ar^+ ions with CO_2 as a function of effective kinetic temperature. $(\text{KE}_{\text{cm}}) = \frac{2}{3} \text{kTeff}$ including both HTFA and Flow-Drift Tube data.

Fig. 4 - Rate constants for the reaction of Ar^+ ions with SO_2 as a function of effective kinetic temperature. $(\text{KE}_{\text{cm}}) = \frac{2}{3} \text{kTeff}$ including both HTFA and Flow-Drift Tube data.

Fig. 5 - Rate constants for the reaction of CO_2^+ ions with O_2 as a function of effective kinetic temperature. $(\text{KE}_{\text{cm}}) = \frac{2}{3} \text{kTeff}$ including HTFA, Variable Temperature Flowing, Afterglow and Flow-Drift Tube data.

Fig. 6 - Rate constants for the reaction of CO_2^+ ions with O_2 as a function of effective kinetic temperature $(\text{KE}_{\text{cm}}) = \frac{2}{3} \text{kTeff}$ including HTFA, Flow-Drift Tube and Ar buffer data.

Fig. 7 - Rate constants for the reaction of N^+ ions with O_2 as a function of temperature, including both HTFA and NOAA variable temperature flowing afterglow data.



11-9

HIGH TEMPERATURE FLOWING AFTERGLOW

Fig 1

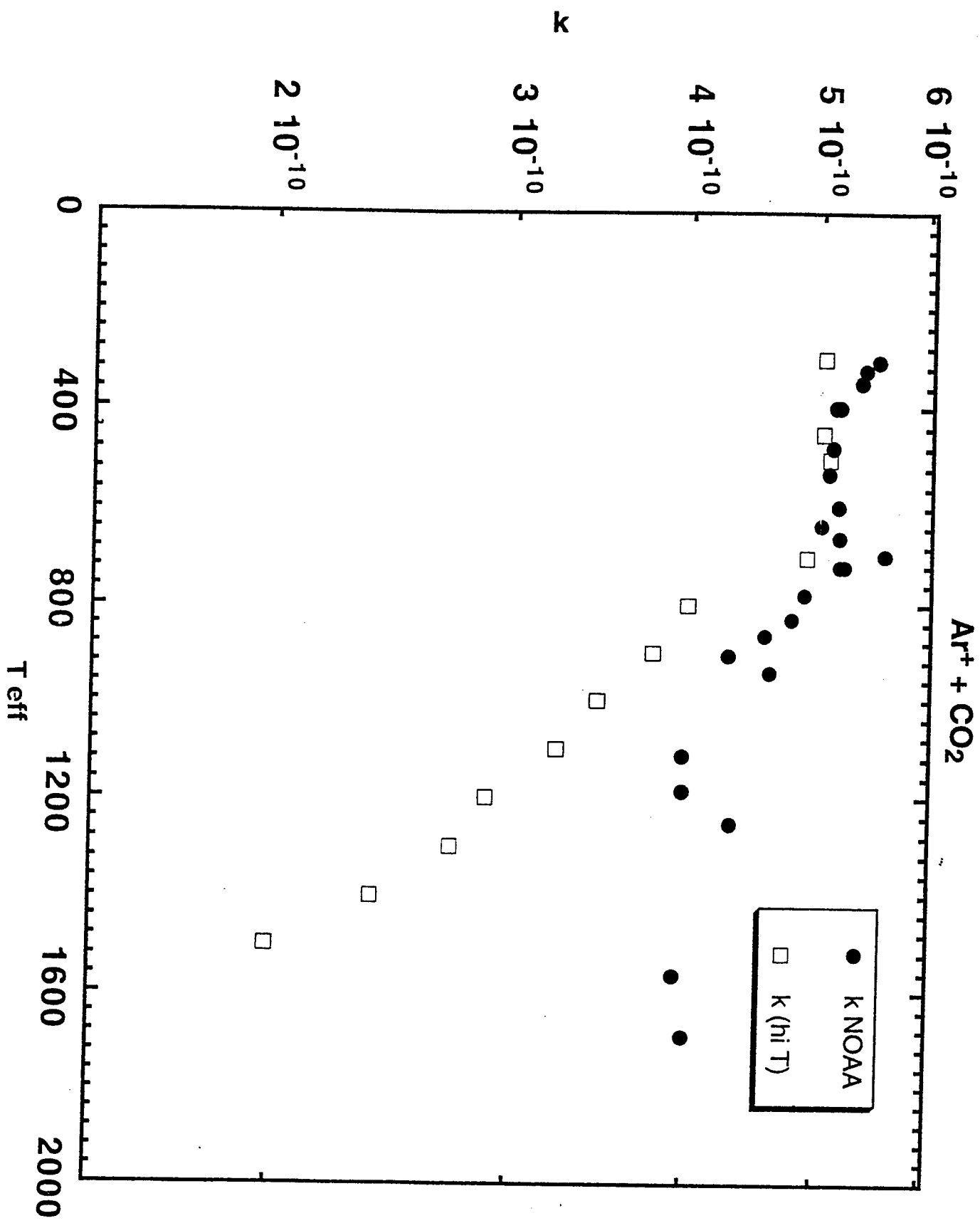
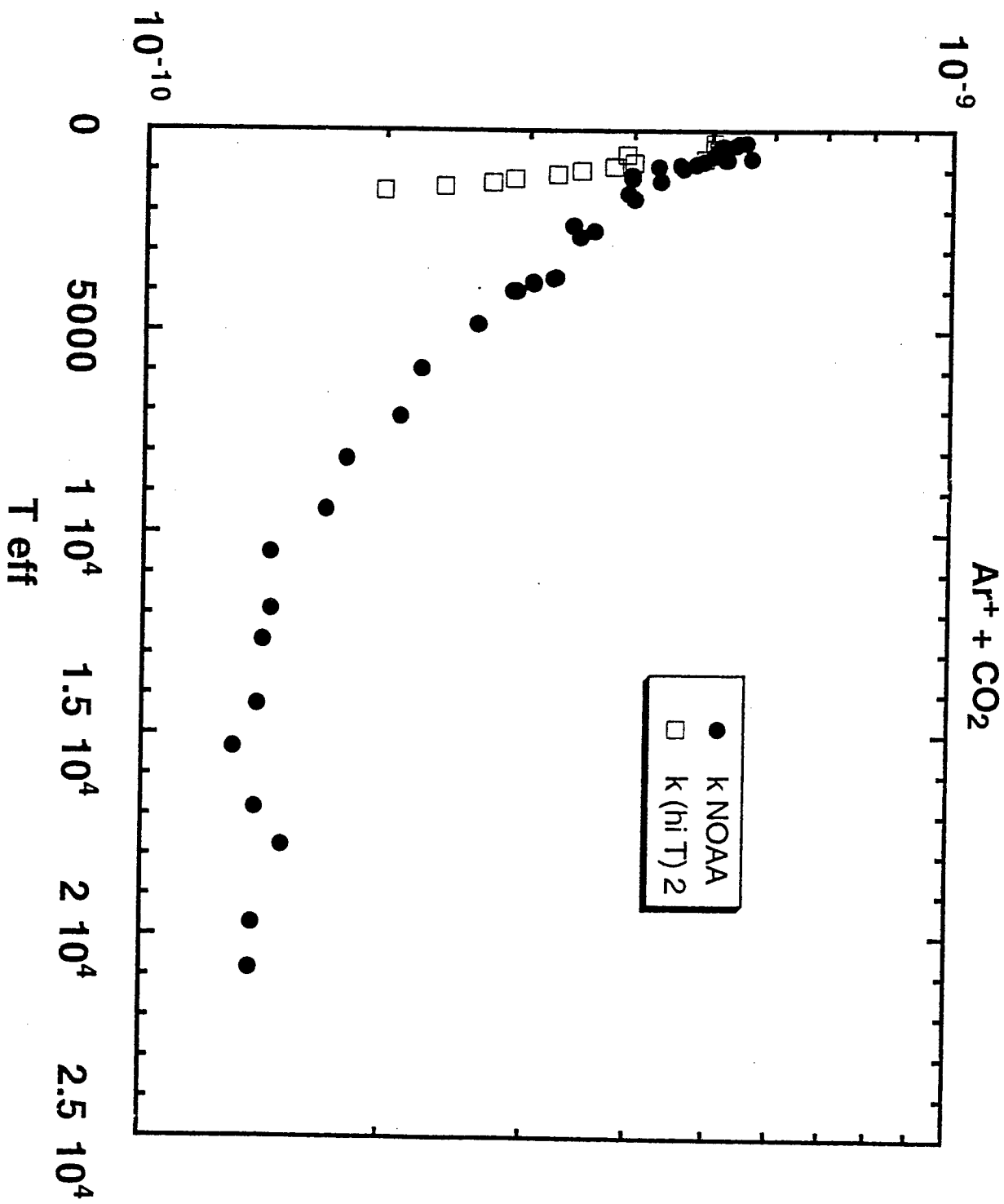


Fig 2

κ



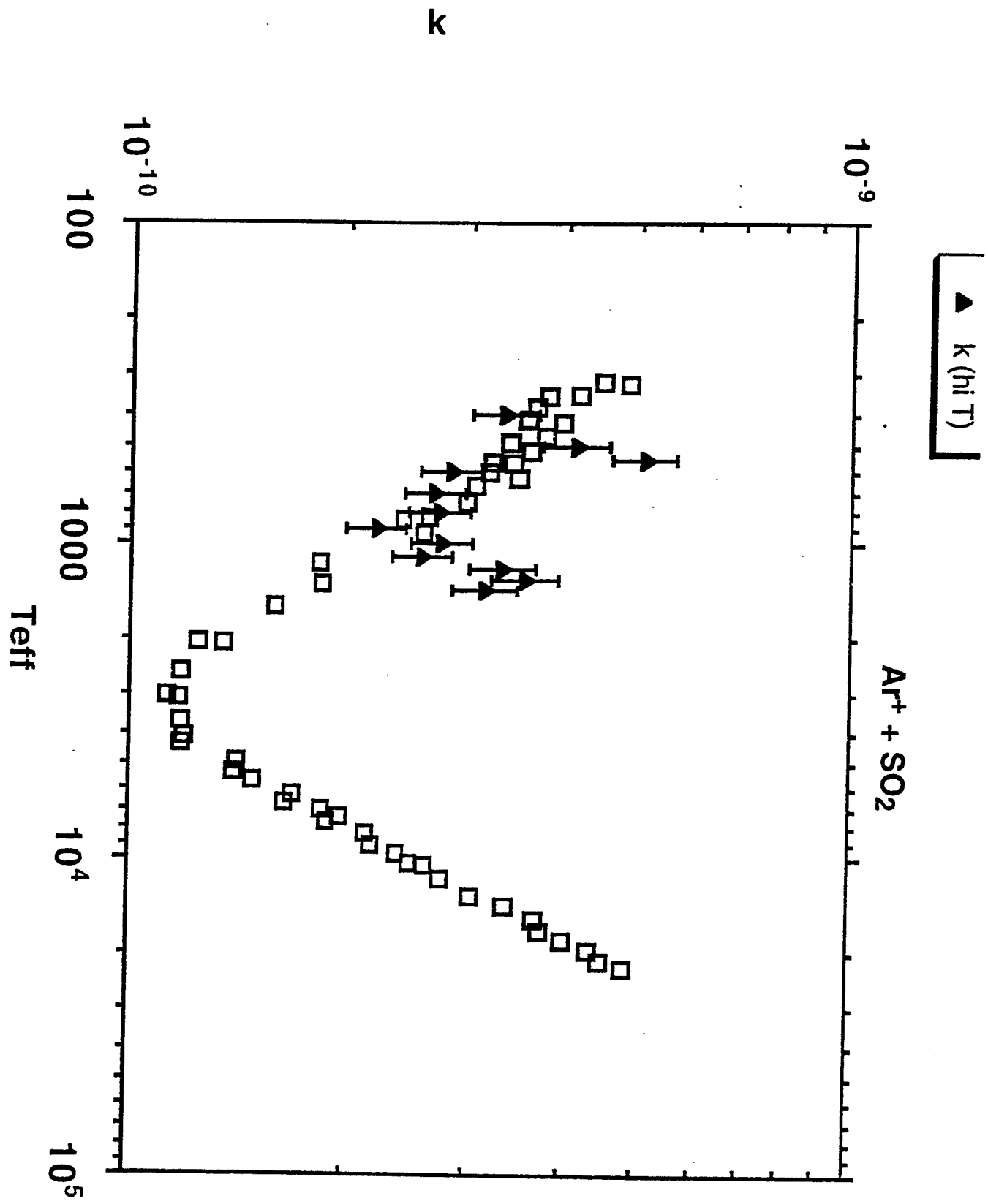
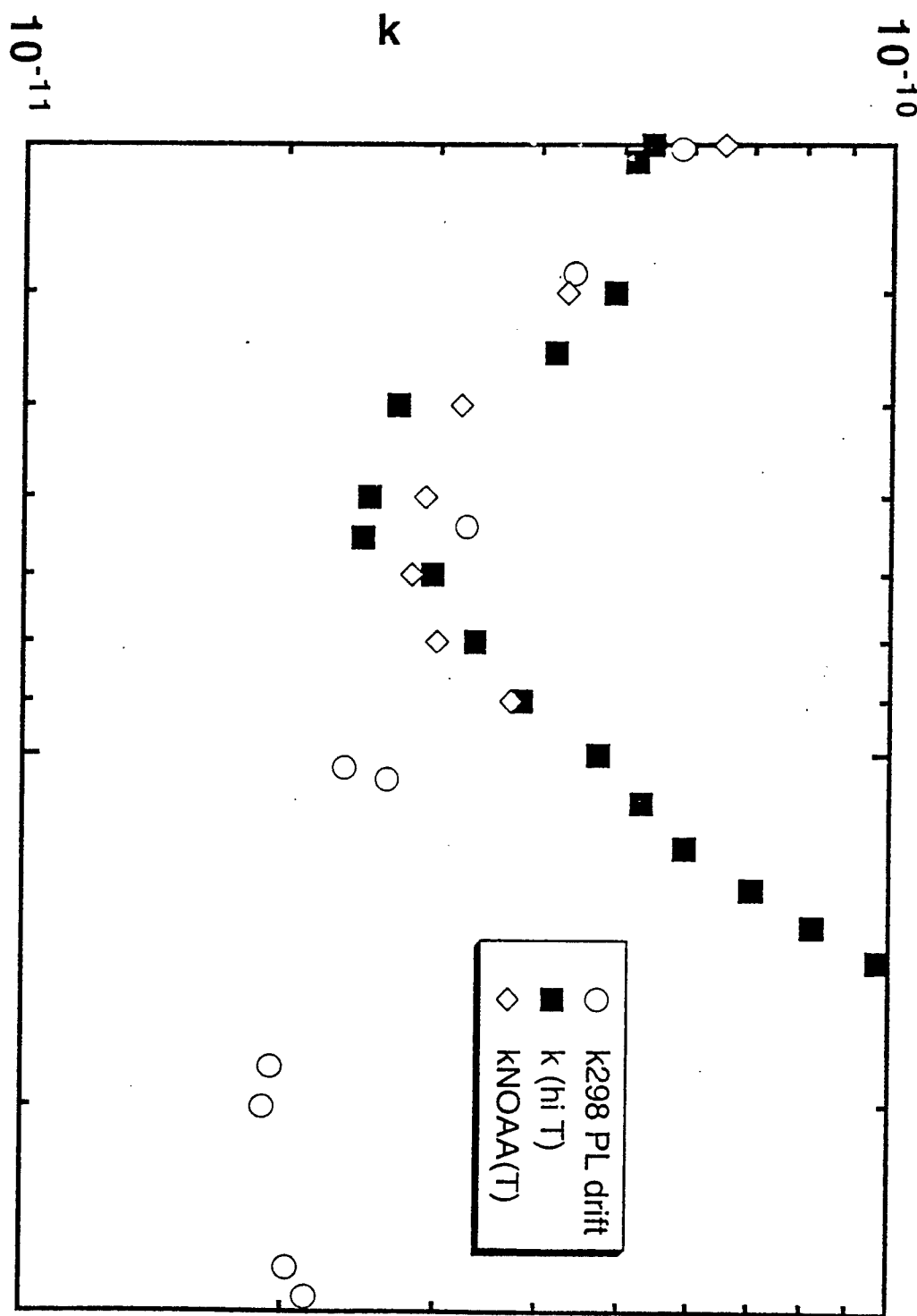
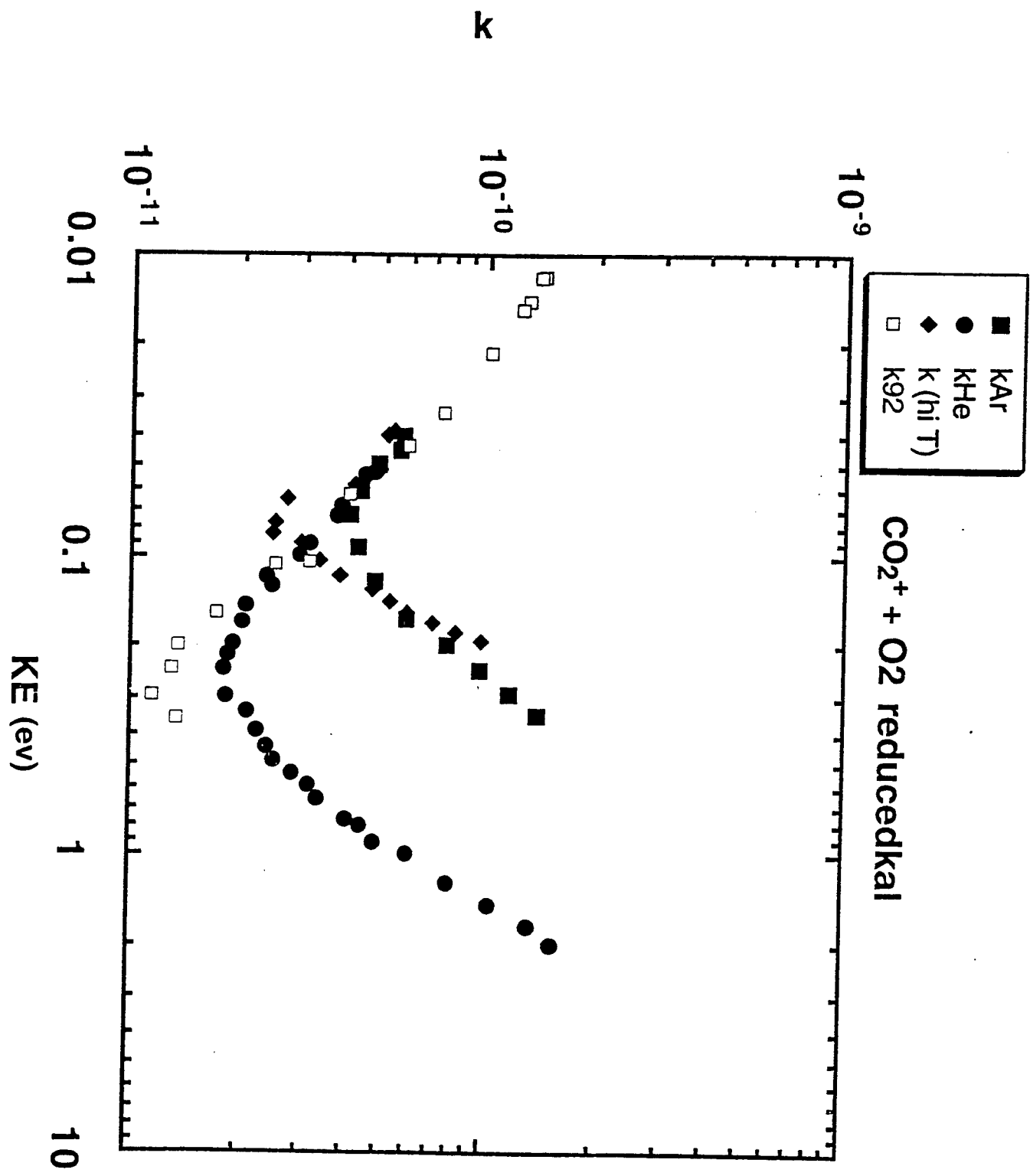


Fig 4

$\text{CO}_2^+ + \text{O}_2$ reduced k_{a1}

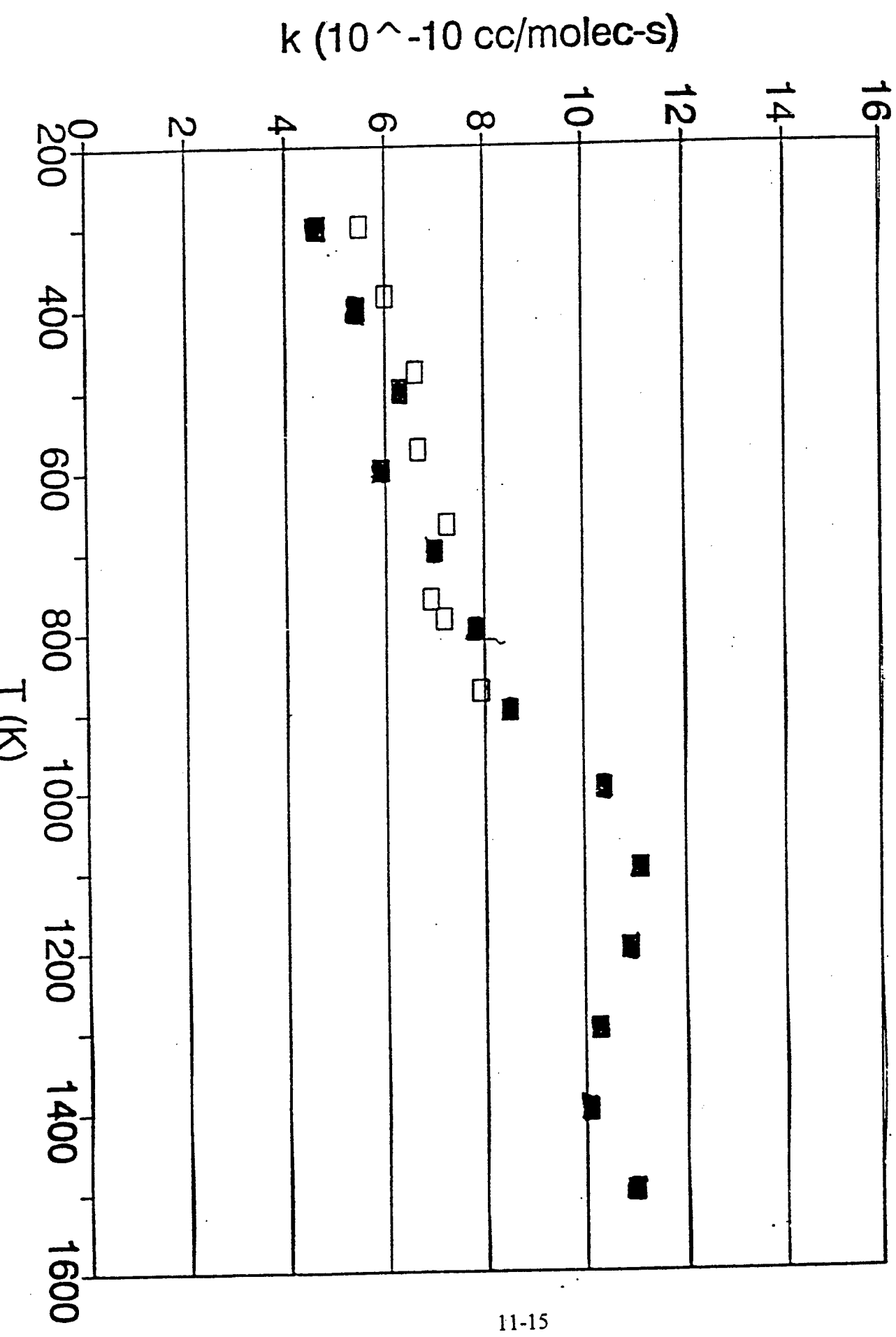




11-14

Fig 6

$N + O_2$



Determination of the Utility of the Berkeley Imaging Spatial Interferometer for Air Force
Needs and a Possible Test of the Atmospheric Frozen Screen Model of Turbulence

Jeffrey Foster Friedman
Assistant Professor
Physics Department

University of Puerto Rico
Mayaguez, P.R.

Final Report for:
Summer Research Program
Phillips Laboratory

Sponsored by:
Air Force Office of Scientific Research
Bolling Air Force Base, Washington DC

and

Phillips Laboratory

July 1995

DETERMINATION OF THE UTILITY OF THE BERKELEY IMAGING SPATIAL
INTERFEROMETER FOR AIR FORCE NEEDS
AND
A POSSIBLE TEST OF THE ATMOSPHERIC FROZEN SCREEN MODEL OF TURBULENCE

Jeffrey Foster Friedman
Assistant Professor
Department of Physics
Recinto Universitario Mayag ez
University of Puerto Rico

Abstract

We (Gary Loos*, Manfred Bester*, William Junor^+, Jeff Friedman^+) have examined the Berkeley Imaging Spatial Interferometer (ISI)¹⁻³ in terms of its light sensitivity and tracking capabilities to determine if it is adequate to acquire and track satellites that may be of interest to the Air Force. The goal is to acquire satellite interference fringes using the ISI heterodyne detection scheme at 11.1 μ m and to use these fringes when the third element of the ISI is installed to resolve images of the satellites.

In addition I have begun investigating a dual frequency laser metrology/atmospheric disturbance experiment design to determine if local atmospheric distortions are carried by the near field wind as in the frozen screen model . The utility of this determination would make it possible to place a detector down wind of an interferometer and post detection correct for some significant portion of the of the atmospheric distortion introduced into the signal . The method relies on a nonuniform change in the index of refraction of air at different frequencies with a change in temperature (and pressure).

- * Phillips Laboratory PL/LIMI
- # University of California, Berkeley
- + Rockwell Power Systems
- ^ AFOSR Summer Faculty Research Program
- | University of Puerto Rico; Mayag ez

DETERMINATION OF THE UTILITY OF THE BERKELEY IMAGING SPATIAL
INTERFEROMETER FOR AIR FORCE NEEDS
AND
A POSSIBLE TEST OF THE ATMOSPHERIC FROZEN SCREEN MODEL OF TURBULENCE

Jeffrey Foster Friedman

Introduction: The ISI:

The ISI is a 11μ interferometer with a heterodyne detection system with two (and a soon to be fabricated 3rd) 1.65 meter mirrors with variable baseline separations in the range of 5 to 100 meters ¹⁻⁸. Some time on this instrument will be made available to the interferometry group at Phillips Laboratory (PL/LIMI) if it can be shown that there is a good likelihood of detecting, tracking, and acquiring fringes on satellites of interest to the Air Force.

Detection is currently achieved with an optical camera (sensitive to about 10th magnitude) but may soon be done in the infrared directly with the addition of a new subsystem. This limits the sensitivity of the entire system but insures target acquisition and tracking. Calculations have been made by the Berkeley group " to determine the flux requirement of the ISI to acquire and track an object; and the Phillips group to determine the flux of sample earth orbiting objects from observation, scaling, and first principles. The calculations indicate that the flux of near earth objects is easily within the grasp of the ISI and any problem will lie in the tracking system; upgraded, but not tested, to near earth satellite parameters. Some details of the calculations can be found in appendix A. Black body calculations are only guesses as the temperatures and albedoes are unknown to us at this time.

Tracking is most severe for near earth satellites and so geosynchronous objects are indicated as test cases, however this introduces the problem of system sensitivity which will be discussed in some detail below. A possible compromise exists in satellites above 1000 km, but significantly closer than geosynchronous heights. The GPS system may provide ideal initial targets.

Scaling and a single example indicate that present geosynchronous objects are marginally detectable. Objects above 1000 km to approximately half geosynchronous heights are certainly within

current system capabilities. The obvious advantage to geosynchronous objects is that tracking is not an issue and long integration times are possible. The ISI, because of its 11 micron operating wavelength, does not suffer from most of the problems associated with atmospheric wavefront distortion and one can take advantage of the availability of the long integration times.

Introduction: Atmospheric Distortion:

A problem common to most, if not all, interferometers is the distortion of wavefronts introduced by light paths through the air, whether it be the atmosphere as a whole or internal to the interferometer. Much atmospheric, and all internal, distortions are caused quite locally⁶. If this local distortion can be determined then it may be possible to correct for it post detection without adaptive optics or some equivalent scheme.

I have considered an experiment to determine if some significant portion of the atmospheric distortion is actually carried by the local wind in the hope of placing a detector down-wind of an interferometer (so as not to introduce any additional turbulence) and recording local changes in the index of refraction of the air as a function of time. This can, in principle, be accomplished by recording temperature and pressure variations and applying a suitable theoretical expression; or measuring the distortion pattern directly with an interferometer with one arm in air and the other in vacuum.

The experimental scheme involves the use of two sets of two lasers (one in the UV or as blue as possible, and the other in the infrared) in two Michelson Interferometers (This can actually be accomplished with two lasers by splitting the beams twice.). The interferometers will be parallel to the ground, parallel to each other and separated by variable distances down (5 to 100 meters) and across (5-100 meters) the local wind. One arm of each interferometer will be in vacuum (as a reference) and the other in air. The dual laser configuration is to determine which variations in the signal are due to changes in the index of refraction, and which are due to actual changes in the path lengths within the interferometer. Two dual interferometers are used to actually track the disturbances down wind. A single frequency scheme is also possible if you analyze the data using correlation techniques with appropriate time delays. Time delay correlations should be used in any case.

The index of refraction of air has a nonlinear dependence on frequency and temperature (and pressure, which is not considered here) in addition to the normal frequency dependence. A uniform change in the index of refraction at all frequencies cannot be differentiated from changes in the physical pathlengths in an interferometer, but frequency dependant changes can.

The ISI:

Operating at 11 microns the ISI can take advantage of large mirrors without the worry of multiple subaperatures and atmospheric correction. Without this limitation long integration times are possible and the possibility of successfully obtaining fringes from satellites is possible. Near earth satellites are typically very bright in this context and tracking becomes the limiting factor. The ISI has recently been upgraded in its tracking capabilities to meet these critria but has not gone through field tests as yet.

Using data supplied by Robert A. Nolan of Rockwell Power Systems we calculate fluxes of several hundred to several tens of thousands (see appendix A) of janskies in the frequency range of interest for satellites from 350 to 590 kilometers above the earth's surface. Inverse square scaling of these values to approximate geosynchronous height (400 to 40000 km) implies a difference of 10000 in flux and a resultant value of a few janskies. The single example we have available for a geosynchronous satellite yields a value of about 30 janskies; in line with our simple estimate as we assume that the higher satellites are typically larger objects. Bester calculates a minimum sensitivity for the ISI of about 3 janskies for an ideal situation and more generally 28 janskies⁵. More recently (personal communication)⁶ he indicated it would be more reasonable to assume a minimum sensitivity of about 100 janskies. These values are for integration times of one hour and unit collecting area. The theoretical calculation is repeated in part in Appendix A and yields a value of $3/A \text{ Jy}$ where A is the aperture and you use an integration time of one hour. This becomes $180/(A \sqrt{t_i})$, for arbitrary integration time t_i (in seconds). For the ISI A is close to one so all of our near earth satellites are easily visible with very short integration times (0.1 - 10 seconds even in the most conservative case). Geosynchronous satellites require long

integration times but this is neither a tracking nor atmospheric distortion concern with the ISI.

Our calculations (appendix A) are of two types; the first takes the observations provided by Rockwell Power Systems and converts the spectral radiant intensities to flux in janskies using a few reasonable simplifying assumptions, the second type calculates the flux expected from small objects at similar heights from black bodies at various temperatures. We used 100, 200, 300, and 5770 K. The first three guess the actual temperature of the source, and the last is for a reflected solar spectrum. All values can be considered reasonable when you realize the size, emissivity, and albedoes of the satellites are unknown. (For this reason we only outline the blackbody calculation in appendix A.)

We conclude that an intermediate altitude object would be most suitable for initial test purposes followed by either a near earth object to test the tracking or a geostationary object to test the sensitivity. A geostationary target is acceptable for test purposes while the tracking system is inoperative as daytime observations are not precluded and essentially infinite integration time is available.

Dual Frequency Interferometry:

Even a cursory search through the literature reveals a small temperature (and pressure) dependance of the index of refraction of air, n , that is not independant of frequency. In particular the dependance is not linear and is quite exaggerated going as the inverse square of the wavelength. It is essentially zero above one micron ($1 \mu\text{m}$ or 1000 nm) in comparison to 200nm or even 400 nm . For this reason I have used a long wavelength cutoff near one micron for convienience as the results are essentially the same for 2.2, 10, and 11.1 microns. I have used 5 different formulae ⁹⁻¹¹ (listed below) from the literature for the value of n as a function of temperature and frequency to determine if the variation for small changes in temperature ($.01^\circ \text{C}$) is detectable for reasonably sized interferometers. [The analysis is essentially the same for pressure-frequency relations but is not included here. It must be considered before any application is attempted.] Some details of the calculations and exact results can be found in appendix B but a figure of $1.6 \text{ nm per meter of physical pathlength per } .01^\circ \text{C change in temperature}$ is a reasonable figure for the difference in optical pathlengths for 200nm and 1000 nm systems. This argues

for a interferometer pathlengths of order 100 meters to have a quarter wave difference in the two optical pathlengths due to a temperature change of .01 Kelvin. Typically adjacent cells will have temperature differences several times this amount. Pressure changes will also enhance the differences.

I have examined and used the following equations as a representative selection from the literature. The first and fourth are for constant temperature but the second of these (equa. 4) has different constants supplied for two other temperatures. It does not give results in good agreement with two other methods at 200 nm but is not as bad at 400 nm. The first equation was not used for any other than baseline comparisons because it's temperature dependance was not given. In all cases for this study the pressure was held constant, but it can easily be seen that it does not fundamentally alter the analysis.

- 1) $(n-1) \times 10^8 = 6432.8 + [2949810 / (146-\sigma^2)] + [25540 / (41-\sigma^2)]^9$
- 2) $(n_{Tp} - 1) = (n_{15,760} - 1) \times \{[p \times (1 + \beta_{Tp}) \times (1 + 15\alpha)] / [760 \times (1 + 760\beta_{15}) \times (1 + \alpha T)]\}^9$
- 3) $n_t - 1 = [(n_0 - 1) / (1 + \alpha T)] \times (p / 760)^9$
- 4) $(n - 1) \times 10^7 = 2726.43 + [12.288 / (\lambda^2 \times 10^{-8})] + [.3555 / (\lambda^4 \times 10^{-16})]^{10}$
- 5) $(n - 1) \times 10^6 = [287.604 + (1.6288 / \lambda^2) + (.0136 / \lambda^4)] \times (p / 1013.25) \times (1 / 1.003661 T)$
 $- [0.055 \times (760 / 1013.25) \times (e / 1.003661 T)]^{11}$

In equations 2) and 3) alpha is wavelength dependant. The betas are temperature (and pressure) dependant. The values of n at 15 degrees C and 760 mmHg in equation 2) are taken directly from the CRC, Handbook of Physic and Chemistry, which are fit by equation 4) and the n_0 values in equation 3) come from equation 1). Equation 5) was used independantly of the others.

I calculated values every 200 nm from 200 to 1400 nm for 6 temperatures; 0.0, 0.01, 15.0, 15.01, 30.0, 30.01 ° C. I then calulated the differences between the extreme frequencies (i.e. 200 and 1400 nm) at each temperature. As a last step I then took the differences between the adjacent temperature steps (i.e. 0.0 and 0.01, 15.0 and 15.01, ... ° C for these extreme frequency differences). The units are meters per meter per .01 ° C; optical pathlength difference (in meters) per meter physical pathlength per .01 ° C.

Appendix A:

From M. Bester (personal communication⁷ and 5) we have (for the ISI):

Flux $F = P/A$ where

$$\text{Power } P = (hv/\eta) \times \sqrt{[r / (\Delta v \times t)]}$$

and A is the area of the telescope

hv is the photon energy

η is the quantum efficiency (for the ISI this is equal to $\sqrt{(0.37 \times 0.30)}$)

r is the desired signal to noise ratio, 5 was assumed to be a reasonable value

Δv is the observational bandwidth, 4000 MHz for the present ISI setup

t is the integration time, initially set as 1 hour, 3600 seconds

so the Flux

$$F = (1/A) \times [(6.626 \times 10^{-34}) \times (27 \times 10^{12}) / \sqrt{(0.37 \times 0.30)}] \times \sqrt{[5 / (4 \times 10^9) \times (3600)]}$$

$$\approx (1/A) \times (3 \times 10^{-26}) \text{ watts/square meter/hertz}$$

$$\text{or } 3/A \text{ janskies (1 Jy} = 10^{-26} \text{ watts/m}^2/\text{Hz})$$

This can be made a function of integration time which yields;

$$F = (1/A) \times [(180) / \sqrt{(t)}].$$

In # the authors state that the 3 Jy should more reasonably be replaced by 28 Jy, and in a later conversation M. Bester stated that perhaps 100 Jy should be used for a reasonable safety factor. This yields;

$$F_{\text{minimum}} = (1/A) \times [(6000) / \sqrt{(t)}].$$

Satellite Data from Rockwell Power Systems, Robert A. Nolan

R.A. Nolan of Rockwell Power Systems supplied us with the observed Spectral Radiant Intensities (SRI) for four satellites through a filter of 2.76 microns width centered on 11.62 microns as follows:

Satellite	Altitude (in Km)	SRI (w/ster/μm)
F	350	906
F'	590	236
K	530	16
C	400	236

Sample calculations were made for the 4 representative satellites in the table above in the spectral band closest to that of the ISI. Converted to janskies (assuming point sources and 1 meter collecting areas) these values are approximately 65,807, 6,032, 5,07, and 13,124 from Gary Loos and recalculated with slight modifications (and insignificant changes in the results) in confirmation by the author. An approximate conversion calculation by W. Junor can be found on page 12-11 below. His rough approximate calculation gives essentially the same result.

Flux (F) = watts/meter²/hertz (janskies, Jy)

Spectral Radiant Intensity (SRI) = watts/steradian/micrometer

$$\therefore F = (SRI \times \text{steradians} \times \text{micrometers}^2) / \text{hertz}$$

For steradians we used $\pi d^2 / 4\pi D^2$ where d is the mirror diameter and D is the satellite altitude. The meters² are the telescope area; the hertz are the filter bandwidth, in hertz, and the micrometers are also the bandwidth, but this time in microns.

From W. Junor we have the following approximate calculation to convert these values to janskies:

$$\text{Flux density } S = (J \times \Omega \times \Delta\lambda) / (A \times \Delta\nu)$$

where J is the SRI above Ω is the solid angle, λ the wavelength, A the area of the collector, and $\Delta\nu$ the passband.

$c = \lambda\nu$ so $1/\lambda = \nu/c$. Taking the derivative of ν with respect to λ we get;

$$-\Delta\lambda/\lambda^2 = \Delta\nu/c \text{ so } |\Delta\lambda/\Delta\nu| = \lambda^2/c.$$

$$S \text{ (flux density)} = J \text{ (Spectral Radiant Intensity)} \times \Omega \text{ (solid angle)} \times \Delta\lambda \text{ (band width)} / A \text{ (collecting area)} \times$$

$$\Delta\sigma \text{ (pass band)} \quad c = \lambda v, \quad dv/d\lambda = -\Delta\lambda/\lambda^2 = v\Delta/c \quad |\Delta\lambda/\Delta v| = \lambda^2/c \quad S = (J \times \Omega)/A \times \lambda^2/c$$

$$\Omega \approx d^2/D^2 \quad \text{where } d \text{ is the collector diameter and } D \text{ is the distance (assuming a point source) and } A \text{ is}$$

approximately d^2 so $S \approx ([J \times (d^2/D^2)]/d^2) \times \lambda^2/c \approx (J \times \lambda^2)/(D^2 \times c)$ $J = 236 \text{ w ster}^{-1} \text{ micron}^{-1}$

$\lambda \sim 10 \mu\text{m} \quad \Delta\lambda \sim 1 \mu\text{m} \quad \text{so } S \approx [236 \times 10^6 \times 10^{-5}] / [(4 \times 10^5)^2 \times (3 \times 10^8)] \approx 2.4 \times 10^{-2} / 4.8 \times 10^{19}$

$\approx 5 \times 10^{-21} \approx 5 \times 10^{-22} \text{ W m}^{-2} \text{ Hz}^{-1} \sim 5 \times 10^4 \text{ Jy}$

Black Body Radiation:

$$B_v(T) = 2hv^3/c^2 \times 1/(e^{hv/kT} - 1)$$

$$B_\lambda(T) = 2hc^2/\lambda^5 \times 1/(e^{hc/\lambda T} - 1)$$

These were numerically evaluated over a 4000 Mhz bandpass centered on 11.1 microns at 100, 200, 300, and 5770 K.

Appendix B:

$$1) \quad (n-1) \times 10^6 = 6432.8 + [2949810 / (146-\sigma^2)] + [25540 / (41-\sigma^2)]^9$$

$$2) \quad (n_{15,760}-1) = (n_{15,760}-1) \times ([p \times (1+\beta_{15}) \times (1+15\alpha)] / [760 \times (1+760\beta_{15}) \times (1+\alpha T)])^9$$

$$3) \quad n_i - 1 = [(n_0 - 1) / (1 + \alpha T)] \times (p / 760)^9$$

$$4) \quad (n-1) \times 10^7 = 2726.43 + [12.288 / (\lambda^2 \times 10^{-8})] + [.3555 / (\lambda^4 \times 10^{-16})]^{10}$$

$$5) \quad (n-1) \times 10^6 = [287.604 + (1.6288 / \lambda^2) + (.0336 / \lambda^4)] \times (p / 1013.25) \times (1 / 1.003661 T) \\ - [0.055 \times (760 / 1013.25) \times (e / 1.003661 T)]^{11}$$

alpha						
200	400	600	800	1000	1200	1400 nm
0.003872	0.003738	0.003700	0.003685	0.003678	0.003674	0.003672

These are well fit by: $\alpha = [2.675 \lambda + 1.229 \lambda^{-1} + 33.08] \times 10^{-4}$ with the wavelength in microns.

$n_{15,760}(\lambda) \times 10^3$				
200	400	600	800	1000 nm
.3256	.2817	.2763	.2746	.2739

$$\beta_{Tp} = (1.049 - 0.015T) \times 10^{-6} \quad \beta_{15} = 0.813 \times 10^{-6}$$

From equation 2)

$\Delta\Delta 0$	$\Delta\Delta 15$	$\Delta\Delta 30$
2.016567×10^{-9}	1.810183×10^{-9}	1.633935×10^{-9}

From equation 3)

1.846245×10^{-9}	1.657293×10^{-9}	1.49593×10^{-9}
---------------------------	---------------------------	--------------------------

From equation 5)

1.598×10^{-9}	1.444×10^{-9}	1.311×10^{-9}
------------------------	------------------------	------------------------

The use of equation 4) alone with 3 sets of coefficients for the 3 temperatures did not give a good fit, compared to the other methods, at 200 nm.

Bibliography

- 1) Spears, D.L., *Infrared Physics*, 1977, 17, 5.
- 2) Danchi, W.C., Arthur, A., Fulton, R., Peck, M., Sadoulet, B., Sutton, E.C., Townes,C.H., and Weitzman, R.H., *Advanced Technology Optical Telescopes III*, 1986, SPIE 628,422.
- 3) Townes, C.H., Danchi, W.C., Sadoulet, B., and Sutton, E.C., *Advanced Technology Optical Telescopes III*, 1986, SPIE 628,422.
- 4) Danchi, W.C., Bester, M., and Townes,C.H., *High Resolution Imaging by Interferometry*, 1988, NOAO/ESO.
- 5) Bester, M., Danchi, W.C., McCullough, P.R., and Townes, C.H., 1989, *Lecture Notes in Physics*, 331, 396.
- 6) Bester, M., Danchi, W.C., Degiacomi, C.G., Greenhill, L.J., and Townes, C.H., 1992, *Ap. J.*,
- 7) Bester, M. 1995A (personal communication)
- 8) Bester, M. 1995B (personal communication)
- 9) Gray, D.E. *American Institute of Physics Handbook* 3rd Edition, 1972, (McGraw Hill, New York)
- 10) *Chemical Rubber Corporation: Handbook of Physics and Chemistry*:
- 11) Marini, J.W., Murray, C.W., Jr. 1973, *Goddard Space Flight Center*, (Greenbelt, Md.).

A STUDY OF VARIOUS HALOGEN-FREE OXIDIZERS AND OXIDIZER MIXTURES

Vincent P. Giannamore
Assistant Professor
Department of Chemistry

Xavier University of Louisiana
7325 Palmetto Street
New Orleans, LA 70125

Final Report for:
Summer Faculty Research Program
Phillips Laboratory

Sponsored by:
Air Force Office of Scientific Research
Bolling Air Force Base, DC

and

Phillips Laboratory

August, 1995

A STUDY OF VARIOUS HALOGEN-FREE OXIDIZERS AND OXIDIZER MIXTURES

Vincent P. Giannamore
Assistant Professor
Department of Chemistry
Xavier University of Louisiana

Abstract

Hydroxylammonium dinitramide (HADN) was prepared by the previously developed method. The method was reviewed and suggestions regarding the procedure have been made. The material prepared is now under study on several fronts. Five ternary mixtures of energetic, oxidizing salts were made and their thermal and impact behavior studied. Three of them appear to have properties worth pursuing, although a number of questions remain unanswered. Only preliminary work was done on hydroxylammonium nitroformate (HANF). A proposed purification method was suggested.

A STUDY OF VARIOUS HALOGEN-FREE OXIDIZERS AND OXIDIZER MIXTURES

Vincent P. Giannamore

Introduction

Environmental concerns as well as related public relations and political issues have caused the propellants community to consider the environmental impact of its activities. Issues related to environmental propellant were discussed in a paper by Hawkins and Wilkerson [1]. One of the principal areas of environmental concern is the presence of hydrogen chloride in the exhaust gases. At the present time, the total amount of hydrogen chloride released to the atmosphere in this manner is small compared to the amount from other sources. However, prudence suggests that the development of propellant options that avoid any such emission be pursued. In addition, replacement of chlorine-containing oxidizers may also help minimize the signature caused by propellant exhaust. Accordingly, the search for new high energy oxidizers to replace chlorine-containing compounds such as ammonium perchlorate (AP) has been an area of much activity in recent years. The compound that has generated the widest interest in this area is probably ammonium dinitramide (ADN) [2, 3]. Hydroxylammonium nitrate (HAN) is another compound under investigation. Last year, we [4] reported on an investigation of a compound related to both ADN and HAN: hydroxylammonium dinitramide (HADN). This report details continuing studies on HADN as well as work with other halogen-free oxidizers and oxidizer mixtures..

Discussion of Problem

Six objectives were set at the beginning of this work. Three of these involved HADN:

1. Review the synthesis developed last year for HADN. When the procedure was scaled-up to the 20 g scale, a precipitate had appeared which had not been detected at lower scales.

2. Prepare 40 g of HADN using the method developed last year. The purpose was to provide material for further study. This included demonstration of its purity by ion chromatography (IC) by Milton McKay.
3. Determine if HADN can be produced by a more direct route.

Two of the objectives involved hydroxylammonium nitroformate (HANF):

4. Produce and determine the purity and stability of HANF. This was to include differential scanning calorimetry (DSC), density, FTIR, IC, and pK_A studies.
5. Determine if a low melting mixture of HANF and hydrazinium nitroformate (HNF) analogous to that of HAN and hydrazinium nitrate (HN) can be made. Discover whether a diluent such as water is necessary to lower the melting point to a desirable range.
6. Prepare five ternary mixtures of oxidizers predicted to be low melting eutectics and study some of their properties.

Methodology

Objective 1 was partly met by discussions with coworkers and partly by synthesis of HADN. Objective 2 was met by employing the ion exchange method for preparation of HADN developed last year. The standard procedure was as follows.

1. Column preparation. The column was cleaned with methanol and deionized water. If needed, a glass wool plug could be inserted. However, the standard columns with built-in frits did not appear to require this plug so it was omitted in all of the preparations described below. It is recommended that it be omitted unless absolutely necessary since it could introduce contaminants into the reaction medium. After the final rinse with deionized water, approximately 10 to 25 mL of deionized water was left in the column. An amount of Dowex 50 x 8-100 (50Wx 8) resin, strong acid (H^+) form, at least equal to 7.1459 times the mass of ADN to be used in the procedure was weighed out. This resin was hydrated by allowing it to stand covered with deionized water for at least one half-hour. The slurry of resin was then added to the column. Excess water was drained from the column, taking care to keep the water level above the top of

the resin bed. The resin was then rinsed by eluting 100 mL of deionized water through the column. As soon as the water level reached the top of the resin bed, 100 mL of methanol was added to the column. The methanol was allowed to elute through the column until its level was just above the top of the resin bed. The column was then ready for use. In the event it was not to be used immediately, a stopper was placed on the column to prevent evaporation of the methanol.

2. Reaction. The following procedures were carried out in low light conditions due to the reported sensitivity of ADN and, possibly, HADN to fluorescent light. ADN was weighed and dissolved in methanol. For amounts of ADN up to 10 g, 100 mL of methanol has proven to be a sufficient volume of solvent. Stirring is required to dissolve all of the ADN. Hydroxylamine was then weighed. This was used as an aqueous solution of the free base. This solution is nominally 50% hydroxylamine. Based on that percentage, the mass of hydroxylamine solution necessary to provide a 1:1 mole ratio of hydroxylamine to ADN is 0.5325 times the mass of ADN. However, it was reported by Milton McKay[5] that an actual analysis of our supply had shown the solution to be only 48% hydroxylamine. In that case, the mass of the solution necessary for a 1:1 mole ratio with ADN is 0.5547 time the mass of ADN. A slight excess of hydroxylamine was used. The hydroxylamine solution was then dissolved in 50 to 100 mL of methanol. The methanol in the column was drained to the top of the resin bed and the ADN solution added immediately. The hydroxylamine solution was placed under the column and stirred magnetically. The column was eluted into the stirred hydroxylamine solution at a dropwise rate. When the ADN solution reached the top of the resin bed, 100 mL of methanol was immediately added to the column. Elution was continued until the methanol level was just above the resin bed. The rate of elution should be dropwise but not too slow during the elution of the ADN solution and the first part of the methanol rinse. The latter portions of the methanol rinse can be done at a faster rate. After elution is completed, the reaction mixture was stirred for at least one half-hour longer. If work-up could not follow immediately, the mixture was stored in a freezer, protected from heat and light until it could be worked up.

3. Work-up. This procedure was developed to minimize the exposure of the HADN to heat. Both exposure to higher temperatures and extended heating at lower temperatures had been found earlier to lead to darkening of the product and to gassing, either immediately or after a shorter storage time than samples not exposed to as much heating. The reaction mixture, or a portion of it, was transferred to a 500-mL round-bottomed flask and placed on a rotary evaporator at 30 °C at the reduced pressure provided by the laboratory vacuum line.. Most of the methanol was stripped in this way. After each portion was stripped of most of its methanol, the residue was transferred to a 50-mL pear-shaped flask. The residues from all portions were combined in the same flask using minimum amounts of methanol to effect the transfer. It had been discovered previously that the residues of each individual portion needed to be removed before adding the next portion. When this was not done, prolonged exposure of the early portions to even this relatively low temperature resulted in a product that was darker and had a shorter shelf life than products obtained by the method described. The residues which had been combined in the 50-mL flask were then placed on the rotary evaporator at reduced pressure again. This time the temperature was raised to 60 °C to remove as much of the water as possible as well as residual methanol. Any free, unreacted hydroxylamine should also be removed by the rotary evaporation. The second evaporation was generally continued for about 2 hours. The product was weighed and analyzed for its water content by Karl Fischer titration using an automatic titrator. If the water content proved too high, the mixture could be returned to the rotary evaporator for further work-up. This was avoided whenever possible, however, to avoid exposing the product to too much heat and because Karl Fischer analysis of the same HADN sample often showed considerable scatter in successive runs of the titrator. The product was stored in the freezer and protected from light until use.

Objective 3 was abandoned for reasons discussed below. The only experiments done in this phase were to study the effects of strong and weak acid resins on the pH of the hydroxylamine solution. The pH of the solution was measured. Then the resin was added, stirred, and the solution decanted. The pH of the solution was measured again. The solution was then returned to the resin and the mixture was allowed to

stand for one hour before the pH measured again. This experiment was done with both the strong acid resin used in the HADN preparation described above and with the weak acid resin Duolite C-464 (8 meq/g). The pH of the hydroxylamine was not significantly reduced in any measurement. Objectives 4 and 5 involving HANF were not accomplished due to the shortening of the planned research period. Some HANF had previously been made by Adam Brand[6]. An attempt was made to produce some more HANF for study using the following method similar to his. An aqueous nitroform solution consisting of 32.3 % nitroform was used. The mass used was 24.889 g of solution or 8.0391 g (0.053224 mole) of nitroform. To this stirred solution was added 3.757 g of the 48% hydroxylamine free base solution (1.803 g hydroxylamine, 0.05459 mole). The reaction mixture was stirred for about 45 minutes and then transferred to the rotary evaporator where it was kept at room temperature at the reduced pressure delivered by the laboratory vacuum line for just over 12 hours. Adam Brand had reported that solid HANF had begun dropping out of solution in less than a day. However, no solid was observed in this case and the solution began to gas upon standing. Possibly, the failure to observe any solid in this case was due to the presence of much more water at this scale. However, no time remained to pursue the investigation any further.

Objective 6 was pursued by preparing the mixtures involved and studying their behavior by DSC and in the case of the solids also by observing their behavior when heated in a Thomas-Hoover melting point apparatus. Drop-weight impact sensitivity measurements of each mixture were also obtained.

Preparation of the mixtures was accomplished by weighing the requisite amount of each component of the mixture, dissolving it in methanol, and combining the methanol solutions. In the case of hydrazinium nitrate, complete dissolution in methanol was not achieved, but it was possible to mix the solid with the methanol solutions of the other components. The methanol was then stripped from the mixtures on a rotary evaporator leaving the desired mixture behind as a residue.

DSC analysis was performed on DuPont DSCs. A dual sample instrument was used for some analyses. For others, a single sample instrument fitted with a liquid nitrogen cooling accessory was employed. All

analyses were performed using hermetically sealed pans in a gaseous nitrogen atmosphere. Both aluminum and polymer coated pans were used. Relevant details concerning particular runs are given in the results section.

Impact testing was done by Scott Strader on the drop-weight tester at Area I-30, Phillips Laboratory, Edwards AFB.

Results

Between the time when the objectives were set for this work and the start of the work, Milton McKay[5] discovered that eluting the column at a faster rate eliminated the presence of the precipitate. This is in agreement with the procedure as it was developed last year. The elution of the ADN and washing with methanol can require a full day if the rate is too slow. The procedure should take about one to two hours. Certainly, if it takes three hours or more, it is too slow. Obviously, the longer the procedure takes, the more chance there is for impurities to appear. These could result from the resin, the glass wool, or other material the solvent encounters. They could also be formed in some unknown side reaction. Since the precipitate had been eliminated no attempt was made to identify it. If it should reappear on further scale-up, it would have to be identified. It is also suggested that an optimum rate for elution be identified. The fastest rate consistent with formation of the product in high yield should be employed. It is also recommended that careful attention be given to work-up procedures since the HADN proved sensitive to this last year. (See methodology section of this report.)

In pursuit of objectives 1 and 2, five syntheses were performed, using the procedure discussed in the methodology section. The results are summarized in the table below.

Run	Mass of ADN Used	Moles of ADN used	Mass of HA Solution Used	Moles of Hydroxylamine Used ¹	Mass of Product Obtained	Percentage Yield of Product ²
1	8.857 g	0.07139	4.794 g	0.06966	9.104 g	93%
2	10.022 g	0.080783	5.441 g	0.07907	10.801 g	98%
3	10.033 g	0.080872	5.387 g	0.07829	10.529 g	96%
4	10.035 g	0.080888	5.384 g	0.07824	10.834 g	99%
5	10.032 g	0.080864	5.589 g	0.08122	10.165 g	90%

1. Only the last run in this table was done using excess hydroxylamine as specified in the standard

procedure in the methodology section. This was due to the fact that the hydroxylamine solution was believed to be 50% when the first four experiments were performed. Later, it was learned that actual analysis had shown it to be 48%. Thus, the amounts used were less than originally believed.

2. These percentage yields do not take into account the percentage water in the samples. This was generally in the 1 - 2% range according to the Karl Fischer titrations.

A total of 51.433 g of HADN was prepared. As noted, this HADN contains water and is liquid at room temperature. While the amount of water in it is determined by Karl Fischer titration immediately after the product is isolated, the amount of water in the sample at any given time is uncertain. Experience in working with this material has shown that it rapidly gains water when exposed to air. Preliminary information from a coworker [7] doing thermal stability studies suggests that water may be associated with the HADN in more than one way. This is still under study.

The HADN prepared in this work has been used in several ways. A portion of it was used in preparing the oxidizer mixtures discussed below. The rest of it was made available to coworkers for thermal stability studies, ion chromatography, and preparation of propellant mixes for various tests.

Objective 3 had been to prepare HADN by a more direct route. After the preliminary work described in the methodology section, we decided not to pursue this objective. Reportedly, another group had prepared HADN by a water-free route. However, this has yet to be confirmed. We decided to postpone further work in that area until more is known about their results.

The proposed work with HANF (objectives 4 and 5) had to be abandoned due to the shortening of the research period. One attempt was made to prepare HANF. However, no solid was isolated from the reaction mixture. This may have been due to the amount of water present at the scale used. HANF is very heat sensitive, gassing when heated only slightly above room temperature or when kept at room temperature for only one or two days. Therefore, if the reason for the solid not forming is the length of time required for removing so much water by rotary evaporation at room temperature, then another method needs to be found for water removal if HANF is to be produced on a reasonable scale.

The five mixtures prepared and studied for objective 6 had been predicted to be low melting eutectics by Block-Bolten, Olson, and Hawkins [8] using theoretical methods. Five ternary mixtures were selected for study. Their compositions are given in the following table.

Mixture	Predicted M.P.	Component 1	Component 2	Component 3
A	242.8 K	11.6% ADN	3.1% HN	85.3% HADN
B	236.0 K	8.5% AN ¹	9.4% ADN	82.1% HADN
C	300.8 K	28.1% AN ¹	40.6% ADN	31.3% HNF
D	287.4 K	19.6% AN ¹	21.0% HN	59.4% HAN
E	302.8 K	29.1% AN ¹	37.5% HN	33.4% HNF

1. AN is ammonium nitrate.

Mixtures A and B were clear, straw-colored liquids. Mixture D was a faintly pink colored liquid.

Mixtures C and E were both bright yellow solids. Mixtures C and E were mixed with water to determine if they could be liquefied. While small amounts of both dissolved in the water, they could not be liquefied. Mixture C with 20% water remained solid. Mixture E was still solid with 10% water. All of the liquid mixtures (A, B, and D) contained some water, since the HADN and S-HAN-5 used to prepare them contained 1 - 2% water. The presence of this water and the rapid uptake of water by HADN when exposed to air makes it difficult to determine the exact composition of the mixtures.

Samples of the two solid mixtures (C and E) were placed in melting point capillaries and heated in a Thomas-Hoover melting point apparatus where their behavior could be observed visually. No clear and distinct melt was observed for either mixture. Mixture C remained solid until well over 373 K. It rapidly decomposed with vigorous production of a gas. No liquid was observed. More precise details on the decomposition temperature are available from the DSC. Mixture E did appear to soften and partially melt in the range from 310 to 324 K. It then remained a mixture of a yellow solid and amber liquid until it vigorously decomposed with evolution of gas at well over 373 K. Again more precise information on the decomposition is available from DSC data.

Impact sensitivity tests were run on all five mixtures. Mixtures C, D, and E proved insensitive. C and E gave negative results up to 160 Kg-cm. D was tested and proved negative as high as 120 Kg-cm. These results are surprising in view of the presence of ADN and HNF in C and of HNF in E. By contrast, mixtures A and B were very sensitive. Mixture A gave positive results as low as 4 Kg-cm. It was negative at 3.5 Kg-cm. Mixture B gave positive results at 6 Kg-cm with negative tests at 5.5 Kg-cm. From these results, it appears that the mixtures that contain HADN are much more impact-sensitive than the others.

DSC thermograms of mixture A were obtained using three different methods. In the initial run, a sample of A was placed in an aluminum pan and the pan placed in the DSC cell. The cell was then cooled to below -75 °C with liquid nitrogen. The coolant was removed, and the sample was heated at a rate of 10 °C/minute to 200 °C. No melt was observed. The baseline appeared flat until an exotherm that began at 137.95 °C and peaked at 155.75 °C. When the cell was opened, it was discovered that the pans had blown apart.

In the second run, the sample was placed in polymer-coated pans and pre-cooled in liquid nitrogen for at least 4 hours. The pans were then transferred to a DSC cell that had been precooled to -150 °C. The sample was heated at the same rate as previously. The baseline was not as flat as in the previous run, but the only clear feature was an exotherm beginning at 132.14 °C and peaking at 160.71 °C. The section of

the thermogram from -125 °C to +125 °C was expanded to observe effects dwarfed by the large exotherm. The expansion revealed the presence of what appeared to be two glass transitions: one from -114.50 °C to -112.37 °C and the second from -78.49 °C to -74.45 °C. There were also three small endotherms around 0 °C, which may have been due to water in the sample or a consequence of the cooling of the cell with liquid nitrogen or both. Still, no melt was observed. The endotherms observed in the first two thermograms were at similar temperatures to one observed for HADN. That endotherm began at 146.60 °C and peaked at 158.87 °C. The HADN exotherm had a heat flow in W/g that was two to three times larger than those in the mixtures, however.

The next approach was based on the presence of the glass transitions reported above. It was believed that the reason no melt was observed might be because too rapid cooling to too low a temperature prevented crystallization. It was decided to try keeping the sample at a temperature between the glass transition and the theoretical melting point (-30.4 °C) because this is said to be the optimum range for crystallization. It was also decided to cool the sample slowly to this range. The sample was placed in polymer-coated plans in a DSC cell fitted with a cooling accessory. It was cooled at a rate of 5°C per minute to -50 °C and held at that temperature for two hours. After two hours, it was heated at the same rate to 80 °C. No melt was observed. There were artifacts present at the lower end of the cooling cycle and the upper end of the heating cycle. When a second run was made under identical conditions except that the temperature range was extended by ten degrees in each direction, the artifacts moved by a corresponding amount.

DSC thermograms were obtained of mixture B using the same procedures described for the first two analyses of mixture A. Results were also similar. In the first run, where the pans were cooled to below -75 °C on the DSC and then heated, the only feature on the thermogram was an exotherm beginning at 147.21 °C and peaking at 154.58 °C. The pans blew apart. In the second run, in which the pans were precooled in liquid nitrogen, a large exotherm was observed in the same region. There was a much smaller exotherm beginning at 97.66 °C and peaking at 104.69 °C. Expansion of the region before the major exotherm again revealed a glass transition from -80.54 °C to -76.50 °C. The sample was not cooled

to a low enough temperature to observe if there was another glass transition as there was in A. There was also an endotherm at 0 °C, which was much larger than the three in the DSC of A. This appeared as single “peak” which appeared to be a combination of two or more unresolved “peaks.” However, no endotherm was observed in the area of the theoretical melting point which was -37.2 °C.

Two DSC thermograms were also obtained for mixture C. Since C was a solid, it was not believed that any cooling would be necessary. The sample was placed in the cell in aluminum pans and heated at 10 °C per minute to 200 °C. It showed a flat baseline until 126.22 °C. At that point it began to rise at first slowly and then more rapidly to an exothermic peak at 165.19 °C. This did not return completely to the baseline, but rose again to a broad peak at about 180 °C. This was much less exothermic than the first peak. The trace was again showing an exothermic rise at the cut off temperature.

The second run on C was similar in method to the first runs on A and B. The sample was placed in the DSC cell and the cell cooled to below -75 °C before being heated at 10 °C per minute to 200 °C. The baseline was much more wobbly than in the first run, but expansion did not show any clear features. There was a large exotherm that peaked at 195.98 °C. This began as at 139.73 °C and had a shoulder at 155.80 °C. The reason for the differences in the exotherms in runs 1 and 2 is unknown. The ADN used in preparing C shows an exotherm peaking at 195.70 °C. None of the components have exotherms similar to the other exotherm in C. AN has no exotherms anywhere in the observed range and HNF showed just one exotherm in this range. It peaked at 134.11 °C. No definite endotherms were observed were observed on either thermogram of mixture C.

One DSC thermogram was obtained for mixture D. It was done using the same method as the first runs on A and B and the second run on C. The thermogram showed an extremely flat baseline from below -50 °C until 170.54 °C. At that point it began to rise slowly. At 189.56 °C, it began to rise rapidly, peaking at 195.09 °C. This is a bit higher than the exotherm displayed by S-HAN-5 under the same conditions (peak at 186.50 °C). Neither AN nor HN show any exotherms in the region under study. No melt was evident in the DSC.

Two DSC thermograms of mixture E were obtained. The same methods used for C were employed. The DSC run without cooling showed an exotherm peaking at 173.48 °C. The DSC in which the sample was cooled showed one peaking at 175.22 °C. There was a second exotherm in the non-cooled sample's DSC at 189.55 °C. In the cooled run there was a shoulder at approximately the same location. The second peak was more exothermic than the first in the non-cooled run. In the cooled run the first exotherm was stronger than the second. This is exactly opposite to the order observed in C.

Two endotherms were observed in the DSC of the cooled sample of E. One of these began at -27.01 °C and reached a minimum at -20.98 °C. The other began about 20 °C and reached its minimum at 43.97 °C. The first of these endotherms was below the range of the thermogram run on the non-cooled sample. There is an endotherm in that DSC that appears to be in progress as the trace is started at about 28 °C. It reaches a minimum at 40.89 °C. Presumably, this is the same endotherm as the second one observed for the cooled sample. It is probably the partial melt observed in the melting point apparatus reported above. The exotherms reported for E do not correspond to exotherms in the DSC of any of its components. AN and HN do not have any exotherms in the region and the only exotherm below 200 °C in the DSC of HNF appears at 134.11 °C. AN does have an endotherm at 55.76 °C in a DSC run under the same conditions as the non-cooled sample of E. However, that endotherm in AN is not a melt.

Finally, it should be noted that the exotherms in the liquid samples (A, B, and E) are much stronger than those in the solids.

Conclusion

Objective 1 was to review the HADN synthesis developed last year. The problem of the precipitate that had appeared upon scale-up had apparently been solved prior to this work. Some suggestions regarding the procedure have been made in the methodology and results sections of this report.

Objective 2 had been to synthesize 40 g of HADN for further studies. More than 50 g of the compound were prepared and supplied to those doing these studies.

Objective 3 was to determine if HADN could be prepared by a more direct route. This objective was abandoned, at least temporarily. However, it does appear that anhydrous HADN would be desirable. As noted, the presence of water in the current HADN causes certain problems. It is difficult to determine exactly how much water is present and in what way it is associated with the HADN. Comparison with the anhydrous material and preparation of samples with known amounts of water from the anhydrous material might prove useful in investigating these matters. On the other hand, the present material is probably more desirable to work with than the anhydrous HADN, since that material is believed to be solid.

Objectives 4 and 5 involving HANF were not completed. Therefore, there is still considerable work that could be done in this area. Reportedly, the HANF that was made by Adam Brand [6] appeared to sublime in a vacuum oven at room temperature. This suggests that vacuum sublimation may be a desirable purification method. A discussion of this procedure and the construction of appropriate apparatus from ordinary laboratory equipment can be found in a laboratory text by Williamson [9]. Trial of the procedure using this apparatus might be done before purchasing specialized glassware.

Objective 6 was the preparation and study of the ternary oxidizer mixtures. The mixtures were prepared and three of them were liquids at room temperature as predicted. None of them appeared to have the predicted melting point and for four of them we were not able to show any melting behavior at all. On the other hand the mixtures appeared to have different thermal properties than their individual components. Because of water in the HADN and HAN samples and possible stabilizer in the HAN, the composition of

the mixtures was not exactly as specified. It would still seem that some melting behavior should have been observed. On the positive side, three mixtures of energetic oxidizers were prepared and found to be liquid at room temperature and, apparently, at considerably colder temperatures. Although the two of them with HADN are impact sensitive, all three may be worth further study. The unusual insensitivity to impact of the mixtures C and E, despite the presence of ADN and HNF may be worth exploring, although the fact that they were not liquid at low temperatures is undesirable. The presence of apparent glass transitions in mixtures A and B is intriguing and may mean that polymer-like associations exist in the mixtures at low temperature.

References

1. Hawkins, T.W. and Wilkerson, B.E., Environmental Propellant: Current Issues and Assessment, JANNAF Propulsion Meeting, 1992.
2. Borman, S., "Advanced Energetic Materials Emerge for Military and Space Applications", *Chemical & Engineering News*, January 17, 1994, p. 18.
3. Rossi, M.J., Bottaro, J.C., and McMillen, D.F., *International Journal of Chemical Kinetics*, **25**, 549 (1993).
4. Giannamore, V.P., An Investigation of Hydroxylammomium Dinitramide: Synthesis, Stability, and Compatibility, Final Report for AFOSR Summer Faculty Research Program, Phillips Laboratory, 1994.
5. McKay, Milton, personal communication.
6. Brand, Adam, personal communication.
7. Ismail, Ismail K, personal communication.
8. Block-Bolten, A., Olson, D., and Hawkins, T., Thermodynamic Properties of Advanced Oxidizer Mixtures for Solid Propellants, JANNAF Propellant Development and Characterization Subcommittee Meeting, April, 1995.
9. Williamson, K.W., *Macroscale and Microscale Organic Experiments*, 2nd ed. D.C. Heath and Company, Lexington, MA, 1994.

A CLOSED-CYCLE CW PHOTOLYTIC IODINE LASER USING t-C₄F₉I

John A. Guthrie
Assistant Professor
Department of Physics

University of Central Oklahoma
100 North University Drive
Edmond, OK 73034

Final Report for
Summer Faculty Research Program
Phillips Laboratory

Sponsored by
Air Force Office of Scientific Research
Bolling Air Force Base, DC

and

Phillips Laboratory

September 1995

A CLOSED-CYCLE CW PHOTOLYTIC IODINE LASER USING t-C₄F₉I

John A. Guthrie
Assistant Professor
Department of Physics
University of Central Oklahoma

Abstract

Perfluoro-t-butyl iodide, t-C₄F₉I, offers at least three potential advantages as a replacement perfluoroalkyl iodide for many of those currently in use in photolytic iodine lasers, such as normal and iso-C₃F₇I. First, the perfluoro-t-butyl radical displays a large overall recombination rate with atomic iodine relative to other alkyl iodides; this property limits production of the contaminant I₂ in the laser medium. Second, the ultraviolet absorption peak of t-C₄F₉I is shifted about 16 nm to the red of that for the more common perfluoroalkyl iodides, such as n-C₃F₇I; this feature offers the prospect of much greater efficiency in absorption of radiation from the excitation lamp. Finally, because t-C₄F₉I has a lower vapor pressure than most other perfluoro compounds used in photolytic iodine lasers (PIL's), there exists the possibility of designing a laser system for which the laser gas requires no condensation/evaporation scheme in order to promote flow of the gas; elimination of this complicated flow mechanism will yield much more efficient and physically compact PIL's.

A closed-cycle continuous-wave (CW) photolytic iodine laser using t-C₄F₉I has been built and operated for the first time as a result of this work. The t-C₄F₉I gas, at pressures near 17 torr, was flowed transversely to the laser beam axis using a turbomolecular blower. A microwave-excited mercury lamp was the laser pump source. The laser demonstrated a maximum multimode output of 2.9 W which corresponded to about 0.6% conversion efficiency of the pumping radiation. During operation the system displayed a monotonically decreasing output power with time due to the continuous production of molecular iodine, which quenched the upper state of the laser transition. Further work will center on development of improved methods to minimize production of molecular iodine, and to remove it efficiently from the iodide gas stream. Success in these efforts will make lasers based on t-C₄F₉I viable alternatives for those currently based on normal or iso-C₃F₇I.

A CLOSED-CYCLE CW PHOTOLYTIC IODINE LASER USING t-C₄F₉I

John A. Guthrie

1. Introduction

Since its discovery in 1964 by Kasper and Pimentel,¹ the photolytic iodine laser (PIL) has undergone continuous development and improvement. Among the potential advantages of this laser are its wavelength (1.315 μm) in an atmospheric absorption window, high power output, extended coherence length, and excellent beam quality. PIL's can be operated either in a continuous-wave (CW) or pulsed mode. Extremely high energy, temporally short pulses can be generated from PIL's for application to inertial confinement fusion.²⁻⁸ Research has also been undertaken to explore the possibility of power transfer in space using PIL's.⁹⁻¹⁶ Continuous development of both pulsed and CW PIL's for other applications has been ongoing for three decades, including extensive work at the Air Force Phillips Laboratory.¹⁷⁻²⁵ Current systems, however, are physically large and their overall efficiency is poor. In particular, the Air Force is interested in developing smaller, more efficient PIL's for use as illuminators for large-scale chemical oxygen-iodine lasers (COIL's).

The technology of CW PIL's lags that of pulsed devices because of stringent requirements on maintenance of laser medium purity. Many CW systems involve the flow of the laser iodide "fuel", from one vessel to another through the laser cavity, and may be classified as "open-cycle" or "blowdown" systems.⁹⁻¹⁵ The flow is produced by a pressure gradient due to the temperature difference of the two vessels. After the fuel has been transferred to the receiving vessel, it must then be transferred back to the original vessel for repeated lasing "runs". Such a system is inherently limited in its utility. Closed-cycle laser systems, both pulsed and CW, have

also been developed, primarily at the Phillips Laboratory.²¹⁻²⁵ These systems have typically produced flow of the alkyl iodide fuel (usually C₃F₇I) by an evaporation/condensation scheme. The flow is again due to the temperature difference between two reservoirs; however, the condensation and evaporation vessels are connected so that the iodide is continuously (and passively) circulated. This technique has the advantage of involving no moving parts, and has shown remarkable success. However, it has the disadvantage of requiring that the two reservoirs be maintained at temperatures near -20 C and -50 C, respectively. Two bulky recirculating coolers are necessary to maintain these temperatures, and they consume substantial electrical power.

There exists considerable evidence that perfluoro-t-butyl iodide, t-C₄F₉I, has superior chemical and physical properties as a laser medium for PIL's compared to the more commonly used heptafluoropropyl iodides, n-C₃F₇I and i-C₃F₇I.^{9,11,12,15,26-28} First, the perfluoro-t-butyl radicals are very slow to combine to form C₈F₁₈,²⁷ this property promotes the recombination of the radical and atomic iodine to give the parent iodide. Perhaps more importantly, the same property inhibits the production of the contaminant I₂ in the laser medium. Second, the ultraviolet absorption peak of t-C₄F₉I is shifted about 16 nm to the red of that for iodides such as n-C₃F₇I.¹⁵ Since most ultraviolet excitation lamps offer higher output powers at longer wavelengths, this characteristic offers the prospect of much greater efficiency in absorption of radiation from the lamp. Finally, because t-C₄F₉I has a lower vapor pressure than most other iodides,¹⁰ there exists the possibility of designing a laser system for which the laser gas is flowed entirely by a mechanical means. This flow mechanism would replace the complicated scheme currently in use which requires repeated condensation and evaporation of the laser fuel.

Elimination of this requirement will yield much more efficient, lightweight, and physically compact PIL's.

Open-cycle, ("blowdown") laser systems using t-C₄F₉I have been built and improved over the past two decades, with most of the work done at the NASA Langley Research Center.^{9,11,12,15,26} However, there has thus far been no demonstration of a closed-cycle system based on t-C₄F₉I. This document reports the first demonstration of such a system. Section 2 discusses the basic chemistry of PIL's employing t-C₄F₉I. Section 3 includes a discussion of the experimental apparatus and procedures, and Section 4 provides a preliminary report of the laser's performance. Section 5 summarizes this work and discusses necessary future work to improve performance.

2. Essential chemistry of photolytic iodine lasers using t-C₄F₉I

Major considerations in the design of moderate-power PIL's have been summarized in previous publications by the group at the Phillips Laboratory.²¹⁻²⁵ The upper state of the laser transition in PIL's is populated by ultraviolet photolysis of an iodide precursor, perfluoro-t-butyl iodide (t-C₄F₉I) in this work. Photolysis is typically produced by either pulsed or continuous ultraviolet lamp irradiation; the peak of the t-C₄F₉I absorption lies at 288 nm.^{26,29} Products of the photolysis in this work are the radical t-C₄F₉[·] and electronically excited atomic iodine, I(5²P_{1/2}), hereafter designated as I*. The laser transition is from the 5²P_{1/2} level to the 5²P_{3/2} level. The transition is dipole-forbidden, and the upper state has an intrinsic lifetime of about 130 ms.³⁰ However, the effective upper state lifetime, and the efficiency of the laser, are governed by quenching reactions. Rate coefficients and other parameters for the most important physical

processes in the laser are summarized in Table 1. Molecular oxygen, molecular nitrogen, and water vapor may appear as contaminants in PIL systems; reactions involving these molecules are included in Table 1 for completeness.

<u>Process</u>	<u>Rate Coefficient</u>	<u>Reference</u>
1. RI + $h\nu_{\text{pump}}$ \rightarrow R $^{\cdot}$ + I	$\sigma_p(\text{max}) = 6.0 \times 10^{-19} \text{ cm}^2$	38
2. I $^{\cdot}$ \rightarrow I + $h\nu_{\text{rad}}$	A = 7.7 sec $^{-1}$	39,40
3. I $^{\cdot}$ \rightarrow I + $h\nu_{\text{laser}}$	$\sigma_{\text{se}} = 5.5 \times 10^{-18} \text{ cm}^2$	41
4. I + R $^{\cdot}$ \rightarrow RI	$6.0 \times 10^{-12} \text{ cm}^3 \text{ s}^{-1}$	9
5. I $^{\cdot}$ + R $^{\cdot}$ \rightarrow RI	$6.3 \times 10^{-12} \text{ cm}^3 \text{ s}^{-1}$	27
6. R $^{\cdot}$ + R $^{\cdot}$ \rightarrow R ₂	$\ll 10^{-13} \text{ cm}^3 \text{ s}^{-1}$	27
7. I $^{\cdot}$ + RI \rightarrow I + RI	$6.1 \times 10^{-16} \text{ cm}^3 \text{ s}^{-1}$	37
8. I $^{\cdot}$ + O ₂ \rightarrow I + O ₂ $^{*}(\Delta_g)$	$2.5 \times 10^{-11} \text{ cm}^3 \text{ s}^{-1}$	43-45
9. I $^{\cdot}$ + H ₂ O \rightarrow I + H ₂ O	$9.6 \times 10^{-13} \text{ cm}^3 \text{ s}^{-1}$	46
10. I $^{\cdot}$ + N ₂ \rightarrow I + N ₂	$5.2 \times 10^{-17} \text{ cm}^3 \text{ s}^{-1}$	43,44
11. I + I + RI \rightarrow I ₂ + RI	$4.2 \times 10^{-30} \text{ cm}^6 \text{ s}^{-1}$	16
12. I + I + I ₂ \rightarrow 2I ₂	$3.7 \times 10^{-30} \text{ cm}^6 \text{ s}^{-1}$	47
13. I $^{\cdot}$ + I ₂ \rightarrow I + I ₂	$9.9 \times 10^{-12} \text{ cm}^3 \text{ s}^{-1}$	43,44

Table 1. Physical processes of importance to the photolytic iodine laser based on t-C₄F₉I. Here R $^{\cdot}$ designates the radical t-C₄F₉ $^{\cdot}$, and RI designates the iodide t-C₄F₉I.

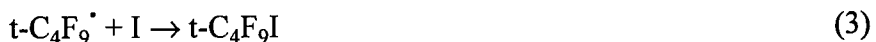
The intrinsic value of t-C₄F₉I as a laser fuel is in the value of the rate constant for reaction 6 in Table 1; the reaction



proceeds only very slowly because the cross shape of the radical physically hinders recombination. On the other hand, the equivalent reaction with the photolysis product of normal heptafluoropropyl iodide,



has a rate coefficient of $1.38 \times 10^{-12} \text{ cm}^3 \text{ s}^{-1}$.³¹⁻³⁵ Other pertinent rate coefficients for the two iodides are comparable in magnitude. Since the t-C₄F₉[•] radicals are slow to combine, the overall kinetics of the system support the recombination reaction



so that free iodine atoms are consumed in regenerating the parent molecules rather than in producing molecular iodine by recombination of two iodine atoms with the aid of a third body (reaction 11 in Table 1). The accumulation of molecular iodine in the iodide gas is particularly detrimental due to the enormity of its quenching rate coefficient with I*, reaction 13 in Table 1. Thus, due to hindered recombination of t-C₄F₉[•] radicals, the kinetics of the t-C₄F₉I laser medium support longer periods of operation at sustained power levels (relative to C₃F₇I) because the parent iodide is regenerated rather than the strong quencher, molecular iodine.^{9,11,12,16} Nevertheless, in PIL's based on both iodides, the gas must be flowed in order to prevent rapid and catastrophic production of I₂; furthermore, in closed-cycle systems, it is extremely desirable to purge the flowing gas of I₂ insofar as possible.

One successful means of removing molecular iodine is to expose the gas to copper so that I₂ is converted to CuI, which adheres to the surface of the copper metal.²⁵ In particular, previous work at the Phillips Laboratory has demonstrated that copper wool serves as an effective iodine removing agent when the laser fuel is in the liquid phase. The effectiveness of this material when exposed to the fuel in gas phase has received less study.

3. Experimental Description

The laser cavity employed in this work was a larger version of that described by Schlie and Rathge²² and is diagrammed schematically in Fig. 1. The cavity was machined from aluminum and had outside dimensions of 8×33×64 cm. The laser gas flowed through the long dimension of the cavity, entering and exiting through ports which were 2.5 cm in diameter. The cavity was designed so that, after entering, the gas expanded to fill the width of the cavity by means of a v-shaped channel; a similar channel funneled the gas into the exit port. Inside the flow channel, aluminum "foam" was used to ensure a uniform flow across the excitation region of the cavity.²² The ultraviolet lamp which excited the gas was oriented transverse to the direction of gas flow. A quartz UV-grade window having dimensions 4×25 cm was fixed in the top of the laser cavity, with its long dimension parallel to the lamp. Channels were milled in the laser cavity to allow cooling by flowing tap water. The normal-incidence antireflection-coated BK-7 windows for the laser beam itself were 5 cm in diameter; the window surfaces were wedged to prevent lasing between them. The clear aperture for the beam was 2.5 cm.

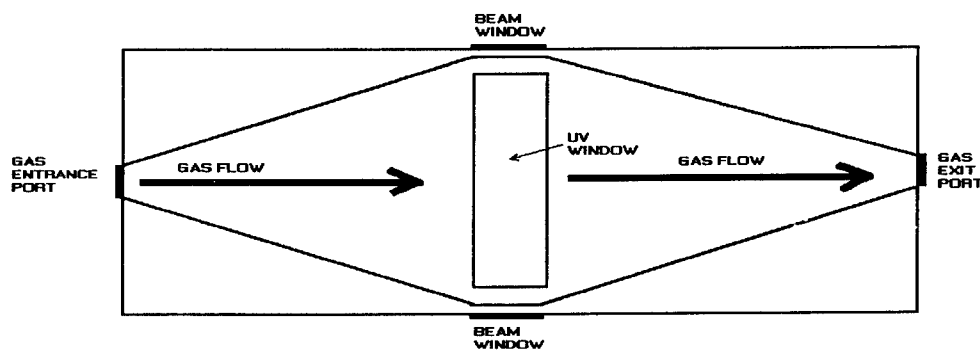


Figure 1. Schematic diagram of the laser cavity (top view).

Fig. 2 illustrates the flow system and supporting plumbing for the laser. The tubing for the gas flow consisted of sections with diameters varying from 2.5 cm to 10 cm; the sections

were sealed by Viton o-rings. The total length of the flow tubing was ~5 m. A portion of the flow system, typically about 0.5 m, was packed with copper wool to remove I₂ from the flowing gas stream. The flow was driven by a modified turbomolecular vacuum pump (blower) similar to one which has been previously described.²⁵ The internal motor of the pump was removed, and the internal fan blade rotation shaft was coupled to the outside of the blower housing by a water-cooled magnetic fluid seal, Ferrofluidic model SC-1000-C. The blower shaft was driven by a Dayton Electric Company variable-speed motor, model 21046. The motor shaft was connected to the external blower shaft by pulleys and a belt. The maximum rotational speed of the blower rotors was 3,200 rpm. The flow rate was measured by a Yewflo vortex flowmeter, model YF102, which was capable of measuring linear flow rates up to 100 m/s. In this work, flow rates in the range 1-10 m/s were employed.

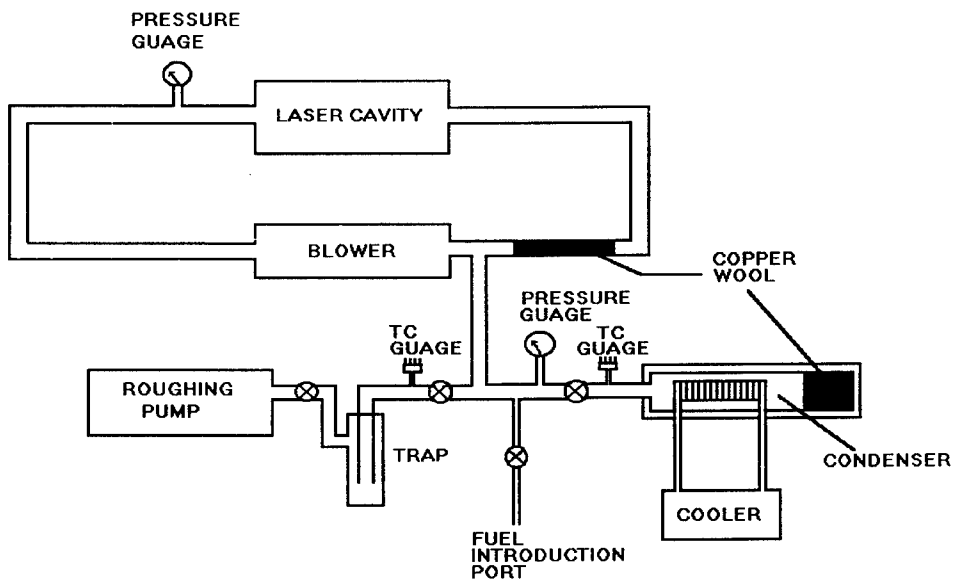


Figure 2. Schematic diagram of the laser system.

The laser cavity and flow system were evacuated to pressures less than 1 mtorr by a forepump fitted with a molecular sieve trap; this trap was preceded by a glass trap immersed in

liquid nitrogen. Laser gases pumped from the cavity were condensed and captured in this trap for purification and reuse. The base pressure of the system was monitored by thermocouple gauges. Before use, the laser fuel was contained in a condenser which consisted of a sealed stainless steel cylindrical vessel containing a stainless steel coil and packed with copper wool. The condenser had an outside diameter of 17 cm and a height of 49 cm. Dimethyl polysiloxane was circulated through the internal coil by an ultralow temperature recirculating cooler, FTS Systems model RC310G20W. The cooler temperature range was -70 C to +40 C. The vapor pressure of the fuel could then be controlled by the set temperature of the cooler.²¹⁻²⁵ The gas pressure was monitored using Wallace and Tiernan gauges.

The laser gas was pumped by a microwave-excited mercury lamp manufactured by Fusion Systems, Inc., model F450.²³ The quartz lamp had an inner diameter of 9 mm, walls of thickness 1 mm, and a length of 24 cm. The lamp was excited by two ac-driven, 1.5 kW magnetrons with output frequencies of 2.4 GHz. The magnetrons and lamp were cooled by a 0.1 m³/s blower, also supplied by Fusion Systems. The specified ultraviolet power of the lamp was 448 W. An elliptical reflector was mounted on top of the lamp, and the radiation passed through the UV window in the laser cavity.

The laser was operated in a stable oscillator configuration. The rear mirror had a radius of curvature of 5.0 m and a reflectance at 1.315 μm greater than 99.9%. Several flat front mirrors with differing values of reflectance at 1.315 μm were used to study the gain of the laser system. The reflectance values of these mirrors ranged from 85% to 99%. The laser power was measured with a Molelectron model PM30 energy-absorbing disk calorimeter and a model PM5200 display.

The laser gases used in this work were iso-heptafluoropropyl iodide, i-C₃F₇I, acquired from PCR, Inc. (at a cost of \$7.80/g), and perfluoro-t-butyl iodide, t-C₄F₉I, acquired from Source Tek, Inc. (at a cost of \$35.00/g). The iodide i-C₃F₇I is a clear liquid at room temperature, while t-C₄F₉I is a white solid. The i-C₃F₇I was periodically cleansed of I₂ after exposure to the intense UV radiation by agitating it in a closed vessel packed with copper wool.³⁶ Further purification can be achieved by distillation; however, distillation was not employed in this work. The t-C₄F₉I was purified of I₂ by refluxing at 85 C in a sealed vessel packed with copper wool.

4. System performance

The performance of the laser system was first studied using iso-heptafluoropropyl iodide, i-C₃F₇I, because of the extensive work previously performed at the Phillips Lab²¹⁻²⁵ using this iodide and its isomer, n-C₃F₇I, which exhibits closely similar chemical and physical properties. The maximum power which could be obtained from (undistilled) i-C₃F₇I was 2.0 W; the power fell over time (~0.1 W/min) due to the gradual increase in I₂ density. The monotonic decrease in power indicated that the copper wool in the flow line was not 100% effective in removing molecular iodine. Maximum power was achieved with a 95% reflective output mirror and at a pressure of about 16 torr, for which the condenser temperature was about -40 C. The linear gas flow rate was 3.5 m/s.

The maximum output achievable using t-C₄F₉I in this work was 2.9 W, corresponding to ~0.6% conversion efficiency of the mercury lamp power. As with i-C₃F₇I, the laser output power was observed to drop gradually with time, and at roughly the same rate. Lasing ceased within a few seconds when the flow was stopped altogether. The optimum gas pressure for lasing with

$t\text{-C}_4\text{F}_9\text{I}$ was 17 torr, which was obtained with a condenser temperature of about -4 C. The laser output power increased slightly with flow rate above about 2.0 m/s, but dropped precipitously below this value. The output power dropped with the addition of a neutral carrier gas, such as Xe or N_2 , in spite of the higher flow rates which could be achieved at higher pressures. The most likely explanation for this result is accelerated production of molecular iodine at higher pressures by three-body recombination of two free iodine atoms.

Methodical studies of laser output as a function of pressure and flow rate were complicated in this work due to the monotonically decreasing laser power with time. The copper wool packed in the flow line served to partially purify the flowing gas of I_2 ; however, irreversible molecular iodine buildup apparently occurred so that the output power dropped with time at rates on the order of 0.1 W/min. The surface of the copper wool in the flow system was rapidly coated with CuI when the laser was in operation. When a significant percentage of the surface area was coated, the scrubber lost its effectiveness. Continuous operating times of only ~2 hours were possible before replacement of the wool was necessary.

As mentioned earlier, beam output mirrors with various values of reflectance were used in an attempt to quantify the gain of the laser system. These measurements were also complicated due to the decrease in power with time. Nevertheless, initial measurements indicate that mirrors with 95% and 98% reflectance produced essentially the same, and maximum, output power. Power dropped drastically, to about 1% of maximum, using a 90% reflector. These observations should be compared with the performance of the same laser cavity and lamp system using $n\text{-C}_3\text{F}_7\text{I}$ in a closed-cycle, passive-flow configuration. (In this configuration the flow is promoted by a temperature differential between two liquid reservoirs.) In this configuration the

highest power (~6 W) was obtained using an output coupler of 87% reflectance. The gain of the blower-driven system as configured in this work was clearly less than that of the passive system. The reason for this reduction in gain is believed to be inadequate elimination of molecular iodine from the flow. At this time the relative merit of t-C₄F₉I to i-C₃F₇I as the laser medium for a blower-driven flow system remains undetermined, and awaits further study.

It is worthwhile to report here one further observation of the relative performance of t-C₄F₉I to i-C₃F₇I under the conditions of these measurements. It was observed throughout testing that the laser output power using t-C₄F₉I increased with each successive fill of the laser cavity, generally increasing until the available fuel in the condenser was exhausted. On the other hand, output power with fills of i-C₃F₇I were generally repeatable at 1.5±0.2 W. The observation of increasing power with each fill of t-C₄F₉I led to the speculation that some strongly quenching impurity (with a higher vapor pressure than t-C₄F₉I at the cavity filling temperature, about -4 C) was present in the fuel. Furthermore, it appeared that the concentration of the impurity relative to that of the fuel decreases with each successive fill of the laser cavity. This theory was supported by measurements of the radiative lifetime of I* in t-C₄F₉I following photolysis at 266 nm in a flowing system. The iodide was flowed from a bulb at 0 C to another at -196 C, and the cell pressure was 10 torr. These experiments showed a gradual increase in the measured lifetime of the excited state from ~50 μs to ~3.2 ms over a period of several hours. The quenching rate coefficient³⁷ for I* by t-C₄F₉I is $6.1 \times 10^{-16} \text{ cm}^3 \text{ s}^{-1}$ so that, if the iodide is the only species present in the flow, the expected lifetime of I* at 10 torr is ~5.5 ms.

Since molecular iodine has a lower vapor pressure than t-C₄F₉I by at least two orders of magnitude at all temperatures used in this work,²⁵ it appears unlikely that molecular iodine was

the quenching impurity. Gas phase chromatographic analysis of the sample used in this work indicated the presence of no impurities; however, it is certain from the results of the lasing experiments that they were present, clearly at concentrations below the detection threshold of the GC. Attempts to remove the impurities by fractional distillation were unsuccessful, but may prove fruitful if the proper distillation temperatures can be determined.

It should furthermore be noted here that an attempt to use activated charcoal in place of the copper wool to adsorb molecular iodine failed because the charcoal rapidly adsorbed t-C₄F₉I as well. Use of activated charcoal with i-C₃F₇I yielded the same results. Previous work at the Phillips Lab has shown that activated charcoal is an effective purifying agent when I₂ is dissolved in liquid i-C₃F₇I, with no apparent detrimental effects on, or significant loss of, the iodide. In the gas phase, however, charcoal shows little promise of serving as a selective getter for I₂.

5. Summary

This document reports the first demonstration of a closed-cycle photolytic iodine laser using t-C₄F₉I as the iodide. The iodide at pressures near 17 torr was driven by a custom turbomolecular blower at linear velocities of ~2 m/s. Power levels as high as 2.9 W were obtained, corresponding to ~0.6% conversion of the incident ultraviolet radiation. The power typically decreased at a rate of ~100 mW/minute due to the irreversible production of the strong quencher I₂ in the flowing gas stream. Use of copper wool in the flow system mitigated, but did not eliminate, production of I₂.

This system, in which the laser fuel remains a gas rather than undergoing condensation and evaporation, holds promise for the future development of much more compact and efficient PIL's than those currently available. Furthermore, the shift of the ultraviolet absorption peak to the red, relative to other iodides, offers the potential for much more efficient absorption of the exciting lamp radiation. In addition, the production of molecular iodine in $t\text{-C}_4\text{F}_9\text{I}$ is, in theory, slower than for other iodides due to enhanced recombination to reform the parent iodide. With further developmental effort, in particular aimed at novel means of purifying the gas of molecular iodine, a laser based on this prototype could serve as a simple probe laser for high-power iodine lasers and as a PIL injector for the illuminator of the airborne laser (ABL), currently of interest to the Air Force. Further work may yield long-term output powers on the order of 150 W for application in industry.

Acknowledgments

The design and construction of the laser system described here were due primarily to the creative efforts of R.D. Rathge. Dr. L.A. Schlie provided advice and guidance throughout the design, construction, and testing phases. The outstanding facilities and support staff of the Phillips Laboratory, in particular with regard to experience gained from previous PIL development efforts, were critical in the successful demonstration of this new device. The support of the Air Force Office of Scientific Research is gratefully acknowledged. The Summer Faculty Research Program serves to significantly increase the research experience of its Associates and prepares them for productive follow-up work at their home institutions.

References

1. J.V.V. Kasper and G.S. Pimentel, *Appl. Phys. Lett.* 5 (1964) 231
2. G. Brederlow, E. Fill, and K.J. Witte, *The High-Power Iodine Laser*, Springer-Verlag, New York, 1983.
3. K.T. Witte, G. Brederlow, K. Eidmann, R. Volk, E. Fill, K. Hohla, and R. Roadmann, *Springer Series Opt. Sci.* 9 (1978) 142.
4. A.J. DeMaria and C.J. Ultee, *Appl. Phys. Lett.* 9 (1966) 67.
5. N.G. Basov and V.S. Zuev, *Il Nuovo Cimento* 31 (1976) 129.
6. H.J. Baker, T.A. King, and W.G. McNaught, *J. Phys. D: Appl. Phys.* 12 (1979) 997.
7. H.J. Baker and T.A. King, *Laser Advances and Applications*, edited by B.S. Wherrett, Wiley, New York, 1980, p.80.
8. S.B. Dormer, *Izv. Akad. Nauk. SSR: Ser. Fizz.* 44 (1980) 2002.
9. B.M. Tabibi, C.A. Terrell, J.H. Lee, and G. Miner, *Optics Comm.* 109 (1994) 86.
10. H. Hwang and B.M. Tabibi, *J. Appl. Phys.* 68 (1990) 4983.
11. J.H. Lee, W.R. Weaver, and B.M. Tabibi, *Optics Comm.* 67 (1988) 435.
12. B.M. Tabibi and M.H. Lee, *Proceedings of the International Conference on Lasers '86*, STS Press, McLean, VA, 1987, p. 144.
13. J.H. Lee, M.H. Lee, and W.R. Weaver, *Proceedings of the International Conference on Lasers '86*, STS Press, McLean, VA, 1987, p. 150.
14. J.H. Lee and W.R. Weaver, *Appl. Phys. Lett.* 39 (1981) 137.
15. J.H. Lee, J.W. Wilson, T. Enderson, D.H. Humes, W.R. Weaver, and B.M. Tabibi, *Optics Comm.* 53 (1985) 367.
16. L.V. Stock and J.W. Wilson, *Advances in Laser Science III*, edited by A.C. Tam, J.L. Gole and W.C. Stwalley, American Institute of Physics, New York, 1988, p. 99.
17. P.O. Andreeva, G.N. Birich, I.I. Sobelman, V.N. Sorokin, and I.I. Struk, *Sov. J. Quantum Electron.* 7 (1977) 1230.
18. K.J. Witte, P. Burkhar, and H.R. Luthi, *Optics Comm.* 28 (1979) 202.

19. V.Y. Zalesskii, E.S. Ershov, A.M. Kokushkin, and S.S. Polikarpov, Sov. J. Quantum Electron. 11 (1981) 498.
20. W. Fuss and I. Hohla, Optics Comm. 18 (1976) 427.
21. L.A. Schlie and R.D. Rathge, IEEE J. Quantum Electron. 20 (1984) 1187.
22. L.A. Schlie and R.D. Rathge, J. Appl. Phys. 63 (1988) 5664.
23. L.A. Schlie and R.D. Rathge, Optics Comm. 66 (1988) 289.
24. L.A. Schlie and R.D. Rathge, Optics Lett. 16 (1991) 1007.
25. L.A. Schlie and R.D. Rathge, IEEE J. Quantum Electron. 31 (1995) 1069.
26. T.L. Andreeva, G.N. Birich, I.I. Sobelman, V.N. Sorokin, and I.I. Struk, Sov. J. Quantum Electron. 7 (1977) 1230.
27. L.S. Ershov, V. Yu. Zaleskii, and V.N. Sokolov, Sov. J. Quantum Electron. 8 (1978) 494.
28. T.L. Andreeva, G.N. Birich, V.N. Sorokin, and I.L. Struk, Sov. J. Quantum Electron. 6 (1976) 781.
29. G.A. Skorobogatov, B.N. Maksimov, V.G. Seleznev, O.N. Slesar, N.D. Torbin, and L.N. Kostyрева, Sov. J. Quantum Electron. 12 (1982) 133.
30. R.S. Derwent and B.A. Thrush, Chem. Phys. Lett. 9 (1971) 591.
31. F.E. Beverly III., Optics Comm. 15 (1975) 204.
32. V.Y. Zalesskii and E.I. Moskalev, Sov. Phys. JETP 30 (1970) 1019.
33. V.Y. Zalesskii and A.A. Venediktov, Sov. Phys. JETP 28 (1969) 1104.
34. I.M. Belousove, N.G. Gorshkov, O.B. Danilov, V.Y. Zalesskii, and I.L. Yachnev, Sov. Phys. JETP 38 (1974) 254.
35. V.Y. Zaleskii, Sov. J. Quantum Electron. 4 (1975) 1009.
36. L.A. Schlie and R.D. Rathge, Rev. Sci. Instrum. 55 (1984) 482.
37. V.I. Babkin, M.B. Ippolitov, and A.I. Maslov, Sov. J. Quantum Electron. 20 (1990) 149.

38. T.P. Zhurilo, V.Y. Zalasskii, and A.M. Kokuschkin, Sov. J. Quantum Electron. 15 (1985) 669.
39. V.S. Zuev, V.A. Katulin, V. Yu Nosach, and O. Yu Nosach, Sov. Phys. JETP 35 (1972) 870.
40. R.S. Derwent and B.A. Thrush, Chem. Phys. Lett. 9 (1971) 591.
41. L.A. Schlie, J. Optical Soc. Am. 71 (1981) 1080.
42. S.L. Dobychin, L.D. Mikheev, A.B. Pavlov, V.P. Fokanov, and M.A. Khodarkovskii, Sov. J. Quantum Electron. 8 (1978) 1383.
43. J.J. Deakin and D. Husain, Chem. Soc. Faraday Trans. II 68 (1972) 1603.
44. D.H. Burde, R.A. McFarlane, and J.R. Wiesenfeld, Chem. Phys. Lett. 32 (1975) 296.
45. R.G. Derwent and B.A. Thrush, J. Chem. Soc. Faraday Trans. II 68 (1972) 720.
46. A.J. Grimley and P.L. Houston, J. Chem. Phys. 69 (1978) 2339.
47. J.A. Blake and G. Burns, J. Chem. Phys. 54 (1971) 1480.

Simulation Studies of Ultrafast Silicon Avalanche Shaper (SAS)
Devices for High Power Switching

R. P. Joshi
Assistant Professor
Electrical and Computer Engineering Department

Old Dominion University
Norfolk, VA

Final Report for:
Summer Research Program
Phillips Laboratory

Sponsored by:
Air Force Office of Scientific Research
Bolling Air Force Base, Washington DC

and

Phillips Laboratory

August 1995

SIMULATION STUDIES OF ULTRAFAST SILICON
AVALANCHE SHAPER (SAS) DEVICES FOR
HIGH POWER SWITCHING

R. P. Joshi

Department of Electrical & Computer Engineering
Old Dominion University, Norfolk, VA 23527-0246

Abstract

The primary goal of this research effort was to conduct a theoretical study and numerical analysis of the Silicon Avalanche Shaper (SAS) devices. The SAS devices are important integral components of an overall semiconductor-based high-power switching technology that is being developed at the Phillips Laboratory. A physical, microscopic mathematical model for these devices was developed. A one-dimensional time-dependent simulation code was subsequently set up for numerical analysis and performance predictions. Results obtained from this work indicate the theoretical possibility of sub-nanosecond current rise times. Such current pulses would provide for the high-power, ultrashort electrical waveforms necessary for the generation of electromagnetic signals. The role of internal impact ionization, the time-dependent internal displacement current within the SAS device, and the propagation dynamics of an "electric field wave" were analyzed. The simulation results are in keeping with the general qualitative trends that have been observed in the experimental work so far. Potential for future continuation of the theoretical work in this area of high-power, non-photoconductive switching technology was identified. Some follow-on research issues have also been discussed.

I. INTRODUCTION

The primary goal of this research effort was to conduct a theoretical study and numerical analysis of the Silicon Avalanche Shaper (SAS) devices. These SAS devices are important integral components of an overall semiconductor-based high-power switching technology that is being developed by the Phillips Laboratory at Kirtland Air Force base. This technology is non-photoconductive in nature, and was pioneered by the Power Semiconductor Electronics team at the Ioffe Physical Technical Institute (PTI) in Russia headed by Prof. Grehov [1-4]. Besides the SAS devices, this type of high power switching relies on the Drift Step Recovery Diode (DSRD) as an additional active circuit device. Both semiconductor devices employ p-n junctions and are based on bulk-effects.

During the developmental work at Phillips Laboratory over the past year, in conjunction with the University of New Mexico (UNM) and PTI, several such semiconductor-based high-power switches have been successfully fabricated and tested. The experimental results to date have been very encouraging [5,6], and the switches have demonstrated exceptionally promising capabilities. The initial assessment is also indicative of potential advantages over the GaAs-based photoconductive switches that have been developed in the past [7,8]. Besides the experimental success and practical demonstrations, some theoretical analysis of the DSRD devices has also been carried out in the past [9,10]. The DSRD is basically a slow opening switch which operates in the sub-microsecond to nanosecond regime. However, a detailed theoretical study and subsequent performance analysis of the SAS devices, which are ultrafast closing switches operating in the sub-nanosecond time scales, has not been performed to date. The device physics of the SAS is more complicated, and needs to be fully understood in order to optimize the overall performance of this technology.

The main task of the present research project was to analyze the physics and understand the theory of SAS device operation. Subsequently, predictions of the dynamic electrical response based on numerical simulations were to be performed. This entire set of tasks was to be carried out over a 8-week period at Albuquerque, N. Mexico. In the following, the device physics and operational principle of the SAS devices are first discussed. The potential advantages of this technology are then listed for completeness. Details of our numerical model for simulations of the transient response of the SAS device is subsequently presented. The electrical response characteristics obtained from the simulations are then discussed. Finally in closing, some final comments relating to potential research efforts and open issues in this area are presented.

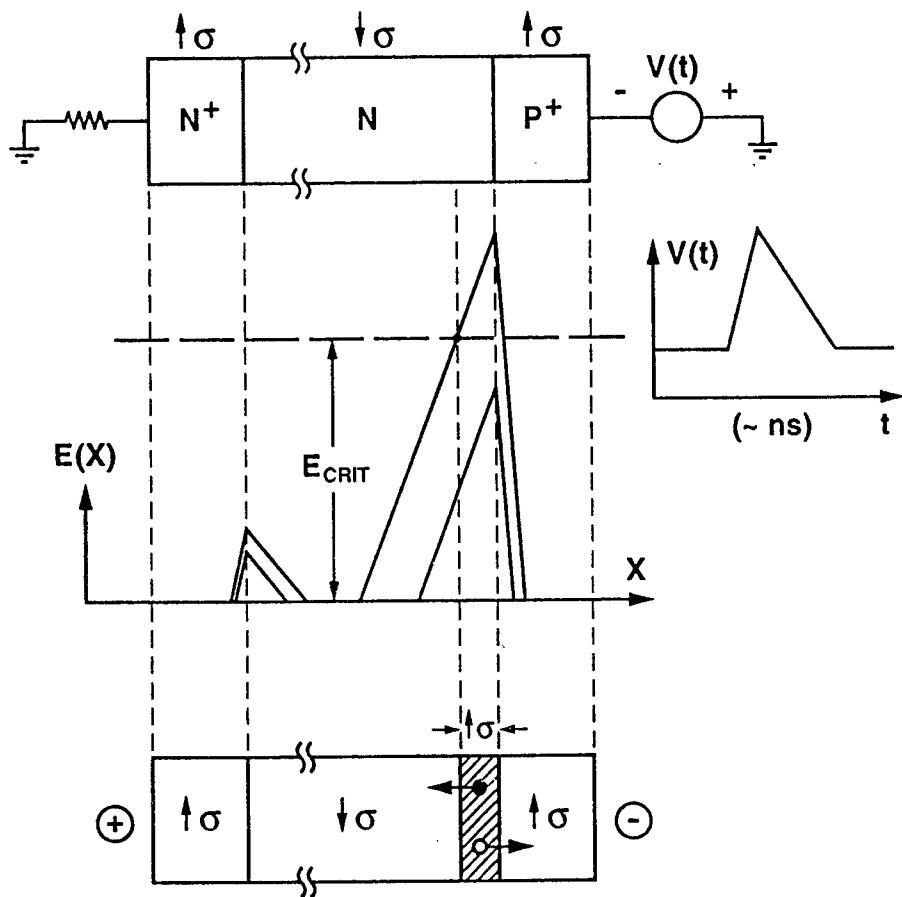
II. SAS OPERATIONAL PRINCIPLE

Simple qualitative discussions of the SAS operating principle have been given in several papers by Grekhov et al. [1-4] over the years. The concept relies on the generation of a fast ionization wave through the application of a rapid reverse bias across a Silicon p-n junction device. The peak bias exceeds the static breakdown voltage, thus creating a rapid avalanche of electron-hole pairs within the high-field regions of the device. The conductivity is therefore enhanced rather quickly, and the switch triggers into the conductive state due to the avalanche. A brief summary of some of the important sequence of physical events are given below. The list not only borrows from the salient concepts enumerated in the Grekhov papers, but also *expands* on the discussion for a more complete insight.

- (i) The SAS is initially in the non-conducting "OFF" state with a moderate reverse bias across the N⁺-N-P⁺ structure. The applied voltage is held to a value below the characteristic avalanche voltage of the Si device. This hold-off voltage can, in principle, be varied by changing either the internal doping densities or the device length.
- (ii) For turn-on, a rapidly increasing reverse voltage pulse is applied. This creates a high-field region across the P⁺-N junction, with field strengths exceeding the critical breakdown value. Impact ionization is thus initiated in a region localized near the P⁺-N junction.
- (iii) Rapid impact ionization creates a high conductivity region at the P⁺-N junction. The electrons and holes thus created through impact ionization, begin to move in opposite directions. The motion of the mobile charge contributes to a current rise.
- (iv) Next, the electric field in the highly conducting region begins to collapse as the separation of mobile charge forms an internal polarization field. The electric field in the adjacent non-conducting N-region, however, increases to sustain the overall voltage drop across the device. This increase in the electric field provides the displacement current necessary to maintain exact continuity of the total current across the entire device.
- (v) As a result of the above mechanism, the electric field grows starting from the P⁺-N junction, towards the N⁺ anode side through the N-region in the middle. A propagating electric field wave is thus set up. This propagating field, in turns, creates a travelling impact ionization front, and is responsible for the uniform turn-on of the entire device.
- (vi) The current in the SAS device can be turned off by lowering the applied bias to a level

below the critical sustaining breakdown voltage. Upon lowering the external voltage, the carriers are removed through a combination of drift flush-out and recombination.

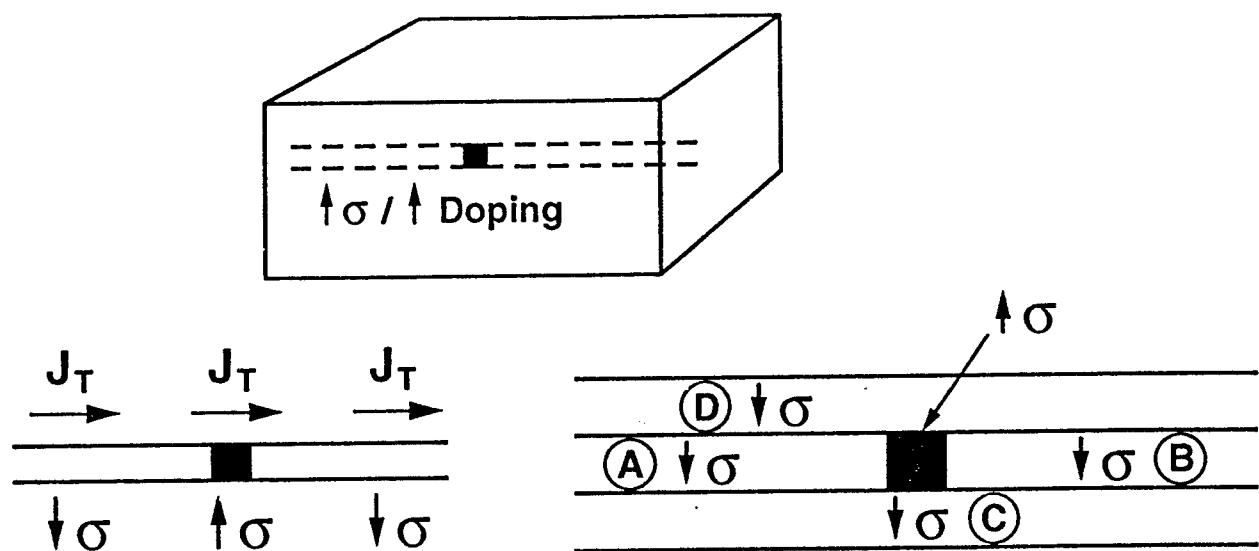
A schematic for the turn-on sequence is shown below. The initial field in the N-P⁺ depletion region is below the critical value for impact ionization. Hence, the carrier concentration and the conductivity remain at a low level. On the application of a large reverse bias, the field increases beyond the critical value, and carrier generation via impact ionization is initiated. This ionization effectively increases the local conductivity, and forces the growth of the electric field in an adjoining low conductivity region. This progressive movement of the electric field away from the junction and into the low conductivity N-region continues, as carriers continually keep getting generated within the N-layer starting from the junction.



III. ADVANTAGES AND BENEFITS OF THE SAS DEVICE

Based on the above summary of the SAS operational principle, several key advantages can be identified. These are based on the inherent operating principle and the device physics. The following is a list of important advantages for this SAS-based high power technology:

- (i) The elimination of external lasers for triggering and turn-on. This simplifies the complexity of the circuit.
- (ii) A natural self-propagation of the electric fields within the device. This facilitates a gradual and more homogeneous turn-on. The potential for instabilities associated with spatial non-uniformities as with localized charge injection, is thus greatly reduced.
- (iii) The application of a rapidly increasing voltage pulse dramatically decreases the likelihood of current filamentation and "micro-channels". As is well known [11], such filamentation is associated with the rapid growth of the electric fields within localized regions of the device due to density fluctuations. This effect is shown in the sketch below. Due to the formation of a localized region of high field within a semiconductor, the fields in the adjacent low conductivity regions "A" and "B" build up. The increased field in turn, causes a further increase in the carrier density through impact ionization and thermal heating. The process builds on itself, and lead to fatal device failure as the high conductivity region rapidly propagates along the micro-pipe. However for an SAS, the field is *intentionally* made to increase rapidly through an external pulse. Consequently, any localized field increases in regions "A" and "B" brought about by density fluctuations, would quickly be swamped by the rapid increase forced by the external circuit. Besides, rapid increases in the field generated by the external bias, would also be produced in the micropipe regions "C" and "D". Consequently, the entire region comprising of the channels "C", "D" and "AB" would collectively grow, instead of the microchannel "AB" alone. This would effectively prevent localized filamentation.



- (iv) Another advantage of this technology is its reliance on Si rather than GaAs. Silicon has the following inherent advantages over GaAs, a material which is often used in photoconducting switches. The advantages include: (a) Ease of fabrication, (b) A higher thermal conductivity for better heat dissipation and better protection against thermal runaway, (c) A higher carrier saturation velocity which should lead to higher currents and faster turn-on, and (d) A material system inherently free of the Negative Differential Resistance (NDR) effect. As is well known, the NDR effect in GaAs associated with inter-valley transfer gives rise to a potential instability [12].
- (v) Furthermore, the SAS by being a p-n junction device, naturally ensures that the regions of high electric field occur within the bulk device and **not** at the end contacts. As a result, the device circumvents many of the "contact problems" that are associated with other devices. These problems include uncontrolled thermionic emission and carrier tunneling due to high fields at the contact, excessive heating and contact degradation.
- (vi) Finally, the SAS also offers the possibility of scaling the hold-off voltage. This could be done by stacking several such devices in series, increasing the size of the central N-region, and by decreasing the doping levels. Therefore there do not appear to be any fundamental limits on the voltage scaling.

IV. MATHEMATICAL MODEL AND THE DEVICE SIMULATION APPROACH

A time-dependent one-dimensional (1D), bipolar numerical model was developed and implemented for simulations of the transient electrical response of the SAS device. The model implemented at basic device level, included details of internal semiconductor processes, and the electrical transport of both electrons and holes. For greater flexibility, the various parameters of the model were incorporated as user-specified input variables. As a result, the electrical performance and output characteristics of devices having different doping densities, operating temperatures, device lengths, and biasing levels could easily be evaluated and compared.

The semiconductor model was implemented by applying the basic semiconductor equations to the SAS geometry. A finite difference scheme was used to discretize the governing equations on a uniform mesh within the simulation region. The mesh spacing " Δx ", was chosen to be 100 Angstroms, which was smaller than the lowest value of the characteristic Debye length. This ensured good spatial resolution. For stability, the time-step " Δt " for the transient response was chosen to satisfy the following Courant-Friedrich-Levy [13] inequality: $\Delta t < [\Delta x/v_{\max}]$, with v_{\max} being the highest carrier drift velocity. The semiconductor equations used in this

implementation were as given below. These expressions characterize total current continuity, particle balance for electrons and holes with inclusion of the time-dependent generation and recombination processes, and the constitutive relations for the drift and diffusion currents.

$$I(t) = \frac{V_o(t) - V_{SAS}(t)}{R} = A [J_p^i + J_n^i] + \epsilon \left[\frac{E^i(t) - E^i(t-\Delta t)}{\Delta t} \right], \quad (1)$$

$$J_p^i(t) = q p^i(t) v_p^i(t) - q D_p \left[\frac{p^{i+1/2}(t) - p^{i-1/2}(t)}{\Delta x} \right], \quad (2)$$

$$J_n^i(t) = q n^i(t) v_n^i(t) + q D_n \left[\frac{n^{i+1/2}(t) - n^{i-1/2}(t)}{\Delta x} \right], \quad (3)$$

$$\frac{\Delta p^i}{\Delta t} = \alpha_p^i v_p^i p^i - \frac{p^i}{\tau_{IND}^{ip}} - n^i p^i K^i + G_{th}^i + \frac{J_p^{i-1/2} - J_p^{i+1/2}}{q \Delta x}, \quad (4)$$

$$\frac{\Delta n^i}{\Delta t} = \alpha_n^i v_n^i n^i - \frac{n^i}{\tau_{IND}^{in}} - n^i p^i K^i + G_{th}^i + \frac{J_n^{i-1/2} - J_n^{i+1/2}}{q \Delta x}. \quad (5)$$

In the above expressions, A is the device cross-sectional area, q the electronic charge, α_n^i and α_p^i denote the impact ionization coefficients for electrons and holes within the i^{th} mesh, G_{th}^i is the thermal generation rate, v_n^i and v_p^i stand for the electron and hole drift velocities, D_p^i and D_n^i are the carrier diffusion coefficients, τ_{IND}^{ip} and τ_{IND}^{in} the indirect recombination rates, and K^i the rate for direct recombination. Most of the above stated parameters are field dependent [14], and this dependence was specifically incorporated into the simulations. A summarizing flowchart of the actual numerical implementation is given below. It lists the sequence of steps necessary for the transient simulation of the SAS device.

- (i) Initial solution of Poisson's equation under zero-bias conditions. This sets the initial conditions for the carrier densities and internal electric field. The discretized one-

dimensional version of Poisson's equation was taken as:

$$\frac{E^{i+1} - E^i}{\Delta x} = \frac{q}{\epsilon} [p^{i+1/2} - n^{i+1/2} + N_A^{i+1/2} - N_D^{i+1/2}] , \quad (6)$$

with a zero electric field value imposed on both the two boundaries of the device.

- (ii) Application of a reverse bias $V(t)$ starting from $t=0$. The current flowing during each subsequent time step was calculated from the left hand side of eqn. (1) for every grid point within the device. The internal fields were then updated based on eqn. (1).
- (iii) The ionization parameters $\alpha_{p,n}$, diffusion coefficients, and carrier velocities were then recalculated corresponding to the updated electric field distribution. The conduction current densities then resulted for every mesh point from equations (2) and (3).
- (iv) At the end of the time step " ΔT ", the carrier densities were updated based on (4) and (5). Physically, this reflects the changes in internal charge between the period " t " and " $t+\Delta T$ " due to carrier drift, current flow, impact ionization, and carrier recombination.
- (v) The sequence of steps (ii) through (iv) were repeated until the end of the applied voltage pulse $V(t)$. Specifically, in the simulation results presented here, the pulse $V(t)$ was taken to have an asymmetric triangular shape. It was held at a constant value V_o for the first 20 ns, then increased linearly to V_1 over the next 1 ns, and subsequently brought back to a fixed value of V_o over the next 4 ns. The program though, is quite general, and hence other waveforms for $V(t)$ can also be specified by the user.

V. SIMULATION RESULTS AND DISCUSSION

The one-dimensional, finite-difference, drift-diffusion approach outlined above was used to simulate the transient electrical response of the SAS device. Both the circuit loading effect and the internal device physics were included on a equal footing. In the following the simulation results obtained are presented and discussed.

V-1. The Current and Voltage Response

- (A1) Figures 1 and 2 show the voltage and current waveforms. These correspond to the applied biasing pulse $V_o(t)$ and the device voltage $V_d(t)$ as functions of time. As expected, $V_d(t)$ does not increase instantaneously, but gradually reaches $V_o(t)$. This can

be easily understood by examining the capacitive nature of the SAS equivalent circuit. During this initial stage when the applied bias is well below the impact ionization level, the SAS acts as a simple parallel combination of a "voltage-controlled" resistor and a capacitor. Due to the capacitance, the device voltage cannot increase instantaneously, but instead rises slowly to a value of V_o within about 2 ns.

- (A2) The current flowing through the circuit is initially a displacement current. It forces an electric field to be built-up within the device. After the initial transient, the current decreases to a low value. This occurs for two reasons. First, as the device is reverse biased the carrier densities are low and the conduction current is small. Secondly, the low biasing level inhibits impact ionization, which again restricts any possibility of current enhancement.
- (A3) The small bump seen at around 5 ns in Fig. 2, represents a space charge current. It arises as the depletion regions broaden in response to the applied reverse bias. The removal of carriers from the regions adjacent to the P⁺-N junction gives rise to a small current flow.
- (A4) After 20 ns, as the voltage $V_o(t)$ begins to be ramped up, the current increases dramatically. There are two contributions to this current rise: (i) the rapid displacement current $\epsilon[dE/dt]$, and (ii) the fast impact ionization internally which enhances the conduction current. The rise time of the current is therefore very rapid, reaching a peak value in less than a 1 ns interval.
- (A5) After 21 ns, as the voltage pulse begins to reduce, and so does the currents. The decrease is a combined result of a negative displacement current and a rapid decrease in the impact ionization rate.
- (A6) The minor ripple seen in the current waveform during the decay process is associated with the time dependence of the impact ionization process and an effective decrease in the equivalent inductance. As is well known [15], the process of impact ionization can be viewed from the standpoint of circuit theory, as the source of an effective inductance "L". For the present SAS device, since the impact ionization changes with time in response to the applied voltage pulse, the associated equivalent inductance also becomes time dependent "L(t)". As a result, the energy storage capacity within the equivalent inductor decreases as a function of time. This decrease can be very non-linear if the impact ionization is strongly non-linear function of the electric field or voltage. Such a strong non-linear relation does indeed exist, as seen through the curves of Fig. 3. The

values of ionization coefficients $\alpha_{p,n}$ are shown as a function of electric field. In response to the decrease in stored inductive energy, the circuit current increases slightly to accommodate a larger energy dissipation within the resistive element. The overall result is the emergence of a positive dI/dt term, which imparts a slight ripple to the current. Clearly, such a ripple can only exist over times during which the impact ionization coefficient is changing rapidly. After the initial decay of "L(t)", the equivalent circuit reverts to a parallel resistor-capacitor combination, and the current monotonically decreases.

V-2. Internal Field and Carrier Profiles

- (B1) Figures 4a and 4b show the internal electric field distribution (efd) and the free carrier profiles (fcp) for the N⁺-N-P⁺ SAS device under **steady state unbiased conditions**. Both graphs exhibit standard behaviour that is to be expected of the two N⁺-N and N-P⁺ junctions. The electron and hole densities are uniform within each of the three constituent regions, and their product equals " n_i^2 ". These curves of Fig. 4 were **not** plotted on the basis of the usual depletion approximation, but instead obtained naturally by running the 1D time-dependent code developed here until steady state with zero bias. The graphs therefore, are indicative of the validity of the numerical program that was implemented.
- (B2) Using the above starting conditions, the internal distributions created in response to the voltage pulse $V_o(t)$ of Fig. 1 were subsequently obtained for analysis. Snapshot pictures of the internal profiles, at various selected times during the application of the pulse $V_o(t)$, are shown in Figs. 5-8 to better understand the transient dynamics. Figures 5a & 5b depict the situation at 19.08 ns. As evident from Fig. 1, a steady state current condition under a constant reverse bias is reached by this time. Most of the applied voltage is dropped across the N-P⁺ junction, across which a significant depletion region exists. This widening of the depletion region and the formation of the high electric field at the junction is again as expected from simple junction theory. The slight non-uniformity in the electron density beyond 300 microns is the result of electron injection from the cathode. The creation of a spatial gradient in the electron density is necessary to provide a diffusive current component to maintain current continuity.
- (B3) Figures 6a and 6b show the "efd" and the "fcp" at 20.89 ns after applying the voltage pulse $V_o(t)$. This instant corresponds to a time after the initiation of the voltage ramp, but before the voltage decay cycle. Two points are immediately obvious from Fig. 6a. First, the electric field mainly builds up in the low conductivity N-region. This is

expected, since the displacement current would be highest in this region of low conductivity. Second, the electric field exhibits a local minima at around 260 microns. This is due to the formation of an internal polarization field as the electron-hole pairs formed by impact ionization move in opposite directions. The creation of such an electron-hole plasma is more clearly seen in Fig. 6b. A slight "bump" appears in the electron density at around 250 microns, due to the avalanche generation. The hole density over the region spanning from 220 microns to 300 microns is also seen to have increased relative to Fig. 5b.

- (B4) The snapshot of the internal distributions at 21.63 ns are shown in Figures 7a and 7b. This instant corresponds to a time during which the voltage pulse $V_o(t)$ has begun to decay down. The electric fields consequently are not as large as in the previous case. The secondary bump at around 230 microns, for example, is seen to have a value of 100 kV/cm as opposed to 136 kV/cm in Fig. 6a. Furthermore, the electric field profile appears to look smoother than at 20.89 ns. This is again to be expected and can be understood in terms of the following argument. Free carrier generation is stronger within the regions of higher field. However, the generation of free carriers and their subsequent separation works to quench and reduce the electric fields. The overall result therefore, is gradual "smoothening" of the electric field profile. The carrier density profiles of Fig. 7b, show the gradual movement of charge towards the opposite electrodes. For example, the local bump in the electron density seen at around 250 microns in Fig. 6b, now appears to be at around 230 microns. In addition, the hole density continues to grow near the N-P⁺ junction in the region around 250 microns.
- (B5) Finally, Figures 8a and 8b show the profiles at 25.68 ns. This corresponds to a time at which the bias voltage has gone back to its value prior to the ramp. The semiconductor system is also seen to nearly return to its previous state of figure 5. For example, the electric field once again has a prominent value only near the N-P⁺ junction. The carrier densities also look similar to those of Fig. 5b. The bump in the electron density seen in figures 6 and 7, is now absent. Furthermore, the hole concentration in Fig. 8b is seen to have dropped down to much lower value as compared to those seen in Figures 6 and 7. A relatively wide "depletion region" around the N-P⁺ junction is also apparent.

VI. SCOPE FOR FUTURE WORK

During the 8-week summer period, detailed theoretical analyses and numerical simulations for the SAS device were carried out. This is an important first step, and should form the

backbone for future research. A basic one-dimensional, drift-diffusion numerical code was also successfully implemented, and used to quantitatively analyze the device response based on the internal semiconductor physics. This effort therefore, established the analytical capability for further work and additional research relating to SAS based high-power technology. Such a theoretical modeling effort provides quantitative evaluations of the performance limits, and furnishes realistic predictions prior to costly and time consuming fabrication.

The work begun here can easily be extended in several directions, all of which are very important to the success and optimization of this technology. Some of the germane issues which need to be examined in this context are described below.

- (i) **Scalability Issue:** In order to make the SAS more versatile, it would be necessary to enhance and vary its hold-off voltage capability. This can, in principle, be accomplished by stacking several devices in series, or by changing the internal doping and device size. A study to determine the parameters necessary to meet the voltage hold-off specification would therefore be useful.
- (ii) **Studies of Two-Dimensional Effects:** There are basically two important aspects that merit attention in this regard: (a) the issue of current filamentation, and (b) a determination of the role of two-dimensional fields near the device surface. As is well known, current filamentation arises from spatial non-uniformities across the device cross-section, and so is basically a two-dimensional effect. Such non-uniformities can arise from any one of the following reasons: (a) Doping inhomogeneities (either intentional or accidental) during the processing and fabrication steps, (b) The formation of spatially non-uniform traps and defects within the semiconductor, (c) The development of non-uniform fields within the semiconductor during device operation which can lead to non-uniform impact ionization with variable charge creation, and (d) Thermal effects which again can lead to non-uniform carrier generation within the device.

In order to explore these issues, a two-dimensional numerical model has to be developed. Such a model would be a natural extension of the present 1-D simulation scheme. By setting up the 2D model, it would be possible to then directly examine and analyze the following aspects: (i) The possibility of current filamentation for a given device geometry and biasing condition, (ii) The potential for quenching such deleterious filamentation effects through rapid increases in the applied voltage pulse. It is expected that a fast voltage rise times, corresponding to high "dV/dt" values, should work to quench the spatial non-uniformities. This would be a direct result of a high plasma

production within the device which would dilute any existing non-uniformity in the carrier density and electric field. (iii) A direct analysis of the 2D field distributions on possible surface breakdown, and current transient response.

- (iii) **Quantitative Accessment of the Role of Traps:** The issue of electrically active traps has largely been ignored in the context of both device fabrication and theoretical analysis. However, traps could play an important role, and have the following effects: (i) Act as triggering points for current filamentation, (ii) Give rise to spatially non-uniform fields within the devices, (iii) Act as the source of strong band-to-trap impact ionization. This could, in principle, be used as a potential current enhancement mechanism for a quicker turn-on. (iv) Provide the possibility for faster turn-off through indirect recombination, thereby providing narrower current pulses. An analytical effort in this direction would help in device optimization.
- (iv) **Thermal Effects:** The semiconductor devices are primarily meant to function as high-power switching elements, and operate in an uninterrupted fashion over long periods of time. Due to the high power nature of the application, one naturally expects internal thermal heating to be an important issue. The critical future tasks in this area would therefore include: (i) An analysis which included heat generation and thermal propagation within the device, (ii) Determination of the time scales beyond which device heating would begin to get significant, and (iii) The potential impact of device heating on the device performance.
- (iv) **Advanced Heterojunction Concepts:** The SAS devices that have been fabricated and tested have all been Silicon based, and employ p-n junctions. While, their performance is very good, it might be possible to optimize and further push the device capability by employing a heterojunction for the p-n boundary. In so doing, one could gain some of the advantages of heterojunction devices. The advantages of heterojunction-based SAS devices would primarily include: (i) A potential for a higher impact ionization coefficients $\alpha_{p,n}$. It would also be possible to tailor their values. (ii) The higher values of $\alpha_{p,n}$ would provide a faster turn-on current.

VII. SUMMARIZING CONCLUSIONS

In conclusion then, a detailed theoretical analyses and numerical simulations for the SAS device was carried out during the 8-week summer period. A basic one-dimensional, drift-diffusion numerical code was also successfully implemented. Such a theoretical modeling effort

provides quantitative evaluations of the performance limits, and furnishes realistic predictions prior to costly and time consuming fabrication. The code is capable of quantitatively analyzing the device response based on the internal semiconductor device physics. This is an important first step, and should form the backbone for future research. This effort therefore, established the analytical capability for further work and additional research relating to SAS based high-power technology. Some of salient conclusions of this study were as follows:

- (i) A good physical understanding of the SAS device operation was achieved. The internal physics relating to the rapid impact ionization, and the propagation of an electric field wave, were relatively well understood.
- (ii) A 1D, time-dependent model based on the drift-diffusion theory was developed and implemented. The simulation code is fully operational and should form the "building block" for further work in this area.
- (iii) Sub-nanosecond current rise times were obtained through the theoretical simulations. These are in keeping with the experimental observations. As a result, a reasonable validation was made for the theory and mathematical model developed here.
- (iv) Potential for future continuation of the theoretical work in this area of high-power, non-photoconductive switching technology was also identified. A number of germane follow-on research issues were identified.
- (v) The theoretical modeling effort should also provide an optimum parameter space prior to a costly and time consuming device fabrication. This would aid the on-going experimental effort, and lower development costs.

VIII. REFERENCES

1. I. V. Grekhov, Solid State Electronics **32**, 923 (1989).
2. I. V. Grekhov and A. F. Kardo-Sysoev, Sov. Tech. Phys. Lett. **5**, 395 (1979); I. V. Grekhov, A. F. Kardo-Sysoev, and L. S. Kostina, Sov. Tech. Phys. Lett. **5**, 399 (1979).
3. I. V. Grekhov, A. F. Kardo-Sysoev, M. Popova, and S. V. Shenderei, Sov. Phys. Semicond. **17**, 877 (1983).
4. I. V. Grekhov, A. F. Kardo-Sysoev, L. S. Kostina, and S. V. Shenderei, Sov. Phys. Tech. Phys. **26**, 984 (1981).

5. A. F. Kardo-Sysoev, V. M. Efanov, and I. G. Chashnikov, "Fast Power Switches From Picosecond to Nanosecond Time Scale and Their Application to Pulsed Power", to appear in Proc. of the IEEE Intl. Pulsed Power Conf., Albuquerque, July 1995.
6. R. J. Focia, E. Schamiloglu, C. B. Fleddermann, W. Nunnally, and J. Gaudet, "Ultrafast High Power Switching Diodes", to appear in Proc. of the IEEE Intl. Pulsed Power Conf., Albuquerque, July 1995.
7. P. Hadizad, J. Hur, et al., J. Appl. Phys. **71**, 3586 (1992); R. L. Druce, M. D. Pocca et al., Proc. of Optically Activated Switching, SPIE Vol. **1378**, 43 (1990).
8. R. A. Falk and J. C. Adams, Proc. of Optically Activated Switching, SPIE Vol. **1378**, 70 (1990); F. J. Zutavern, G. M. Loubliel et al., Proc. of Optically Activated Switching III, SPIE Vol. **1873**, 50 (1992).
9. I. V. Grekhov, V. M. Efanov, A. F. Kardo-Sysoev, and S. Shenderey, Solid State Electronics **28**, 597 (1985).
10. I. V. Grekhov, V. Efanov, A. F. Kardo-Sysoev, and S. Shenderei, Sov. Tech. Phys. Lett. **9**, 188 (1983); A. F. Kardo-Sysoev and M. V. Popova, Sov. Phys. Semicond. **25**, 1 (1991).
11. B. L. Gelmont and M. Shur, Sov. Phys. JETP Lett. **11**, 350 (1970).
12. J. B. Gunn, IBM J. Res. Dev. **8**, 141 (1964).
13. R. Courant, K. Friedrichs, and H. Lewy, IBM J. Res. Dev. **11**, 215 (1967).
14. For example, S. Selberherr in *Analysis and Simulation of Semiconductor Devices*, (Springer-Verlag, Wein, 1984).
15. For example, W. T. Read, Bell Sys. Tech. J. **37**, 401 (1958).

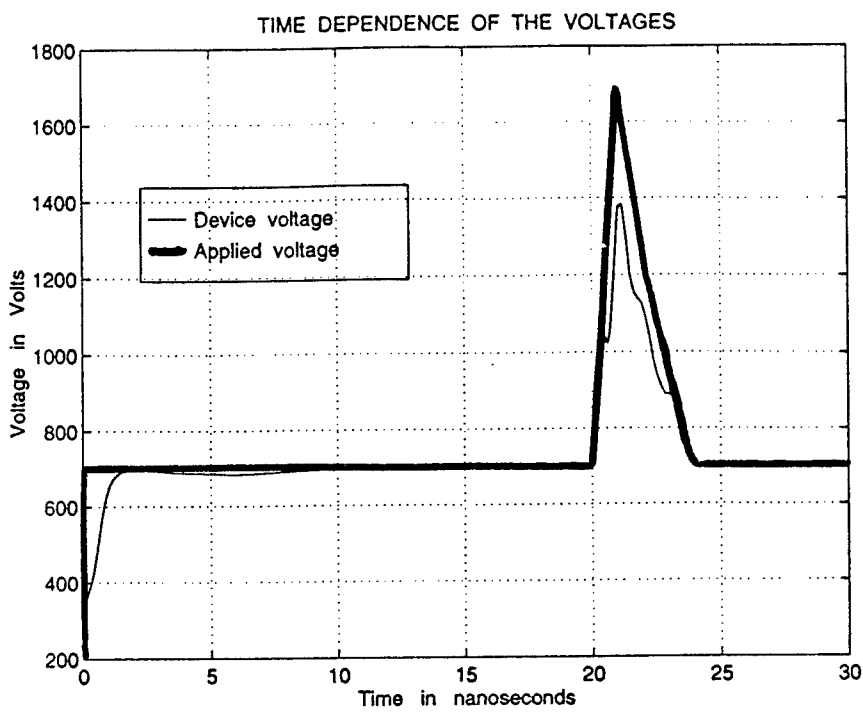


Fig. 1. Waveforms corresponding to the biasing pulse and the SAS device voltage.

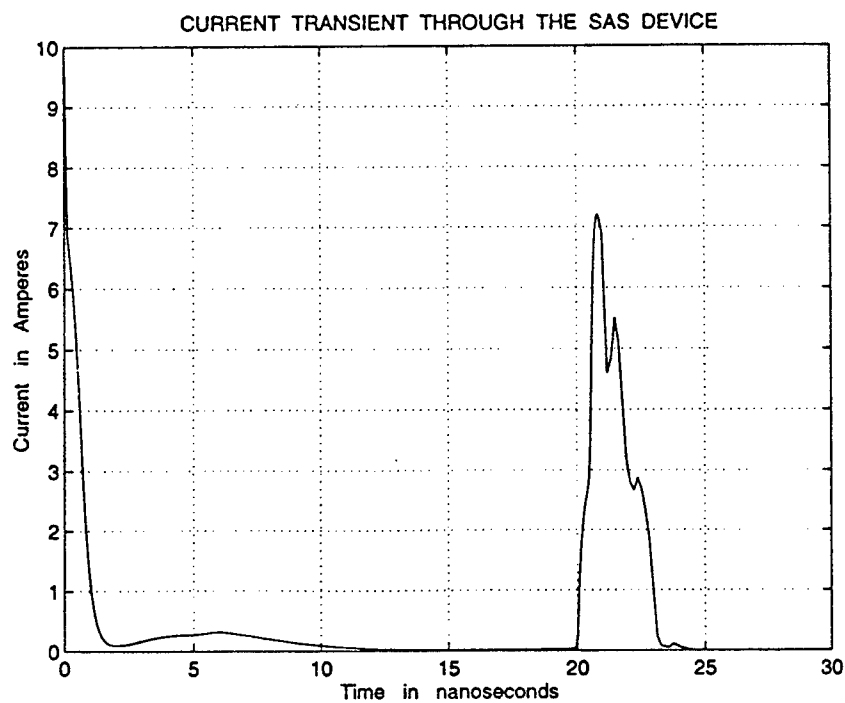


Fig. 2. Simulation result showing the current transient through the SAS device.

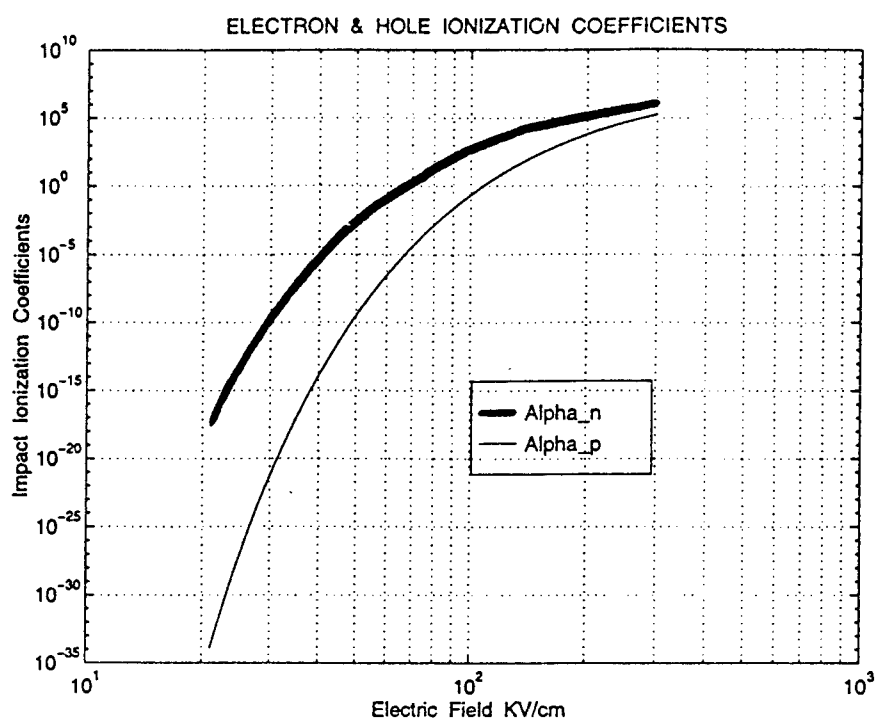


Fig. 3. Field dependence of the electron and hole ionization coefficients in Si at 300 K.

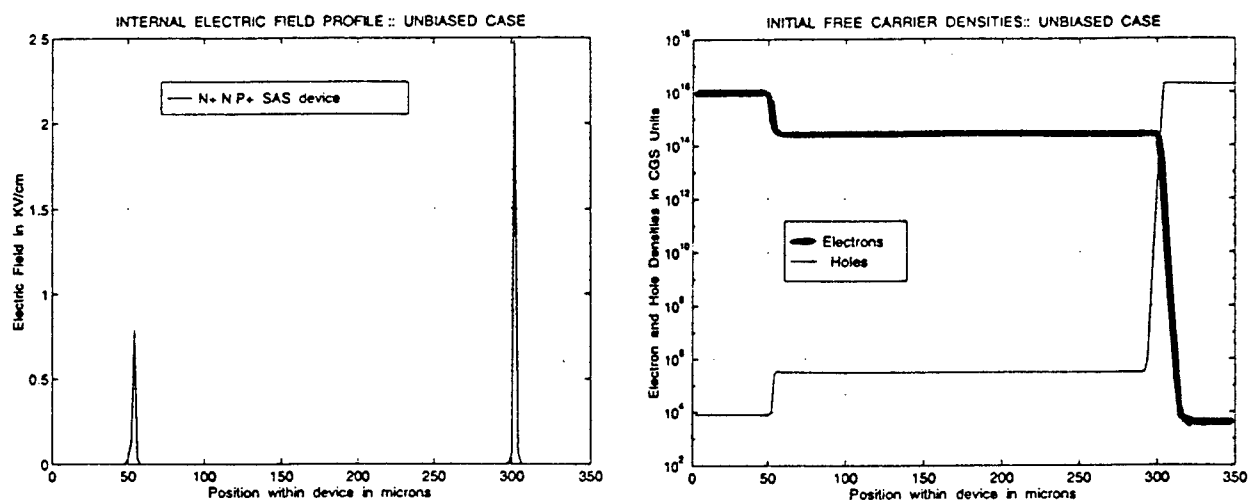


Fig. 4 Initial internal distribution profiles under steady-state unbiased conditions.
 (a) The electric field profile, and (b) The electron and hole density profiles.

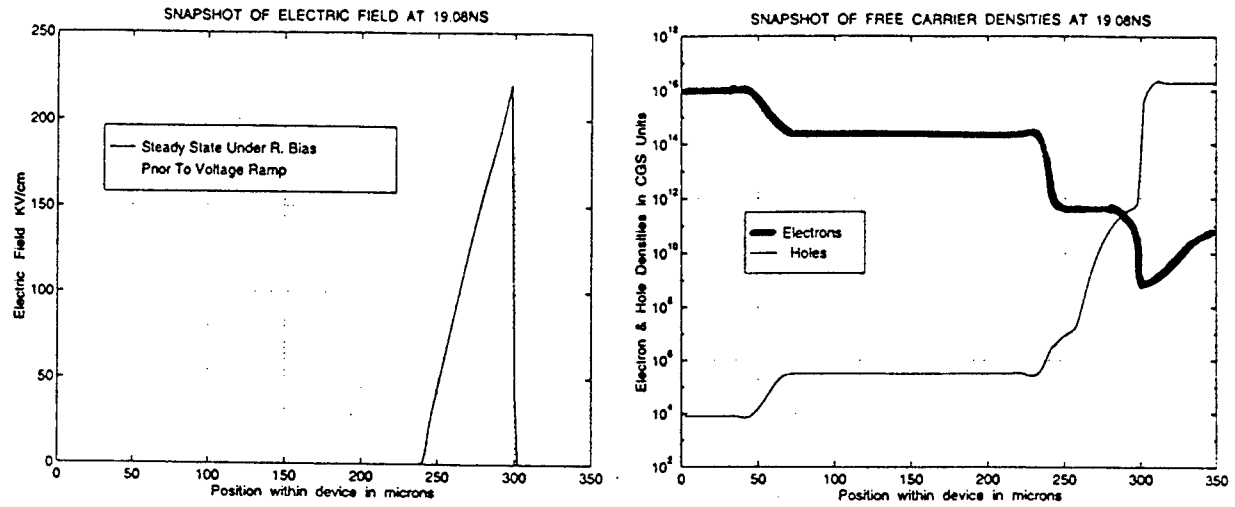


Fig. 5 Internal profiles at 19.08 ns in response to the voltage pulse of Fig. 1. (a) The electric field profile, and (b) The electron and hole density profiles.

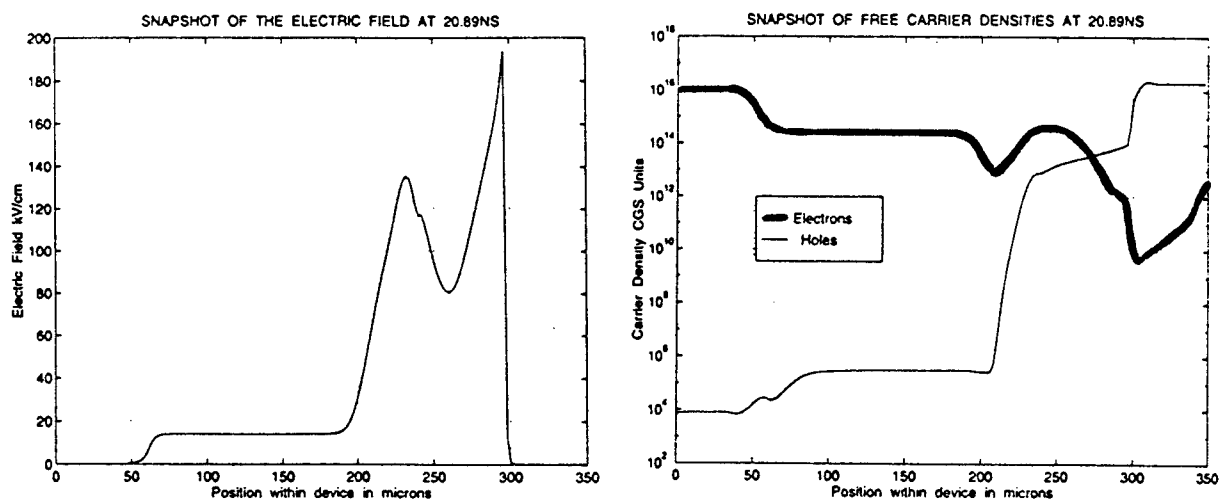


Fig. 6 Internal profiles at 20.89 ns in response to the voltage pulse of Fig. 1. (a) The electric field profile, and (b) The electron and hole density profiles.

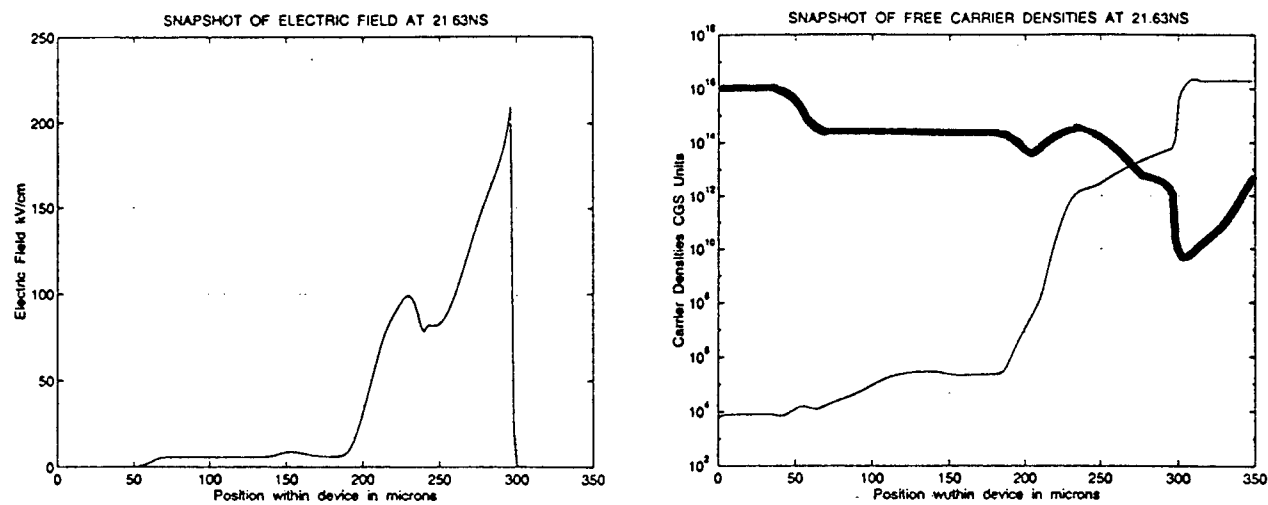


Fig. 7 Simulation results showing the internal profiles at 21.63 ns. (a) The electric field profile, and (b) The electron and hole density profiles.

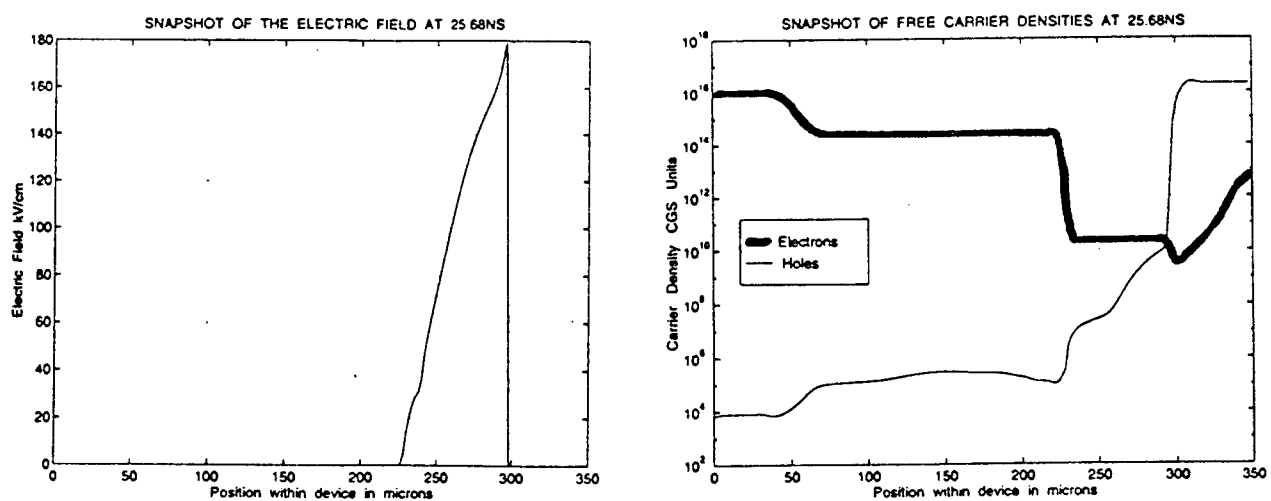


Fig. 8 Internal profiles obtained from numerical simulations at 25.68 ns. (a) The electric field profile, and (b) The electron and hole density profiles.

**THEORY AND APPLICATION OF THE PRINCIPLE OF FREQUENCY SHIFTING OF A
SOURCE WAVE BY A SWITCHED TIME-VARYING MAGNETOPLASMA MEDIUM**

Dikshitulu K. Kalluri
Professor
Department of Electrical Engineering

University of Massachusetts Lowell
Lowell, MA 01854

Final Report for:
Summer Faculty Research Program
Phillips Laboratory / Geophysics Directorate

Sponsored by:
Air Force Office of Scientific Research
Bolling Air Force Base, DC

and

Phillips Laboratory / Geophysics Directorate

September 1995

THEORY AND APPLICATION OF THE PRINCIPLE OF FREQUENCY SHIFTING OF A
SOURCE WAVE BY A SWITCHED TIME-VARYING MAGNETOPLASMA MEDIUM

Dikshitulu K. Kalluri
Professor
Department of Electrical Engineering
University of Massachusetts Lowell
Lowell, MA 01854

Abstract

The author of this report had investigated earlier some aspects of the transformation in the properties of an electromagnetic signal brought out by a switched time-varying magnetoplasma medium. The main effect of switching the medium is the splitting of the source (incident) wave into new waves whose frequencies are different from the incident wave frequency. The author has solved the following three frequency-shifting related research problems during the summer of 1995:

- A. Developed a perturbation technique to find the reflection coefficient of the upshifted wave due to rapid creation of a plasma medium and relate it to the rise time of the electron density profile.
- B. Completed the study of the phenomenon of the frequency upshifting and power intensification of a whistler wave due to the decay of the electron density.
- C. Completed the study of the phenomenon of the conversion of the whistler wave into a helical magnetic wiggler field when the strength of the static magnetic field decays with time.

These topics are of immediate interest to the Ionospheric Effects Division of Phillips Laboratory at Hanscom in connection with their investigations on lightning induced effects in the ionosphere. One of the important parameters in these investigations is the time-varying plasma frequency due to the transient enhancement of the ionization. To focus on this effect, a simplifying assumption is made that the plasma is spatially homogeneous and unbounded.

THEORY AND APPLICATION OF THE PRINCIPLE OF FREQUENCY SHIFTING OF A SOURCE WAVE BY A SWITCHED TIME-VARYING MAGNETOPLASMA MEDIUM

Dikshitulu K. Kalluri

I. General Introduction

The author of this report had investigated [1] - [11] some aspects of the transformation in the properties of an electromagnetic signal brought out by a switched time-varying magnetoplasma medium. The main effect of switching the medium is the splitting of the source (incident) wave into new waves whose frequencies are different from the incident wave frequency. Frequency shifting of electromagnetic radiation by rapid creation has drawn considerable attention in recent years due to its potential applications in generation of tunable radiation over a broad frequency range. The frequency shifting property is also useful in diagnosing the time evolution of the electron density of the plasma medium.

Most of the work done so far involved isotropic plasmas. Preliminary work done by the author on magnetized plasmas indicates that remarkable effects may be obtained by modifying magnetoplasma parameters in time. The effect of the anisotropy in the switched medium is to increase the number of new waves (some with frequency upshifts and some with frequency down shifts), increase the shift ratio and also increase the power intensity. The resonance phenomena in a magnetoplasma offer some more possibilities for signal generation and processing applications. Some of the applications like diagnosing the transient plasmas in fusion machines and the study of lightning -induced effects in the ionosphere require a well developed theory for wave propagation in time-varying magnetoplasma medium.

Theoretical work done so far assumed two extreme cases of approximation for the creation of the medium: (1) Sudden creation (2) The medium properties change slowly enough that WKB approximations may be applied. The author has a broad objective of developing perturbation and variational methods to obtain accurate solutions when the time profile of the particle density is of arbitrary nature. Specific results have to be obtained by making suitable approximations based on physical principles and mathematical techniques. The important parameters are (i) frequency of the source wave (ii) rise time or decay time of the electron density profile and peak electron density (iii) strength and direction of the static magnetic field.

As a first step in achieving these broad objectives, the author, in consultation with his focal point, has investigated the following three problems during the summer of 1995:

- A. Develop a perturbation technique to find the reflection coefficient of the upshifted wave due to rapid creation of a plasma medium and relate it to the rise time of the electron density profile.
- B. Continue the study of the phenomenon of the frequency upshifting and power intensification of a whistler wave due to the decay of the electron density.
- C. Continue the study of the phenomenon of the conversion of the whistler wave into a helical magnetic wiggler field when the strength of the static magnetic field decays with time.

These topics are of immediate interest to the Ionospheric Effects Division of Phillips Laboratory at Hanscom in connection with their investigations on lightning induced effects on the ionosphere. One of the important parameters in these investigations is the time-varying plasma frequency due to the transient enhancement of the ionization. To focus on this effect, a simplifying assumption is made that the plasma is spatially homogeneous and unbounded. In due course the theory will be extended to cover the cases of simultaneous variation of magnetoplasma parameters in space and time, and the effect of these changes on the propagation of pulses and wave packets.

Full reports on these three topics are being prepared for publication and a brief account including results are given below.

SECTION A

Green's Function and a Perturbation Technique for a Switched Plasma Medium

A1. Introduction

The main effect of switching (creating a temporal discontinuity in the properties of a medium) a medium is the splitting of the source (incident) wave into new waves whose frequencies are different.

Lightning induced effects in the ionosphere cause a temporary enhancement of ionization. Such transient plasmas have a time-varying plasma density $\omega_p(t)$ with a rise time T_r . If the period t_0 of a source wave existing before the transient effect begins is much less than the rise time, the

ionization change may be idealized as a sudden switching of the medium. The solution to this initial value problem with a step-change electron density profile is known [1], [12] and will be considered as a reference profile.

The switching action gives rise to a reflected wave (propagating in the opposite direction to that of the source wave) and a transmitted wave at an upshifted frequency $\omega_2 = (\omega_0^2 + \omega_p^2)^{1/2}$.

The topic of this paper is the solution of the initial value problem when t_0 is comparable to the rise time T_r . The initial motivation for investigating the problem is given below.

There is considerable interest in the ionospheric physics community to investigate the recently discovered 'Sprites' phenomenon [13], [14], [15] which are red emissions in the lower D region induced by the lightning discharges from cloud to ground. The preliminary indications are that the 'Sprite' is a plasma with electron density enhanced by about 10^1 to 10^3 / cc in a rise time of about 100 μ s.

The evolution of the electron density in the Sprite can be diagnosed by tracking from ground the instantaneous frequency of the upshifted reflected wave with a suitable instrument [16]. If the source wave frequency is very high (as in the case of incoherent scatter radar, the reflection coefficient is negligible and the wave can not be detected by the most sensitive receivers). A source wave in VLF range is suitable but in this case the rise time is comparable to the period of the source wave.

A2. Reflection Coefficient

Let an electromagnetic wave of angular frequency ω_0 be propagating in positive z direction in a time varying plasma medium with plasma density $\omega_p(t)$. The time-varying component of the electric field $e(t)$ satisfies the differential equation

$$\frac{d^2 e}{dt^2} + \omega^2(t) e = 0 \quad (1a)$$

where

$$\omega^2(t) = \omega_0^2 + \omega_p^2(t) \quad (1b)$$

The solution of (1) will be sought in terms of the known solution (also called as reference solution) of the step profile problem [1], [12] $\omega_p^2(t)$ given in (2):

$$\tilde{\omega}_p^2(t) = \omega_{p1}^2, t < 0; \quad \tilde{\omega}_p^2(t) = \omega_{p2}^2, t > 0; \quad (2a)$$

$$\frac{d^2 e_0}{dt^2} + \tilde{\omega}_p^2(t) e_0 = 0 \quad (2b)$$

$$\tilde{\omega}_p^2(t) = \omega_0^2 + \omega_p^2(t) \quad (2c)$$

$$e_0 = \exp(j\omega_1 t), t < 0; \quad e_0 = R_0 \exp(-j\omega_2 t) + T_0 \exp(j\omega_2 t), t > 0 \quad (3a)$$

$$\omega_1 = (\omega_0^2 + \omega_{p1}^2)^{1/2}, \quad \omega_2 = (\omega_0^2 + \omega_{p2}^2)^{1/2} \quad (3b)$$

$$R_0 = (\omega_2 - \omega_1)/(2\omega_2), \quad T_0 = (\omega_2 + \omega_1)/(2\omega_2) \quad (3c)$$

We seek the solution of (1) subject to the same asymptotic behavior at $t \rightarrow -\infty$ and $t \rightarrow \infty$, i. e.,

$$e(t) = \exp(j\omega_1 t), t \rightarrow -\infty; \quad e(t) = R \exp(-j\omega_2 t) + T \exp(j\omega_2 t), t \rightarrow \infty \quad (4)$$

The parameters R and T are to be determined in terms of R_0 , T_0 and $\Delta\omega_p^2(t)$, where

$$\Delta\omega_p^2(t) = \Delta\tilde{\omega}_p^2(t) = \omega_p^2(t) - \tilde{\omega}_p^2(t) \quad (5)$$

The electric field e may be expressed in a series in powers of $\Delta\omega^2$:

$$e = e_0 + e_1 + e_2 + \dots \quad (6)$$

From (1) and (2) the successive corrections to e_0 are obtained by solving

$$\frac{d^2 e_n}{dt^2} + \omega^2(t) e_n = -\Delta \omega^2 e_{n-1} \quad (7)$$

The solution of (7) may be given in terms of Green's function $G(t, \tau)$:

$$\frac{d^2 G}{dt^2} + \omega^2(t) G = \delta(t - \tau) \quad (8)$$

$$e_n(t) = - \int_{-\infty}^t d\tau \Delta \omega^2(\tau) G(t, \tau) e_{n-1}(\tau) \quad (9)$$

$$e(t) = e_0(t) - \int_{-\infty}^t d\tau \Delta \omega^2(\tau) G(t, \tau) e(\tau) \quad (10)$$

Green's function is constructed in terms of e_0 given by (3) and $e^{(0)}$ given by (11):

$$e^{(0)} = \exp(-j\omega_2 t), t > 0; \quad e^{(0)} = R^{(0)} \exp(+j\omega_1 t) + T^{(0)} \exp(-j\omega_1 t), t < 0 \quad (11a)$$

$$R^{(0)} = (\omega_1 - \omega_2) / (2\omega_1), \quad T^{(0)} = (\omega_1 + \omega_2) / (2\omega_1) \quad (11b)$$

In analogy with the spatial case [17], [18], $e^{(0)}$ is constructed from the complementary problem in which the source wave is in medium 2. This is an artificial problem since the independent variable here is t and the second medium is the medium for $t > 0$. However the problem will have physical meaning if we consider that the second equation in (11b) represents two source waves, one of strength $R^{(0)}$ propagating along positive z axis and another of strength $T^{(0)}$ propagating along the negative z -axis. It is easy to show that the solution for $t > 0$ is then given by the first equation in (11a).

In terms of these two functions

$$G(t, \tau) = e_0(t_>) e^{(0)}(t_<) / D \quad (12a)$$

where

$$t_> = \max(t, \tau), \quad t_< = \min(t, \tau) \quad (12b)$$

and D is the Wronskian of e_0 and $e^{(0)}$:

$$D = \begin{vmatrix} e^{(0)} & e_0 \\ e^{(0)}/ & e_0/ \end{vmatrix} \quad (12c)$$

Here the superscript (/) stands for the time derivative. It is verified that (12) satisfies the requirements that G is continuous and G' has a unit discontinuity at $t = \tau$. Evaluation of the Wronskian gives $D = j(\omega_1 + \omega_2)$. Explicit expressions for $G(t, \tau)$ valid for various regions of (t, τ) plane are given in (13) on the next page.

As $t \rightarrow \infty$, $t_> = t$, $t_< = \tau$ and

$$G(t, \tau) = e_0(t) e^{(0)}(\tau) / D \quad (14)$$

$$e_n(t) = -\frac{e_0(t)}{D} \int_{-\infty}^{\infty} d\tau \Delta\omega^2(\tau) e^{(0)}(\tau) e_{n-1}(\tau) \quad (15)$$

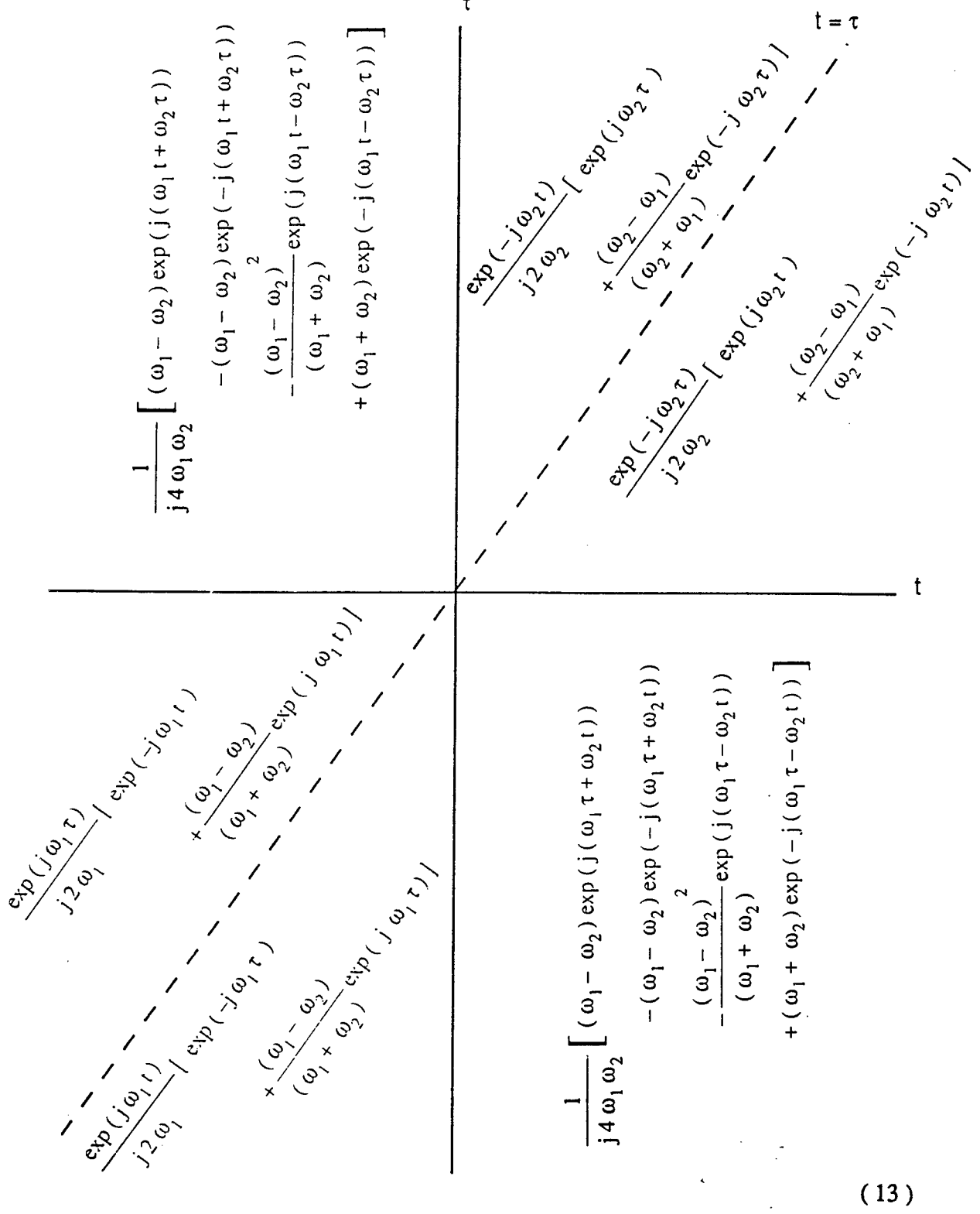
$$e(t) = (1 - \frac{1}{D}) e_0(t) \int_{-\infty}^{\infty} d\tau \Delta\omega^2(\tau) e^{(0)}(\tau) e(\tau) \quad (16)$$

$$R = (1 - \frac{1}{D}) R_0 \int_{-\infty}^{\infty} d\tau \Delta\omega^2(\tau) e^{(0)}(\tau) e(\tau) \quad (17)$$

$$T = (1 - \frac{1}{D}) T_0 \int_{-\infty}^{\infty} d\tau \Delta\omega^2(\tau) e^{(0)}(\tau) e(\tau) \quad (18)$$

The first order correction term in the reflection coefficient R_1 is therefore given by

$$R_1 = \frac{j}{\omega_1 + \omega_2} \int_{-\infty}^{\infty} d\tau \Delta\omega^2(\tau) e^{(0)}(\tau) e(\tau) \quad (19)$$



The term $e^{(0)}(t) e_0(t)$ involves exponential functions and may be expanded in powers of $\omega_1 t$ and $\omega_2 t$. If these are small in magnitude in the range $-T_{r1} < t < T_{r2}$, we can approximate by keeping up to the first order terms in $(\omega_1 t)$ and $(\omega_2 t)$:

$$e^{(0)}(\tau) e_0(\tau) \approx 1 + j 2 \omega_1 \tau R^{(0)}, \quad -\infty < \tau < 0 \quad (20a)$$

$$e^{(0)}(\tau) e_0(\tau) \approx 1 - j 2 \omega_2 \tau R_0, \quad 0 < \tau < \infty \quad (20b)$$

$$R_1 = R_0 \left[\frac{j}{\omega_2 + \omega_1} \int_{-\infty}^{\infty} d\tau \Delta\omega^2(\tau) + \frac{\omega_2 - \omega_1}{\omega_2 + \omega_1} \int_{-\infty}^{\infty} d\tau \tau \Delta\omega^2(\tau) \right] \quad (21)$$

Equation (21) is obtained by making use of (22):

$$R_0 \omega_2 = -R^{(0)} \omega_1 = \frac{1}{2} (\omega_2 - \omega_1) \quad (22)$$

If we choose the origin so that $\Delta\omega_2(t)$ curve has odd symmetry as shown in Figure 1 and the rise time T_r is given by

$$T_r = 2 T_{r1} = 2 T_{r2} \quad (23)$$

the first integral on the right side of (21) is zero and the second term gives

$$R_1 = R_0 \left[\frac{\omega_2 - \omega_1}{\omega_2 + \omega_1} \int_{-\infty}^{\infty} d\tau \tau \Delta\omega^2(\tau) \right] \quad (24)$$

A3. Illustrative Example

The data for the illustrative example is chosen so as to be relevant to VLF diagnostics of the time evolution of the electron density in Sprite induced by the lightning. The source frequency f_0 is chosen to be 25 kHz in the VLF range. The plasma frequency rises from $f_{p1} = 0$ and $f_{p2} = 28.5$ kHz (9 kHz) corresponding to an ionization from 0 electron density to $10^2 / \text{cc}$ (10^1) in a rise

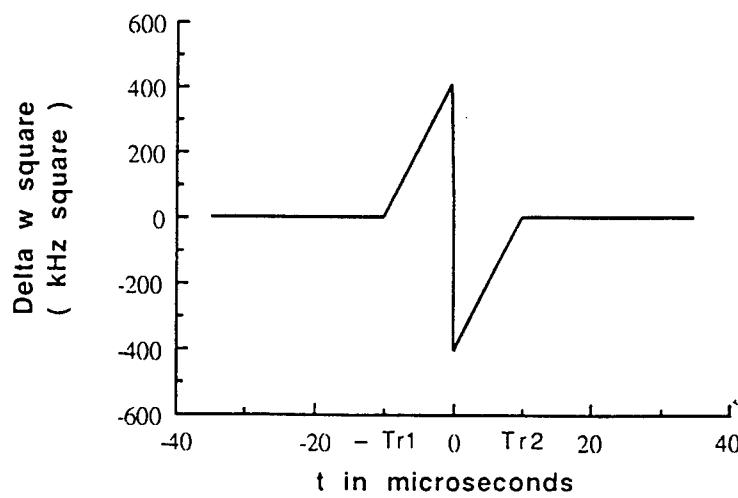
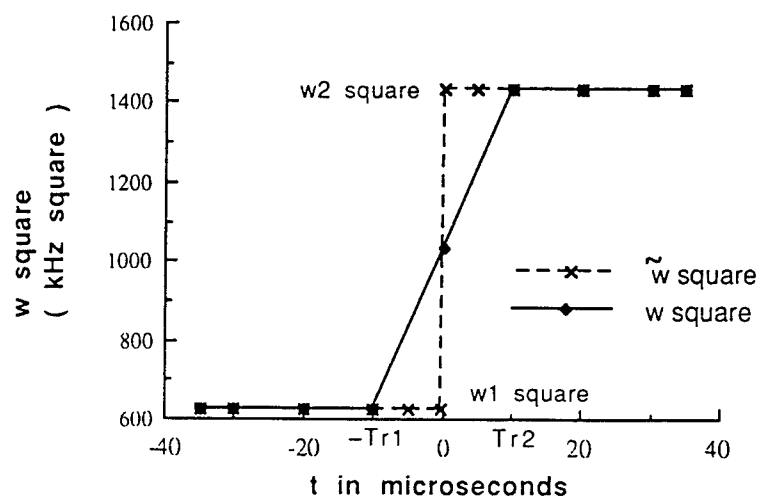
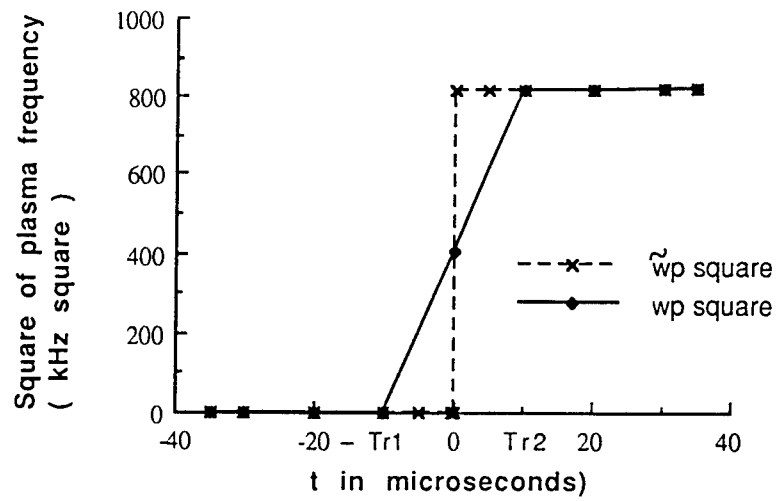


Figure 1

time T_r . If the ω_{p2} time profile is linear, R_1 , from (24),

$$R_1 \approx - R_0 (\omega_2 - \omega_1)^2 T_r^2 / 24 \quad (25)$$

and $R \approx R_0 + R_1$ is given by:

$$R \approx R_0 \left[1 - \frac{2}{3} (\prod R_0 f_2 T_r)^2 \right] \quad (26)$$

where f_2 is the final upshifted frequency and is given by

$$f_2 = (f_0^2 + f_{p2}^2)^{1/2} \quad (27)$$

Figure 2 shows the reflection coefficient vs. rise time for two values of ω_p .

The reflected wave is of sufficient strength for detection and the instantaneous frequency of the reflected signal

$$f(t) = (f_0^2 + f_p^2(t))^{\frac{1}{2}} \quad (28)$$

tracks the time profile of the electron density.

A 4. Future Work

In a sprite, the electron density may reach up to $10^3/\text{cc}$ corresponding to a plasma frequency $f_{p2} = 90 \text{ kHz}$ and the rise time may reach up to a millisecond. For these higher range values the second term in (26) which is a correction term is too large and the approximations break down.

Further work is needed to make this technique applicable to a larger range of parameters. Variational techniques can be developed. It is also possible to develop perturbation and variational techniques taking the reference profile to be a very slow profile and obtain the corrections for a profile faster than the reference profile.

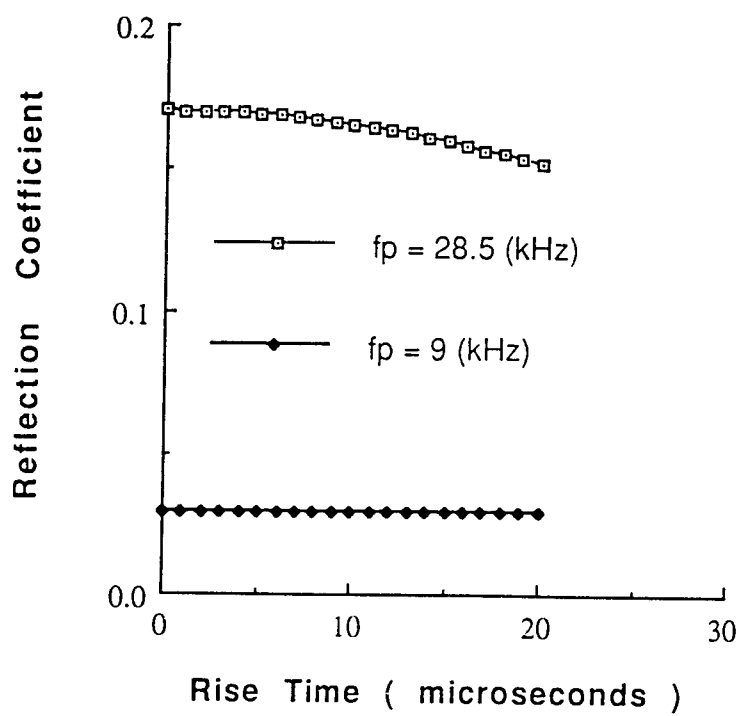


Figure 2

The application of these techniques to the switched magnetized plasma is more involved. The author has extensively worked on the solution of the reference profiles and has all the pieces of information and experience to develop the solutions of the magnetized plasma cases.

SECTION B

Frequency Upshifting with Power Intensification of a Whistler Wave by a Collapsing Plasma Medium

A full report on this topic is being prepared for publication [19]. Summary and an illustrative example are included in this report.

B1. Summary

A source wave is assumed to be present in an unbounded magnetoplasma medium. The parameters are such that the refractive index is greater than one. A wave propagating in 'whistler mode' is an example of such a wave [20]. By collapsing the ionization , it is possible to obtain a frequency upshifted wave with power intensification.

Two limiting cases of (i) sudden collapse and (ii) slow decay are considered. In either case , it is shown that the final upshifted frequency is the source frequency multiplied by the refractive index.

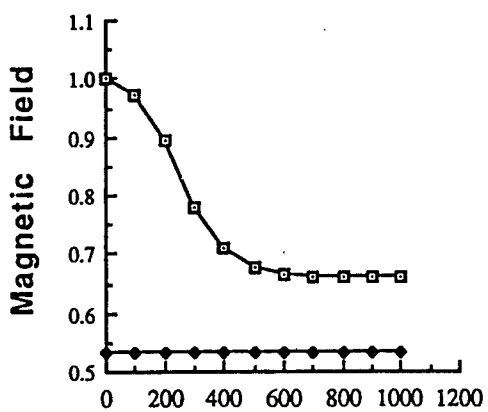
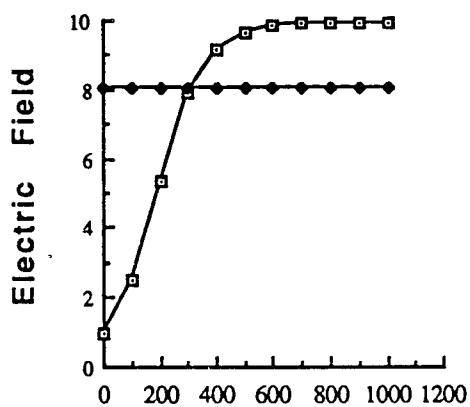
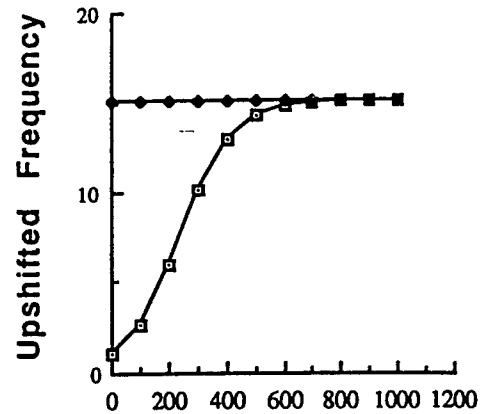
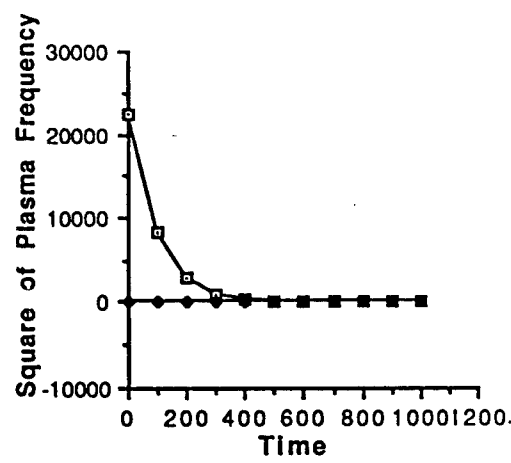
When the source frequency is much less than electron gyrofrequency the refractive index n_w is quite large and the electric field is intensified by a factor of $n_w / 2$ for the case of sudden collapse and by a factor of $n_w / \sqrt{2}$ for the case of slow decay. The corresponding intensification factors for the power density are $n_w / 4$ and $n_w / 2$. A physical explanation of the results, based on energy balance, is offered.

B2. Illustrative example

Figure 3. illustrates the results for an exponential decay profile whose time constant is (1/b):

$$\omega_p^2(t) = \omega_{p0}^2 e^{-bt} \quad (29)$$

All variables are normalized with reference to the source wave quantities. The source wave



$$\omega_0 = 1, \quad \omega_b = 100, \quad \omega_{p0} = 150, \quad b = 0.01$$

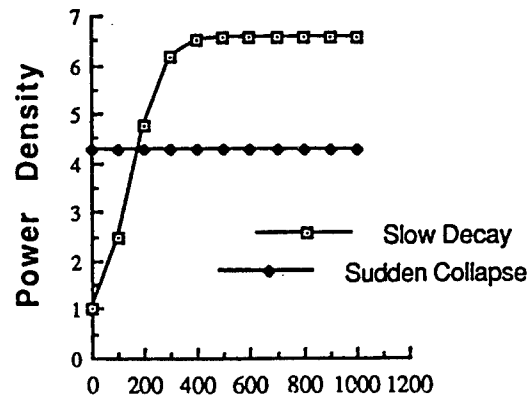


Figure 3

frequency ω_0 is taken to be 1 so that ω_1 gives the frequency upshift ratio. The parameters ω_b and ω_{p0} are assigned the values 100 and 150 respectively. The parameters are such that Eckersley approximation is valid. A value of 0.01 is assigned to b . The parameter describes a slow decay since $(100 / 2\pi)$ cycles of the source wave are accommodated in one time constant. The independent variable, time, is normalized with respect to the period of the source wave.

The results shown in the Figure B1 for slow decay are numerically computed from (12), (14), and (15) of [19] and the following values are obtained at $t = 1000$: $\omega_1 / \omega_0 = 15.10$, $E_1 / E_0 = 9.96$, $H_1 / H_0 = 0.657$ and $S_1 / S_0 = 6.57$. Approximate values computed from (17) give for $t \rightarrow \infty$: $\omega_1 / \omega_0 \approx n_w \approx 15$, $E_1 / E_0 \approx 9.81 \approx 10.6$, $H_1 / H_0 \approx 0.654 \approx 0.707$ and $S_1 / S_0 \approx 6.38 \approx 7.5$.

Figure 3 also shows, for comparison, horizontal lines which are the results for sudden collapse. These are obtained from (2b) and (7) of [19] and are $n_0 = \omega_1 / \omega_0 = 15.11$, $E_1 / E_0 = 8.06$, $H_1 / H_0 = 0.533$ and $S_1 / S_0 = 4.294$: Approximate values obtained from (9) are: $n_w \approx 15$, $E_1 / E_0 \approx 7.5$, $H_1 / H_0 \approx 1/2$ and $S_1 / S_0 \approx 3.75$. Here S stands for the power density. The approximate results are in agreement with numerically computed results confirming (9) and (17) of [19] may be used as simple approximate expressions under Eckersley approximation.

SECTION C

Conversion of a Whistler Wave into a Controllable Helical Wiggler Magnetic Field

A full report on this topic is being prepared for publication [21]. Summary and an illustrative example are included in this report.

C1. Summary

Coherent radiation generated in a Free Electron Laser (FEL) [22] is due to the interaction of an electron beam with a wiggler magnetic field which is a spatially varying static (zero frequency) magnetic field. Linear or helical wigglers can be constructed from electromagnets or permanent magnets. The tunability of FEL comes from the variability of the parameter γ_0 through the kinetic energy of the electrons. When once a FEL is constructed λ_w is fixed.

This section deals with the principle of establishing a helical wiggler magnetic field with

controllable λ_w even if the source wave is of fixed frequency. A whistler wave [20] which propagates in a magnetoplasma when the source frequency ω_0 is less than the electron gyrofrequency ω_b , gives rise to a wiggler magnetic field in the plasma when the static magnetic field is switched off. The strength and the period of the wiggler field depends on the parameters of the magnetoplasma medium . When the parameters are such that ω_0 is much less than ω_b and ω_p , the total energy of the source wave is converted into the magnetic energy of the wiggler field.

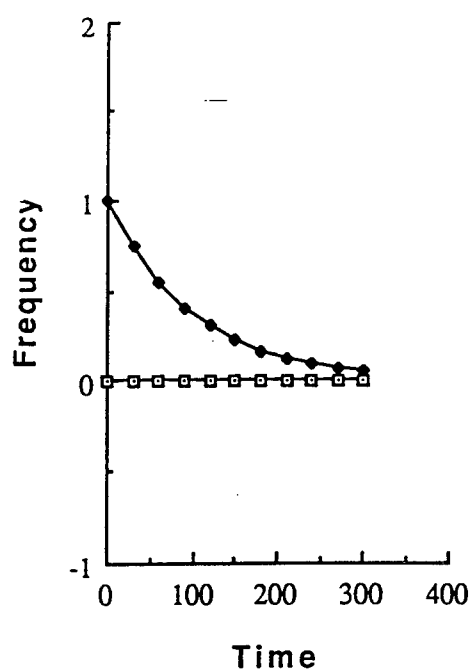
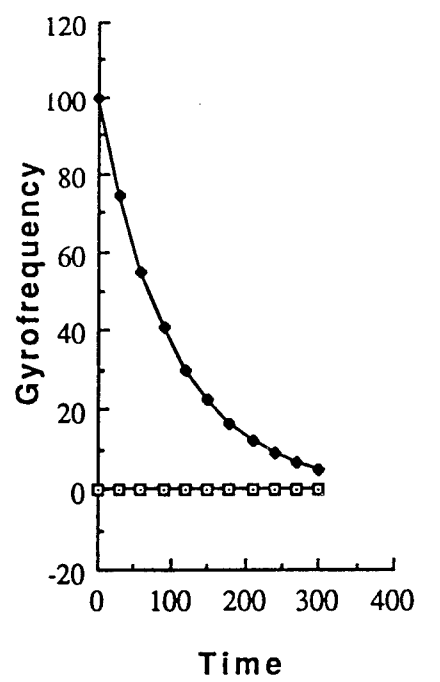
C2. Illustrative example

Figure 4. illustrates the results for an exponential decay profile whose time constant is (1/b):

$$\omega_b(t) = \omega_{b0} e^{-bt} \quad (30)$$

All variables are normalized with reference to the source wave quantities. The source wave frequency ω_0 is taken to be 1. The parameters ω_{b0} and ω_p are assigned the values 100 and 1000 respectively. .The parameters are such that Eckersley approximation [20] is valid. A value of 0.01 is assigned to b. The parameter describes a slow decay since (100 / 2π) cycles of the source wave are accommodated in one time constant. The independent variable, time, is normalized with respect to the period of the source wave.

The results shown in the Figure 4 for slow decay are numerically computed from the equations (18), (28 a) and (28 b) derived in the paper [21] and the following values are obtained at t = 1000: $\omega_b / \omega_0 = (4.54) 10^{-3}$, $\omega_3 / \omega_0 = (4.54) 10^{-5}$, $E_3 / E_0 = (4.54) 10^{-5}$ and $H_3 / H_0 = 1.000048$. Figure 4 shows also, for comparison, horizontal lines which are the results for sudden collapse given by (11) of [21] for the third wave. Irrespective of the rate of collapse of B_s , a strong wiggler field is generated.



$$\omega_0 = 1, \quad \omega_{b0} = 100,$$

$$\omega_p = 1000, \quad b = 0.01$$

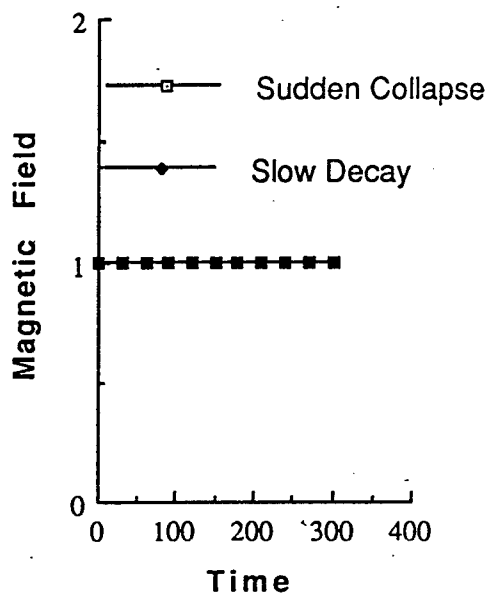
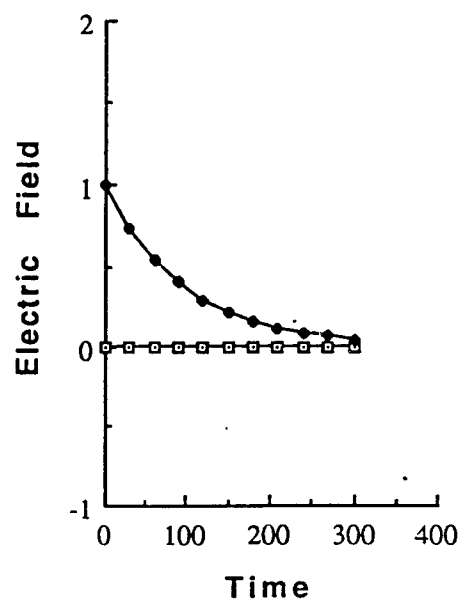


Figure 4

REFERENCES

- [1] D. K. Kalluri (1988), " On Reflection from a Suddenly Created Plasma Half-Space : Transient solution ", *IEEE Trans. Plasma Science* , Vol. 16, No. 2, pp 11 - 16; Vol. 16, No. 5, p. 597.
- [2] D. K. Kalluri (1989), " Effect of Switching a Magnetoplasma Medium on a Traveling Wave: Longitudinal Propagation ", *IEEE Trans. Antennas and Propagation* , Vol. 37, No. 12, pp.1638 - 1642.
- [3] V. R. Goteti and D. K. Kalluri (1989), "Wave Propagation in a Switched-On Time-Varying Plasma Medium", *IEEE Transactions on Plasma Science* , Vol. 17, No. 5, pp. 828 -833.
- [4] D. K. Kalluri and V. R. Goteti (1989), "WKB Solution for Wave Propagation in a Decaying Plasma Medium", *Journal of Applied Physics* , Vol. 66, No. 8, pp. 3472 - 3475.
- [5] V. R. Goteti and D. K. Kalluri (1990), " Wave propagation in Switched Magnetoplasma Medium: Transverse Propagation", *Radio Science* , Vol. 25, No. 1, pp. 61 - 72.
- [6] D. K. Kalluri and V. R. Goteti (1990), " Damping Rates of Waves in a Switched Magnetoplasma Medium: Longitudinal Propagation", *IEEE Transactions on Plasma Science* , Vol. 18, No. 5, pp. 797 - 801.
- [7] D. K. Kalluri and V. R. Goteti (1992), " Frequency Shifting of Electromagnetic Radiation by Sudden Creation of a Plasma Slab," *Journal of Applied Physics*, 72(10): pp. 4575–4580.
- [8] S. R. V. Madala and D. K. Kalluri (1992), " Frequency - Shifting of a Wave Traveling in an Isotropic Plasma Medium due to Slow Switching of a Magnetic Field," *Plasma Sources Science & Technology*, 1(4): pp. 242–248.
- [9] S. R. V. Madala and D. K. Kalluri (1993), " Longitudinal Propagation of Low Frequency Waves in a Switched Magnetoplasma Medium," *Radio Science*, 28(2): pp. 121 - 128.
- [10] D. K. Kalluri (1993), " Frequency-Shifting Using Magnetoplasma Medium," *IEEE Transactions on Plasma Science*, 21(1): pp. 77–81.

- [11] D. K. Kalluri, V. R. Goteti and Andrew Sessler (1993), "WKB Solution for Wave Propagation in a Time - varying Magnetoplasma Medium: Longitudinal Propagation," *IEEE Transactions on Plasma Science*, 21(1):pp. 70–76.
- [12] C.L Jiang (1975), " Wave Propagation and Dipole Radiation in a Suddenly Created Plasma ", *IEEE Trans. Antennas and Propagation* , Vol. 23, No. 1, pp 83 - 90.
- [13] J. V. Rodriguez, U. S. Inan and T. F. Bell (1992), "D Region Disturbances Caused by Electromagnetic Pulses From Lightning", *Geophys. Res. Lett.*, Vol. 19, p. 1815.
- [14] D. D. Sentman, E. M. Wescott, D. L. Osborne, D. L. Hampton and M. J. Heavner (1995), " Preliminary REsults from the Sprites 94 Aircraft CAmpaign: 1. Red Sprites ", *Geophysical Research Letters*, Vol. 22, pp. 361 - 364.
- [15] H. L. Rowland, R. F. Fernsler, J. D. Huba and P. A. Bernhardt (1995), " Lightning Driven EMP in the Upper Atmosphere ", Vol. 22, pp. 361 - 364.
- [16] K. Fitzgerald (1988), " Instrumentation ", *IEEE Spectrum*, Vol. 25, No. 1, p. 49.
- [17] D. G. Triezenberg (1973), " Capillary Waves in a Diffuse Liquid-Gas Interface ", Ph. D. Thesis, University of Maryland.
- [18] J. Lekner, *Theory of Reflection*, Boston: Kluwer, 1987.
- [19] D. K. Kalluri (1994), " Frequency Upshifting with Power Intensification of a Whistler Wave by a Collapsing Plasma Medium", Submitted for publication.
- [20] H. G. Booker, *Cold Plasma Waves* . Hingham, Mass.: Kluwer, 1984
- [21] D. K. Kalluri (1995), " Conversion of a Whistler Wave into a Controllable Helical Wiggler Magnetic Field ", to be published.
- [22] V. L. Granatstein and I. Alexeff, Editors (1987), *HHigh-Power Microwave Sources*. Artech House, Boston .

**DETERMINATION OF CHEMICAL OXYGEN-IODINE LASER SCALING
REQUIREMENTS FOR LASER MATERIALS PROCESSING**

Aravinda Kar

Assistant Professor

Department of Mechanical and Aerospace Engineering
Center for Research and Education in Optics and Lasers

University of Central Florida
P. O. Box 162450
Orlando, FL 32816-2450

Final Report for:
Summer Faculty Research Program
Phillips Laboratory, Applied Laser Technology Branch (PL/LIDB)

Sponsored by:
Air Force Office of Scientific Research
Bolling Air Force Base, DC

and

Phillips Laboratory, Applied Laser Technology Branch (PL/LIDB)

July 1995

DETERMINATION OF CHEMICAL OXYGEN-IODINE LASER SCALING REQUIREMENTS FOR LASER MATERIALS PROCESSING

Aravinda Kar

Assistant Professor

Department of Mechanical and Aerospace Engineering

Center for Research and Education in Optics and Lasers

University of Central Florida

Abstract

A simple mathematical model of thick-section stainless steel cutting with a high power Chemical Oxygen-Iodine Laser (COIL) is presented and compared with experimental results obtained with a 10-kilowatt COIL at the U.S. Air Force's Phillips Laboratory. This model uses a lumped-parameter technique to relate the cutting kerf depth with various process parameters and can be used to predict the laser power scaling requirements for carrying out laser materials processing of very thick sections. The model is similar to an empirical model developed by researchers in Japan, but includes predictive capabilities for thick metal cutting at very low velocities. The effects of various process parameters such as laser power, spot size and dimensions, and processing speed on the cutting depth are discussed and demonstrated. Finally, the ramifications of this model on thick-section processing of metals are presented, with emphasis on potential applications of COIL to high-speed, thick stainless steel cutting.

Since the natural shape of a typical Chemical Oxygen-Iodine Laser (COIL) beam is rectangular with several modes, a three-dimensional quasi-steady-state heat conduction model is presented to understand the basic mechanisms of heat transfer in the workpiece during materials processing with such complex beams.

DETERMINATION OF CHEMICAL OXYGEN-IODINE LASER SCALING REQUIREMENTS FOR LASER MATERIALS PROCESSING

Aravinda Kar

1. Introduction

Metal cutting was recognized early on as one of the most valuable potential applications of laser technology. Several years of laser development and maturation, however, were required before the use of lasers in industry for metal cutting became a practical. Currently, lasers are viewed with high expectations for revolutionary advances in manufacturing technology, with emphasis on the automated, robotic delivery of the laser beam to the workplace. Recently, interest has arisen for the concept of the delivery of several kilowatts of laser power through optical fibers to the workplace to simplify the use of lasers in industrial settings. This paper describes the development and verification of a model for the high-speed cutting of thick-section stainless steel using a Chemical Oxygen-Iodine Laser (COIL).

1.1 COIL Development

The COIL was invented in 1977 by McDermott, et al.¹ at what was then the Air Force Weapons Laboratory (now part of the Phillips Laboratory) and is the shortest wavelength, high-power chemical laser ever developed. The engineering scalability of a supersonic gas flow COIL was demonstrated at the U. S. Air Force's Phillips Laboratory by Truesdell, et al. with the 39 kW RotoCOIL device^{2,3}. The operation of a COIL for long durations was demonstrated by Fujii, et al. at Kawasaki Heavy Industries, Ltd., in Japan^{4,5,6} with the operation of a 1 kW subsonic gas flow COIL for 2 hours. Sustained high power operation a supersonic COIL was demonstrated at the Phillips laboratory with operation at 9 kW for 2 minutes⁷ and at 430 Watts for 13 minutes on a compact COIL test stand⁸. A comprehensive list of references on COIL development in the United States is given by Truesdell, et al.², with additional references on the theoretical operation of COIL given by Avizonis and Truesdell⁹.

Fujioka¹⁰ and Atsuta, et al. reported the transmission of a 1 kW COIL beam through a 300 micron diameter silica fiber^{11,12} at an intensity of 1.4 MW/cm². The material processing capability of COIL was investigated by Atsuta, et al.¹¹ using the ALEC COIL to cut stainless steel up to 5 mm thick, demonstrating the cutting capability of a 1 kW COIL to be equivalent to a 1 kW

Nd:YAG laser and about 2.5 times better than a 1 kW CO₂ laser.. They modeled the processing capability with a simple two-parameter model and empirically fit the model to experimental data to predict the scaled cutting capability of COIL¹¹.

1.2 Laser Cutting Development

A variety of overviews of laser cutting of materials have appeared over the last decade, with guidelines and data for the laser cutting of various types of materials can be found in Tikhomirov¹³, Schuocker¹⁴, and Powell¹⁵. The development of mathematical models of material processing has kept pace with the experimental developments. Atsuta, et al.¹¹ presented a simple model and compared the cutting performance of COIL, Nd:YAG and CO₂ lasers. This report presents a new, simple mathematical model to predict the cutting capability of a high power COIL, with the validation of the model using experimental data to understand the materials processing capability of COIL for very thick material.

1.3 Heat Conduction Model Development

The conversion of the optical energy of a laser beam into thermal energy and the propagation of this thermal energy in the substrate play an important role in laser materials processing. A lot of work has been done to understand the heat conduction process during laser heating. Cline and Anthony¹⁶ solved the heat conduction equation using Green's function for a Gaussian beam moving at a constant velocity. Moody and Hendel¹⁷ solved the heat conduction equation by using a numerical technique to determine the temperature distribution in an infinite medium during laser heating. Kar and Mazumder¹⁸ presented a three-dimensional transient thermal model to determine the temperature distribution in finite slabs moving at a constant velocity by considering temperature-dependent thermophysical properties and laser irradiation with a Gaussian beam.

In all these studies, a single beam having a single mode, particularly TEM₀₀ mode, was used. Kannatey-Asibu¹⁹, Liu and Kannatey-Asibu²⁰, and Chen and Kannatey-Asibu²¹ have examined the heat transfer phenomena due to laser heating with two Gaussian beams. In most cases, the laser beam contains several modes. Also, the natural shape of the laser beam that comes out of the resonator of some special types of lasers, such as COIL and slab lasers, is rectangular. A heat

conduction model is presented in this report to understand the heating phenomena due to rectangular, multimode, multiple laser beams.

2. Mathematical Model

As mentioned earlier, two mathematical models are developed under this Summer Faculty Research Program. One of them is based on the average temperature of the material at the laser-substrate interaction zone, and the other is based on the pointwise variation of the substrate temperature during laser materials processing. These two models are briefly discussed below. The details of the first and second models are planned to be submitted for publication in the *Journal of Laser Applications* and the *Journal of Applied Physics* respectively.

2.1. Average Temperature Model

To understand the effects of various process parameters such as the laser power, laser scanning speed on the kerf width, a simple mathematical model is developed by using a lumped parameter technique. The overall energy balance is written as

$$AP\tau = \rho w_k d v \tau [c_p(T_m - T_0) + L_m + c_p(T_a - T_m) + \beta L_b] + E_{cond} \quad (2.1.1)$$

where A is the absorptivity of the workpiece for COIL (1.315 μm) light, P is the power of the incident laser beam, ρ and c_p are, respectively, the density and specific heat of the workpiece. L_m and L_b are the latent heats of melting and boiling respectively. β is defined here as the “boiling coefficient” and is the fraction of the kerf width, w_k , over which the temperature of the melt exceeds the boiling temperature of the material. τ is the laser-substrate interaction time which is given by $\tau = l/v$, where l is the length of the rectangular COIL beam spot, v is the scanning velocity of the laser beam with respect to the workpiece. w_k and d are, respectively, the kerf width and depth. T_0 , T_a and T_m are, respectively, the initial temperature of the workpiece, average final temperature of the liquid metal and melting temperature of the workpiece. E_{cond} represents heat loss due to conduction in the solid substrate across three sides of the kerf.

The energy loss due to heat conduction into the substrate can be determined from the Fourier law of heat conduction, and then Eq. (2.1.1) can be written as

$$d = \frac{AP}{\rho v w_k [c_p(T_a - T_0) + L_m + \beta L_b] + (w_k + 2l)k \frac{T_m - T_0}{2\sqrt{\alpha\tau}}} \quad (2.1.2)$$

α and k are the thermal diffusivity and thermal conductivity of the workpiece respectively. In this model, the kerf width, w_k , is taken to be equal to the width of the rectangular COIL beam spot.

If we neglect the conduction heat loss and assume $T_a = (T_m + T_b)/2$, where T_b is the boiling temperature of the workpiece, and $T_0 = 293$ K, Eq. (2.1.2) becomes

$$d = 10.043 AP / (vw_k) \quad (2.1.3)$$

using typical values for the thermophysical properties of steel as given in Table 1, and where P , v , w_k and d are measured in units of kW, cm/s, mm and mm, respectively. Because the energy loss due to heat conduction is neglected, Eq. (2.1.3) is valid only for high speed material processing which results in a short laser-substrate interaction time.

Table 1. Typical values for the thermophysical properties of iron (Brandes²²). Due to the lack of high temperature data, these values were used in this study to obtain various results although the substrate was 400 series stainless steel.

Density (ρ): 7870 kg m⁻³, Melting point (T_m): 1809 K, Boiling point (T_b): 3133 K

Thermal conductivity (k): 78.2 W m⁻¹ K⁻¹, Specific heat (c_p): 456 J kg⁻¹ K⁻¹

Effective specific heat ($c_{pe} = c_p + L_m/T_m$): 606 J kg⁻¹ K⁻¹

Thermal diffusivity ($\alpha = k/(\rho c_p)$): 2.18×10^{-5} m² s⁻¹

Effective thermal diffusivity ($\alpha_e = k/(\rho c_{pe})$): 1.64×10^{-5} m² s⁻¹

Latent heat of melting (L_m): 2.72×10^5 J kg⁻¹, Latent heat of boiling (L_b): 6.10×10^6 J kg

Atsuta et al.¹¹ presented an expression to determine the kerf depth, d , in terms of the laser power, spot diameter, cutting speeed and two empirically-determined parameters, α' and β' ,

which they refer to as a laser parameter and material parameter respectively. By fitting their expression,

$$\frac{d}{P} = \alpha' / (vw_k^* + \beta') \quad (2.1.4)$$

to experimentally collected data obtained by using their 1 kW COIL, they determined that for stainless steel, $\alpha' = 5.0$ and $\beta' = 0.7$. In Eq. (2.1.4), d , P , v and w_k^* are measured in units of mm, kW, m/min and mm respectively, where w_k^* is the Kerf width which is taken to be the diameter of a circular laser spot. Eq. (2.1.4) is, however, not applicable for very low speeds as seen from the fact that as the processing speed goes to zero, d/P asymptotically approaches a constant value, α'/β' . This limitation is overcome by rewriting Eq. (2.1.2) as follows:

$$\frac{d}{P} = \frac{A}{vw_k [\rho c_p (T_m - T_0) + \rho L_m + \beta \rho L_b] + vw_k [\rho c_p (T_a - T_m)] + \frac{w_k + 2l}{\sqrt{lw_k}} k \frac{T_m - T_0}{2\sqrt{\alpha}} \sqrt{vw_k}} \quad (2.1.5)$$

If T_a is estimated by considering energy balance across the melt front at the kerf wall, Eq. (2.1.5) can be written as

$$\frac{d}{P} = \frac{A_0}{vw_k + A_1(vw_k)^2 + A_2(vw_k)^{3/2} + A_3(vw_k)^{1/2}} \quad (2.1.6)$$

where

$$A_0 = 10^6 \times \frac{1}{a_0} A, \quad A_1 = 2.78 \times 10^{-10} \times \frac{1}{a_0} \frac{\rho^2 c_p L_m}{2kl} \varepsilon, \quad A_2 = 6.8 \times 10^{-8} \times \frac{1}{a_0} \frac{\rho c_p (T_m - T_0)}{2\sqrt{\alpha l w_k}} \varepsilon, \\ A_3 = 4.08 \times 10^{-3} \times \frac{1}{a_0} \frac{w_k + 2l}{\sqrt{lw_k}} \frac{k(T_m - T_0)}{2\sqrt{\alpha}}, \text{ and } a_0 = 1.67 \times 10^{-5} \rho [c_p (T_m - T_0) + L_m + \beta L_b]$$

where ε is the thickness of the solidified layer at the kerf wall, and d , l , w_k and ε are given in units of mm, v is in m/min, and P is in kW. All other variables are in MKS units.

Using the thermophysical data for steel given in Table 1, and assuming $T_0 = 293$ K, $\varepsilon = 0.1$ mm and $\beta = 0.1$, we find: $A_0 = 4.85$ A, $A_1 = 3.896 \times 10^{-3}$, $A_2 = 1.35 \times 10^{-2}$ and $A_3 = 4.72$ for a rectangular COIL beam with spot dimensions $l = 1.7$ mm and $w_k = 1.2$ mm. Here, we see that the

values of A_1 and A_2 are small with respect to the other coefficients and their effects on d/P as given by Eq. (2.1.6) are correspondingly small and can be neglected. Thus, Eq. (2.1.6) becomes

$$d/P = A_0 / (vw_k + A_3 \sqrt{vw_k}) \quad (2.1.7)$$

which, while having a similar form as Eq. (2.1.4), has a dependence on the cutting speed that does not become constant for very low speeds.

2.2. Heat Conduction Model

The beam that comes out of a typical COIL cavity is rectangular in shape, and is consisted of several modes. To understand the energy distribution in the workpiece during laser heating with rectangular, multimode and single or multiple beams, a mathematical model is developed by considering the three-dimensional quasi-steady state heat conduction phenomena. Figure 2.2.1 shows the geometric configuration used in this model.

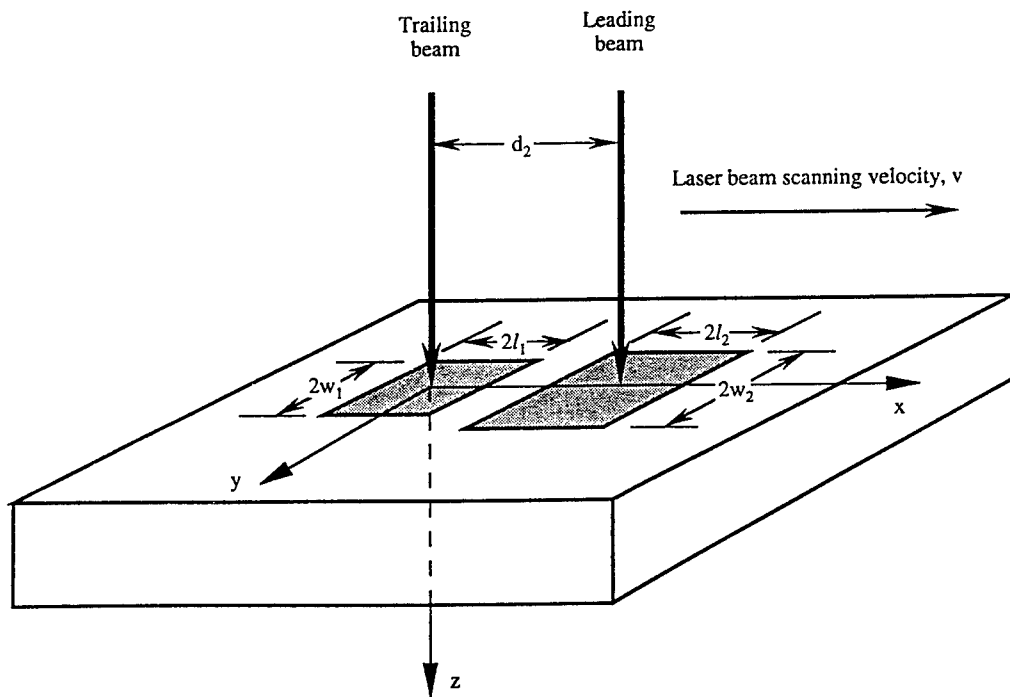


Figure 2.2.1. Laser beam geometry and coordinate system for the mathematical model.

The governing equation for the temperature distribution is given by

$$\alpha_e \left(\frac{\partial^2 T}{\partial x^2} + \frac{\partial^2 T}{\partial y^2} + \frac{\partial^2 T}{\partial z^2} \right) = -v \frac{\partial T}{\partial x} \quad (2.2.1)$$

for $-\infty \leq x \leq \infty$, $-\infty \leq y \leq \infty$, and $0 \leq z \leq \infty$. Here α_e is the effective thermal diffusivity of the workpiece, which is defined by $\alpha_e = k/(\rho c_{pe})$, where k and c_{pe} are the thermal conductivity and effective specific heat of the workpiece respectively. In this study, c_{pe} is taken to be $c_{pe} = c_p + L_m/T_m$ to model the consumption of the latent heat of melting, L_m , when the workpiece temperature reaches the melting temperature T_m . Here c_p is the specific heat of the workpiece. v is the velocity of the laser beam in the x direction. All beams are assumed to move in the x direction at a constant velocity v . Also, the centers of all beams are assumed to lie on the x axis. Eq. (2.2.1) is written in a moving Cartesian coordinate system whose origin lies at the center of one of the beams. The temperature T in Eq. (2.2.1) is defined by $T = (T_1 - T_0)/(T_m - T_0)$, where T_1, T_0 are the actual and initial temperature of the substrate respectively.

The boundary conditions for Eq. (2.2.1) are given by

$$T \rightarrow 0 \text{ as } x \rightarrow \pm\infty, \quad T \rightarrow 0 \text{ as } y \rightarrow \pm\infty, \quad T \rightarrow 0 \text{ as } z \rightarrow \infty$$

$$k \frac{\partial T}{\partial z} = -\frac{1}{T_m - T_0} \sum_{s=1}^S \sum_{m=0}^M \sum_{n=0}^N I_{s,mn} \quad \text{at } z = 0$$

where S is the total number of beams used for heating the workpiece. M and N are the mode number of the beam in the x and y directions, respectively. $I_{s,mn}$ is the intensity of the s -th rectangular beam of m -th and n -th order modes, which is given by

$$I_{s,mn} = \frac{2A_s P_{s,mn}}{\pi 2^{m+n} m! n! l_{s0} w_{s0}} H_m^2 \left(\frac{\sqrt{2}(x - d_s)}{l_{s0}} \right) H_n^2 \left(\frac{\sqrt{2}y}{w_{s0}} \right) \exp \left(-\frac{2(x - d_s)^2}{l_{s0}^2} \right) \exp \left(-\frac{2y^2}{w_{s0}^2} \right)$$

Here $P_{s,mn}$ is the total power of the s -th laser beam of m -th and n -th order modes. d_s is the distance of the center of the s -th laser beam from the origin of the chosen coordinate system. A_s is the absorptivity of the workpiece for the s -th beam. H_m and H_n are, respectively, m -th and n -th degree Hermite polynomials for the m -th and n -th order modes of the laser beam. Using Fourier transform, the solution of this problem can be written as

$$T(x, y, z) = \frac{\exp(-bx)}{\pi} \sum_{s=1}^S \sum_{m=0}^M \sum_{n=0}^N a_{mn,s} \int_0^\infty r' dr' f_{m,s}(x - r' \cos\theta) \\ \int_0^\pi d\theta g_{n,s}(y - r' \sin\theta) \frac{\exp\left(-b\sqrt{r'^2 + z^2}\right)}{\sqrt{r'^2 + z^2}} \quad (2.2.2)$$

where

$$a_{mn,s} = \frac{1}{k(T_m - T_0)} \frac{2A_s P_{s,mn}}{\pi 2^{m+n} m! n! I_{s0} w_{s0}}, \quad f_{m,s}(x) = H_m^2\left(\frac{\sqrt{2}(x - d_s)}{l_{s0}}\right) \exp\left(bx - \frac{2(x - d_s)^2}{l_{s0}^2}\right),$$

$$\text{and } g_{n,s}(y) = H_n^2\left(\frac{\sqrt{2}y}{w_{s0}}\right) \exp\left(-\frac{2y^2}{w_{s0}^2}\right)$$

Eq. (2.2.2) is used to calculate the temperature distribution for various process parameters using typical values for the thermophysical properties of steel as given in Table 1.

3. Metal Cutting Experiment Setup

The COIL device used for the experiments was the 10 kW RADICL device (Research Asessment, Device Improvement Chemical Laser) located at the U.S. Air Force's Phillips Laboratory in Albuquerque, New Mexico. The laser was operated with multiple transverse modes with a stable resonator consisting of a 10 m radius of curvature high reflectivity mirror with a flat outcoupler spaced 3.0 m apart. A focusing lens ($f_1 = 1.025$ m) was located 7.63 m from the outcoupler, followed by a second lens ($f_2 = 0.5$ m) to produce a focal point 0.33 m away. The multimode focal spot size was determined to be 1.2 mm wide by 1.7 mm long. The spot was horizontally oriented such that the leading edge of the spot was the smallest dimension. The power on target ranged from 5.2 to 7.2 kW.

The targets consisted of two types: stainless steel (400-series) plates that were milled on the back side to a stepped-taper shape with thicknesses ranging from 0.06 m (6 mm) to 0.135 m (13.5 mm) for the thin targets to 0.2 m (20 mm) up to 0.27 m (27 mm) for the thick targets, and plates greater than 27 mm thick that were not tapered. The targets were mounted on a stepper motor-controlled, horizontal translation stage capable of speeds up to 0.05 m/s (3.0 m/min) and scanned through the focal region at constant speed such that the thin side of the taper entered the beam first. Scans were conducted at various speeds. The laser would cut the sample at a given speed

until the maximum thickness was reached. Targets thicker than 27 mm were scanned through the beam at various speeds and the depth of the cut was measured. Figure 3.1 illustrates the target assembly.

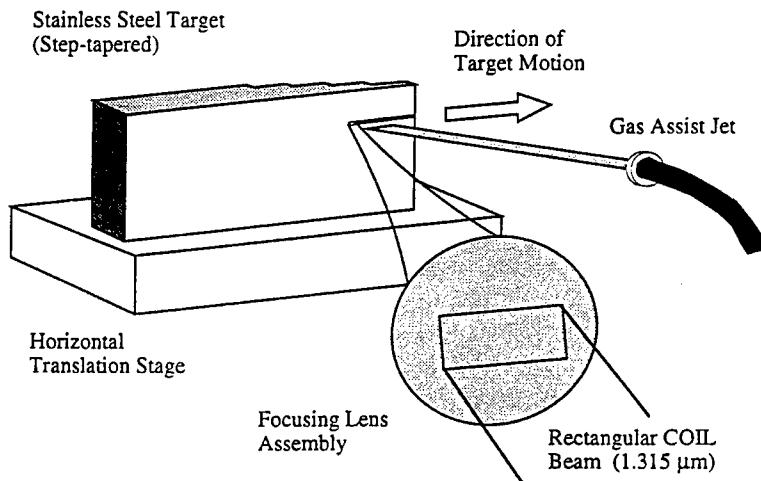


Figure 3.1. The experimental set up for the thick section stainless steel cutting experiments with the Phillips Laboratory 10 kW COIL.

An assist gas nozzle was constructed from a 3.2 mm diameter stainless steel tube that was flattened and shaped to form a rectangular nozzle with dimensions approximately 1 mm wide by 2 mm long. The nozzle was oriented horizontally so as to coincide with the laser focal spot, and was fixed at a 45 degree angle from the normal of the target. The gas consisted of helium or nitrogen at pressures that ranged up to 3500 kP (500 psi).

4. Results and Discussion

This section is divided into two parts to discuss the results obtained by the above-mentioned two mathematical models.

4.1 Results and Discussion: Average Temperature Model and Experimental Data

To determine the sensitivity of the theory presented in this paper, parameters in Eq. (2.1.2) were analytically varied to observe the effects of their change on the depth of cut in steel. Figure 4.1.1 illustrates the thick metal cutting capability for three different incident laser powers. It can be noted that the cut depth increases significantly for low cutting speeds for each power, with even the lowest power capable of cutting very thick sections, but at very slow speeds.

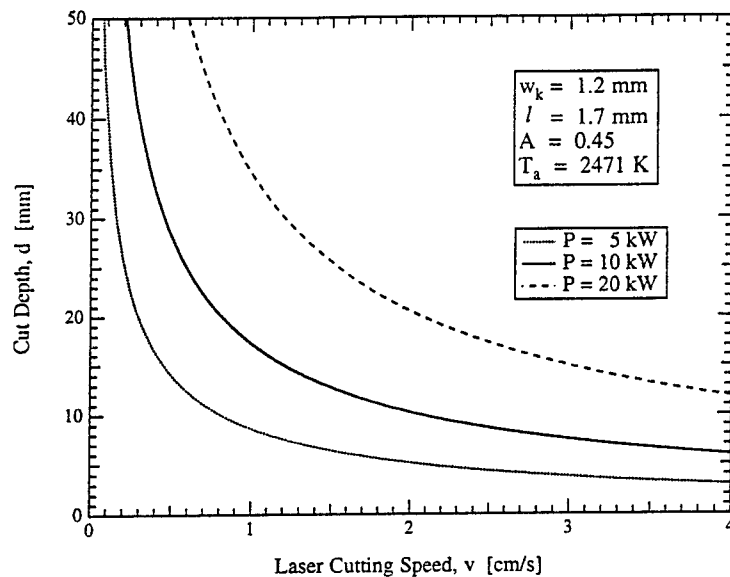


Figure 4.1.1. Variation of kerf depth with laser scanning speed for various incident laser powers with fixed spot length and width, average temperature and absorptivity.

The behavior of the simplified lumped parameter model given in Eq. (2.1.3) (without the heat loss terms) and in Eq. (2.1.7) (with the heat loss terms) are shown as curves A and B respectively in Figure 4.1.2. These are compared with the Kawasaki model given by Eq. (2.1.4) which is shown as curve C. It should be noted that all three equations predict similar results for high speed, large spot width cutting ($vw_k > 1\text{ [m min}^{-1}\text{ mm]}$), but predict significantly different results

for lower values of vw_k . Curve C approaches a limiting ratio for d/P for slow speeds with small spot sizes. This predicts reduced laser cutting capability of thick metals under these conditions. Eq. (2.1.7) (curve B) predicts lower cutting capability for higher speeds, but enhanced capability for lower speeds.

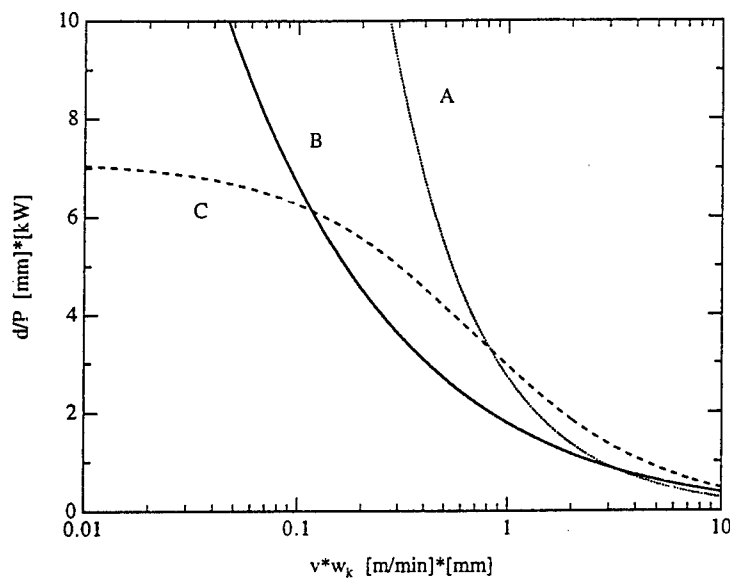


Figure 4.1.2. Comparison between the results of various models:
 Our model: Curve A (Eq. 6), Curve B (Eq. 17), and
 the Kawasaki model: Curve C (Eq. 7).

The results of the experimental studies of stainless steel metal cutting that were conducted at the U.S. Air Force's Phillips Laboratory using a 10 kW COIL are shown in Table 2 and the data are plotted in Figure 9. The data obtained using the small assist gas nozzle are shown as solid points and those obtained with the large nozzle as outlined points to show the effect of nozzle size.

Due to the relatively low intensity of the laser (on the order of 10^5 W/cm^2) in the focal region, it is assumed that the average temperature of the melt is below the boiling temperature such that the boiling coefficient, β , is negligible. Assuming the absorption coefficient to be $A = 0.45$, A_0 and A_3 are calculated to express Eq. (2.1.7) in the following form.

$$d / p = 3.55 / (vw_k + 1.32\sqrt{vw_k}) \quad (4.1.1)$$

Table 2. Experimental data for stainless steel cutting (400-series) with a focused COIL beam with focal spot dimensions $w_k = 1.2 \text{ mm}$, $l = 1.7 \text{ mm}$ (calculated).

Power on Target, P [kW]	Laser Scanning Speed, v [m/min]	Assist Gas Nozzle Outlet Dimensions [mm × mm]	Cut Depth, d [mm]	v w _k [m/min] [mm]	d/P [mm]/[kW]
7.2	0.12	0.6 × 2.5	30.2	0.14	4.19
6.2	0.24	0.6 × 2.5	22.6	0.29	3.65
7.2	0.30	0.6 × 2.5	22.6	0.36	3.14
5.2	0.90	0.6 × 2.5	9.4	1.08	1.81
7.1	1.20	0.6 × 2.5	11.2	1.44	1.58
5.2	1.50	0.6 × 2.5	8.5	1.80	1.63
5.2	1.80	0.6 × 2.5	7.1	2.16	1.37
7.2	1.92	0.6 × 2.5	7.6	2.30	1.06
6.7	2.22	0.6 × 2.5	6.5	2.66	0.97
5.4	0.06	0.6 × 14.5	39.8	0.07	7.35
6.2	0.12	0.6 × 14.5	35.1	0.14	5.66
5.3	0.21	0.6 × 14.5	25.4	0.25	4.76
5.6	0.36	0.6 × 14.5	22.5	0.43	4.00

Eq. (4.1.1) and the data listed in Table 2 are plotted in Figure 4.1.3 to compare the theoretical predictions with experimental data. This figure shows that the kerf depth can be increased by increasing the size of the assist gas nozzle outlet.

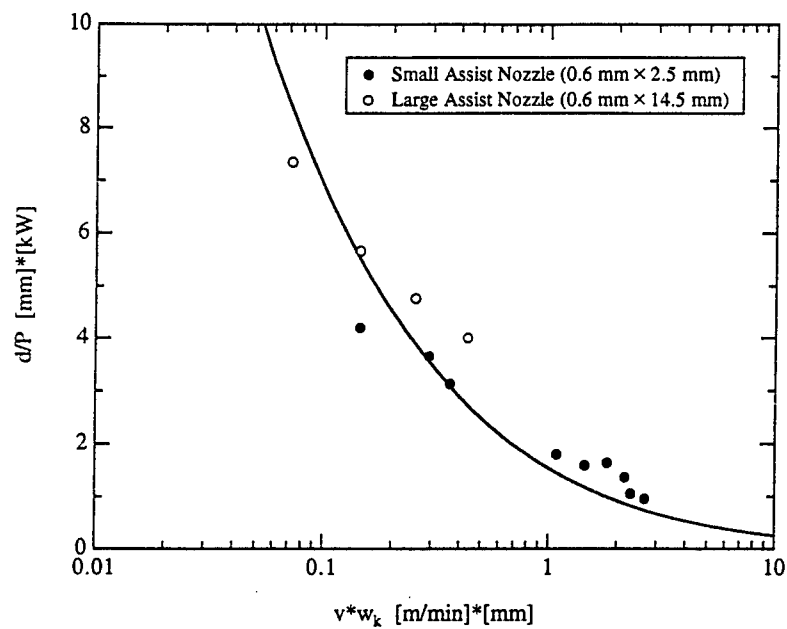


Figure 4.1.3. Comparison of theoretical results with experimental data.

4.2. Results and Discussion: Heat Conduction Model

Figures 4.2.1 and 4.2.2 are based on a laser having TEM_{31} mode. Due to the particular

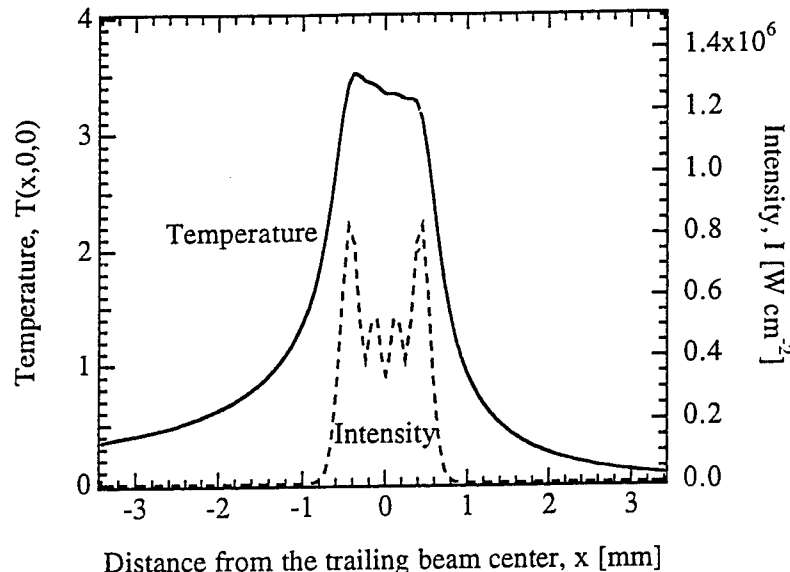


Figure 4.2.1. Surface temperature and intensity profiles along the x axis ($y = 0$ and $z = 0$) for a single multimode (TEM_{mn}) beam.

$P = 6 \text{ kW}$, $2l_1 = 1.7 \text{ mm}$, $2w_1 = 1.2 \text{ mm}$, $v = 1 \text{ cm/s}$, $m = 3$ and $n = 1$.

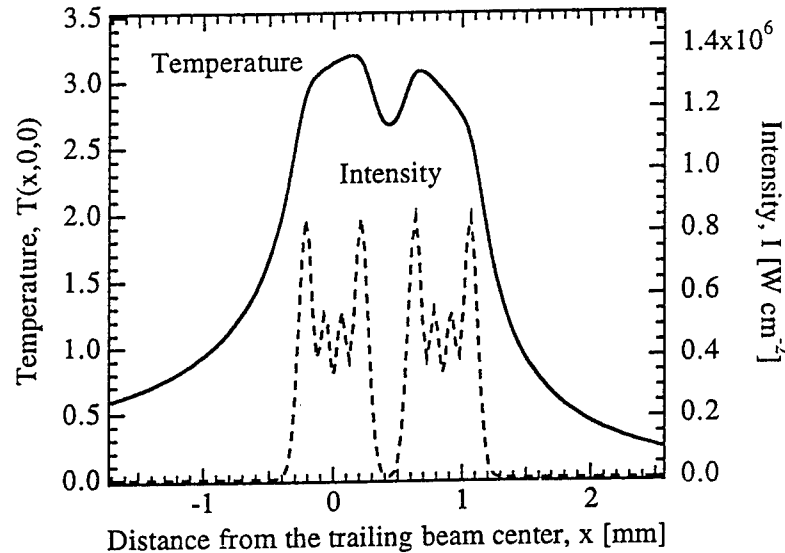


Figure 4.2.2. Surface temperature and intensity profiles along the x axis ($y = 0$ and $z = 0$) for two multimode (TEM_{mn}) beams.

$P_i = 3 \text{ kW}$, $2l_i = 0.85 \text{ mm}$, $2w_i = 1.2 \text{ mm}$ for $i = 1$ and 2 , $v = 1 \text{ cm/s}$, $m = 3$, $n = 1$ and $d_2 = 0.85 \text{ mm}$.

choice of the modes and power distribution in each mode, the intensity has M-shaped distribution in the x-direction as shown in Figs. 4.2.1 and 4.2.2. Although the laser intensity is the same in both figures, the peak temperature in the case of a single beam is higher than in the case of two beams because the intensity is confined in a region of length 1.7 mm in Fig. 4.2.1, whereas it is confined in two regions of length 0.85 mm each in Fig. 4.2.2. The intensity is very low in an area near $x = 0.425$ mm where the boundaries of these two regions meet, and therefore, heat is conducted into this area of low intensity to raise the substrate temperature as shown in Fig. 4.2.2. Due to this, two beams heat up a larger area than a single beam does, which causes the peak temperature to rise less in the former case than in the latter case, even though the substrate surface areas irradiated by the laser are the same in both cases. Also, the temperature is lower in front of the beam than at the back of the beam because heat is convected away towards the back of the beam (negative x direction) due to the motion of the substrate in the negative x direction relative to the beam.

Figure 4.2.3 shows the effects of the spot shape, that is the aspect ratio $a = l_1/w_1$, on the

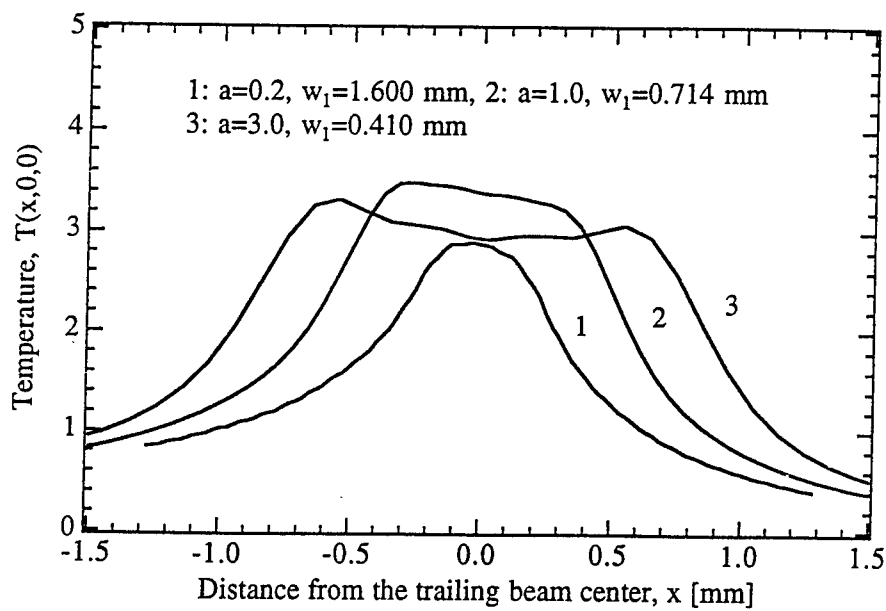


Figure 4.2.3. Effects of the aspect ratio ($a = l_1/w_1$) on the surface temperature distribution along the x axis ($y = 0$ and $z = 0$). A single multimode (TEM_{mn}) beam is used. $P = 6$ kW, $v = 1$ cm/s, $m = 3$ and $n = 1$.

surface temperature distribution for a single multimode (TEM_{31}) beam. The widths of the spots for curves 1, 2 and 3 are 3.2, 1.428 and 0.82 mm respectively. The aspect ratios for curves 1, 2 and 3 are 0.2, 1 and 3 respectively which make the spot area to be about 2 mm^2 for these three curves. It can be seen from Fig. 4.2.3 that the peak temperature is higher for curve 2 than those for curves 1 and 3. This is because the surface area per unit length of a parallelopiped with a square cross section is lower than that with a rectangular cross section. Since heat loss is directly proportional to the surface area, less heat is lost for the case of curve 2 for which the spot is a square. Therefore, more energy is utilized for the case of curve 2 to heat up the material than for the cases of curves 1 and 3 for which the spots are rectangular.

5. Conclusions

The following conclusions can be drawn from the results of the average temperature model. Eq. (2.1.7) presents a simple, analytical model that accurately describes the thick metal cutting capabilities of a COIL using a rectangular focal spot. This study indicates that it may be possible to improve thick metal cutting performance by using high aspect ratio rectangular beams. It also indicates a potential improvement in cutting performance using large dimension nozzles and high assist gas pressures. These results point out the need for additional theoretical development and experimental verification of thick-section materials processing with high power lasers.

The results of the heat conduction model lead to the following conclusion. Due to the particular choice of the TEM_{31} mode beam in this study, the laser intensity, I , is found to have an M-shaped nonuniform profile. However, the substrate surface temperature during laser heating with a single beam having such a nonuniform intensity profile is found to increase steadily from the front edge of the beam to the rear edge of the beam in the laser spot region. The shape of the laser spot also has an interesting effect on the peak temperature in the laser spot region during laser heating with a single beam. The peak temperature is found to be higher for a square spot than for rectangular spots for the same laser intensity and material processing conditions. This is because of less energy loss for a square spot than for rectangular spots, which means that the energy utilization is improved if a square laser spot is used.

6. References

1. W. E. McDermott, N. R. Pchelkin, D. J. Benard and R. R. Bousek, "An Electronic Transition Chemical Laser," *Appl. Phys. Lett.* 32, pp. 469-470, 1978.
2. K. A. Truesdell, C. A. Helms and G. D. Hager, "COIL Development in the USA," 25th Plasmadynamics and Lasers Conference, AIAA 94-2421, June 1994.
3. J. E. Scott, J. L. R. Shaw, K. A. Truesdell, G. D. Hager and C. A. Helms, "Design Considerations for the Chemical Oxygen-Iodine Supersonic Mixing Nozzle," 25th Plasmadynamics and Lasers Conference, AIAA 94-2436, 1994.
4. H. Fujii, S. Yoshida, M. Iizuka and T. Atsuta, "Long-term stability in the operation of a chemical oxygen-iodine laser for industrial use," *J. Appl. Phys.* 66, pp. 1033-1037, August 1989.
5. F. Wani, N. Naitou, T. Nagai, M. Iizuka, H. Tsuji and H. Fujii, "Development of 1 kW CW Iodine Laser for Industrial Use," Proceedings of Laser Advanced Materials Processing (LAMP '92), Niigata, Japan, pp. 127-132, June 1992.
6. H. Fujii and T. Atsuta, "Current Status of Industrial COIL Development," Third International Workshop on Iodine Lasers and Applications, SPIE Vol. 1980, Bechyne Castle, Czechoslovakia, pp. 148-152, 1992.
7. K. A. Truesdell, T. Lonergan, C. Wisniewski, K. Healey, J. Scott and C. Helms, "COIL Thermal Management," 25th Plasmadynamics and Lasers Conference, AIAA 94-2441, June 1994.
8. S. Phipps, C. A. Helms and K. A. Truesdell, "Compact CW Supersonic Chemical Oxygen Iodine Laser (COIL)," 25th Plasmadynamics and Lasers Conference, AIAA 94-2453, June 1994.
9. P. V. Avizonis and K. A. Truesdell, "Historical Perspectives of the Chemical Oxygen-Iodine Laser (COIL)," 25th Plasmadynamics and Lasers Conference, AIAA 94-2416, June 1994.
10. T. Fujioka, "Industrial Gas Lasers Between 1.05-10.6 μm Range," *Infrared Phys.*, 32, pp. 81-90, 1991.
11. T. Atsuta, K. Yasuda, T. Matsumoto, T. Sakurai and H. Okado, "COIL and the Material Processing," in Conference on Lasers and Electro-Optics (CLEO) '94, Vol. 8, 1994 OSA Technical Digest Series (Optical Society of America, Washington, D.C.), p. 351, 1994.
12. H. Fujii, "COIL Development in Japan," 25th Plasmadynamics and Lasers Conference, AIAA 94-2410, June 1994.
13. A. V. Tikhomirov, "State of Laser Cutting Technology and Prospects for its Development," *Bull. Academy of Sciences of the USSR*, Vol. 47, 1983, pp. 23-28.

14. D. Schuocker, "Laser Cutting," in The Industrial Laser Annual Handbook, D. Belforte and M. Levitt, Editors, (PennWell Books, Tulsa, Oklahoma), 1986, pp. 87-107.
15. J. Powell, "Guidelines and Data for Laser Cutting," in The Industrial Laser Annual Handbook, D. Belforte and M. Levitt, Editors, (PennWell Books, Tulsa, Oklahoma), 1990, pp. 56-67.
- ¹⁶ H. E. Cline and T. R. Anthony, *J. Appl. Phys.* **48**, 3895 (1977).
- ¹⁷ J. E. Moody and R. H. Hendel, *J. Appl. Phys.* **53**, 4364 (1982).
- ¹⁸ A. Kar and J. Mazumder, *J. Appl. Phys.* **65**, 2923 (1989).
- ¹⁹ E. Kannatey-Asibu, *J. Eng. Mater. Tech.* **113**, 215 (1991).
- ²⁰ Y. N. Liu and E. Kannatey-Asibu, *J. Heat Transfer*, **115**, 34 (1993).
- ²¹ T. C. Chen and E. Kannatey-Asibu, in *Proceedings of the International Congress on the Applications of Lasers and Electro-Optics, 1994 (ICALEO '94): Laser Materials Processing*, edited by T. D. McCay, A. Matsunawa and H. Hugel (Laser Institute of America, Florida, 1994), Vol. 2500, pp. 668 - 677.
- ²² E. A. Brandes, editor, Smithells Metals Reference Book, Sixth edition, (Butterworths, London), 1983, pp. 8-2 and 14-1.

**THEORY OF MONTE-CARLO SIMULATIONS OF THE MAGNETIC CIRCULAR DICHROISM (MCD)
SPECTRA OF ALKALI METAL/RARE GAS SYSTEMS**

**John W. Kenney, III
Associate Professor of Chemistry
Department of Physical Sciences**

**Eastern New Mexico University
Portales, NM 88130**

**Final Report for:
Summer Faculty Research Program
Phillips Laboratory**

**Sponsored by:
Air Force Office of Scientific Research
Bolling Air Force Base, DC**

and

**Phillips Laboratory (PL/RK)
Edwards AFB, CA**

August 1995

THEORY OF MONTE-CARLO SIMULATIONS OF THE MAGNETIC CIRCULAR DICHROISM (MCD)
SPECTRA OF ALKALI METAL/RARE GAS SYSTEMS

John W. Kenney, III
Associate Professor of Chemistry
Eastern New Mexico University
Portales, NM 88130

Abstract

The history of magnetic circular dichroism (MCD) spectroscopy in the study of alkali metal/rare gas (M/Rg) cryogenic systems is reviewed in the context of developing a better understanding of alkali metal/hydrogen systems of current interest to the U.S. Air Force as enhanced-performance cryogenic rocket propellants. A new theory for simulating the MCD spectra of M/Rg systems is presented together with careful a discussion of the theory's implicit and explicit approximations and their implications. This theory uses a classical Monte Carlo (MC) simulation scheme to model the perturbing effects of the Rg environment on the $^2S \rightarrow ^2P$ MCD-active transition of the M atom. The theory sets up the MC-MCD simulation as 6×6 matrix eigenvalue/eigenvector problem in the 2P manifold. This 6×6 eigenvalue/eigenvector problem is solved for a number of randomly generated and suitably averaged Rg configurations to yield the simulated MC-MCD spectrum for the M/Rg system of interest.

THEORY OF MONTE-CARLO SIMULATIONS OF THE MAGNETIC CIRCULAR DICHROISM (MCD)
SPECTRA OF ALKALI METAL/RARE GAS SYSTEMS

John W. Kenney, III

Introduction

Alkali metal/rare gas solids (M/Rg solids) constitute an important class of model systems of interest to the U.S. Air Force in simulating the properties of enhanced-performance cryogenic rocket propellants.¹ In particular, the M/Rg systems share many physical, chemical, and spectroscopic characteristics with M/hydrogen systems, where in a potential rocket propulsion application, M is a high energy density material (HEDM); e.g., a low mass alkali metal or Group 13 or 14 element.^{2,3} Boatz and Fajardo recently modeled $^2S \rightarrow ^2P$ electronic absorption spectra in M/Rg systems by using quantum mechanical first-order degenerate perturbation theory in conjunction with a classical Monte Carlo (MC) method to account statistically for the effects of the Rg perturbations on the 2S and 2P terms of the M/Rg systems.⁴ Their simulations, while not completely quantitative, do recover many of the key attributes of the electronic absorption spectra of these systems including the characteristic three-peaked or "triplet" absorption band shape. Lawrence and Apkarian take a very similar approach in modeling the 2P terms of halogen atoms doped in cyrogenic matrices.⁵ Boatz and Fajardo make the reasonable assumption that spin-orbit coupling represents a small perturbation of the 2P term compared to the Rg perturbation, at least for the lighter alkali metals of interest to them as HEDM rocket propellant dopants, and on this basis justify the exclusion of 2P spin-orbit coupling terms in their model. The Boatz and Fajardo first-order perturbation matrix for the 2P term is, therefore, a 3 x 3 matrix whose matrix elements are defined with respect to a suitable zeroth-order orbital p basis in the angular momentum representation $\{|n/m\rangle = |n11\rangle, |n10\rangle, |n1-1\rangle\}$. Spin is not considered. Lawrence and Apkarian do include a 2P spin-orbit term for the halogen in their treatment. They argue convincingly that the large halogen 2P spin-orbit coupling interaction is not greatly affected by the matrix environment; i.e., the use of the atomic spin-orbit coupling constant of the halogen in the formalism represents a good approximation. The Lawrence and Apkarian 2P perturbation matrix is a 6 x 6 matrix whose individual matrix elements are defined with respect to a suitable zeroth-order Cartesian p basis with spin $\{|n/esm_s\rangle = |n1x 1/2 1/2\rangle, |n1y 1/2 1/2\rangle, |n1z 1/2 1/2\rangle, |n1x 1/2 -1/2\rangle, |n1y 1/2 -1/2\rangle, |n1z 1/2 -1/2\rangle\}$.

¹(a) Fajardo, M. E.; Carrick, P. G.; Kenney, J. W., III *J. Chem. Phys.* **1991**, *94*, 5812-5825. (b) Fajardo, M. E. *J. Chem. Phys.* **1993**, *98*, 110-118. (c) Tam, S.; Fajardo, M. E. *J. Chem. Phys.* **1993**, *99*, 854-860. (d) Corbin, R. A.; Fajardo, M. E. *J. Chem. Phys.* **1994**, *101*, 2678-2683.

²Fajardo, M. E.; Tam, S.; Thompson, T. L.; Cordonnier, M. E. *Chem. Phys.* **1994**, *189*, 361-365.

³Carrick, P. G. *Specific Impulse Calculations of High Energy Density Solid Cryogenic Rocket Propellants, I: Atoms in Solid H₂*, PL-TR-93-3014; Phillips Laboratory: Edwards AFB, CA, 1993.

⁴Boatz, J. A.; Fajardo, M. E. *J. Chem. Phys.* **1994**, *101*, 3472-3487.

⁵Lawrence, W. G.; Apkarian, V. A. *J. Chem. Phys.* **1994**, *101*, 1820-1831.

Magnetic Circular Dichroism (MCD) spectroscopy, which measures the differential absorption of left circularly polarized (LCP) light vs. right circularly polarized (RCP) light in a sample placed in a magnetic field aligned parallel to the propagation direction of the light, has a long and venerable history of providing insights to the nature of the chemical and physical environment surrounding the MCD-active chromophore.⁶ In particular, the MCD-active $^2S \rightarrow ^2P$ electronic transitions of alkali halide F centers⁷ and M/Rg systems⁸ have attracted considerable experimental and theoretical attention over the years. The usual approach is to extract parameters such as the g value, the spin-orbit coupling constant, and linear vibrational coupling constants from a moment analysis of the experimental MCD spectrum (or spectra).^{6,7b} Only a few full MCD spectral simulations exist in the literature. These simulations of $^2S \rightarrow ^2P$ MCD spectra rely upon dynamic Jahn-Teller models in which an *a priori* choice is made as to which *specific* interaction vibrational modes will act to lift the degeneracy of the 2P term.⁹ This simulation approach is of limited value in modeling the MCD spectra of M atoms trapped in novel and heretofore unobserved sites in Rg matrices for which specific site geometries and lattice mode types are, as yet, unknown. A MC approach for handling Rg perturbation in MCD simulations of M/Rg systems naturally suggests itself. A full development of the theory of Monte Carlo-MCD (MC-MCD) simulations of $^2S \rightarrow ^2P$ MCD spectra is presented in the sections that follow. The MC-MCD simulation method is a first order degenerate perturbation method that straightforwardly extends the MC absorption simulation methods of Boatz and Fajardo⁴ and Lawrence and Apkarian⁵ by (1) including both spin-orbit and Zeeman perturbations in the Hamiltonian and (2) separately treating the $^2S \rightarrow ^2P$ transitions associated with LCP and RCP light. The MC-MCD perturbation matrix for the 2P term is a 6 x 6 matrix whose individual matrix elements are expressed in terms of a suitable uncoupled angular momentum p basis set with spin $\{|n/m, sm_s\rangle = |n1\ 1/2\ 1/2\rangle, |n10\ 1/2\ 1/2\rangle, |n1-1\ 1/2\ 1/2\rangle, |n11\ 1/2\ -1/2\rangle, |n10\ 1/2\ -1/2\rangle, |n1-1\ 1/2\ -1/2\rangle\}$.

Theory

As noted above, the theory of MC-MCD spectroscopy of $^2S \rightarrow ^2P$ excitations in M/Rg systems represents an extension of the formalism for MC-absorption spectroscopy developed by Boatz and Fajardo⁴ (for

⁶Piepho, S. B.; Schatz, P. N. *Group Theory in Spectroscopy with Applications to Magnetic Circular Dichroism*; Wiley: New York, 1983.

⁷(a) Luty, F.; Mort, J. *Phys. Rev. Lett.* **1964**, *12*, 45-57. (b) Henry, C. H.; Schnatterly, S. E.; Slichter, C. P. *Phys. Rev.* **1965**, *137*, A583-A602. (c) Mort, J.; Luty, F.; Brown, F. C. *Phys. Rev.* **1965**, *137*, A566-A573. (d) Merle d'Aubinge, Y.; Roussel, A. *Phys. Rev. B* **1971**, *3*, 1421-1427. (e) Osborne, G. A.; Stephens, P. J. *J. Chem. Phys.* **1972**, *56*, 609-618.

⁸(a) Hormes, J.; Schiller, J. *Chem. Phys.* **1983**, *74*, 433-439. (b) Lund, P. A.; Smith, D.; Jacobs, S. M.; Schatz, P. N. *J. Phys. Chem.* **1984**, *88*, 31-42. (c) Lund, P. A.; Smith, D.; Williamson, B. E.; Schatz, P. N.; O'Brien, M. C. *M. J. Phys. Chem.* **1986**, *90*, 2608-2615. (d) Samet, C.; Rose, J. L.; Williamson, B. E.; Schatz, P. N. *Chem. Phys. Lett.* **1987**, *142*, 557-561.

⁹(a) O'Brien, M. C. M. *J. Phys. C: Solid State Phys.* **1985**, *18*, 4963-4973. (b) O'Brien, M. C. M. *J. Chem. Phys.* **1985**, *82*, 3870-3871.

M/Rg systems) and Lawrence and Apkarian⁵ (for X/Rg systems). Key aspects of both the Boatz and Fajardo and Lawrence and Apkarian notational schemes are adopted in the following formal development.

Total Hamiltonian and zeroth-order eigenvectors/eigenvalues: The total Hamiltonian for an alkali metal M atom imbedded in a cryogenic rare gas matrix comprised of N Rg atoms in the presence of an applied external magnetic field is given by

$$H = H_M(\mathbf{r}) + H_{\text{int}}(\mathbf{r}; \mathbf{R}_1, \mathbf{R}_2, \dots, \mathbf{R}_N), \quad (1)$$

where

$$H_M(\mathbf{r}) = T_M(\mathbf{r}) + V_M(\mathbf{r}) \quad (2)$$

is the one-electron Hamiltonian for the optically active electron on M at position \mathbf{r} , comprised of a kinetic energy component $T_M(\mathbf{r})$ and an electrostatic potential energy component $V_M(\mathbf{r})$. The potential $V_M(\mathbf{r})$ is the potential experienced by the optically active electron in the free gas-phase M atom in the absence of spin-orbit coupling or an external magnetic field. The unperturbed Schrodinger equation for the optically active electron of the free M atom is given by

$$H_M|n/m_l m_s\rangle = \epsilon_{nl}|n/m_l m_s\rangle. \quad (3)$$

To describe completely the 2S ground term of M, two zeroth-order eigenvectors $\{|n00 1/2 m_s\rangle; m_s = 1/2, -1/2\}$ are needed for the 2P excited term, six zeroth-order eigenvectors $\{|n1m_l 1/2 m_s\rangle; m_l = 1, 0, -1, m_s = 1/2, -1/2\}$ are required. An uncoupled angular momentum representation $\{|n/m_l m_s\rangle\}$ for the zeroth-order eigenvectors is chosen, without loss generality, because of the transparent way in which MCD selection rules may be expressed in terms of this representation (*vide infra*). However, it is equally valid to use zeroth-order eigenvector sets expressed in the coupled angular momentum representation $\{|n/sjm\rangle\}$ or the Cartesian representation $\{|n/esm_s\rangle\}$ ($e = x, y, z$ for $l = 1$) since the uncoupled, coupled, and Cartesian representations are mutually related by unitary transformations.¹⁰ In this treatment, the interaction Hamiltonian is comprised of four terms, each of which depends upon the nuclear position vectors $\{\mathbf{R}_k\}$ of all of the N Rg atoms in the matrix: a metal-rare gas interaction term, a rare gas-rare gas interaction term, a spin-orbit term, and a Zeeman term,

$$\begin{aligned} H_{\text{int}}(\mathbf{r}; \mathbf{R}_1, \mathbf{R}_2, \dots, \mathbf{R}_N) &= V_{M-\text{Rg}}(\mathbf{r}; \mathbf{R}_1, \mathbf{R}_2, \dots, \mathbf{R}_N) + V_{\text{Rg-Rg}}(\mathbf{R}_1, \mathbf{R}_2, \dots, \mathbf{R}_N) \\ &\quad + H_{SO}(\mathbf{r}; \mathbf{R}_1, \mathbf{R}_2, \dots, \mathbf{R}_N) + H_{\text{Zeeman}}(\mathbf{r}; \mathbf{R}_1, \mathbf{R}_2, \dots, \mathbf{R}_N). \end{aligned} \quad (4)$$

¹⁰Weissbluth, M. *Atoms and Molecules*; Academic: New York, 1978.

The M nucleus is taken to be the origin of the coordinate system with respect to which \mathbf{r} and the $\{\mathbf{R}_k\}$ are defined. In this treatment, it is assumed, following Lawrence and Apkarian, that M-Rg interactions do not affect Rg-Rg interactions; all polarization and electron exchange effects are ignored.⁵

The Rg-Rg and M-Rg potentials: The Rg-Rg interaction potential in Eq. (4) can be approximated as a simple sum over the appropriate Σ symmetry Rg-Rg diatomic potentials

$$V_{Rg-Rg}(\mathbf{R}_1, \mathbf{R}_2, \dots, \mathbf{R}_N) = \sum_{m=1,N} \sum_{m < k} V_{Rg-Rg}(|\mathbf{R}_m - \mathbf{R}_k|) \quad (5)$$

The M-Rg potential, which, in general, exhibits a complicated dependence upon the Rg positions $\{\mathbf{R}_k\}$, is expressed in terms of a Legendre polynomial expansion¹⁰

$$V_{M-Rg}(\mathbf{r}; \mathbf{R}_1, \mathbf{R}_2, \dots, \mathbf{R}_N) = \sum_{k=1,N} \sum_{L=0,\infty} V_L(r, \mathbf{R}_k) P_L(\theta, \phi; \theta_k, \phi_k) \quad (6)$$

where $\mathbf{r} = (r, \theta, \phi)$ is the optically active electron position vector, $\mathbf{R}_k = (\mathbf{R}_k, \theta_k, \phi_k)$ is the position vector for Rg nucleus k . $V_L(r, \mathbf{R}_k)$ is the radial potential function of order L , and $P_L(\theta, \phi; \theta_k, \phi_k)$ is the Legendre polynomial of order L .

$$P_L(\theta, \phi; \theta_k, \phi_k) = 4\pi(2L + 1)^{-1} \sum_{M=-L,L} Y_{LM}(\theta, \phi) Y_{LM}^*(\theta_k, \phi_k) \quad (7)$$

and the Y_{LM} are spherical harmonic functions expressed in the standard Condon and Shortley phase convention.¹¹ Eq. (7) is an expression of one of the possible forms of the spherical harmonic *addition theorem*.¹⁰

The matrix elements of the Rg-Rg perturbation given in Eq. (5) are trivially diagonal in the uncoupled zeroth order eigenvector set $\{|n/m_l s m_s\rangle\}$

$$\langle n' l' m'_l s' m'_s | V_{Rg-Rg} | n/m_l s m_s \rangle = U_{Rg-Rg} \delta(n', n) \delta(l', l) \delta(m'_l, m_l) \delta(s', s) \delta(m'_s, m_s) \quad (8)$$

where, following the notation of Boatz and Fajardo,⁴

$$U_{Rg-Rg} = V_{Rg-Rg}(\mathbf{R}_1, \mathbf{R}_2, \dots, \mathbf{R}_N) = \sum_{m=1,N} \sum_{m < k} V_{Rg-Rg}(|\mathbf{R}_m - \mathbf{R}_k|). \quad (9)$$

It should be noted that U_{Rg-Rg} has the same value for both the 2S and 2P terms at this level of approximation. The matrix elements of the M-Rg interaction potential, Eq. (6), are

¹¹(a) Condon, E. U.; Shortley, G. H. *The Theory of Atomic Spectra*; Cambridge: London, 1963. (b) Weissbluth, Ref. 10, contains a very clear and thorough discussion of the Condon and Shortley spherical harmonic convention.

$$\begin{aligned} & \langle n'l'm_l's'm_s | V_{M-Rg} | n'm_lsm_s \rangle = \\ & \sum_{k=1,N} \sum_{L=0,\infty} \langle n'l' | V_L(r, R_k) | n \rangle \langle l'm_l's'm_s | P_L(\theta, \phi; \theta_k, \phi_k) | l'm_lsm_s \rangle. \end{aligned} \quad (10)$$

Within the 2S manifold where $l = l' = 0$, only the $L = 0$ term in the summation survives

$$\begin{aligned} \langle n'00\ 1/2 m_s | V_{M-Rg} | n00\ 1/2 m_s \rangle &= \sum_{k=1,N} \langle n'0 | V_0(r, R_k) | n0 \rangle \langle 00\ 1/2 m_s | P_0(\theta, \phi; \theta_k, \phi_k) | 00\ 1/2 m_s \rangle \\ &= \sum_{k=1,N} \langle n'0 | V_0(r, R_k) | n0 \rangle \delta(n', n) \delta(m_s', m_s). \end{aligned} \quad (11)$$

Moreover, it can be shown that the radial matrix element is equal to the ground state $X\Sigma$ M-Rg diatomic pair potential at M-Rg separation distance R_k

$$\langle n'0 | V_0(r, R_k) | n0 \rangle = V_{X\Sigma}(R_k). \quad (12)$$

For the 2P matrix elements (where $l' = l = 1$) of the M-Rg interaction potential, only the $L = 0$ and $L = 2$ terms survive

$$\begin{aligned} & \langle n'1m_l's'm_s | V_{M-Rg} | n1m_lsm_s \rangle = \\ & \sum_{k=1,N} \langle n'1 | V_0(r, R_k) | n1 \rangle \langle 1m_l's'm_s | P_0(\theta, \phi; \theta_k, \phi_k) | 1m_lsm_s \rangle + \\ & \sum_{k=1,N} \langle n'1 | V_2(r, R_k) | n1 \rangle \langle 1m_l's'm_s | P_2(\theta, \phi; \theta_k, \phi_k) | 1m_lsm_s \rangle. \end{aligned} \quad (13)$$

The restriction to $L = 0$ and $L = 2$ comes from the Gaunt formula for evaluating integrals involving spherical harmonic functions.¹⁰ The Gaunt formula conditions for $l = 1$ ($l + L + l = \text{even} \#$ greater than or equal to zero) can be satisfied only for $L = 0$ or 2. The radial matrix elements appearing in Eq. (13) may be expressed in terms of M-Rg diatomic pair potentials^{4,5,12} as

$$\langle n'1 | V_0(r, R_k) | n1 \rangle = \langle V_0 \rangle = 1/3 [V_{B\Sigma}(R_k) + 2V_{A\Pi}(R_k)], \quad (14)$$

$$\langle n'1 | V_2(r, R_k) | n1 \rangle = \langle V_2 \rangle = 5/3 [V_{B\Sigma}(R_k) - V_{A\Pi}(R_k)]. \quad (15)$$

^{12(a)} Reid, R. H. G.; Daigarno, A. *Phys. Rev. Lett.* **1969**, 22, 1029. (b) Becker, C. H.; Casavecchia, P.; Lee, Y. T.; Olson, R. E.; Lester, W. A., Jr. *J. Chem. Phys.* **1979**, 70, 5477. (c) Aquilanti, V.; Grossi, G. *J. Chem. Phys.* **1980**, 93, 7187.

The $L = 0$ summation on the right side of Eq. (13) is diagonal in the uncoupled 2P basis

$$\sum_{k=1,N} \langle n' l | V_0(r, R_k) | n l \rangle \langle 1 m_l' s' m_s' | P_0(\theta, \phi; \theta_k, \phi_k) | 1 m_l s m_s \rangle = \\ \sum_{k=1,N} \langle n' l | V_0(r, R_k) | n l \rangle \delta(m_l', m_l) \delta(s', s) \delta(m_s', m_s). \quad (16)$$

The matrix elements of the $L = 2$ summation on the right hand side of Eq. (13) are evaluated by substituting in the explicit form of the Legendre function $P_2(\theta, \phi; \theta_k, \phi_k)$ in terms of spherical harmonics as listed in Eq. (7) and using the Gaunt formula and appropriate Wigner 3-J and/or Clebsch-Gordon relationships¹⁰ to evaluate the resulting spherical harmonic integrals,

$$\sum_{k=1,N} \langle n' l | V_2(r, R_k) | n l \rangle \langle 1 m_l' s' m_s' | P_2(\theta, \phi; \theta_k, \phi_k) | 1 m_l s m_s \rangle = \\ \sum_{k=1,N} \langle n' l | V_2(r, R_k) | n l \rangle \times \\ \{ [4\pi/5] \sum_{M=-2,2} Y_{2M}^*(\theta_k, \phi_k) \langle 1 m_l' | Y_{2M}(\theta, \phi) | 1 m_l \rangle \delta(s', s) \delta(m_s', m_s) \}. \quad (17)$$

The resulting matrix elements from Eq. (17), simplified to the final form reported by Boatz and Fajardo,⁴ are listed in Table 1. The order in which the matrix elements appear in Table 1 is chosen to coincide with the ordering adopted by Boatz and Fajardo⁴ in their spin-free formalism. As such, the 3×3 M-Rg spin-free 2P interaction matrix of Boatz and Fajardo is reproduced as two 3×3 diagonal blocks in the 6×6 2P matrix of Table 1 where the spin of the optically active electron is included explicitly.

Spin-orbit coupling operator: The spin-orbit coupling operator for the optically active electron may be written, using the standard defining equation for the spin-orbit interaction,¹³ in terms of the potential gradient of the free M and M-Rg interaction potentials

$$H_{SO}(r; R_1, R_2, \dots, R_N) = H_{SO,M}(r) + H_{SO,M-Rg}(r; R_1, R_2, \dots, R_N) \\ = \{(2m_e^2 c^2)^{-1} \text{grad}[V_M(r) + V_{M-Rg}(r; R_1, R_2, \dots, R_N)] \times p\} \cdot S \quad (18)$$

where p and S are, respectively, the linear momentum and spin operators for the optically active electron. At this juncture, it is helpful to remember that the free M atom core potential $V_M(r)$ is spherically symmetric, thus

$$H_{SO,M}(r) = \{(2m_e^2 c^2)^{-1} \text{grad}[V_M(r)] \times p\} \cdot S = (2m_e^2 c^2 r)^{-1} d[V_M(r)]/dr \{r \times p\} \cdot S = \xi_M(r) L \cdot S \quad (19)$$

where $L = r \times p$ is the angular momentum operator for the optically active electron and

¹³Griffith, J. S. *The Theory of Transition-Metal Ions*; Cambridge: London, 1961, p 125.

Table 1. Matrix Elements of the $L = 2$ M-Rg Interaction Term in Eq. (17) for the Uncoupled 2P Zeroth-Order Eigenvector Set $\{|n\ell m_s m_{s'}\rangle\}$.

	$ n 1 1 1/2 1/2\rangle$	$ n 1 0 1/2 1/2\rangle$	$ n -1 1 1/2 1/2\rangle$	$ n 1 1 1/2-1/2\rangle$	$ n 1 0 1/2-1/2\rangle$	$ n -1 1 1/2-1/2\rangle$
$\langle n 1 1 1/2 1/2 $	$(1/10)\langle V_\gamma, x \rangle$ $\{-3\cos^2\theta_\nu - 1\}$ $\{3 2^{1/2}\sin\theta_\nu\cos\theta_\nu e^{-i\phi_k}\}$	$(1/10)\langle V_\gamma, x \rangle$ $\{-3 2^{1/2}\sin\theta_\nu\cos\theta_\nu e^{i\phi_k}\}$	$(1/10)\langle V_\gamma, x \rangle$ $\{-3 \sin^2\theta_\nu e^{-2i\phi_k}\}$			
$\langle n 1 0 1/2 1/2 $	$(1/10)\langle V_\gamma, x \rangle$ $\{-3 2^{1/2}\sin\theta_\nu\cos\theta_\nu e^{i\phi_k}\}$	$(1/10)\langle V_\gamma, x \rangle$ $\{2(3\cos^2\theta_\nu - 1)\}$	$(1/10)\langle V_\gamma, x \rangle$ $\{3 2^{1/2}\sin\theta_\nu\cos\theta_\nu e^{-i\phi_k}\}$			
$\langle n -1 1 1/2 1/2 $	$(1/10)\langle V_\gamma, x \rangle$ $\{-3 \sin^2\theta_\nu e^{2i\phi_k}\}$	$(1/10)\langle V_\gamma, x \rangle$ $\{3 2^{1/2}\sin\theta_\nu\cos\theta_\nu e^{i\phi_k}\}$	$(1/10)\langle V_\gamma, x \rangle$ $\{-(3\cos^2\theta_\nu - 1)\}$			
$\langle n 1 1 1/2-1/2 $				$(1/10)\langle V_\gamma, x \rangle$ $\{-(3\cos^2\theta_\nu - 1)\}$	$(1/10)\langle V_\gamma, x \rangle$ $\{-3 2^{1/2}\sin\theta_\nu\cos\theta_\nu e^{-i\phi_k}\}$	$(1/10)\langle V_\gamma, x \rangle$ $\{-3 \sin^2\theta_\nu e^{-2i\phi_k}\}$
$\langle n 1 0 1/2-1/2 $				$(1/10)\langle V_\gamma, x \rangle$ $\{-3 2^{1/2}\sin\theta_\nu\cos\theta_\nu e^{i\phi_k}\}$	$(1/10)\langle V_\gamma, x \rangle$ $\{2(3\cos^2\theta_\nu - 1)\}$	$(1/10)\langle V_\gamma, x \rangle$ $\{3 2^{1/2}\sin\theta_\nu\cos\theta_\nu e^{-i\phi_k}\}$
$\langle n -1 1 1/2-1/2 $				$(1/10)\langle V_\gamma, x \rangle$ $\{-3 \sin^2\theta_\nu e^{2i\phi_k}\}$	$(1/10)\langle V_\gamma, x \rangle$ $\{3 2^{1/2}\sin\theta_\nu\cos\theta_\nu e^{i\phi_k}\}$	$(1/10)\langle V_\gamma, x \rangle$ $\{-(3\cos^2\theta_\nu - 1)\}$

$$\xi_M(r) = (2m_e^2 c^2 r)^{-1} d[V_M(r)]/dr \quad (20)$$

is the standard spin-orbit coupling operator for the free M atom. The M-Rg interaction potential of Eq. (6) can be broken up into spherical and non-spherical components

$$V_{M-Rg}(r; R_1, R_2, \dots, R_N) = \sum_{k=1,N} V_0(r, R_k) + \sum_{k=1,N} \sum_{L=1,\infty} V_L(r, R_k) P_L(\theta, \phi; \theta_k, \phi_k), \quad (21)$$

from which the gradient of the M-Rg potential can be written as

$$\text{grad}V_{M-Rg}(r; R_1, R_2, \dots, R_N) = \sum_{k=1,N} r^{-1} d[V_0(r, R_k)]/dr +$$

$$\text{grad} \left\{ \sum_{k=1,N} \sum_{L=1,\infty} V_L(r, R_k) P_L(\theta, \phi; \theta_k, \phi_k) \right\}. \quad (22)$$

The spin-orbit coupling operator arising from the M-Rg interaction potential is, therefore,

$$H_{SO,M-Rg}(r; R_1, R_2, \dots, R_N) = \xi_{M-Rg}(r) \mathbf{L} \cdot \mathbf{S} + \\ [(2m_e^2 c^2 r)^{-1} \text{grad} \left\{ \sum_{k=1,N} \sum_{L=1,\infty} V_L(r, R_k) P_L(\theta, \phi; \theta_k, \phi_k) \right\} \times \mathbf{p}] \cdot \mathbf{S} \quad (23)$$

where the spherical M-Rg spin orbit coupling operator is given by

$$\xi_{M-Rg}(r) = (2m_e^2 c^2 r)^{-1} \sum_{k=1,N} d[V_0(r, R_k)]/dr. \quad (24)$$

In the form of the theory currently in use for MC-MCD simulations, it is assumed that the gradient expression in Eq. (23) is small and can be neglected; i.e., no $L > 0$ terms are assumed to contribute to the spin-orbit coupling interaction. The total spin-orbit coupling operator of the M/Rg system in the spherical approximation is thus given by

$$H_{SO}(r) = H_{SO,M}(r) + H_{SO,M-Rg}(r) = [\xi_M(r) + \xi_{M-Rg}(r)] \mathbf{L} \cdot \mathbf{S} = \xi(r) \mathbf{L} \cdot \mathbf{S}, \quad (25)$$

where the dependence on the Rg position vectors $\{R_k\}$, while present, is not explicitly shown in the interest of preserving a compact notation in the final form of the equations used. For the purposes of matrix element evaluation with respect to the uncoupled zeroth-order angular momentum eigenvectors in the 2P manifold, it is convenient to express $\mathbf{L} \cdot \mathbf{S}$ in terms of the appropriate spherical tensor operator components¹⁰

$$\mathbf{L} \cdot \mathbf{S} = -L_{+1}S_{-1} + L_0S_0 - L_{-1}S_{+1} \quad (26)$$

to give

$$\langle n'l'm_l's'm_s | H_{SO} | n'm_l'sm_s \rangle = \langle nl | \xi(r) | nl \rangle \langle l'm_l's'm_s | -L_{+1}S_{-1} + L_0S_0 - L_{-1}S_{+1} | l'm_l'sm_s \rangle. \quad (27)$$

The spin-orbit perturbation is not diagonal in uncoupled 2P zeroth order eigenvector set. The non-zero matrix elements of Eq. (27) are given in Table 2 below where $\zeta_{nl} = \langle nl | \xi(r) | nl \rangle$.

Table 2. Matrix Elements of H_{SO} for the Uncoupled 2P Zeroth-Order Eigenvector Set $\{|n/l, m_l, s_m\rangle\}$.

	$ n 1 1 1/2 1/2\rangle$	$ n 1 0 1/2 1/2\rangle$	$ n 1-1 1/2 1/2\rangle$	$ n 1 1 1/2-1/2\rangle$	$ n 1 0 1/2-1/2\rangle$	$ n 1-1 1/2-1/2\rangle$
$\langle n 1 1 1/2 1/2 $	$(1/2)\zeta_{nl}$					
$\langle n 1 0 1/2 1/2 $				$(2^{-1/2})\zeta_{nl}$		
$\langle n 1-1 1/2 1/2 $			$-(1/2)\zeta_{nl}$		$(2^{-1/2})\zeta_{nl}$	
$\langle n 1 1 1/2-1/2 $		$(2^{-1/2})\zeta_{nl}$		$-(1/2)\zeta_{nl}$		
$\langle n 1 0 1/2-1/2 $			$(2^{-1/2})\zeta_{nl}$			
$\langle n 1-1 1/2-1/2 $						$(1/2)\zeta_{nl}$

No spin-orbit coupling is possible when the optically active electron is in the 2S ground state manifold where $l = 0$. In the 2P excited state manifold where $l = 1$, the spin-orbit coupling constant is expressed formally as the sum of the radial expectation values of the spherically symmetric M and M-Rg spin-orbit coupling operators

$$\zeta_{nl} = \langle nl | \xi_M(r) | nl \rangle + \langle nl | \xi_{M-Rg}(r) | nl \rangle = \zeta_M + \zeta_{M-Rg}. \quad (28)$$

If the radial eigenvector $|nl\rangle$ is the free atom P state atomic radial eigenvector for M, or if $|nl\rangle$ closely approximates this eigenvector, then ζ_M is the free alkali atom spin-orbit coupling constant and ζ_{M-Rg} is the spherical perturbation to the spin-orbit coupling constant induced in M by the Rg matrix environment. Eq. (28) provides an insightful context for discussing the possibilities of (1) spin-orbit coupling constant sign reversal or (2) reduction of the magnitude of a spin-orbit coupling constant (partial quenching) in a 2P M-Rg system. For any given alkali metal M the free atom 2P spin-orbit coupling constant is positive; i.e., $\zeta_M > 0$. Thus, for a 2P spin-orbit coupling constant ζ_{nl} to be negative in a M-Rg system, the M-Rg spin orbit contribution must be negative and larger in magnitude than the free M atom spin-orbit coupling constant; i.e., $\zeta_{M-Rg} < 0$ and $|\zeta_{M-Rg}| > \zeta_M$. The conditions for the partial quenching case, where ζ_{nl} is still positive but smaller than ζ_M , are: $\zeta_{M-Rg} < 0$ and $|\zeta_{M-Rg}| < \zeta_M$. In the actual MC-MCD simulations, ζ_{nl} is introduced as an adjustable parameter. The two cases may be explored in the MC-MCD simulations by making appropriate choices for ζ_{nl} with respect to the known positive ζ_M of the alkali metal M atom of interest.

Zeeman Perturbation: The Zeeman perturbation operator is given by

$$H_{Zeeman}(r; \mathbf{R}_1, \mathbf{R}_2, \dots, \mathbf{R}_N) = \mu_B \mathbf{B}_{local} \cdot (\mathbf{L} + 2\mathbf{S}) \quad (29)$$

where μ_B is the Bohr magneton, \mathbf{L} and \mathbf{S} are the orbital and spin angular momentum operators for the optically active electron, and \mathbf{B}_{local} is the magnetic field locally experienced by the optically active electron as a result of the

application of an external magnetic field \mathbf{B} to the M/Rg system. The both the magnitude and the direction local magnetic field vector are influenced by the positions of the Rg atoms and by the nature of the electronic state of the optically active electron (i.e., 2S or 2P). The relationship between the external magnetic field and the local magnetic field thus may be expressed as

$$\mathbf{B}_{\text{local}} = \mathbf{B}_{\text{local}}(\mathbf{R}_1, \mathbf{R}_2, \dots, \mathbf{R}_N) = [1 - \sigma_{n,l}(\mathbf{R}_1, \mathbf{R}_2, \dots, \mathbf{R}_N)]\mathbf{B} \quad (30)$$

where $\sigma_{n,l}(\mathbf{R}_1, \mathbf{R}_2, \dots, \mathbf{R}_N)$ is a 3×3 shielding tensor whose individual components depend upon both the nature of the electronic state being shielded and the positions of the Rg atoms in the matrix. In actual MC-MCD simulations, it is assumed that the local magnetic field is aligned along the laboratory z axis

$$\mathbf{B}_{\text{local}} = B_{\text{local}} \mathbf{e}_z \quad (31)$$

which gives

$$H_{\text{Zeeman}} = \mu_B B_{\text{local}} (L_z + 2S_z) = \mu_B B (1 - \sigma_{n,l}) (L_z + 2S_z). \quad (32)$$

Different values of B_{local} can be chosen, if desired, to model the effects of slightly different 2S and 2P shielding constants $\sigma_{n,0}$ and $\sigma_{n,1}$. Changes in the direction of $\mathbf{B}_{\text{local}}$ away from the z axis arising from the tensor character of $\sigma_{n,l}$ can be modeled by preserving the laboratory z axis orientation of the Zeeman perturbation, which is very desirable from the standpoint of matrix element evaluation, and rotating the Rg position vector set through an arbitrary unitary rotation transformation $U\{\mathbf{R}_k\} = \{\mathbf{R}'_k\}$. In any event, it is expected that differences between \mathbf{B} and $\mathbf{B}_{\text{local}}$ will be comparatively small for closed shell Rg atoms in their ground 1S electronic states. Certainly within the chosen MC-MCD simulation restrictions mentioned earlier of neglecting polarization effects and the higher excited states of the Rg atoms, \mathbf{B} will not differ much from $\mathbf{B}_{\text{local}}$. The Zeeman perturbation as expressed in Eq. (20) is diagonal in the chosen zeroth-order uncoupled angular momentum eigenvector space

$$\langle n' m'_l s' m'_s | H_{\text{Zeeman}} | n m_l s m_s \rangle = \mu_B B_{\text{local}} (m_l + 2m_s) \delta(n', n) \delta(l', l) \delta(m'_l, m_l) \delta(s', s) \delta(m'_s, m_s) \quad (33)$$

It is assumed that states with different values of the radial quantum numbers n do not mix.

Diagonalization of the full Hamiltonian matrix in the 2S and 2P manifolds: An implementation of degenerate first-order perturbation theory is required to arrive at approximate 2S and 2P eigenvalues and eigenvectors of the full M/Rg Hamiltonian given in Eq. (1). These eigenvalues and eigenvectors contain the effects of the various terms in the interaction Hamiltonian Eq. (4). First-order perturbation theory gives eigenvalues that

are correct through first order. The associated eigenvectors are those *particular* zeroth-order eigenvectors, expressed as orthonormal linear combinations of the zeroth-order eigenvector set $\{|n'l'm_lsm_s\rangle\}$,

$$\Psi_i = |n'i\rangle = \sum_{m_{l=-l,l}} \sum_{m_s=-1/2,1/2} C_i^{nlm_l m_s} |n'm_l sm_s\rangle, \quad (34)$$

$$\langle n'i' | n'i \rangle = \delta(i', i), \quad (35)$$

that diagonalize the 2×2 (2S manifold) or 6×6 (2P manifold) matrix formed by sandwiching the full Hamiltonian, Eq. (1), within the same uncoupled zeroth-order eigenvector set $\{|n'l'm_lsm_s\rangle\}$; i.e.,

$$\langle n'l'm_l's'm_s | H | n'm_l sm_s \rangle = \langle n'l'm_l's'm_s | H_M | n'm_l sm_s \rangle + \langle n'l'm_l's'm_s | H_{int} | n'm_l sm_s \rangle. \quad (36)$$

Both the first-order eigenvalues and the associated zeroth-order eigenvectors are needed for MC-MCD simulations. Since the first matrix element on the right side of Eq. (36) is the zeroth-order matrix element of the free M Hamiltonian (see Eq. 3), it is automatically diagonal in either the original zeroth-order basis $\{|n'l'm_lsm_s\rangle\}$

$$\langle n'l'm_l's'm_s | H_M | n'm_l sm_s \rangle = \varepsilon_n \delta(n', n) \delta(l', l) \delta(m_l', m_l) \delta(s', s) \delta(m_s', m_s), \quad (37)$$

or the new zeroth-order basis $\{|n'i\rangle\}$

$$\langle n'l'i' | H_M | n'i \rangle = \varepsilon_n \delta(n', n) \delta(l', l) \delta(i', i). \quad (38)$$

Within the 2S manifold, the interaction matrix on the right side of Eq. (36) also is diagonal, thus

$$\Psi_i(^2S) = |n0i\rangle = \sum_{m_s=-1/2,1/2} C_i^{n00m_s} |n001/2 m_s\rangle, \quad (34)$$

which reduces to

$$\Psi_1(^2S) = |n00 1/2 1/2\rangle, \quad (35a)$$

$$\Psi_2(^2S) = |n00 1/2 -1/2\rangle. \quad (35b)$$

The i index is mapped onto the m_s index one-to-one in this specific case. The final expressions for the 2S eigenvalues, correct through first order, are obtained by collecting together the matrix elements previously derived for the Rg-Rg, M-Rg, and Zeeman perturbations in Eqs. (8)-(9), (11)-(12), and (33), respectively:

$$\begin{aligned} E_i(^2S) &= \varepsilon_{n0}(^2S) + E_{n0i}(^2S) \\ &= \varepsilon_{n0}(^2S) + U_{Rg-Rg}(^2S) + U_{M-Rg}(^2S) + U_{Zeeman}(^2S) \\ &= \varepsilon_{n0}(^2S) + \sum_{m=1,N} \sum_{m< k} V_{Rg-Rg,X\Sigma}(|\mathbf{R}_m \cdot \mathbf{R}_k|) + \sum_{k=1,N} V_{M-Rg,X\Sigma}(\mathbf{R}_k) + \mu_B B_{local}(2m_s). \end{aligned} \quad (39)$$

In Eq. (39) the eigenvalue convention of Boatz and Fajardo⁴ is adopted; E_i is an eigenvalue of a specific 2S state Ψ_i correct through first order, ε_{n0} is the zeroth order 2S eigenvalue for the optically active electron of the free M atom, and E_{n0i} is the first-order eigenvalue correction term arising from the interaction Hamiltonian.

To obtain 2P final state eigenvalues correct through first order

$$E_f(^2P) = \varepsilon_{n1}(^2P) + E_{n1f}(^2P), \quad (40)$$

the first-order eigenvalue set $\{E_{n0f}(^2P); f = 1, 6\}$ must be calculated by diagonalizing the 6×6 2P interaction matrix in Eq. (36). The individual matrix elements of this interaction matrix, shown below in Table 3, are obtained by collecting together the matrix elements previously derived for the 2P Rg-Rg, M-Rg, spin-orbit, and Zeeman perturbations in Eqs. (8)-(9), Table 1, Table 2, and Eq. (33), respectively. It should be noted that the U_{Rg-Rg} and the $\langle V_0 \rangle_{M-Rg}$ perturbations are diagonal perturbations in this 6×6 matrix and can be separated from the 6×6 matrix eigenvalue problem, as illustrated by Boatz and Fajardo in their Eqs. (6) and (8).⁴ The associated final state 2P eigenvectors, which diagonalize this matrix, are

$$\Psi_f(^2P) = |n1f\rangle = \sum_{m_l=-1,1} \sum_{m_s=-1/2,1/2} C_f^{nlm_lm_s} |n1m_l 1/2 m_s\rangle, \quad (41)$$

where $f = 1, 6$ and

$$\langle n1f | n1f \rangle = \delta(f,f). \quad (42)$$

$^2S \rightarrow ^2P$ transition energies and transition moment integrals for M/Rg MCD spectroscopy: The combined effects of the Rg-Rg, M-Rg, spin-orbit, and Zeeman perturbations on the optically active electron of a M/Rg system act to split the ground 2S manifold into two energetically distinct states $\{\Psi_i; i = 1, 2\}$ and the excited 2P manifold into six energetically distinct states $\{\Psi_f; f = 1, 6\}$. The specific characteristics of the 2S and 2P eigenvalues and their associated eigenvectors are dependent upon the particular Rg configuration $\{\mathbf{R}_1, \mathbf{R}_2, \dots, \mathbf{R}_N\}$

within which the problem is solved. Thus, for a given Rg configuration $\{R_1, R_2, \dots, R_N\}$ and magnitude the magnetic field, up to 12 energetically and optically distinct transitions may be identified within the manifold-to-manifold $^2S \rightarrow ^2P$ transition of the M/Rg system. The transition energies of these 12 $^2S \rightarrow ^2P$ transitions are given as

$$\hbar v_{fi} = E_f(^2P) - E_i(^2S) \quad (43)$$

Table 3. Matrix Elements of the 6×6 2P Interaction Matrix in the Uncoupled Angular Momentum Representation $\{|n, m_s, m_{ls}\rangle\}$.

	$ n 1 1 1/2 1/2\rangle$	$ n 1 0 1/2 1/2\rangle$	$ n 1-1 1/2 1/2\rangle$	$ n 1 1 1/2-1/2\rangle$	$ n 1 0 1/2-1/2\rangle$	$ n 1-1 1/2-1/2\rangle$
$\langle n 1 1 1/2 1/2 $	$\langle V_\alpha \rangle + (1/10)\langle V_\gamma \rangle$ $\times \{-3\cos^2\theta_L - 1\}$ $+ (1/2)\zeta_{\alpha\beta} + 2\mu_B B$ $+ U_{\alpha\beta\gamma\delta}$	$(1/10)\langle V_\gamma \rangle x$ $\times \{-3 2^{1/2}\sin\theta_L \cos\theta_L$ $e^{-i\phi_k}\}$	$(1/10)\langle V_\gamma \rangle x$ $\times \{-3 \sin^2\theta_L e^{-2i\phi_k}\}$			
$\langle n 1 0 1/2 1/2 $	$(1/10)\langle V_\gamma \rangle x \{-3 2^{1/2}\sin\theta_L \cos\theta_L$ $e^{i\phi_k}\}$	$\langle V_\alpha \rangle + (1/10)\langle V_\gamma \rangle$ $\times \{2(3\cos^2\theta_L - 1)\}$ $+ \mu_B B + U_{\alpha\beta\gamma\delta}$	$(1/10)\langle V_\gamma \rangle x$ $\times \{3 2^{1/2}\sin\theta_L \cos\theta_L$ $e^{-i\phi_k}\}$	$2^{-1/2}\zeta_{\alpha\beta}$		
$\langle n 1-1 1/2 1/2 $	$(1/10)\langle V_\gamma \rangle x$ $\times \{-3 \sin^2\theta_L e^{2i\phi_k}\}$	$(1/10)\langle V_\gamma \rangle x$ $\times \{3 2^{1/2}\sin\theta_L \cos\theta_L$ $e^{i\phi_k}\}$	$\langle V_\alpha \rangle + (1/10)\langle V_\gamma \rangle$ $\times \{-3(\cos^2\theta_L - 1)\}$ $- (1/2)\zeta_{\alpha\beta} + U_{\alpha\beta\gamma\delta}$		$2^{-1/2}\zeta_{\alpha\beta}$	
$\langle n 1 1 1/2-1/2 $		$2^{-1/2}\zeta_{\alpha\beta}$		$\langle V_\alpha \rangle + (1/10)\langle V_\gamma \rangle$ $\times \{-3(\cos^2\theta_L - 1)\}$ $- (1/2)\zeta_{\alpha\beta} + U_{\alpha\beta\gamma\delta}$	$(1/10)\langle V_\gamma \rangle x$ $\times \{-3 2^{1/2}\sin\theta_L \cos\theta_L$ $e^{-i\phi_k}\}$	$(1/10)\langle V_\gamma \rangle x$ $\times \{-3 \sin^2\theta_L e^{-2i\phi_k}\}$
$\langle n 1 0 1/2-1/2 $			$2^{-1/2}\zeta_{\alpha\beta}$	$(1/10)\langle V_\gamma \rangle x$ $\times \{3 2^{1/2}\sin\theta_L \cos\theta_L$ $e^{i\phi_k}\}$	$\langle V_\alpha \rangle + (1/10)\langle V_\gamma \rangle$ $\times \{2(3\cos^2\theta_L - 1)\}$ $- \mu_B B + U_{\alpha\beta\gamma\delta}$	$(1/10)\langle V_\gamma \rangle x$ $\times \{3 2^{1/2}\sin\theta_L \cos\theta_L$ $e^{-i\phi_k}\}$
$\langle n 1-1 1/2-1/2 $				$(1/10)\langle V_\gamma \rangle x$ $\times \{-3 \sin^2\theta_L e^{2i\phi_k}\}$	$(1/10)\langle V_\gamma \rangle x$ $\times \{-3 2^{1/2}\sin\theta_L \cos\theta_L$ $e^{i\phi_k}\}$	$\langle V_\alpha \rangle + (1/10)\langle V_\gamma \rangle$ $\times \{-3(\cos^2\theta_L - 1)\}$ $- (1/2)\zeta_{\alpha\beta} - 2\mu_B B$ $+ U_{\alpha\beta\gamma\delta}$

where $i = 1,2$ and $f = 1,6$. The Rg - Rg interaction energy terms cancel in Eq. (43) since $U_{Rg-Rg}(^2P) = U_{Rg-Rg}(^2S) = U_{Rg-Rg}$.

Electronic transitions involving the optically active electron of a M/Rg system are well described as electric dipole transitions. In MCD spectroscopy, each of the 12 transitions may be induced to a greater or lesser extent by either LCP or RCP light interacting with the M/Rg system in the electric dipole limit and tuned to the particular transition energy $h\nu_{fi}$. Thus, both LCP and RCP electric dipole transition moment integrals must be computed for each of the 12 possible combinations of initial and final states; i.e., 24 transition moment integrals, 12 for LCP light and 12 for RCP light, are needed to describe the MCD spectrum of a $^2S \rightarrow ^2P$ transition in M/Rg system in a particular Rg configuration $\{R_1, R_2, \dots, R_N\}$; i.e.,

$$\langle \Psi_f(^2P) | O_{LCP} | \Psi_i(^2S) \rangle, \quad (44a)$$

$$\langle \Psi_f(^2P) | O_{RCP} | \Psi_i(^2S) \rangle, \quad (44b)$$

where $i = 1,2$ and $f = 1,6$. O_{LCP} and O_{RCP} are the electric dipole transition operators for LCP and RCP light in Eqs. (44a) and (44b). The electric dipole moment operator m of the M/Rg system is, to a very good initial approximation, determined by the position $r = (x, y, z)$ and charge $-e$ of the optically active electron. The Rg atoms are electrically neutral and their contributions to the dipole moment can be neglected if polarization effects are assumed to be small. The M^+ core is positioned at the origin of the chosen coordinate system and thus does not contribute to the expression for the dipole moment at this level of approximation; i.e.,

$$m = \sum_i q_i r_i = -er + e0 = -e(xe_x + ye_y + ze_z) + e(0e_x + 0e_y + 0e_z) = -e(xe_x + ye_y + ze_z). \quad (45)$$

However, the optically active electron at position r will induce a slight polarization in the M^+ core and the Rg matrix. This polarization can be represented as a small negative electrostatic image charge $-q'$ at $-r$. Thus, polarization effectively reduces the charge of the optically active electron to

$$-e' = -e + q' \quad (46)$$

where $|e'| < |e|$, and the dipole moment operator of the M/Rg system becomes

$$m = -e'r = -e'(xe_x + ye_y + ze_z).^{14} \quad (47)$$

¹⁴It can be argued that the image charge $-q'$ (and hence $-e'$) is not, strictly speaking, a constant, but will exhibit both a radial dependence (i.e., different q' for small r vs. large r) and angular dependence arising from the specific positions of the Rg atoms (R_1, R_2, \dots, R_N) in the M/Rg system. These effects are neglected at this level of theory.

Within the Piepho and Schatz unit vector conventions for LCP and RCP light⁶

$$\pi_{LCP} = 2^{-1/2}(\mathbf{e}_x - i\mathbf{e}_y), \quad (48a)$$

$$\pi_{RCP} = 2^{-1/2}(\mathbf{e}_x + i\mathbf{e}_y), \quad (48b)$$

the LCP and RCP electric dipole moment operators for the M/Rg system become

$$O_{LCP} = \mathbf{m} \cdot \pi^*_{LCP} = -e' 2^{-1/2}(x + iy) = e'(4\pi/3)^{1/2} Y_{11}(\theta, \phi) r, \quad (49a)$$

$$O_{RCP} = \mathbf{m} \cdot \pi^*_{RCP} = -e' 2^{-1/2}(x - iy) = -e'(4\pi/3)^{1/2} Y_{1-1}(\theta, \phi) r. \quad (49b)$$

Since each of the $\Psi_i(^2S)$ and $\Psi_f(^2P)$ states is expressed in terms of the uncoupled zeroth-order angular momentum eigenvector set $\{|n/m_l s m_s\rangle\}$ (see Eqs. (34) and (41)), the specific form of the transition moment integrals given in Eqs. (49a) and (49b) may be determined by evaluating the integrals

$$\langle n'm_l's m_s | O_{LCP} | n'm_l s m_s \rangle = \langle n1 m_l' 1/2 m_s | O_{LCP} | n00 1/2 m_s \rangle = f \delta(m_l', 1) \delta(m_s', m_s), \quad (50a)$$

$$\langle n'm_l's m_s | O_{RCP} | n'm_l s m_s \rangle = \langle n1 m_l' 1/2 m_s | O_{RCP} | n00 1/2 m_s \rangle = -f \delta(m_l', -1) \delta(m_s', m_s), \quad (50b)$$

where

$$f_{LCP} = f = (e'[4\pi/3]^{1/2}) \langle n1|r|n0 \rangle \langle Y_{11}|Y_{11} \rangle = (e'[3]^{-1/2}) \langle n1|r|n0 \rangle, \quad (51a)$$

$$f_{RCP} = -f = (-e'[4\pi/3]^{1/2}) \langle n1|r|n0 \rangle \langle Y_{1-1}|Y_{1-1} \rangle = -(e'[3]^{-1/2}) \langle n1|r|n0 \rangle. \quad (51b)$$

Eqs. (50a) and (51a) express the fact that an LCP electric dipole transition acts on the orbital angular momentum component of the uncoupled wave function, increasing both l and m_l by one unit while leaving s and m_s unchanged. The corresponding RCP electric dipole transition described in Eqs. (50b) and (51b) also acts on the orbital angular momentum in the uncoupled wave function, increasing l by one unit and decreasing m_l by one unit. In Eqs. (51a) and (51b) f is the magnitude of the evaluated transition moment integral. Note that the value of f is the same for all allowed transitions. By combining the transition moment integral expressions in Eqs. (44), (50), and (51) with the appropriate expressions for $\Psi_i(^2S)$ and $\Psi_f(^2P)$ in the uncoupled basis as given in Eqs. (34), (35), and (41), final expressions for the contribution to the MCD spectrum by the transition $i \rightarrow f$ at energy $h\nu_{fi}$ can be written:

$$\begin{aligned}
\Delta A'(v_{fi}) &= A_{LCP}'(v_{fi}) - A_{RCP}'(v_{fi}) \\
&= \alpha \{ |<\Psi_f(2P)|O_{LCP}|\Psi_i(2S)>|^2 - |<\Psi_f(2P)|O_{RCP}|\Psi_i(2S)>|^2 \} \\
&= \alpha f^2 \{ |C_f^{n1,m_i=1,m_s}|^2 - |C_f^{n1,m_i=-1,m_s}|^2 \} \times [1 + (e^{-2\mu_B B/kT} - 1) \delta(m_s, 1/2)]
\end{aligned} \quad (52)$$

where α is a numerical constant that relates the squared transition moment integrals to the absorbances and the initial state index i is associated with $m_s = -1/2$ or $1/2$ in the 2S manifold. The MCD spectral amplitude at energy $h\nu_{fi}$ for the Rg configuration $\{\mathbf{R}_1, \mathbf{R}_2, \dots, \mathbf{R}_N\}$ is seen to be related to differences of squares of selected 2P eigenvector coefficients computed for that configuration. The term in square brackets on the right side of Eq. (52) is a Boltzmann factor for the 2S manifold. The Zeeman perturbation splits the energies of the $m_s = -1/2$ and $1/2$ states of the 2S manifold by a factor of $2\mu_B B$. The $m_s = -1/2$ and $1/2$ states will, therefore, have different thermal populations. This must be accounted for in computing the various contributions to the MCD spectrum.

Monte Carlo Simulation of the MCD Spectrum: The full MCD spectrum for a $^2S \rightarrow ^2P$ transition in a M/Rg system in a specific Rg configuration $\{\mathbf{R}_1, \mathbf{R}_2, \dots, \mathbf{R}_N\}$ is, therefore, a "stick MCD spectrum" consisting of 12 lines, appropriately placed on the x (energy) axis at transition energies $h\nu_{fi}$, whose magnitudes and directions (+ or -) on the y ($\Delta A'$) axis are determined by computing Eq. (52) for all possible choices of i and f . To simulate real MCD spectrum, many stick MCD spectra, each arising from a different Rg configuration, are appropriately averaged together using a MC scheme based upon the original Metropolis et al. algorithm¹⁵ exactly as implemented by Boatz and Fajardo for the case of electronic absorption spectroscopy.⁴ A MC-MCD simulation begins by choosing an initial Rg configuration $\{\mathbf{R}_1, \mathbf{R}_2, \dots, \mathbf{R}_N\}_{\text{initial}}$, typically representing an idealized trapping site (e.g., a single substitutional site with O_h symmetry). The MC energy optimization scheme operates in the 2S ground state manifold. At this stage, the very small Zeeman perturbation of the 2S manifold is neglected. MCD stick spectra arising from more favorable configurations are weighted more heavily in the averaging process than those arising from the less favorable configurations. In actual practice, the LCP and RCP contributions to the MCD spectrum appearing in Eq. (52) are accumulated and stored separately. This allows the electronic absorption spectrum to be recovered from the MC-MCD simulation as⁶

$$A' = A = 1/2[A_{LCP}' + A_{RCP}']. \quad (53)$$

Eq. (53) expresses the fact that the electronic absorption spectra of M/Rg systems are essentially unaffected by the application of an external magnetic field.

Orientational averaging in MC-MCD simulations: In an MCD experiment, the propagation direction of the light, which is always parallel to the \mathbf{B} vector, rigorously defines the laboratory frame z axis. The laboratory frame x and y axes are set parallel to the sapphire deposition window and perpendicular to \mathbf{B} with the origin at the

¹⁵Metropolis, N.; Rosenbluth, A. W.; Rosenbluth, M. N.; Teller, A. H.; Teller, E. *J. Chem. Phys.* **1953**, *21*, 1087.

M nucleus. All Rg positions, eigenvectors, and selection rules are described with respect to this laboratory frame. To model the effects of arbitrary Rg lattice orientation relative to the laboratory frame, the 6×6 2P matrix listed in Table 3 is separated into M/Rg and spin-orbit + Zeeman matrices

$$[M/Rg + SO + Zeeman] = [M/Rg] + [SO + Zeeman]. \quad (54)$$

Arbitrary orientations of the Rg matrix relative to the laboratory frame can be modeled by re-writing Eq. (54) as

$$[M/Rg + SO + Zeeman] = [U][M/Rg][U]^{-1} + [SO + Zeeman], \quad (55)$$

where U is an arbitrary randomly generated unitary rotation matrix (e.g., an Eulerian rotation matrix). The MC-MCD simulation process is carried out as before using Eq. (55) rather than Eq. (54).

Lattice temperature vs. magnetic temperature in MC-MCD simulations: Temperature effects appear in two distinct places in MC-MCD simulations. A lattice temperature must be specified for the MC simulation process. It may be argued that a proper representation of quantum mechanical zero point vibrational motions of the M/Rg lattice at temperature T requires the classical MC simulation to be carried out at a classical lattice temperature $T' > T$.⁵ However, a temperature for the Boltzmann factor of the Zeeman-split 2S term also must be included. This "magnetic temperature" always should be the actual system temperature T. The MC-MCD simulation code has the option of specifying separate values for the lattice temperature T' and the magnetic temperature T. Lawrence and Apkarian discuss the relationship between T' and T in classical MC simulations of doped Rg systems.⁵

MC-MCD Simulations:

Detailed MC-MCD simulations for the Na/Ar system will be presented in the near future by Terrill-Stolper.¹⁶ At this point it should be noted that the MC-MCD simulation code based upon the theory outlined above has passed the following tests in Na/Ar. The MC-MCD spectra (and associated absorption spectra) (1) exhibit MCD and absorption band profiles that look very similar to the experimental spectra of M/Rg systems, (2) the MCD and absorption band profiles properly overlay each other in energy, (3) properly invert when the direction of the magnetic field is reversed, (4) increase or decrease in amplitude with increases or decreases in B, (5) yield proper spin-orbit coupling constant magnitudes and signs from band moment⁶ analyses, (6) are suitably responsive to temperature effects and orientational averaging.

¹⁶Terrill-Stolper, H. A. *Final Report, AFOSR GSRP Program; 1995*, to be published.

Hulya Kirkici Report not available at time of publication.

A STUDY OF NOISE EFFECTS IN PHASE RECONSTRUCTION
FROM PHASE DIFFERENCES

Thomas F. Krile
Professor
Department of Electrical Engineering

Texas Tech University
Lubbock, TX 79409-3102

Final Report for:
Summer Faculty Research Program
Phillips Laboratory

Sponsored by:
Air Force Office of Scientific Research
Bolling Air Force Base, DC

and

Phillips Laboratory

July, 1995

A STUDY OF NOISE EFFECTS IN PHASE RECONSTRUCTION FROM PHASE DIFFERENCES

Thomas F. Krile
Professor
Department of Electrical Engineering
Texas Tech University

Abstract

Linear phase reconstruction algorithms, which determine phase from phase differences, are used in several areas, such as adaptive optics and speckle imaging. The purpose of this study is to examine the effects of noisy phase difference measurement inputs on reconstructor output phase noise. Both non-phasor and phasor-based path averaging techniques are considered, along with uncorrelated and correlated input noise. Analytic expressions for the output reconstructor noise variance and noise gain as functions of the input noise variance, input noise covariance matrix (for the correlated case), reconstructor matrix and system dimension are shown for the non-phasor case. A procedure for finding an analytic expression for the probability density function of the output noise in a general phasor-based path averaging operation is given for the uncorrelated noise case. Noise performance comparisons between the non-phasor and phasor-based techniques are shown.

A STUDY OF NOISE EFFECTS IN PHASE RECONSTRUCTION FROM PHASE DIFFERENCES

Thomas F. Krile

Introduction

In the areas of adaptive optics and speckle imaging, measurements of phase differences in an incident wavefront are used to reconstruct an estimate of the wavefront's phase field. In the case of adaptive optics, the phase information is then used to compensate for the effects of atmospheric turbulence [1]. Speckle imaging techniques use the phase information, along with measured intensity information, to reconstruct the complex field of the original object via Fourier transformation [2]. Sheared-beam speckle imaging is a recent active imaging variation which has the advantage of cancelling atmospheric disturbances without requiring adaptive optics elements [3,4,5].

In all of these techniques, a key operation is the recovery of phase information from noisy phase-difference data. Optimal linear reconstruction techniques are addressed by Hudgin [1] and Hunt [6], and a nonlinear phasor variant is given by Idell and Ginglewski in [2]. In this paper, the effects of noise on these linear and nonlinear techniques will be addressed for the cases of both uncorrelated and correlated noise.

Linear Model for Reconstruction

For a least-mean-square-error (LMS) reconstruction of phase from phase differences, a linear matrix-vector formulation can be used, such that

$$\Phi_t = [H] S, \quad (1)$$

where Φ_t is the true phase vector and S is a vector of phase differences in the x and y directions, S_x and S_y , respectively [1, 6]. The vectors are obtained by concatenating successive rows of the phase and phase difference matrices, respectively, and $[H]$ is the LMS reconstruction matrix. In the case of noisy phase difference measurements, the phase estimate is given by

$$\Phi = [H] (S + n) \quad (2)$$

where Φ is the LMS estimate of Φ_t and n is a noise vector of n_x and n_y noisy phase difference values. We will first examine the error in this linear phase estimate for the cases of uncorrelated and correlated noise vector components.

1. Uncorrelated noise.

By uncorrelated noise, we mean that each component n_i in the noise vector n is uncorrelated with any other component n_j . Also, all noise components are uncorrelated with all S (phase difference) components. We define a mean-square-error as

$$E^2 = \langle (1/N^2) (\Phi_t - \Phi) (\Phi_t - \Phi)^T \rangle \quad (3)$$

where $\langle \cdot \rangle$ is the expectation operator, T is the transpose operation and N^2 is the number of phase values being estimated. In the linear case with uncorrelated noise, E^2 is found to be: [7]

$$E^2 = (\sigma_n^2 / N^2) T_r \{ [H] [H]^T \} \quad (4)$$

where σ_n^2 is the variance of each individual noise component and $T_r \{ \cdot \}$ is the matrix trace operation. Thus we see that E^2 is linearly proportional to σ_n^2 for a given N , because $T_r \{ [H] [H]^T \}$ is a constant.

We also define a noise gain as the ratio of the output phase mean-square-error to the input noise variance, i.e.

$$\text{noise gain} = E^2 / \sigma_n^2. \quad (5)$$

In the linear, uncorrelated noise case, this becomes:

$$\text{noise gain} = (1 / N^2) T_r \{ [H] [H]^T \}, \quad (6)$$

which is a constant for a given N .

It should be noted that different phase constraints (e.g. zero piston) and different iteration techniques used when implementing a linear reconstructor will result in different effective $[H]$ matrices being used, and hence different error and noise gain results. However, the error will still be a linear function of σ_n^2 for a given N and noise gain will be constant for a given N , independent of σ_n^2 .

2. Correlated noise.

For the case of correlated noise components, we assume at least wide-sense stationarity, giving a noise covariance model of the form:

$$\langle n n^T \rangle = \sigma_n^2 \begin{bmatrix} 1 & \rho_1 & \rho_2 & \dots & \rho_{2N(N-1)} \\ \rho_1 & 1 & \rho_1 & \dots & \rho_{2N(N-1)-1} \\ \rho_2 & \rho_1 & 1 & \dots & \rho_{2N(N-1)-2} \\ \vdots & & & & \vdots \\ \vdots & & & & \vdots \\ \rho_{2N(N-1)} & \dots & & & 1 \end{bmatrix}. \quad (7)$$

From Eq. (3), the phase mean-square-error for the correlated case then becomes

$$E^2_{\text{cor.}} = (1 / N^2) T_r \{ [H] \langle n n^T \rangle [H]^T \}, \quad (8)$$

which can be separated into two components as:

$$\begin{aligned}
E^2_{\text{cor.}} &= (\sigma_n^2 / N^2) T_r \{ [H] [H]^T \} \\
+ (\sigma_n^2 / N^2) T_r \left[[H] \begin{bmatrix} 0 & \rho_1 & \rho_2 & \dots & \rho_{2N(N-1)} \\ \rho_1 & 0 & \rho_1 & \dots & \rho_{2N(N-1)-1} \\ \rho_2 & \rho_1 & 0 & \dots & \rho_{2N(N-1)-2} \\ \vdots & & & \ddots & \vdots \\ & & & \rho_{2N(N-1)} & \dots & 0 \end{bmatrix} [H]^T \right] & (9) \\
&= E^2 + E^2_{\text{cor. extra}}
\end{aligned}$$

Also, the new noise gain is

$$\text{noise gain correlated} = (E^2 + E^2_{\text{cor. extra}}) / \sigma_n^2. \quad (10)$$

Since $[H]$ and the correlation matrix are constants for a given N , we see that the phase noise again varies linearly with input noise σ_n^2 for a given N (albeit with larger slope than in the uncorrelated case) and the noise gain is still independent of σ_n^2 (but larger than for the uncorrelated case).

Fig. 1 shows some Monte Carlo simulation results for linear reconstructor output noise variance (E^2 for the uncorrelated case or $E^2_{\text{cor.}}$ for the correlated cases) vs. input noise variance for various correlation values. The correlations were obtained by separately passing x and y phase difference noise components through unweighted windows of length LAG (LAG = 1 means uncorrelated noise). The windowing was performed on the S vector noise components, so the resulting correlation was of a raster-scan (rather than block) form for the correlation matrix. Fig. 2 shows a plot of noise gain versus noise correlation, where gain was independent of σ_n^2 , as expected.

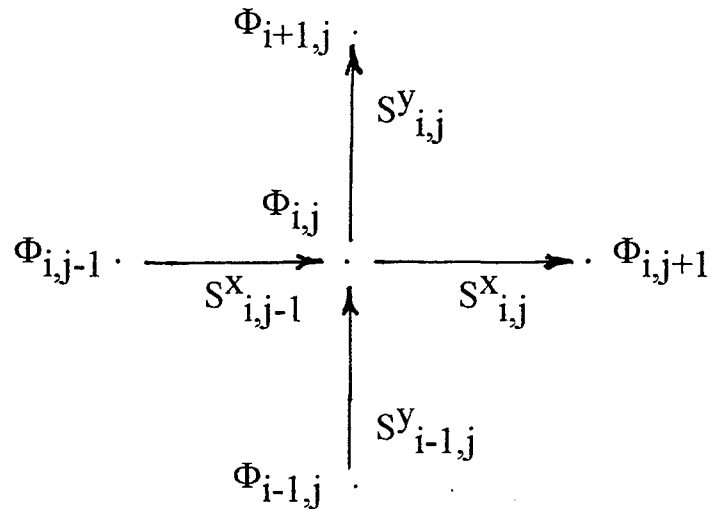
The simulation results shown in the figures demonstrate behaviour that is consistent with the equations. The noise performance numbers one will get

in practice will depend on the particular linear algorithm used ([H]) and the actual noise model (covariance matrix) in effect. Thus, using the equations developed above, we are now in a position to analytically predict linear phase reconstructor output noise performance in the uncorrelated and correlated noise cases, given appropriate reconstructor ([H]) and noise (covariance matrix) models, as was done for a special case in [7].

Phasor Variant of the Linear Model

In a typical LMS phase reconstruction algorithm, forming a weighted sum of phases and/or phase differences is an often-repeated operation. This presents a problem because of 2π phase ambiguities which can occur at points of zero field amplitude and has led to the idea of averaging phasor paths instead of phase(phase difference paths [2]. This introduces a nonlinearity into the reconstruction process, as far as noise is concerned, and leads to markedly different noise behaviour than for the non-phasor case.

Consider the following scenario for determining the phase $\Phi_{i,j}$ from its neighboring phases and phase differences.



where $S^X_{k,l} = \Phi_{k,l+1} - \Phi_{k,l}$ and $S^Y_{k,l} = \Phi_{k+1,l} - \Phi_{k,l}$. For the linear, non-phasor case, the LMS estimator for $\Phi_{i,j}$ is

$$\begin{aligned}\Phi_{i,j} = & w_1 * (\Phi_{i,j-1} + S^X_{i,j-1}) + w_2 * (\Phi_{i-1,j} + S^Y_{i-1,j}) \\ & + w_3 * (\Phi_{i+1,j} - S^Y_{i,j}) + w_4 * (\Phi_{i,j+1} - S^X_{i,j})\end{aligned}\quad (11)$$

where the weights are chosen to minimize the variance of $\Phi_{i,j}$. If all noise variances are assumed equal, then $w_i = 1/4$, $i=1$ to 4. Further, if each noise component is uncorrelated, normally distributed $N(0, \sigma_n^2)$, then the mean-square-error of $\Phi_{i,j}$ is given by $E^2 = \sigma^2 = (1/2) \sigma_n^2$.

For the phasor case, the phase at (i,j) is given by:

$$\begin{aligned}\Phi_{i,j} = & \text{Arg} \{ w_1 * \exp[j(\Phi_{i,j-1} + S^X_{i,j-1})] + w_2 * \exp[j(\Phi_{i-1,j} + S^Y_{i-1,j})] \\ & + w_3 * \exp[j(\Phi_{i+1,j} - S^Y_{i,j})] + w_4 * \exp[j(\Phi_{i,j+1} - S^X_{i,j})] \}. \quad (12)\end{aligned}$$

Assuming equal weights, the noise component of $\Phi_{i,j}$ is given by the random variable:

$$\begin{aligned}\Phi_{\text{noise}} = & \text{Arg} \{ \exp[j(\sum_{i=1}^2 n_i)] + \exp[j(\sum_{k=1}^2 n_k)] \\ & + \exp[j(\sum_{l=1}^2 n_l)] + \exp[j(\sum_{m=1}^2 n_m)] \}\end{aligned}\quad (13)$$

where the n 's are assumed here to be independent, $N(0, \sigma_n^2)$ random variables. This can be put into trigonometric form by setting:

$$\begin{aligned}X &= \sin(\sum_{i=1}^2 n_i) + \sin(\sum_{k=1}^2 n_k) + \sin(\sum_{l=1}^2 n_l) + \sin(\sum_{m=1}^2 n_m) \\ \text{and} \\ Y &= \cos(\sum_{i=1}^2 n_i) + \cos(\sum_{k=1}^2 n_k) + \cos(\sum_{l=1}^2 n_l) + \cos(\sum_{m=1}^2 n_m).\end{aligned}$$

Then

$$\Phi_{\text{noise}} = \tan^{-1}(X/Y), \quad -\pi \leq \Phi_{\text{noise}} \leq \pi. \quad (14)$$

Our main objective in this section of the study is to find the probability density function (pdf), and thence the variance, of Φ_{noise} as a function of σ_n^2 , so error performance can be compared to that of the linear, non-phasor case. Although the equal-weights case will be treated here, a parallel development for the non-equal weights situation has also been accomplished.

1. Development of noise pdf model.

Let $T = \sum_{h=1}^H n_h$. then T is normally distributed $N(0, 2*\sigma_n^2)$, so the random variable $U = \sin(T)$ has pdf:

$$f_U(u) = [1 / \text{sqr}(4 * \pi * \sigma_n^2 * (1-u^2))] * \sum \exp[-T^2 / (4 * \sigma_n^2)]$$

where the sum is taken over all T such that $t = \arcsin(u)$ and u varies from -1 to 1. For small values of σ_n^2 (say $< .3$), the pdf of U is distributed normal $N(0, 2*\sigma_n^2)$, while for large values of σ_n^2 (say > 3), the pdf of U becomes $1 / (\pi * \text{sqr}(1 - u^2))$, the pdf of a general sinusoid with uniformly distributed phase angle.

For terms of the form $V = \cos(T)$, the pdf is found to be:

$$f_V(v) = [1 / \text{sqr}(4 * \pi * \sigma_n^2 * (1-v^2))] * \sum \exp[-T^2 / (4 * \sigma_n^2)]$$

where the sum this time is taken over all T such that $T = \arccos(u)$. For $\sigma_n^2 = 0$, $f_V(v) = \delta(v-1)$, and as noise variance increases, the pdf eventually approaches $1 / (\pi * \text{sqr}(1 - v^2))$ as in the sine case for large σ_n^2 .

Now that the pdf's for the individual sine and cosine terms have been found, the pdf of X can be obtained by performing a four-fold convolution of the sine pdf, and the same operation can be performed on the cosine pdf to get the pdf of Y. These operations were carried out in practice both by using discrete convolutions and by utilizing the Fast Fourier transform (FFT). The range for both X and Y is now -4 to 4.

Given the pdf's of X and Y, one can obtain the pdf of $Z = X / Y$ by

performing the following "Mellin-like" transformation:

$$f_Z(z) = \int |y| f_X(zy) f_Y(y) dy. \quad (15)$$

This was done digitally, and the pdf $f_Z(z)$ was found to vary from normal $N(0, \sigma_n^2/2)$ for small σ_n^2 to $1 / (\pi * (1 + z^2))$ [Cauchy] for large σ_n^2 .

At this point, one would normally put the random variable Z through the transformation $\Phi_{\text{noise}} = \text{Tan}^{-1}(z)$, but the result would be in the range $-\pi/2$ to $\pi/2$, and for this application we need a range of $-\pi$ to π . This necessitated taking the density $f_X(x)$ and splitting it into disjoint positive and negative parts, so $f_X(x) = f_{X+}(x) + f_{X-}(x)$, and similarly for $f_Y(y)$. Then $f_Z(z)$ can be re-written as:

$$\begin{aligned} f_Z(z) &= \int |y| \{ [f_{X+}(zy) + f_{X-}(zy)] * [f_{Y+}(y) + f_{Y-}(y)] \} dy \\ &= f_{Z++}(z) + f_{Z+-}(z) + f_{Z-+}(z) + f_{Z--}(z). \end{aligned} \quad (16)$$

Now, letting $\Phi_{\text{noise}} = W = \text{Tan}^{-1}(z)$, the pdf of W can be written as:

$$\begin{aligned} f_W(w) &= [f_Z(\tan(w)) / \cos^2(w)], \quad -\pi \leq w \leq \pi \\ &= \begin{cases} [f_{Z++}(\tan(w)) + f_{Z-+}(\tan(w))] / \cos^2(w), & -\pi/2 \leq w \leq \pi/2 \\ f_{Z+-}(\tan(w)) / \cos^2(w), & \pi/2 \leq w \leq \pi \\ f_{Z--}(\tan(w)) / \cos^2(w), & -\pi \leq w \leq -\pi/2. \end{cases} \end{aligned} \quad (17)$$

This desired density for $W = \Phi_{\text{noise}}$ is found to vary from normal $N(0, \sigma_n^2/2)$ for small σ_n^2 to uniform $U[-\pi, \pi]$ for large σ_n^2 . A plot of this density variation is shown in Fig. 3. Thus we finally have a procedure for finding an analytic expression for the noise pdf at the output of a generic path-averaging operation in the phasor case. This pdf can now be used to

answer a number of questions, such as what the optimal path weights should be for given estimates of the path variances and how robust the weights are for variations in the path variance estimates. At present, the path weights to minimize mean-square-error are chosen as if the system were linear, and it is not known what effect this has on the actual nonlinear phasor reconstructor performance. This is a study which remains in the realm of future work.

Phasor vs. Non-phasor Noise Performance

A Monte-Carlo simulation of the variance of Φ_{noise} for the phasor and non-phasor cases as a function of σ_n^2 for the preceding path-averaging situation is shown in Fig. 4. We find that the behaviours are the same for small σ_n^2 , but the phasor noise then exceeds that of the non-phasor case for a range of σ_n^2 (and its slope, which is the noise gain, also exceeds that of the non-phasor case), and then saturates (with resulting small noise gain). This same type of relative behaviour has been observed at the output of full-blown non-phasor and phasor reconstructors. The dashed curves show the results of having correlated noise, and in this case we see that, although the phasor performance for moderate values of σ_n^2 is still worse than the non-phasor case, the deterioration in performance is more pronounced in the non-phasor case, i.e. the non-phasor case is less robust to correlation effects for the particular covariance model used.

Conclusions

In this study, several analytical formulations were developed which can be used to study the noise performance of linear non-phasor and

phasor-based phase reconstruction algorithms. In the non-phasor case, analytic expressions were shown for the output phase noise and reconstructor noise gain for both the situations of uncorrelated noise and correlated noise. Given the particular linear reconstructor model and input phase difference noise covariance model, one can determine the output noise parameters directly, without recourse to Monte-Carlo simulations. In the phasor case, for uncorrelated noise, a procedure was developed for analytically obtaining the probability density function (pdf) of the output noise for a generic path-averaging operation that is ubiquitous in linear reconstructors. Some special correlation cases (e.g. correlated noise within paths and uncorrelated noise terms between paths) can also be handled with this technique. The procedure does not depend on the form of the input noise pdfs (they don't have to be Gaussian) or on the particular path weighting used (not restricted to uniform weights). Thus one can use the results to determine optimal path weights for the nonlinear phasor averaging operations and can also study the robustness of these weights with respect to the phase-difference variances from which they are usually derived. It is hoped that the analytical techniques developed in this paper will be useful in studying these types of phase reconstructor noise performance questions.

References

1. R.H. Hudgin, "Wavefront Reconstruction for Compensated Imaging", J. Opt. Soc. Am., Vol. 67, 375-378, March, 1977.
2. P.S. Idell and J.D. Ginglewski, "Image Synthesis from Wave-Front Sensor Measurements of Coherent Diffraction Field", Opt. Letters, Vol. 15, 1309-1311, Nov. 15, 1990.

3. J.D. Ginglewski, P.S. Idell, D.G. Voelz, D.C. Dayton, B.K. Spielbusch and R.E. Pierson, "Coherent Image Synthesis from Wave-Front Sensor Measurements of a Non-Imaged Laser Speckle Field: A Laboratory Demonstration", Opt. Letters, Vol. 16, 1893-1895, Dec. 1, 1991.
4. R.A. Hutchin, "Sheared Coherent Interferometric Photography: A Technique for Lensless Imaging", Proc. SPIE, Vol. 2029, 161-168, 1993.
5. D.G. Voelz and J.D. Ginglewski, "SCIP Computer Simulation and Laboratory Verification", Proc. SPIE, Vol. 2029, 169-176, 1993.
6. B.R. Hunt, "Matrix Formulation of the Reconstruction of Phase Values from Phase Differences", J. Opt. Soc. Am. Vol. 69, 393-399, March, 1979.
7. K.E. Steinhoff, "Fast Wavefront Reconstruction on Specialized Rectangular Arrays", Report No. TR-723, the Optical Sciences Company, Placentia, CA, 1986.

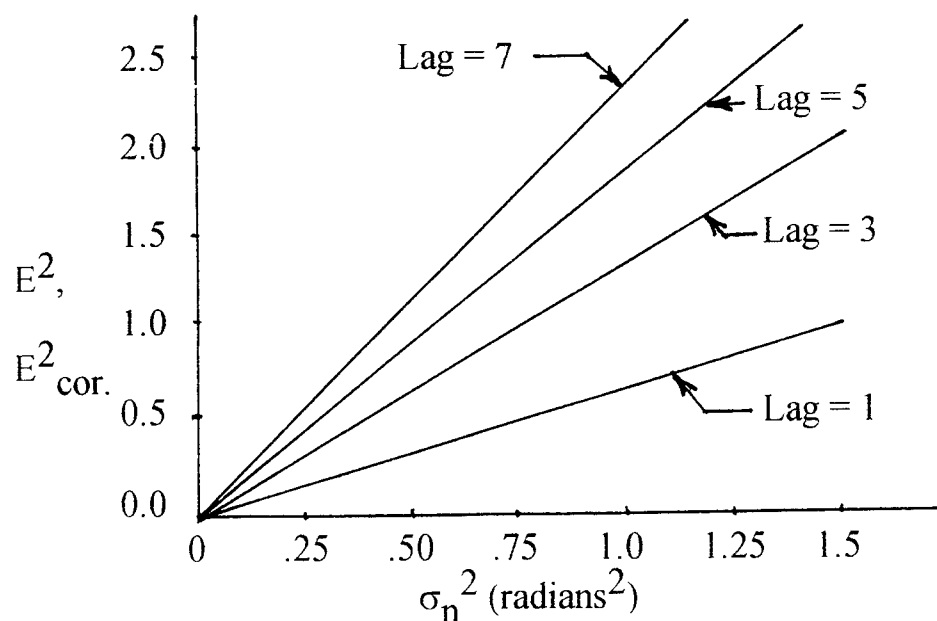


Figure 1. E^2 and $E^2_{\text{cor.}}$ vs σ_n^2 for various correlation lags.

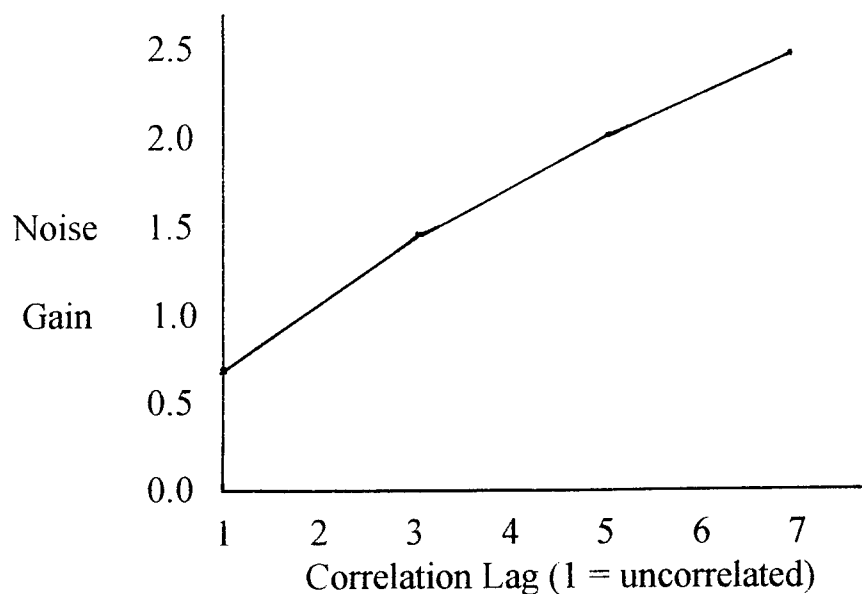


Figure 2. Noise gain vs correlation lag for given N.

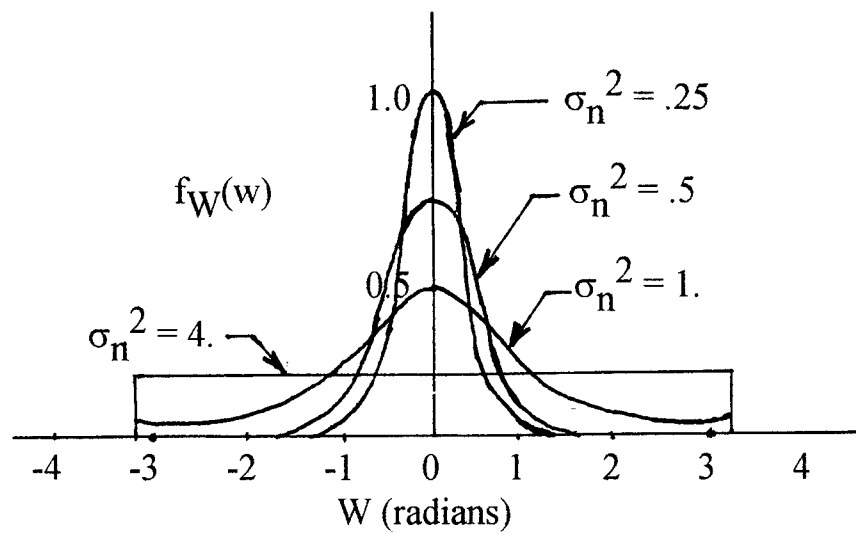


Figure 3. Density of $W = \Phi_{\text{noise}}$ for various σ_n^2 .

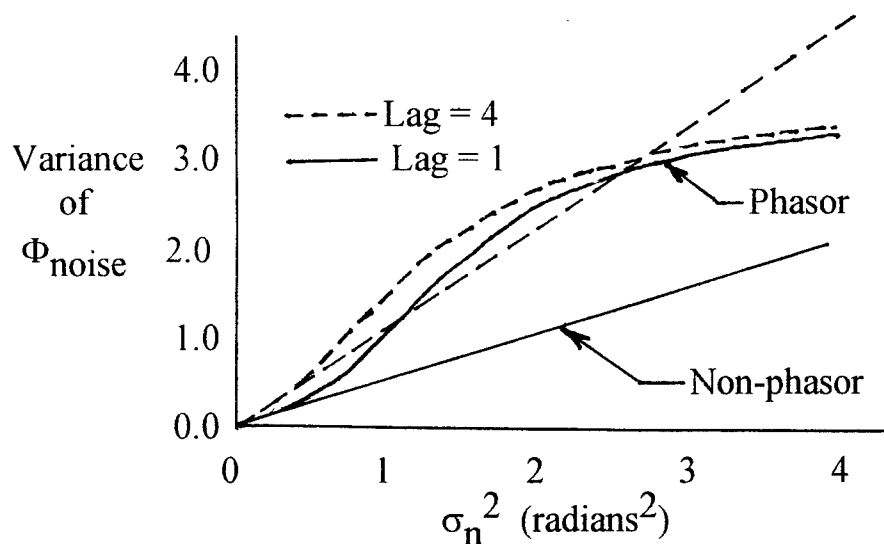


Figure 4. Variance of output noise vs. σ_n^2 .

Ionospheric Tomography via Iterative Cross-Entropy Minimization

**Walter S. Kuklinski
Associate Professor
Department of Electrical Engineering**

**University of Massachusetts Lowell
One University Avenue
Lowell MA 01854**

**Final Report for:
Summer Research Program
Phillips Laboratory**

**Sponsored by:
Air Force Office of Scientific Research
Bolling Air Force Base, DC**

and

**Phillips Laboratory Hanscom
Air Force Base**

Ionospheric Tomography via Iterative Cross-Entropy Minimization

Walter S. Kuklinski

Associate Professor

Department of Electrical Engineering
University of Massachusetts Lowell

Abstract

The problem of reconstructing ionospheric electron densities from ground-based receiver to satellite TEC (Total Electron Content) measurements is formulated as an underdetermined linear inverse problem. By assuming the ionospheric electron density is constant in a fixed set of J spatial cells an (Lx1) vector of TEC measurements \underline{c} can be related to a (Jx1) vector of electron densities \underline{d} as: $\underline{c} = \underline{A}\underline{d}$ where \underline{A} is an (LxJ) matrix of ray path distances. The algorithm presented here utilized an iterative cross-entropy optimization technique. In this technique the Kullback-Leibler distance between any two nonnegative vectors \underline{a} and \underline{b} , $KL(\underline{a},\underline{b})$, is used to define a functional $\alpha KL(P\underline{x},\underline{y}) + (1-\alpha)KL(\underline{x},\underline{p})$ that is minimized using an alternating projection iterative method. The method requires \underline{x} and \underline{y} be nonnegative vectors, related as: $\underline{y} = P\underline{x}$. P is further constrained to contain only nonnegative elements and have unity column sums. \underline{p} is a prior estimate of \underline{x} used to regularize the solution. α allows a tradeoff to be made between data consistency and regularization. Using a factored representation of $A = PD_C$ where, D_C is a diagonal scaling matrix with elements equal to the column sums of A , the Ionospheric Tomography problem can be transformed to satisfy the convergence criteria of the alternating projection iterative minimization technique.

This algorithm has been evaluated using TEC data corresponding to known incoherent scatter radar electron density measurements. Maximum entropy reconstructions, which did not require a prior estimate of the electron density, and minimum cross-entropy reconstructions that utilized model electron density data as the prior vector \underline{p} have been produced. The results, which were obtained using a 100 Mhz 80486 processor, required less than 20 seconds of CPU time and less than 8 Mbytes of RAM. The high quality of these reconstructions coupled with computational efficiency of this algorithm indicates the potential utility of this technique for real-time Ionospheric Tomography.

Introduction

The problem of reconstructing ionospheric electron densities from ground based receiver to satellite TEC measurements has been addressed in a number of previous studies [1-6]. The majority of these algorithms have assumed the ionospheric electron density is constant within a set of J fixed grid cells producing a linear relationship between an (Lx1) vector of TEC measurements \underline{c} and a (Jx1) vector of electron densities \underline{d} as:

$$\underline{c} = A \underline{d} \quad (1)$$

where A is an (LxJ) matrix of raypath distances.

In a typical case J < L, ie. there are fewer measurements than electron density values, yielding an under-determined system of equations. Even if more measurements were available, the measurement geometry typically limits the number of independent measurements such that the rank of A is always less than J, precluding a unique solution without the use of additional information or constraints. There are both spatial and temporal sources of error that cause these equations to be inconsistent as well. The actual electron density may not be constant within a grid cell, hence two rays which pass through that cell may produce TEC data consistent with different values of electron density. Since the individual receiver to satellite TEC data are not obtained at the same time the electron density within a given cell may not be consistent for all measurements.

The Ionospheric Tomography problem does have certain characteristics that set it apart from a general inconsistent under-determined linear inverse problem and, which can be exploited to produce a computationally efficient inversion algorithm. The ionospheric electron densities, grid cell raypath distances, and associated TEC measurements are all nonnegative quantities. In addition the A matrix is quite sparse, having on the order of 1 to 2% non-zero elements. A computationally efficient iterative image reconstruction algorithm for problems with nonnegative densities and measurement matrices that has been presented by Byrne[7] was adapted here. In this algorithm the Kullback-Leibler distance between any two nonnegative vectors \underline{a} and \underline{b} ,

$$KL(\underline{a}, \underline{b}) = \sum a_n \log(a_n/b_n) + b_n - a_n \quad (2)$$

is used to define a functional

$$G(\underline{x}) = \alpha KL(P\underline{x}, \underline{y}) + (1-\alpha) KL(\underline{x}, \underline{p}) \quad (3)$$

that is minimized using an iterative alternating projection method. The method requires \underline{x} and \underline{y} be nonnegative vectors, related as: $\underline{y} = P\underline{x}$. The constant α ($0 < \alpha < 1$) is a scale factor that controls the tradeoff between the consistency of the solution \underline{x} to the observed measurements \underline{y} , which is quantified by the cross-entropy term $KL(P\underline{x}, \underline{y})$, and the degree to which the cross-entropy regularization term $KL(\underline{x}, \underline{p})$ forces the solution \underline{x} to be near a prior estimate \underline{p} . For convergence P is further constrained to contain only nonnegative elements and have unity column sums.

Tomography problems that utilize TEC data obtained from uniformly spaced satellite positions and arbitrary receiver positions within the angular limits of a uniformly spaced two dimensional polar, or three dimensional spherical, array of grid cells, do not yield A matrices that have unity column sums. These problems can be solved via the iterative alternating projection method using a factored representation of $A = PD_C$. D_C is a diagonal scaling matrix with elements equal to the corresponding column sums of A . D_C represents a coordinate transformation from the native domain determined by the specific grid structure and satellite-receiver geometry to a solution domain where the convergence requirements of the iterative projection solution technique are satisfied. Using this factored representation TEC data is related to electron density as:

$$\underline{c} = PD_C \underline{d} \quad (4)$$

Defining $\underline{x} = D_C \underline{d}$ and $\underline{y} = \underline{c}$ and $P = AD_C^{-1}$ the ionospheric electron density can be obtained by determining \underline{x} that minimizes:

$$G_s(\underline{x}) = \alpha KL(P\underline{x}, \underline{y}) + (1-\alpha) KL(\underline{x}, \underline{p}_C)$$

(5)

where $\underline{p}_C = D_C \underline{p}$ is solution domain representation of the prior electron density estimate. The native domain representation of this solution can then be obtained as $\underline{d} = D_C^{-1} \underline{x}$

The solution domain vector \underline{x} that minimizes $G_S(\underline{x})$ is obtained from the limit as n approaches infinity of the following iteration:

$$\underline{x}^{n+1} = (\underline{x}^n)^\alpha * (\underline{p}_c)^{(1-\alpha)} * \exp[\alpha P^T * \log(\underline{y} / P\underline{x}^n)] \quad (6)$$

Where $*$ represents vector element by element multiplication, $/$ vector element by element division, and the superscript T denoting matrix transpose. The indicated log and exponentiations are vector element by element operations as well.

This iterative scheme will converge to the unique minimizer of $G_S(\underline{x})$ for $\alpha < 1$. For $\alpha = 1$ the solution depends on the consistency of the equations $\underline{y} = P\underline{x}$. For those cases where a nonnegative solution of $\underline{y} = P\underline{x}$ does not exist the iterative scheme will also converge to the unique minimizer of $G_S(\underline{x})$. In both of these cases the solution is independent of \underline{x}^0 the starting point of the iteration. For those cases where a nonnegative solution of $\underline{y} = P\underline{x}$ does exist the iterative scheme will converge to the unique solution of these equations that also minimizes $KL(\underline{x}, \underline{x}^0)$ the cross-entropy between the solution and \underline{x}^0 .

Results

The algorithm was evaluated using TEC data corresponding to known incoherent scatter radar measurements of electron density [9]. A contour plot representation of the source electron density is seen in figure 1. The raypath sums for the cells defined by a polar grid with 15 altitude divisions from 160 to 600 Km and 90 latitude divisions from 34 to 57 N with receiver positions at 41.05 N, 42.47 N, 44.77 N, 48.31 N and 231 coplanar uniform satellite positions from 34 to 57 N latitude is seen in figure 2. Maximum entropy reconstructions and minimum cross-entropy reconstructions, that utilized a PIM generated prior electron density vector \underline{p} , have been produced and are seen in figures 3 and 4. An additional reconstruction was produced using a modified prior vector \underline{p}_m . This vector was produced by modifying the PIM model before applying the iterative solution process.

The model was modified by adding a constant offset electron density that minimized the total squared difference between the observed TEC data and the TEC data produced by the modified model. All of these reconstructions were performed using $\alpha = 1$. Since this TEC data and geometry was produced an underdetermined consistent set of equations which had nonnegative solutions the initial solution vector \underline{x}^0 was used to produce different solutions. The maximum entropy solution was produced using equation (6) with $\underline{x}^0 = D_c [S/e \ S/e \ S/e \ \dots]^T$ where S is the sum of cD_c^{-1} . The two minimum cross-entropy reconstructions were produced using equation(6) with $\underline{x}^0 = D_c \underline{p}$ and $\underline{x}^0 = D_c \underline{p}_m$ respectively.

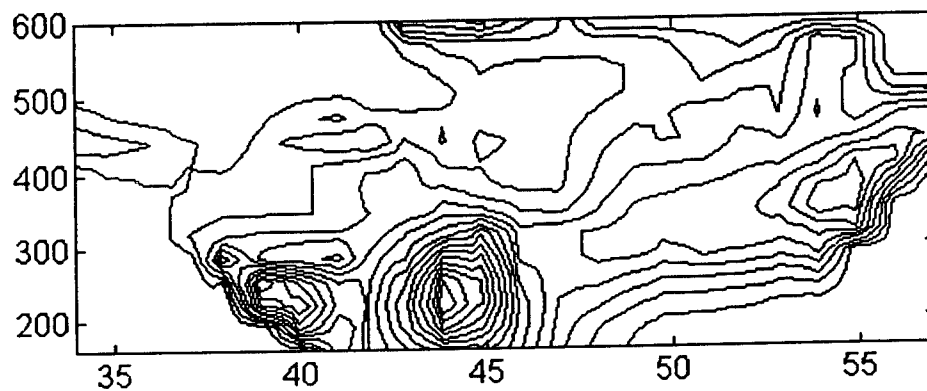


Figure 1. Contour Plot of Electron Density Measured by Millstone Hill Incoherent Scatter Radar

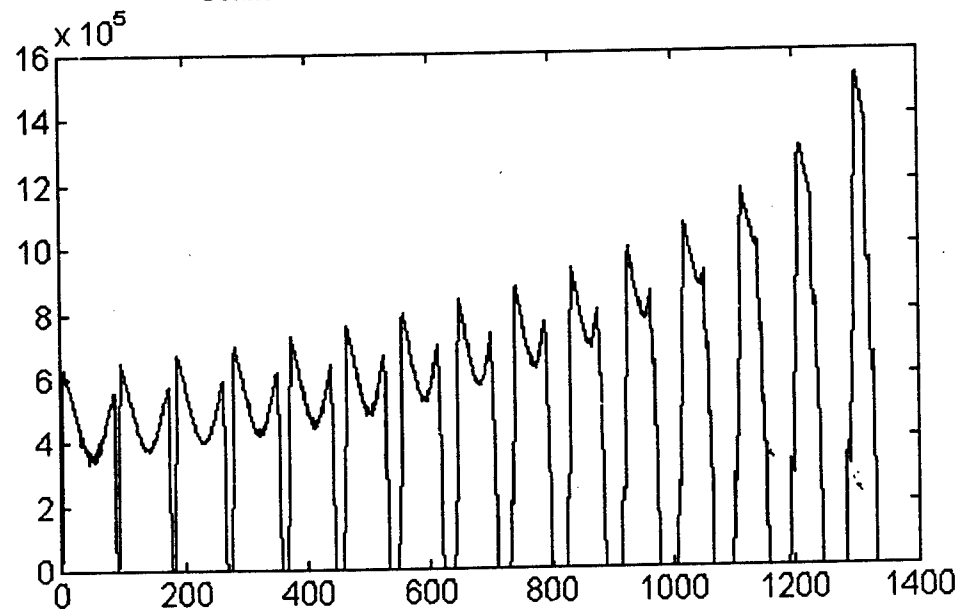


Figure 2. Cell Raypath Sums

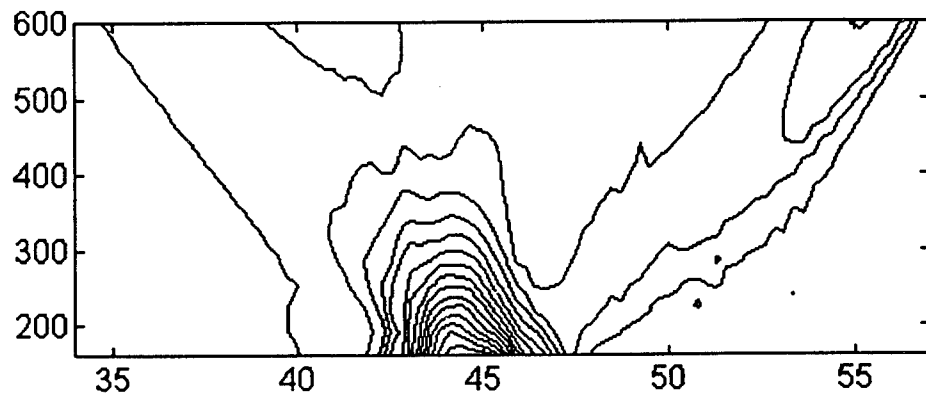


Figure 3. Contour Plot of Maximum Entropy Electron Density Reconstruction

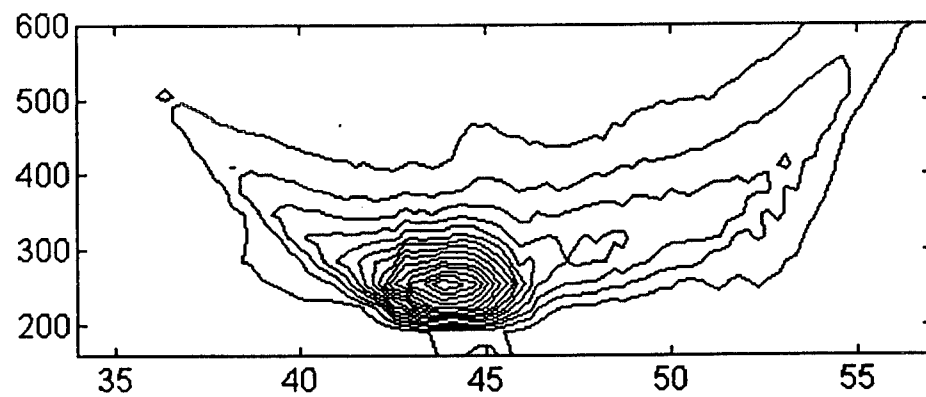


Figure 4. Contour Plot of Minimum Cross-Entropy Electron Density Reconstruction Using PIM Model

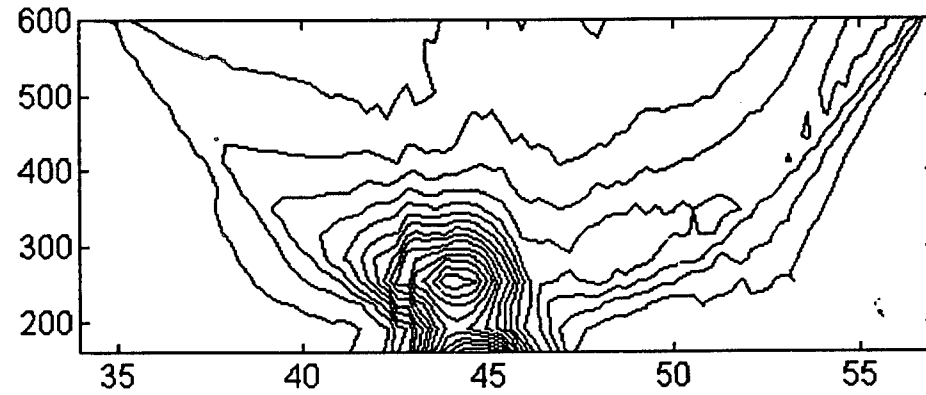


Figure 5. Contour Plot of Minimum Cross-Entropy Electron Density Reconstruction Using Modified PIM Model

Discussion

The results obtained using the iterative projection method represent a significant increase in the development of a computationally efficient ionospheric tomography algorithm. The sparse nature of the native domain A matrix and the related solution domain P matrix greatly reduce the number of operations required to update \underline{x}^{n+1} as indicated in equation (6). The transformation to the solution domain is straightforward and allows ionospheric tomography problems to be represented in a manner that can be solved using the iterative projection method. The use of the transformation matrix does however change the way the resulting solutions are related to the initial solution vector. For example, in maximum entropy restorations use a native domain initial solution $\underline{d}^0 = [S/e \ S/e \ S/e \ . \ . \ .]^T$. Rather than a direct minimum cross-entropy relationship between the native domain electron density vectors \underline{d} and \underline{d}^0 , consistent equations sets will produce an iterative scheme that converges to the unique solution that minimizes $KL(D_c \underline{d}, D_c \underline{d}^0)$, the weighted cross-entropy between \underline{d} and \underline{d}^0 . Since the elements of D_c are the total raysum distances through a given cell, cells with fewer rays passing through them contribute less to the cross-entropy and allow proportionally larger variations in the corresponding element in \underline{d} . To reduce these variations, which can produce reconstructions with nonrealistic sharply peaked features, a modified cell structure is required. This cell structure would selectively increase the size of cells in regions where a uniform grid has low total ray sum distances. The this algorithm is presently under development, and will allow true maximum entropy and minimum cross-entropy reconstrunctions to be produced using the iterative projection method.

References

1. J. R. Austen, S.J. Franke, C.H. Liu, "Ionospheric imaging using computerized tomography," Radio Science Vol. 23, pp. 299-307 1988
2. T. D. raymund, J. R. Austen, S. J. Franke, C. H. Liu, J. A. Klobuchar, " Application of computerized tomography to the investigation of ionospheric structures," Radio Science Vol. 25, pp. 771-789
3. H. NA, H. Lee, "Resolution analysis of tomography reconstruction of electron density profiles in the ionosphere," Int.J. of Imaging Systems and Technology, Vol. 2, pp. 209-218 1990
4. H. NA, H. Lee, "Orthogonal deccompositions technique fro ionospheric tomography" Int.J. of Imaging Systems and Technology, Vol. 3, pp. 354-365 1991

5. S. E. Pryse, L. Kersely,"A preliminary experimental test of ionospheric tomography," J. of Atmospheric and Terrestrial Physics, Vol. 7, pp. 721-732
6. E.J. Fremouw, J.A. Secan, B.M. Howe, "Application of stochastic inverse theory to ionospheric tomography," Radio Science Vol. 27, pp. 721-732 1992
7. P.F. Fougere, "Ionospheric radiotomography using maximum entropy 1. Theory and simulation studies," Vol. 30, pp.429-444
8. C. Byrne, "Iterative image reconstruction algorithms based on cross-entropy minimization," IEEE Trans.Image Proc., Vol. 2., pp. 96-103 (1993)
9. T. Raymund , " Comparison of several tomography algorithms,"